UC Merced

UC Merced Electronic Theses and Dissertations

Title

Modeling Optical Spectroscopy and Resonance Energy Transfer for Chromophores in Explicit Solvent Environments

Permalink

https://escholarship.org/uc/item/5dn5g85v

Author

Khanna, Ajay

Publication Date

2024

Copyright Information

This work is made available under the terms of a Creative Commons Attribution License, available at https://creativecommons.org/licenses/by/4.0/

Peer reviewed|Thesis/dissertation

eScholarship.org Powered by the California Digital Library
University of California

UNIVERSITY OF CALIFORNIA, MERCED

Modeling Optical Spectroscopy and Resonance Energy Transfer for Chromophores in Explicit Solvent Environments

A dissertation submitted in partial satisfaction of the
requirements for the degree
Doctor of Philosophy

in

Theoretical Chemistry

by

Ajay Khanna

Committee in charge:

Professor Hrant Hratchian, Chair
Professor Christine Isborn, Advisor
Professor Liang Shi
Professor Ashlie Martini

2024

Copyright
Ajay Khanna, 2024
All rights reserved.

The dissertation of Ajay Khanna is approved, and
it is acceptable in quality and form for publication
on microfilm and electronically:

_____
(Professor Christine Isborn, Advisor)

_____
(Professor Liang Shi)

_____
(Professor Ashlie Martini)

_____
(Professor Hrant Hratchian, Chair)

University of California, Merced

2024

DEDICATION

To my family.

To my partner.

To my friends.

Stay resilient and don't give up on your dreams.

EPIGRAPH

To work alone you have the right, and not to the fruits.
Do not be impelled by the fruits of work.
Nor have attachment to inaction.
—Bhagavad Gita

TABLE OF CONTENTS

Signature Page iii

Dedication iv

Epigraph v

Table of Contents vi

List of Figures x

List of Tables xviii

Acknowledgements xix

Vita and Publications xx

Abstract xxi

Chapter 1 Introduction 1
1.1 Schrödinger's Quantum Mechanics 1
1.1.1 The Hydrogen Atom 2
1.1.2 The Harmonic Oscillator 4
1.1.3 The Born-Oppenheimer Approximation 6
1.2 Ground State Electronic Structure Methods 8
1.2.1 Hartree-Fock (HF) 8
1.2.2 Density Functional Theory (DFT) 11
1.2.3 The Kohn-Sham Equation 13
1.3 Excited State Electronic Structure Methods 14
1.3.1 Configuration-Interaction Singles (CIS) 15
1.3.2 Time Dependent Density Functional Theory (TDDFT) 16
1.4 Fundamentals of UV-Visible Spectroscopy 18
1.4.1 Fermi's Golden Rule 19
1.4.2 The Jablonski Diagram 20
1.4.3 Electronic Transitions 21
1.4.4 The Stokes Shift 22
1.4.5 The Mirror-Image Rule 22
1.4.6 Environmental Influence 23

Chapter 2 Benchmark of Density Functionals for Vibronic Spectra 26
2.1 Introduction 26
2.2 Jacob's Ladder of Density Functional Theory 28
2.2.1 Rung 1: Local Density Approximation (LDA) . . . 29
2.2.2 Rung 2: Generalized Gradient Approximation (GGA) 30

2.2.3 Rung 3: Meta-Generalized Gradient Approximation (mGGA) . . . 31
2.2.4 Rung 4: Hybrid Functionals . . . 31
2.2.5 Rung 5: Double-Hybrid Functionals . . . 32
2.3 Charge Transfer (CT) Excitations . . . 33
2.3.1 The Role of Exact Hartee-Fock Exchange . . . 34
2.3.2 Range-separated/long-range hybrid functionals . . . 35
2.4 Hybrid DFT Functionals for Vibronic Spectra . . . 36
2.4.1 Benchmark Study: Effect of Density Functional on Spectral Lineshapes . . . 38
2.4.2 Computational Details . . . 39
2.4.3 Nile Red in Water and Cyclohexane: Implicit Solvent Models . . . 40
2.4.4 Vibronic Spectra in Explicit Solvent Environment . . . 45
2.5 Conclusions . . . 50

Chapter 3 Ensemble Franck-Condon Methods For Absorption and Fluorescence Spectroscopy . . . 51
3.1 Introduction . . . 51
3.2 Environmental Effect on Molecular Spectra . . . 52
3.3 Configuration Sampling Techniques . . . 54
3.4 Vertical Excitation Energy (VEE) Approach . . . 58
3.5 Nuclear Ensemble Approach . . . 59
3.6 The Franck-Condon Approach . . . 60
3.7 Combined Ensemble Franck-Condon (E-FC) Approaches . . . 61
3.7.1 Summation of an Ensemble of Finite Temperature Franck-Condon Spectra . . . 62
3.7.2 Optimized Ensemble Average Finite Temperature Franck Condon Approach . . . 63
3.7.3 Ensemble Average Zero Temperature Franck Condon Approach . . . 64
3.8 Case Study: Cresyl Violet Cation in Methanol . . . 65
3.9 Conclusion . . . 69

Chapter 4 Calculating Absorption and Fluorescence Spectra for Chromophores in Solution with Ensemble Franck-Condon Methods . . . 70
4.1 Introduction . . . 71
4.2 Computational Details . . . 73
4.2.1 Sampling Configurations Using Ab Initio Molecular Dynamics . . . 73
4.2.2 Performing Electronic Structure Calculations . . . 76
4.2.3 Generating Spectra Using Combined Ensemble-Franck-Condon (E-FC) Methods . . . 77
4.2.4 Spectral Simulation Parameters and Alignment . . . 78

4.3 Result and Discussion 80
4.3.1 NBD in DMSO 81
4.3.2 Nile Red in DMSO 91
4.3.3 7MC in Methanol 98
4.3.4 Relative Computational Cost of E-FC Methods . . 105
4.4 Conclusions 107

Chapter 5 Going Beyond Förster Theory: Resonance Energy Transfer Processes in Explicit Environment 109
5.1 Introduction 109
5.2 Theoretical Details 112
5.2.1 The Spectral Overlap Integral 112
5.2.2 Coupling Methods 113
5.2.3 Transition Densities 113
5.2.4 Transition Charges 114
5.2.5 Transition Dipoles 114
5.2.6 Diabatization 115
5.2.7 Environmental Factors 116
5.3 Computational Details 117
5.3.1 Configuration Sampling 118
5.3.2 Electronic Structure Calculations 120
5.4 Preliminary Results and Discussion 120
5.4.1 Orientation Factor from the AIMD simulation for NBD-NR in DMSO 120
5.4.2 Coupling between NBD-NR in DMSO 122
5.4.3 Coupling between CV+ dimer 126
5.5 Next Steps 128
5.6 Conclusion 129
5.7 Future Outlook 130

Chapter 6 Uncharted Frontier for Relative Binding Free Energy Using Hybrid QM/MM Methods 131
6.1 Introduction 131
6.2 Theoretical Details 135
6.3 Computational Details 136
6.3.1 PDB Structure preparation and Docking 136
6.3.2 MD Simulations with OpenMM 137
6.3.3 QM/MM Optimization and Energy Calculations with OpenMM-Terachem 138
6.4 Preliminary Results and Discussion 139
6.4.1 Impact of QM Region on Free Energies 139
6.5 Conclusion 148

Appendix A Chapter 3 Supplemental Information 151
A.1 Combined Ensemble Franck Condon Code 151
A.1.1 Generating The Nuclear Ensemble Spectra 151
A.1.2 Generating The EsumFTFC Spectra 157
A.1.3 Generating The Average FC Lineshape 163
A.1.4 Generating The Approximate EFC Spectra: EoptavgFTFC and EavgZTFC 170

Appendix B Chapter 4 Supplemental Information 177
B.1 Intensity to Lineshape Transformations 177
B.1.1 Transforming Experimental Intensity Spectra to Lineshapes 177
B.1.2 Transforming Computed Intensity Spectra to Lineshapes 182

Appendix C Chapter 5 Supplemental Information 186
C.1 Computing Excitonic Couplings Between Chromophores Using Various Methods 186
C.1.1 Transition Coupling Via Transition Charges 186
C.1.2 Transition Coupling Via Transition Dipole Moments 193
C.1.3 Transition Coupling Via Diabatization 197

Bibliography 204

LIST OF FIGURES

Figure 1.1: The simple harmonic oscillator model 4
Figure 1.2: One form of Jablonski diagram showing absorption, internal crossing (IC), vibrational relaxation(VR), and emission processes . . . 20
Figure 1.3: Electronic Transitions 21
Figure 1.4: Absorption and emission spectra of anthracene showing mirror image relation. Adapted from Byron, C.M. and Werner, T.C., *J. Chem. Ed.*, 1991, 68, 433.[85] 23
Figure 1.5: Absorption and fluorescence lineshape spectra of NBD in various implicit solvents of increasing dielectric constant. The level of theory used is TDA/CAM-B3LYP/6-31G(d) with IEFPCM solvent model 23

Figure 2.1: The Jacob's Ladder 29
Figure 2.2: The density difference plot of 4Amino-4'Nitrostilbene push-pull electron system 33
Figure 2.3: Mean absolute and mean signed error relative to experimental λ_{max} and vertical excitation energies. The figure is reproduced from article[230] with permission obtained from the International Journal of Quantum Chemistry 37
Figure 2.4: Chemical structures of the three chromophores used as benchmarks in this chapter: 7-nitrobenz-2-oxa-1,3-diazol-4-yl (NBD), Nile red (NR), and 7-methoxy coumarin-4-acetic acid (7MC). . . 38
Figure 2.5: Experimental absorption spectra of NR in water and cyclohexane. The experimental data was extracted using the WebPlot digitizer from article[326] 41
Figure 2.6: Nile Red in Water: Density functional comparison for FTFC absorption spectra in an implicit water solvent. The level of theory used here is TDA/6-31G and the IEFPCM implicit solvent model was used for solvent effects. The spectra are reproduced with permission from the Journal of Chemical Physics found in the SI of article[146] 42
Figure 2.7: Nile Red in cyclohexane: Density functional comparison for FTFC absorption spectra in an implicit cyclohexane solvent. The level of theory used here is TDA/6-31G and the IEFPCM implicit solvent model was used for solvent effects. The spectra are reproduced with permission from the Journal of Chemical Physics found in the SI of article[146] 44

Figure 2.8: Comparison of average FTFC lineshape with experimental lineshape for NR in DMSO obtained from CAM-B3LYP, LC-wHPBE, and M06-2X. The average FTFC lineshape is generated using 5 snapshots for both absorption and emission spectra. The inset plot shows absorption and emission spectra generated with the implicit solvent model. All spectra are generated using the adiabatic Hessian approach with the TDA/6-31G* level of theory. 46
Figure 2.9: Comparison of average FTFC lineshape with experimental lineshape of NBD in DMSO obtained from CAM-B3LYP, LC-ωHPBE, and M06-2X. The average FTFC lineshape is generated using 5 snapshots for both absorption and emission lineshape. The inset plot shows absorption and emission lineshapes generated with the implicit solvent model. All lineshapes are generated using the adiabatic Hessian approach with the TDA/6-31G* level of theory. 48
Figure 2.10: Comparison of average FTFC lineshape with experimental spectra of 7MC in methanol obtained from CAM-B3LYP, LC-wHPBE, and M06-2X. The average FTFC lineshape is generated using 5 snapshots for both absorption and emission spectra. The inset plot shows absorption and emission spectra generated with the implicit solvent model. All spectra are generated using the adiabatic Hessian approach with TDA/6-31G* level of theory. 49

Figure 3.1: Effect of the expanding protein environment of the absorption spectra of Fluorescent Protein mKeima. Adapted from Marc Nadal-Ferret et al., J. Chem. Theory Comput. 2013, 9, 3, 17311742[347] 53
Figure 3.2: Absorption lineshapes of CV^+ in Methanol: Filled gray spectra are experimental lineshapes, transformed from Ref.[433] All lineshapes are shifted energetically to align with the experimental lineshape maxima. 66
Figure 3.3: Pictorial representation of the E-avg$_{10}$ZTFC and E$_{opt}$-avg$_{10}$FTFC methods for CV^+ in methanol: The two columns a) and b) absorption. The top row shows the distribution of VEEs from a) unoptimized and b) optimized geometries on the ground state, respectively. The middle row depicts the procedure of generating the average FC lineshape by aligning the $0 \rightarrow 0$ transition energies. The bottom row represents the dressing of the ω_{00} shifted unoptimized and optimized VEEs with avg$_{10}$ZTFC and avg$_{10}$FTFC lineshapes, resulting in E-avg$_{10}$ZTFC and E$_{opt}$-avg$_{10}$FTFC methods, respectively. 67

Figure 4.1: Computational procedure for modeling absorption and fluorescence spectra of dyes in an implicit and explicit solvent environment using various spectroscopy methods. 74

Figure 4.2: Average FTFC lineshapes generated for absorption and emission. The average FTFC lineshapes were computed using 10 random snapshots from 5 sampling procedures 77
Figure 4.3: Original experimental spectra and lineshape transformation of NBD and NR in DMSO[286] and 7MC in methanol.[287] 79
Figure 4.4: Unshifted lineshapes of all three dyes: a) NBD in DMSO, b) NR in DMSO, and c) 7MC in methanol 79
Figure 4.5: E-sum$_{30}$FTFC absorption lineshape of NR in explicit DMSO generated using HWHM of 10 cm^{-1} and 135 cm^{-1} on each FTFC lineshape. 80
Figure 4.6: Chemical structures of the three chromophores studied in this work: 7-nitrobenz-2-oxa-1,3-diazol-4-yl (NBD), Nile red (NR), and 7-methoxy coumarin-4-acetic acid (7MC). 81
Figure 4.7: NBD in DMSO: Vertical excitation energies obtained from ground state AIMD snapshots and vertical de-excitation energies obtained from excited state AIMD snapshots. Energy gaps are also shown for the same snapshots after geometry optimization in a frozen QM solvent environment. Corresponding oscillator strengths are included as an inset. 82
Figure 4.8: Absorption and fluorescence lineshapes of NBD in DMSO: Filled gray spectra are experimental lineshapes, transformed from Ref.286. a) Ensemble and implicit solvent FTFC methods, b) E-sum$_{100}$FTFC and individual FTFC spectra, and c) E-avg$_{10}$ZTFC, E$_{opt}$-avg$_{10}$FTFC, and E-sum$_{100}$FTFC lineshapes. All lineshapes are shifted energetically to align with the experimental lineshape maxima. 84
Figure 4.9: NBD in DMSO: a) VEEs computed for ground state AIMD configurations and b) VDEs computed for S_1 excited state AIMD configurations computed for both QM solvent and chromophore-only (strip solvent) configurations. 85
Figure 4.10: Frequency distribution of a) absorption and b) emission vibronic lineshape FWHM values of NBD in DMSO. The dotted gray lines correspond to the FWHM of the implicit solvent FTFC spectra (Abs: 0.330 eV, Ems: 0.381 eV). The dashed black lines represent the average values of the FWHM of the explicit solvent FTFC spectra (Abs: 0.366 eV, Ems: 0.514 eV). 87

Figure 4.11: Pictorial representation of the E-avg$_{10}$ZTFC and E$_{opt}$-avg$_{10}$FTFC methods for NBD in DMSO: The first two columns a) and b) represent emission, and the columns c) and d) represent absorption. The top row shows the distribution of VDEs from a) unoptimized and b) optimized geometries and VEEs from c) unoptimized and d) optimized geometries on the excited and ground state PESs, respectively. The middle row depicts the procedure of generating the average FC lineshape by aligning the $0 \rightarrow 0$ transition energies. The bottom row represents the dressing of the ω_{00} shifted unoptimized and optimized VDEs and VEEs with avg$_{10}$ZTFC and avg$_{10}$FTFC lineshapes, resulting in E-avg$_{10}$ZTFC and E$_{opt}$-avg$_{10}$FTFC methods, respectively. 88
Figure 4.12: NBD in DMSO: Comparison of FC methods, including adiabatic Hessian, vertical gradient, and adiabatic shift with the TDA/CAM-B3LYP/6-31G* level of theory. 90
Figure 4.13: Comparison of average FTFC vibronic lineshape generated using five randomly selected explicit solvent snapshots using TD and TDA for NBD in DMSO using CAM-B3LYP/6-31G* level of theory. 90
Figure 4.14: NR in DMSO: Vertical excitation energies obtained from ground state AIMD snapshots and vertical de-excitation energies obtained from excited state AIMD snapshots. Energy gaps are also shown for the same snapshots after geometry optimization in a frozen QM solvent environment. Corresponding oscillator strengths are included as an inset. 91
Figure 4.15: Absorption and fluorescence lineshapes of NR in DMSO: Filled gray spectra are experimental lineshapes, transformed from Ref.286. a) Ensemble and implicit solvent FTFC methods, b) E-sum$_{100}$FTFC and individual FTFC spectra, and c) E-avg$_{10}$ZTFC, E$_{opt}$-avg$_{10}$FTFC, and E-sum$_{100}$FTFC lineshapes. All lineshapes are shifted energetically to align with the experimental lineshape maxima. 92
Figure 4.16: NR in DMSO: a) VEEs and b) VDEs trend across the snapshots in QM and chromophore-only (strip solvent) configurations. . . . 94

Figure 4.17: Pictorial representation of the E-avg$_{10}$ZTFC and E$_{opt}$-avg$_{10}$FTFC methods for NR in DMSO: The first two columns from the left represent emission lineshape spectra, and the remaining two columns represent absorption lineshape spectra. The top row shows the distribution of VDEs and VEEs from unoptimized and optimized geometries on the excited and ground state PES, respectively. The middle row depicts the procedure of generating the average FC lineshape by aligning the $0 \rightarrow 0$ transition energies. The bottom row represents the dressing of the zero-point transition energy corrected unoptimized and optimized VDEs and VEEs with avg$_{10}$ZTFC and avg$_{10}$FTFC lineshape resulting in E-avg$_{10}$ZTFC and E$_{opt}$-avg$_{10}$FTFC, respectively. 95
Figure 4.18: Frequency distribution of a) absorption and b) emission vibronic lineshape widths computed at 25% intensity, Full Width at Half-Half Maximum (FWHHM), of NR in DMSO. The dotted gray lines correspond to the FWHHM value of the implicit solvent FTFC spectra (Abs: 0.452 eV, Ems: 0.470 eV), which includes the second main vibronic peak. The dashed black lines represent the average values of the FWHHM of the explicit solvent FTFC spectra that include the second main vibronic peak (Abs: 0.274 eV, Ems: 0.264 eV). 97
Figure 4.19: Comparison of average FTFC vibronic lineshape spectra generated using five randomly selected explicit solvent snapshots using TD and TDA for NR in DMSO using CAM-B3LYP/6-31G* level of theory. 98
Figure 4.20: Absorption and fluorescence lineshapes of 7MC in methanol: Filled gray spectra are experimental lineshapes, transformed from Ref.287, 288. a) Ensemble and implicit solvent FTFC methods, b) E-sum$_{100}$FTFC and individual FTFC spectra, and c) E-avg$_{10}$ZTFC, E$_{opt}$-avg$_{10}$FTFC, and E-sum$_{100}$FTFC lineshapes. All lineshapes are shifted energetically to align with the experimental lineshape maxima. 98
Figure 4.21: 7MC in methanol: Vertical excitation energies obtained from ground state AIMD snapshots and vertical de-excitation energies obtained from excited state AIMD snapshots. Energy gaps are also shown for the same snapshots after geometry optimization in a frozen QM solvent environment. Corresponding oscillator strengths are included as an inset. 99
Figure 4.22: 7MC in methanol: a) VEEs and b) VDEs for QM solvent and chromophore-only (strip solvent) configurations. 100

Figure 4.23: Pictorial representation of the working of computational efficient E-avg$_{10}$ZTFC and E$_{opt}$-avg$_{10}$FTFC methods for 7MC in methanol: The first two columns from the left represent emission lineshape spectra, and the remaining two columns represent absorption lineshape spectra. The top row shows the distribution of VDEs and VEEs from unoptimized and optimized geometries on the excited and ground state PES, respectively. The middle row depicts the procedure of generating the average FC lineshape by aligning the $0 \rightarrow 0$ transition energies. The bottom row represents the dressing of the zero-point transition energy corrected unoptimized and optimized VDEs and VEEs with avg$_{10}$ZTFC and avg$_{10}$FTFC lineshape resulting in E-avg$_{10}$ZTFC and E$_{opt}$-avg$_{10}$FTFC, respectively. . . . 102
Figure 4.24: Frequency distribution of a) absorption and b) emission vibronic lineshape FWHM values of 7MC in methanol. The dotted gray lines correspond to the FWHM of the implicit solvent FTFC spectra (Abs: 0.539 eV, Ems: 0.766 eV). The dashed black lines represent the average values of the FWHM of the explicit solvent FTFC spectra (Abs: 0.416 and Ems: 0.630 eV). 103
Figure 4.25: Comparison of average FTFC vibronic lineshape spectra generated using five randomly selected explicit solvent snapshots using TD and TDA for 7MC in methanol using CAM-B3LYP/6-31G* level of theory. 104
Figure 4.26: 7MC in Methanol: Comparison of FC methods for two explicit solvent snapshots with a) planar and b) non-planar optimized excited state geometries, including adiabatic Hessian, vertical gradient, and adiabatic shift with the TDA/CAM-B3LYP/6-31G* level of theory. 105
Figure 4.27: The average relative computational cost of all explicit solvent absorption spectroscopy methods for all three dyes. 106

Figure 5.1: Pictorial representation of three fixed orientation dynamic solvent MD simulations 119
Figure 5.2: Distribution of the orientation factor between NBD and NR in DMSO solvent. The atoms in N_1 and N_2 in NBD and C_{21} and C_{31} in NR are chosen as proxies for the transition dipole moments. The dashed-blacked line represents the standard isotropic value of the orientation factor; the red dashed line represents the average value computed from the snapshots along the entire trajectory; the blue dashed line represents the average value computed after the 70^{th} snapshot. 121
Figure 5.3: Distribution of the orientation factor between NBD and NR in DMSO solvent as a function of distance. 121

Figure 5.4: Comparison of Coulombic coupling calculated using the transition densities cube, Mullliken transition charges, and transition dipole moment methods for orientation B of NBD-NR in a) implicit and b) explicit QM/MM DMSO solvent. 123
Figure 5.5: Oscillator strength of the first four excited states of a) NBD and b) NR as a function of distance in MM point charge environment 126
Figure 5.6: Comparison of Coulombic coupling calculated using the transition densities cube, Mulliken transition charges, and transition dipole moment methods for a parallel orientation CV+ dimer in a) vacuum and b) implicit water solvent. 128

Figure 6.1: Bruton's tyrosine kinase (BTK) with GDC-0853 132
Figure 6.2: Pictorial representation on how to calculate relative binding free energies. The image is adapted from Relative protein-ligand binding free energy Website 134
Figure 6.3: BTK inhibitors selected for computing the ligand binding relative free energy calculations 136
Figure 6.4: Pictorial representation of the selection process for choosing the protein-ligand environment region for calculating relative binding free energy. Each region represents a part of the system treated with QM (quantum mechanics) and MM (molecular mechanics). The size and complexity of the selected region increase as we move from region 1 to region 2. 140
Figure 6.5: Region-1: Only the ligand is treated using quantum mechanics, while the rest of the system is treated as a point-charge environment. 141
Figure 6.6: Region 1: Correlation of inhibitory activity with ligand binding free energies when only the chromophore is treated quantum mechanically and the remainder of the system is treated like a point charge environment 142
Figure 6.7: Region-2: The ligand and hydrogen-bonded residues are treated using quantum mechanics, the remaining system as point-charge environment. 142
Figure 6.8: Region 2: Correlation of inhibitory activity with ligand binding free energies when the chromophore and the hydrogen bonding protein residues are treated quantum mechanically and the remaining system is treated like a point charge environment 143
Figure 6.9: Region-3: An area of 10A region within the geometric center of the ligand is treated quantum mechanically for relative binding free energy calculations, and the rest of the system was discarded 144
Figure 6.10: Region 3: Correlation of inhibitory activity with ligand binding free energies when the chromophore and about 10 Angstrom of protein regions are treated quantum mechanically and the remaining system is treated like a point charge environment 145

Figure 6.11: Affinity ranking of ligands: The blue histograms display the ordering of ligands based on their relative solvation energies. The orange histograms represent the ordering of the relative strain energy of ligands. The purple histogram illustrates the relative interaction energies, while the dark green histogram shows the relative binding free energies of the ligands. For the relative rank ordering, ligand 12 was chosen as the reference due to its higher potency. 146

LIST OF TABLES

Table 3.1: CV^+ in Methanol: FWHM, and applied energy shift from experiment, ensemble, implicit FTFC, and E-FC methods for absorption lineshapes. All values are given in eV. 68

Table 4.1: NBD in DMSO: FWHM, applied energy shift, and Stokes shift from experiment, ensemble, implicit FTFC, and E-FC methods for absorption and emission lineshapes. All values are given in eV. . . . 83

Table 4.2: NBD VEE/VDE distribution mean, standard deviation, E_{max}, and FWHM for QM, MM solvent (point charges) and chromophore-only (strip solvent) configurations. Sampled from 100 AIMD snapshots. * indicates S_1 and S_2 electronic state mixing 85

Table 4.3: NR in DMSO: FWHM, applied energy shift, and Stokes shift from experiment, ensemble, implicit FTFC, and E-FC methods for absorption and emission lineshapes. All values are given in eV. . . . 93

Table 4.4: NR VEE/VDE distribution mean, standard deviation, E_{max}, and FWHM for QM solvent, MM solvent, and chromophore-only configurations. Sampled from 100 AIMD snapshots. 94

Table 4.5: 7MC VEE/VDE distribution mean, standard deviation, E_{max}, and FWHM for QM and MM solvent, and chromophore-only configurations. Sampled from 100 AIMD snapshots. 100

Table 4.6: 7MC in methanol: FWHM, applied energy shift, and Stokes shift from experiment, ensemble, implicit FTFC, and E-FC methods for absorption and emission lineshapes. All values are given in eV. . . 101

Table 5.1: The trend of oscillator strength and vertical excitation energies of NBD and NR as a function of distance in a QM/MM point charge environment 127

ACKNOWLEDGEMENTS

I wish to extend my sincere gratitude to my advisor, Prof. Christine Isborn, for her invaluable guidance and patience throughout my doctoral studies. Her advice has been instrumental in my academic journey. I am also deeply thankful to my committee members, Prof. Hrant Hratchian, Prof. Liang Shi, and Prof. Ashlie Martini, for their insightful feedback and support during my doctoral journey. I would like to express my gratitude to Dr. Anne M. Kelley for patiently addressing my questions and offering valuable guidance and support in understanding molecular spectroscopy. Sapana Shedge and Tim Zuehlsdorff, I am deeply appreciative of your unique and individual approaches to mentoring me throughout my graduate studies. Your guidance has been invaluable, and I could not have asked for more.

My heartfelt appreciation goes to my family for their unwavering support and encouragement. To my dad, thank you for breaking traditional boundaries and providing endless support for me to pursue my dreams. To my partner, Lalita Tanwar, you have seen me fail many times in my journey, and no matter what, you have always been there for me, no matter how tough the situation became. I am lucky to have you in my life. Lastly, I reflect on my journey with gratitude. I acknowledge my resilience and tenacity in overcoming challenges and surpassing expectations to achieve this doctoral degree.

VITA

2014	B.Sc.(H) in Chemistry, University of Delhi, New Delhi, India
2017	M.Sc in Chemistry, National Institute of Technology Rourkela, Orissa, India
2020	M.Sc. in Chemistry and Chemical Biology, University of California, Merced, CA, USA
2024	Ph.D. in Chemistry and Chemical Biology, University of California, Merced, CA, USA

PUBLICATIONS

Ajay Khanna, Sapana V. Shedge, Tim J. Zuehlsdorff, Christine M. Isborn; Calculating absorption and fluorescence spectra for chromophores in solution with ensemble FranckCondon methods. J. Chem. Phys., 161 (4): 044121, DOI:10.1063/5.0217080

Christopher A. Myers, Shao-Yu Lu, Sapana Shedge, Arthur Pyuskulyan, Katherine Donahoe, Ajay Khanna, Liang Shi, and Christine M. Isborn, Axial H-Bonding Solvent Controls Inhomogeneous Spectral Broadening, While Peripheral H-Bonding Solvent Controls Vibronic Broadening: Cresyl Violet in Methanol, The J. Phys. Chem. B 2024 128 (23), 5685-5699, DOI: 10.1021/acs.jpcb.4c01401

Chiao-Yu Cheng, Nina Krainova, Alyssa Brigeman, Ajay Khanna, Sapana Shedge, Christine Isborn, Joel Yuen-Zhou, and Noel C. Giebink, Molecular Polariton Electroabsorption, Nat Commun 13, 7937, 2022, DOI:10.1038/s41467-022-35589-4

Sapana V. Shedge, Tim J. Zuehlsdorff, Ajay Khanna, Stacey Conley, and Christine M. Isborn, Explicit Environmental and Vibronic Effects in Simulations of Linear and Nonlinear Optical Spectroscopy, J. Chem. Phys. 154, 084116, 2021, DOI: 10.1063/5.0038196

ABSTRACT OF THE DISSERTATION

Modeling Optical Spectroscopy and Resonance Energy Transfer for Chromophores in Explicit Solvent Environments

by

Ajay Khanna

Doctor of Philosophy in Theoretical Chemistry

University of California Merced, 2024

Professor Hrant Hratchian, Chair

This thesis aims to provide an understanding of computational methods for modeling light-matter interactions through the lens of UV-visible spectroscopy and excitation energy transfer processes. Chapter 1 lays down the foundation of fundamentals required to understand the basics of electronic structure theory and UV-visible spectroscopy. Chapter 2 provides an overview of DFT and various functional approximations, followed by my density functional benchmark study for vibronic spectra in both implicit and explicit solvent environments. Chapter 3 introduces the combined ensemble Franck-Condon (E-FC) method, a practical tool for modeling UV-visible spectra of molecules in explicit solvent environments, where I have extended and generalized the E-FC methods for the first time to compute the fluorescence spectra of molecules in an explicit solvent environment. This hybrid method, developed by merging the advantages of nuclear ensemble and Franck-Condon methods, effectively incorporates the influence of molecular configurations in an explicit solvent environment with vibronic coupling. Chapter 4 showcases the application of E-FC methods to calculate the UV-visible spectra of three commonly used dyes: NBD and NR in DMSO and 7MC in Methanol. Additionally, we compare the performance of the family of E-FC methods, namely E-sumFTFC, Eopt-avgFTFC, and E-avgZTFC, with each other. The chapter concludes with results indicating a significant improvement over traditional linear optical spectroscopy methods. We also compare the computed absorption and fluorescence lineshapes with experimental data, validating the ac-

curacy of our results and discussing the relative computational efficiency of these methods.

Chapter 5 compares Coulombic coupling values computed using various methods for NBD-NR and CV+ dimer systems involved in the excitation energy transfer process both in an implicit and explicit solvent environment. The methods used include coupling via transition dipole moments, transition charges, and transition densities from both isolated dyes and supramolecular systems. We compare the relative accuracy of these methods for both systems. The results presented in this section represent ongoing progress on the project and will be included in a future paper.

Chapter 6 summarizes the project carried out during the summer of 2023 as an intern in the computational chemistry division at Frontier Medicines, San Francisco. The project aimed to develop a computational procedure to rank-order potent ligands bound to Bruton's Tyrosine Kinase (BTK) using their relative binding free energies (RBFEs). The chapter introduces BTK and its role in signaling pathways, the computational procedure used, the results, and a discussion on the impact of the protein region definition on RBFE. It concludes with recommendations for improved RBFE calculations.

Chapter 1

Introduction

This chapter provides a comprehensive overview of quantum mechanical principles and electronic structure methods essential for understanding molecular spectroscopy. It starts with the basics of quantum mechanics, including the Schrödinger's equation and its applications to simple systems that can be solved analytically. Then, it explores ground-state electronic structure methods, focusing on Hartree-Fock theory and Density Functional Theory (DFT), elucidating their theoretical foundations and practical implementations. Excited state methods, like Configuration-Interaction Singles and Time-Dependent DFT, are discussed, highlighting their importance in calculating excited state properties. The chapter examines UV-visible spectroscopy fundamentals, covering key concepts such as the Jablonski diagram, electronic transitions, and environmental effects on spectroscopic properties. This chapter provides a solid theoretical framework for understanding and interpreting molecular spectroscopic data that will be generated in the following chapters.

1.1 Schrödinger's Quantum Mechanics

Schrödinger's wave mechanics revolutionized our understanding of the quantum world.[1] It provides a mathematically elegant framework built on the concept of wave-particle duality. Rather than describing particles with definite trajectories, Schrödinger's formulation introduces the wavefunction,$\psi(r,t)$, a mathematical entity that represents the probabilistic nature of quantum mechanics.

At the core of Schrödinger's theory lies the time-dependent Schrödinger's equation,

a fundamental law governing the evolution of a quantum system:[2]

$$i\hbar\frac{\partial}{\partial t}\Psi(\mathbf{x},t) = \hat{H}\Psi(\mathbf{x},t) \tag{1.1}$$

where $\Psi(\mathbf{x},t)$ is the time-dependent wavefunction, i is the imaginary unit, $\hbar$ is the reduced Planck constant, $\hat{H}$ is the Hamiltonian operator, representing the total energy.

For systems where the potential does not explicitly depend on time, we can use separation of variables to derive the time-independent Schrödinger's equation. We assume a solution of the product form:

$$\Psi(\mathbf{x},t) = \psi(\mathbf{x})f(t) \tag{1.2}$$

The wavefunction, ψ, is a complex-valued function. Its absolute value squared, $|\psi(x)|^2$, represents the probability density of locating the particle at a specific position. Furthermore, the wave function must satisfy certain properties to be physically meaningful. These include normalization, ensuring the total probability of finding the particle somewhere is 1, and single-valuedness, meaning the wavefunction has a unique value at any point in space. Substituting into the time-dependent equation leads to the famous time-independent Schrödinger's equation:

$$\begin{aligned} \hat{H}\psi(\mathbf{x}) &= E\psi(\mathbf{x}) \\ \frac{-\hbar^2}{2m}\frac{\partial^2\psi}{\partial x^2} + V(x)\psi(x) &= E\psi(x), \end{aligned} \tag{1.3}$$

where $\hat{H}$ is the Hamiltonian operator, which is a sum of the kinetic energy and potential energy terms. This equation is central to finding the stationary states and allowed energy levels of quantum systems. Schrödinger's wave mechanics offers a powerful tool for modeling various quantum phenomena. Its success in explaining atomic spectra, chemical bonding, and the behavior of materials solidified its role as a cornerstone of modern physics.

1.1.1 The Hydrogen Atom

The hydrogen atom, composed of a single proton and a single electron, represents the simplest atomic system. Remarkably, it offers one of the very few examples in

quantum mechanics where we can find exact analytical solutions. Its study has been pivotal in the development of quantum theory and continues to provide fundamental insights into the behavior of matter at the atomic scale.

In the quantum description, the electron's state is described by a wavefunction, $\psi(r, \theta, \phi)$, where we here employ spherical coordinates and choose the proton coordinate as the origin, governed by the time-independent Schrödinger's equation:

$$\left[-\frac{\hbar^2}{2m_e}\nabla^2 - V(r)\right]\psi(r, \theta, \phi) = E\psi(r, \theta, \phi) \tag{1.4}$$

where $V(r) = \frac{e^2}{4\pi\epsilon_0 r}$ is the Coulombic potential, m_e is the electron's mass, e is the fundamental charge, ϵ_0 is the vacuum permittivity, $\hbar$ is the reduced Planck constant, ∇^2 is the Laplacian operator (representing the kinetic energy), r, θ, ϕ are spherical coordinates of the electron position.

The Schrödinger's equation solution for the hydrogen atom leads to fascinating consequences:

1. Quantized Energy: The allowed energy levels of the hydrogen atom are discrete, given by the formula:
$$E_n = -\frac{13.6eV}{n^2}$$
where n is the principal quantum number (n = 1, 2, 3, ...).

2. Quantum Numbers: In addition to the principal quantum number, n, the solutions yield further quantum numbers: l (the angular momentum quantum number) and m (the magnetic quantum number). These quantum numbers dictate the shape and spatial orientation of the electron's probability distribution.

3. Orbitals: The wavefunctions, $\psi_{nlm}(r, \theta, \phi)$, are known as atomic orbitals. They represent the probability amplitude of finding the electron at a particular location in space. Familiar notations like $1s$, $2s$, and $2p$ orbitals refer to specific solutions.

The hydrogen atom is one of the rare examples in quantum mechanics that can be solved exactly. It serves as a foundation for comprehending more intricate atomic

and molecular systems, which typically require numerical solutions using iterative techniques. The quantized energy levels explain the emission and absorption lines in the hydrogen spectrum. The transitions between levels give rise to series like the Lyman,[3] Balmer,[4] and Paschen[5] series. The concepts of orbitals and quantum numbers carry over to multi-electron atoms. While exact solutions are no longer possible, the hydrogen atom forms the basis for approximate models and the development of the periodic table. Studies of the hydrogen atom have played a crucial role in testing and refining fundamental concepts of quantum mechanics throughout its history.

1.1.2 The Harmonic Oscillator

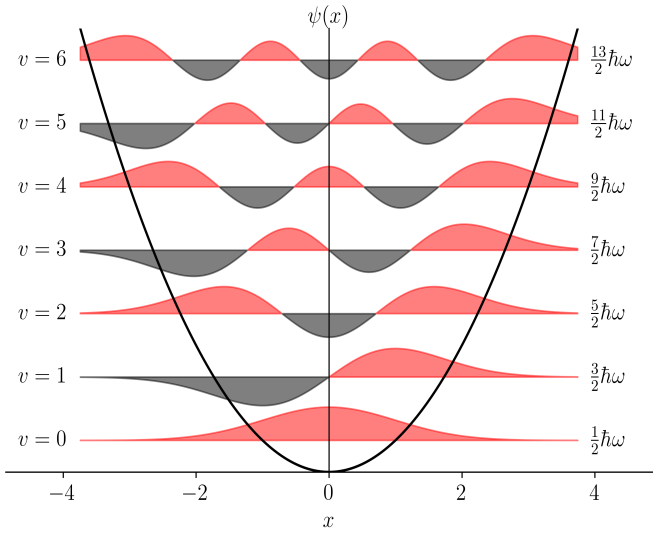

Figure 1.1: The simple harmonic oscillator model

In classical physics, the harmonic oscillator provides a fundamental model for systems that exhibit oscillatory behavior near a stable equilibrium point. A quintessential example is the motion of a mass attached to a spring: when displaced slightly from equilibrium, the mass experiences a restoring force proportional to its displacement, leading to simple harmonic motion. Remarkably, the harmonic oscillator paradigm extends its significance to the quantum realm, where it forms one of the cornerstones of quantum mechanics. The quantum harmonic oscillator offers an exceptionally valuable system for study, as it's one of the very few systems for which we can find exact,

analytical solutions.[6–10] Its implications reach across various domains of physics, encompassing molecular vibrations, the behavior of atoms in crystal lattices, and even the quantization of light itself.

In computational vibronic spectroscopy, the quantum harmonic oscillator model allows for the efficient computation of vibrational wavefunctions and energies, which are crucial for determining Franck-Condon factors and simulating vibronic spectra. Consider a particle of mass m subject to a one-dimensional harmonic potential. The potential energy is given by:

$$V(x) = \frac{1}{2}m\omega^2 x^2 \tag{1.5}$$

where ω is the angular frequency of the oscillator. In quantum mechanics, the system is described by the time-independent Schrödinger's equation:

$$\hat{H}\psi(x) = E\psi(x) \tag{1.6}$$

where $\hat{H}$ is the Hamiltonian operator, E represents the energy eigenvalues, and $\psi(x)$ denotes the wavefunction of the system. The Hamiltonian for the quantum harmonic oscillator takes the form:

$$\hat{H} = \frac{-\hbar^2}{2m}\frac{d^2}{dx^2} + \frac{1}{2}m\omega^2 x^2 \tag{1.7}$$

where $\hbar$ is the reduced Planck constant. Solving the Schrödinger's equation is a somewhat involved process, but it leads to a beautiful and powerful result: the energy levels of the quantum harmonic oscillator are quantized. The allowed energies are given by:

$$E_n = \hbar\omega\left(n + \frac{1}{2}\right) \tag{1.8}$$

where $n = 0, 1, 2, ...$ is the quantum number.

Unlike the continuous energy spectrum of a classical harmonic oscillator, the quantum version has discrete energy levels spaced $\hbar\omega$ apart. The lowest possible energy is not zero but rather $E_0 = \frac{1}{2}\hbar\omega$. This zero-point energy means the quantum oscillator can never be truly at rest, a direct consequence of the uncertainty principle.

The wavefunctions corresponding to each energy level are expressed in terms of Hermite polynomials[11] multiplied by Gaussian functions. For example, the ground

state wavefunction is:

$$\psi_0(x) = \left(\frac{m\omega}{\pi\hbar}\right)^{1/4} e^{-m\omega x^2/2\hbar} \tag{1.9}$$

The far-reaching applications of the quantum harmonic oscillator model are what solidify its importance in physical science:

1. The electromagnetic field itself can be quantized. The resulting energy quanta are known as photons, and surprisingly, their behavior can be modeled using the quantum harmonic oscillator formalism. This framework provides a foundation for the entire field of quantum optics.

2. In a crystalline solid, atoms are arranged in a regular lattice. The vibrations of these atoms around their equilibrium positions can be modeled as a collection of coupled quantum harmonic oscillators. These vibrations, called phonons, play a crucial role in understanding the heat capacity and thermal conductivity of solids.

3. Diatomic molecules can be approximated as quantum harmonic oscillators to a surprising degree of accuracy. The model explains the quantized vibrational energy levels of molecules, which form the basis of infrared spectroscopy. The harmonic oscillator model is used with the Franck-Condon principle to explain the intensity distribution in vibronic spectra. According to this principle, electronic transitions happen so quickly that the nuclear positions don't change significantly during the transition. While FC methods don't require potential energy surfaces to be harmonic, in practice, harmonic potentials are assumed because the quantum mechanical harmonic oscillator model provides easily accessible nuclear wave functions needed to determine the intensity distribution in vibronic spectra.

1.1.3 The Born-Oppenheimer Approximation

The Born-Oppenheimer (BO) approximation[12] is a fundamental approximation that lies at the heart of molecular structure and dynamics. It offers a way to simplify the complex quantum mechanical treatment of molecules. The principle is based on the observation that atomic nuclei are much more massive than electrons. As a

result, electrons move and adjust much more rapidly in response to changes in nuclear positions than the nuclei themselves.

In essence, we can "freeze" the nuclei at a fixed configuration and focus on solving for the electronic states based on that arrangement. This separation of electronic and nuclear motion has been remarkably successful and is the foundation of much of computational chemistry.

Consider a molecule with a total Hamiltonian that we can split into three components:

$$\hat{H} = \hat{T}_n + \hat{T}_e + \hat{V}(\mathbf{r}, \mathbf{R}), \tag{1.10}$$

where $\hat{T}_n$ represents the kinetic energy of the nuclei, $\hat{T}_e$ represents the kinetic energy of the electrons, $\hat{V}(\mathbf{r}, \mathbf{R})$ is the potential energy, depending on both the electron positions, $\mathbf{r}$ and the nuclear positions, $\mathbf{R}$.

The BO approximation introduces a separation of variables for the total molecular wavefunction:

$$\Psi(\mathbf{r}, \mathbf{R}) \approx \psi_e(\mathbf{r}; \mathbf{R})\chi(\mathbf{R}) \tag{1.11}$$

where: $\psi_e(\mathbf{r}; \mathbf{R})$ is the electronic wavefunction, which depends on the electron positions and parametrically on the nuclear positions (as if they were fixed) $\chi(\mathbf{R})$ is the nuclear wavefunction.

Solving the electronic Schrödinger's equation at fixed nuclear positions gives us electronic energies that act as an effective potential for the nuclear motion:

$$[\hat{T}_e + \hat{V}(\mathbf{r}; \mathbf{R})]\psi_e(\mathbf{r}; \mathbf{R}) = E_e(\mathbf{R})\psi_e(\mathbf{r}; \mathbf{R}) \tag{1.12}$$

The implications of the BO principle are wide-ranging:

1. Potential Energy Surfaces: For each electronic state, the electronic energy $E_e(\mathbf{R})$ acts as a potential energy function for the nuclei. These 'potential energy surfaces' govern nuclear motion and provide a starting point for studying molecular vibrations[13] and chemical reactions.[14]

2. Molecular Spectroscopy: Analyzing vibrational and rotational transitions within these potential energy surfaces lies at the heart of diverse spectroscopic techniques, giving us information about the structure and interactions within molecules.[15]

3. Computational Chemistry: Most electronic structure methods rely fundamentally on the Born-Oppenheimer approximation. Techniques like density functional theory (DFT) begin by solving for electronic structures for given nuclear arrangements.

While the Born-Oppenheimer approximation is widely employed in many quantum mechanics applications, it's essential to be cautious about its limitations.[16–19] Situations like conical intersections,[20,21] quantum nuclei,[22] and non-adiabatic effects[23,24] demonstrate when the Born-Oppenheimer approximation is invalid. If these effects impact UV-visible spectra, it is crucial to account for the coupling between different electronic states and the quantum properties of nuclei when computationally modeling vibronic spectra.[25–28]

1.2 Ground State Electronic Structure Methods

1.2.1 Hartree-Fock (HF)

The Hartree-Fock method in quantum mechanics provides a practical way to solve the Schrödinger's equation for many-electron systems by reducing the problem to a set of self-consistent field equations.[29–31] It aims to find the best single-electron wave functions (orbitals) that variationally minimize the total energy of a many-electron system. It assumes that each electron moves independently in an average field created by all other electrons. The single-electron wave function ψ can be approximated by a single Slater determinant[32] as

$$\psi(x_1, x_2, x_3, ..., x_N) = \frac{1}{\sqrt{N!}} det[\phi_i(x_j)], \tag{1.13}$$

where x_i includes spatial and spin coordinates and $\phi_i(x_j)$ are the spin orbitals. The Hartree-Fock energy can then be written as

$$\begin{aligned} E^{HF} &= \int \psi^* \hat{H}_{el} \psi = \langle \psi | \hat{H} | \psi \rangle \\ &= \sum_i \langle i | \hat{h} | i \rangle + \frac{1}{2} \sum_{ij} \langle ij || ij \rangle \\ &= \sum_i \langle i | \hat{h} | i \rangle + \frac{1}{2} \sum_{ij} [\langle ij | ij \rangle - \langle ij | ji \rangle] \end{aligned} \tag{1.14}$$

where, i and j are occupied orbitals and $\hat{h}$ is a one-electron Hamiltonian. The double-bar bra-ket notation denotes the Coulomb and exchange integral arising from the antisymmetric nature of the Slater determinant. The Coulomb and exchange integrals can be evaluated as

$$\begin{aligned} J_{ij} &=< ij|ij >= \int d\vec{x_1} \int d\vec{x_2} \phi_i^*(\vec{x_1}) \phi_j(\vec{x_2}) \frac{1}{r_{12}} \phi_i^*(\vec{x_1}) \phi_j(\vec{x_2}) \\ K_{ij} &=< ij|ji >= \int d\vec{x_1} \int d\vec{x_1} \phi_i^*(\vec{x_1}) \phi_j(\vec{x_2}) \frac{1}{r_{12}} \phi_j^*(\vec{x_1}) \phi_i(\vec{x_2}) \end{aligned} \tag{1.15}$$

The HF method determines the set of spin-orbitals that minimizes the HF energy and gives us the "best single determinant". An implicit assumption in this process is that the orbitals ϕ_i are orthonormal. To minimize the energy with respect to change in orbitals $\phi_i + \delta\phi_i$, we can apply the Lagrangian multiplier, $\mathcal{L}$, defined as

$$\mathcal{L}[\phi_i] = E^{HF}[\{\phi_i\}] - \sum_{ij} \epsilon_{ij} \left[\langle i|j \rangle - \delta_{ij} \right], \tag{1.16}$$

where $\langle i|j \rangle = \int d\vec{x_1} \phi_i^*(\vec{x_1}) \phi_j^*(\vec{x_1})$, is the overlap integral, and,

$$\delta_{ij} = \begin{cases} 1, & \text{if } i = j \\ 0, & 0. \end{cases}$$

Introducing a variation in the $\mathcal{L}$, we get

$$\delta\mathcal{L} = \delta E^{HF}[\{\phi_i\}] - \sum_{ij} \epsilon_{ij} \left[\delta\langle i|j \rangle \right] \tag{1.17}$$

On further expansion and after applying some linear algebra techniques, we get

$$\delta\mathcal{L} = \sum_i \langle \delta i|\hat{h}|i\rangle + \sum_{ij} [\delta ii|jj] - [\delta ij|ji] - \sum_{ij} \epsilon_{ij} \langle \delta i|j\rangle + \text{Complex conjugate} \tag{1.18}$$

If the system is already at a minimum or at maximum, $\delta\mathcal{L} = 0$, then rearranging the equations leads to

$$\begin{aligned} \delta\mathcal{L} = \sum_i \int d\vec{x_1} \delta\phi_i^*(\vec{x_1}) \Bigg[& \hat{h}(\vec{x_1}) \phi_i(\vec{x_1}) + \sum_j \phi_i(\vec{x_1}) \int d\vec{x_2} \frac{1}{r_{12}} \phi_j^*(\vec{x_2}) \phi_j(\vec{x_2}) \\ & - \phi_j(\vec{x_1}) \int d\vec{x_2} \frac{1}{r_{12}} \phi_j^*(\vec{x_2}) \phi_i(\vec{x_2}) - \sum_{ij} \epsilon_{ij} \phi_j(\vec{x_1}) \Bigg] + \text{Complex conjugate} \\ = 0 \end{aligned} \tag{1.19}$$

rearranging the above equation gives,

$$\begin{aligned}\hat{h}(\vec{x_1})\phi_i(\vec{x_1}) + \sum_{j\neq i}\left[\int d\vec{x_2}\,|\phi_j(\vec{x_2})|^2\,\frac{1}{r_{12}}\right]\phi_i(\vec{x_1}) \\ - \sum_{j\neq i}\left[\int d\vec{x_2}\phi_j^*(\vec{x_2})\phi_i(\vec{x_2})\frac{1}{r_{12}}\right]\phi_j(\vec{x_1}) \\ = \sum_j \epsilon_{ij}\phi_j(\vec{x_1})\end{aligned} \tag{1.20}$$

$$\left[\hat{h}(\vec{x_1}) + \sum_{j\neq i}\vec{J}_j(\vec{x_1}) - \sum_{j\neq i}\vec{K}_j(\vec{x_1})\right]\phi_i(\vec{x_1}) = \sum_j \epsilon_{ij}\phi_j(\vec{x_1}) \tag{1.21}$$

$$\hat{f}(x_1)\phi_i(\vec{x_1}) = \epsilon_i\phi_i(\vec{x_1}) \tag{1.22}$$

where $\hat{f}(\vec{x_1}) = \hat{h}(\vec{x_1}) + \sum_j \hat{J}_j(\vec{x_1}) - \hat{K}_j(\vec{x_1})$ is the Fock operator.

This is the Hartree-Fock equation. One thing to note here is that it is necessary to have $\phi_i(\vec{x_1})$ to solve for $\hat{f}(\vec{x_1})$ because the $\hat{J}$ and $\hat{K}$ in $\hat{f}$ require $\phi_i(\vec{x_1})$ as input. However, one cannot get the $\phi_i(\vec{x_1})$ until it is solved, so it becomes a circle, and that is why it is called the self-consistent field (SCF) procedure. The SCF process starts with a guess $\phi_i(\vec{x_1})$, then forms $\hat{f}$, then solves for $\phi_i(\vec{x_1})$ then uses the new set of $\phi_i(\vec{x_1})$ and repeats.

The Hartree-Fock (HF) method, despite being foundational in quantum chemistry and computational methods, has several limitations that restrict its accuracy and applicability in certain chemical systems:[33]

1. Missing Electron Correlation: A significant limitation of the HF method is its inability to account for electron correlation, specifically the dynamic correlation among electrons. HF calculations only include the mean-field interaction of electrons and do not capture the correlated motion of electrons that avoid each other more effectively than predicted by mean-field theories. This limitation results in the overestimation of total energies and can lead to inaccuracies in predicting reaction energetics and barrier heights.

2. Basis Set Dependence: The quality of results from HF calculations is heavily basis set dependent. Since HF uses a finite set of basis functions to describe the molecular orbitals, the completeness of the basis set significantly influences

the accuracy of the results. Larger and more flexible basis sets typically give better results but at the cost of increased computational expense. Inadequate basis sets can lead to errors in calculated properties like bond lengths, angles, and vibrational frequencies.

3. Spin Contamination: In systems with unpaired electrons (e.g., radicals, transition states), HF calculations, especially when using unrestricted Hartree-Fock (UHF) formulations, can suffer from spin contamination.[34] This occurs when the wavefunction includes contributions from states with different spin multiplicities, leading to erroneous energy and property calculations.

4. Size Consistency and Size Extensivity: Hartree-Fock (HF) methods exhibit size extensivity but may not be size consistency.[35] Size extensivity refers to the property where the energy of a system is calculated as a sum of non-interacting subsystems equals the sum of the energies of the individual subsystems. HF does not possess this property, which can result in errors in the energies of large systems or systems at dissociation limits. Similarly, size consistency, which ensures that the method's results for dissociated systems match the results for systems calculated separately, is also not perfectly maintained in HF calculations.

Despite its limitations, the Hartree-Fock method is still a valuable tool in computational chemistry. It serves as a foundation for more advanced methods like Moller Plesset 2,[36] Configuration Interaction (CI),[37] Coupled Cluster (CC),[38–40] and DFT, which address these limitations by incorporating electron correlation to different extents.

1.2.2 Density Functional Theory (DFT)

Density Functional Theory (DFT) has evolved significantly since its inception in the mid-20th century.[41,42] It is a computational quantum mechanical modeling method used to investigate the electronic structure of many-body systems, such as atoms, molecules, materials, and the condensed phases of matter.[43–46] It is one of the most popular and versatile methods available for studying molecular properties from first principles. DFT provides an approach for approximating the incredibly complex

many-body problem of interacting electrons by using functionals, which are functions of the spatially dependent electron density.

The foundation of DFT lies in the Hohenberg-Kohn theorems, published in 1964.[47] **Hohenberg-Kohn Theorem 1**: states that the ground state energy of a many-electron system is a unique functional of the electron density. This theorem signifies a pivotal departure from the wave function formalism, as seen in the HF method, asserting that all observable properties of a ground state system can be determined uniquely by its electron density. Mathematically, this can be expressed as:

$$E = E[\rho(r)] \tag{1.23}$$

where E is the total energy, and ρ represents the ground state electron density. This functional dependency implies that the electron density, $\rho(\mathbf{r})$, encompasses all the necessary information to describe the ground state of the system fully. The profound implication of this theorem is its simplification of the many-body problem from a wave function in a 3N-dimensional space (where N is the number of electrons) to a function in a three-dimensional space, greatly reducing the complexity of the problem.

Hohenberg-Kohn Theorem 2: The second Hohenberg-Kohn theorem[47] states that there exists a universal functional that delivers the exact ground-state energy of the system when given the exact ground-state electron density. This functional, known as the universal density functional, is the key to DFT. If this universal functional were known exactly, DFT would provide the exact solution to the many-body Schrödinger's equation.

$$E_0 \leq E[\rho(r)] = \int dr \rho(r)\nu(r) + F[\rho(r)] \tag{1.24}$$

for any trial density ρ that integrates to the number of electrons, N, and where E_0 is the true ground state energy of the system. Here, $E[\rho(r)]$ is the energy functional of the density ρ, and the equality holds if and only if $\rho(r)$ is the true ground state density. This theorem underpins the optimization strategies in DFT calculations, where one seeks the density that minimizes the energy functional.

As a consequence of the Rayleigh-Ritz (aka variational) principle,[48–51] $E[\rho(r)]$ follows the variational properties:

$$\begin{aligned} E_0[\rho(r)] &> E_0, if \rho(r) \neq \rho_0(r) \\ E_0[\rho(r)] &= E_0, if \rho(r) = \rho_0(r) \end{aligned} \tag{1.25}$$

Using the Euler equation, the exact ground state density $\rho_0(r)$ for an N-electron interacting system can be found as,

$$\frac{\delta}{\delta\rho(r)}\left[E_0[\rho(r)] - \mu\int d^3r'\rho(r')\right] \tag{1.26}$$

here, μ is a Lagrange multiplier ensuring the total number of electrons remains unchanged.

1.2.3 The Kohn-Sham Equation

In the realm of DFT, the exact form of the universal functional remains a mystery, necessitating the use of approximations. This is where the true ingenuity of DFT shines. DFT calculations often involve solving the Kohn-Sham equations,[52] a set of equations derived by Kohn and Sham in 1965 that ingeniously map the interacting many-body problem onto an auxiliary non-interacting problem of electrons in single particle orbitals with the same ground-state electron density as the fully interacting system. The Kohn-Sham equations, a simpler version of the original many-body Schrödinger's equation, are the key to unlocking the ground-state electron density and other ground-state properties of the system and provide an accurate estimation of the kinetic energy contribution to the total energy, showcasing the complexity and brilliance of DFT.

Kohn and Sham's key insight was to decompose the complex problem of interacting electrons into simpler, non-interacting particles moving in an effective potential. This effective potential includes the external potential (due to nuclei), the Hartree potential (describing classical electron-electron repulsion), and the exchange-correlation potential, which encapsulates all non-classical interactions (exchange and correlation effects).

The Kohn-Sham equations can be written as a set of one-electron Schrödinger's -like equations,

$$\left[-\frac{1}{2}\nabla^2 + V_{\text{eff}}(\mathbf{r})\right]\psi_i(\mathbf{r}) = \epsilon_i\psi_i(\mathbf{r}), \tag{1.27}$$

where $\psi_i(\mathbf{r})$ are the Kohn-Sham orbitals, ϵ_i are the orbital energies, and $V_{\text{eff}}(\mathbf{r})$ is the effective potential given by:

$$V_{\text{eff}}(\mathbf{r}) = V_{\text{ext}}(\mathbf{r}) + V_{\text{H}}(\mathbf{r}) + V_{\text{xc}}(\mathbf{r}) \tag{1.28}$$

Here, $V_{\text{ext}}(\mathbf{r})$ is the external potential, $V_{\text{H}}(\mathbf{r})$ is the Hartree potential, and $V_{\text{xc}}(\mathbf{r})$ is the exchange-correlation potential. The Hartree potential is defined as:

$$V_{\text{H}}(\mathbf{r}) = \int \frac{\rho(\mathbf{r}')}{|\mathbf{r} - \mathbf{r}'|} d\mathbf{r}' \tag{1.29}$$

and the exchange-correlation potential, $V_{\text{xc}}(\mathbf{r})$, is the functional derivative of the exchange-correlation energy functional with respect to the electron density:

$$V_{\text{xc}}(\mathbf{r}) = \frac{\delta E_{\text{xc}}[\rho]}{\delta\rho(\mathbf{r})} \tag{1.30}$$

To solve the Kohn-Sham equations, one starts with an initial guess for the density, constructs the effective potential, solves the eigenvalue problem to obtain the Kohn-Sham orbitals, and constructs a new density from these orbitals. This process is repeated iteratively until the density converges, indicating self-consistency, and following the same SCF procedure as used in HF theory. The success of DFT hinges on the accuracy of the exchange-correlation functional, which encapsulates all the quantum mechanical interactions among electrons beyond classical electrostatics.[53–56] Over the decades, a variety of functionals have been developed, each aiming to balance computational feasibility and accuracy. The Jacobs Ladder of DFT provides a classification system for these functionals, ranked from simple local density approximations (LDAs) to more sophisticated meta-generalized gradient approximations(meta-GGAs) and hybrid functionals; Jacob's Ladder will be discussed more in chapter-2.2.

1.3 Excited State Electronic Structure Methods

Up to this point, our discussion of electronic structure methods has focused on ground-state properties. To account for phenomena such as excited states, optical

spectroscopy, and resonance energy transfer, appropriate electronic structure methods that can accurately describe molecules' excited states are required. Here, I highlight two such methods routinely used in the calculation of molecules' absorption and fluorescence spectra.

1.3.1 Configuration-Interaction Singles (CIS)

Configuration-Interaction Singles (CIS)[57] is one of the simplest methods for calculating excited states of molecules. CIS is built upon the HF ground state and involves constructing excited states by promoting electrons from occupied to virtual molecular orbitals. The CIS method starts from the Hartree-Fock ground state wavefunction, Ψ_0^{HF}, and constructs excited states by single excitations. The CIS wavefunction for an excited state is a linear combination of these single excitations:

$$\Psi_{\mathrm{CIS}} = c_0\psi_0^{HF} + \sum_{ia} c_i^a \Psi_i^a \tag{1.31}$$

where i and a are occupied and virtual orbitals, respectively. The coefficients c_i^a are determined by solving the CIS eigenvalue problem, which is derived from the time-independent Schrödinger's equation:

$$\hat{H}\Psi_{\mathrm{CIS}} = E_{\mathrm{CIS}}\Psi_{\mathrm{CIS}} \tag{1.32}$$

Substituting the CIS wavefunction and projecting onto a single-excitation determinant leads to the CIS Hamiltonian matrix:

$$\sum_{jb}\langle\Psi_i^a|\hat{H}|\Psi_j^b\rangle c_j^b = E_{\mathrm{CIS}}c_i^a \tag{1.33}$$

This can be rewritten in matrix form as:

$$\mathbf{H}_{\mathrm{CIS}}\mathbf{c} = E_{\mathrm{CIS}}\mathbf{c} \tag{1.34}$$

The elements of the CIS Hamiltonian matrix $\mathbf{H}_{\mathrm{CIS}}$ are given by:

$$H_{ia,jb} = \langle\Psi_i^a|\hat{H}|\Psi_j^b\rangle = \delta_{ij}\delta_{ab}(\epsilon_a - \epsilon_i) + \langle ai||bj\rangle \tag{1.35}$$

where ϵ_i and ϵ_a are the Hartree-Fock occupied and virtual orbital energies, and $\langle ai||bj\rangle$ represents the anti-symmetrized two-electron integrals:

$$\langle ai||bj\rangle = \langle ai|bj\rangle - \langle ai|jb\rangle \tag{1.36}$$

According to Brillouin's theorem, singly excited determinants, Ψ_i^a, do not interact directly with a reference HF determinant, ψ_0^{HF}. Thus, on mixing of the two states, the off-diagonal element does not contribute to the energy, i.e.

$$\langle \psi_0^{HF} | H | \Psi_i^a \rangle = 0 \tag{1.37}$$

The main advantage of CIS is its simplicity and relatively low computational cost. It provides a qualitative understanding of excited states and is often used as a starting point for more accurate calculations. However, CIS has several limitations:[58,59]

1. It neglects electron correlation effects, as it only considers single excitations from the Hartree-Fock reference.

2. It often overestimates excitation energies due to the lack of correlation.

3. It is not suitable for describing double excitations.

1.3.2 Time Dependent Density Functional Theory (TDDFT)

Time-dependent Density Functional Theory is a powerful and widely used method for studying the excited states of molecular systems.[60] It extends the concepts of ground-state DFT to the time-dependent regime, allowing for the calculation of electronic excitations and response properties.

TDDFT is based on the Runge-Gross theorem,[61] which is the time-dependent analog of the Hohenberg-Kohn theorem in DFT. According to the Runge-Gross theorem, there is a one-to-one correspondence between the time-dependent external potential and the time-dependent electron density. This allows the use of a time-dependent Kohn-Sham (KS) system of non-interacting electrons to describe the dynamics of the interacting system. The time-dependent Kohn-Sham equations are given by:

$$i\frac{\partial}{\partial t}\psi_i(\mathbf{r},t) = \left[-\frac{1}{2}\nabla^2 + v_{\mathrm{KS}}(\mathbf{r},t)\right]\psi_i(\mathbf{r},t), \tag{1.38}$$

where $v_{\mathrm{KS}}(\mathbf{r},t)$ is the time-dependent Kohn-Sham potential, which includes the external potential, the Hartree potential, and the exchange-correlation potential as shown in Eq. 1.29 and Eq. 1.30:

In the linear response regime,[62] TD-DFT can be used to calculate excitation energies by perturbing the system slightly and examining its response. This approach leads to Casida's equations,[63] which are central to TD-DFT calculations of excited states. These equations relate the response of the electron density to the external perturbation and can be written as:

$$\sum_j \left[\delta_{ij}\delta_{ab}(\epsilon_a - \epsilon_i) + 2\sqrt{(\epsilon_a - \epsilon_i)(\epsilon_b - \epsilon_j)}K_{ia,jb} \right] F_{jb} = \omega F_{ia} \tag{1.39}$$

where ϵ_i and ϵ_a are the KS orbital energies, F_{ia} are the excitation amplitudes, ω is the excitation energy, and $K_{ia,jb}$ are the coupling matrix elements involving the exchange-correlation kernel:

$$K_{ia,jb} = \int\int \phi_i^*(\mathbf{r})\phi_a(\mathbf{r}) f_{\text{xc}}(\mathbf{r}, \mathbf{r}'; \omega)\phi_j(\mathbf{r}')\phi_b^*(\mathbf{r}') d\mathbf{r} d\mathbf{r}' \tag{1.40}$$

where f_{xc} is the exchange-correlation kernel.

The Tamm-Dancoff Approximation (TDA) is a simplification of the full TD-DFT equations.[64–66] In the TDA, the coupling between the excitation and de-excitation terms is neglected, reducing the complexity of the problem. This approximation often provides a good estimate of excitation energies with significantly less computational effort. The TDA reduces Casida's equations to a simpler form:

$$\sum_j \left[\delta_{ij}\delta_{ab}(\epsilon_a - \epsilon_i) + 2\sqrt{(\epsilon_a - \epsilon_i)(\epsilon_b - \epsilon_j)}K_{ia,jb} \right] F_{jb} = \omega F_{ia} \tag{1.41}$$

However, the coupling matrix elements $K_{ia,jb}$ are only considered for the direct interaction terms, ignoring the coupling with de-excitations. This simplifies the eigenvalue problem:

$$\sum_{jb} A_{ia,jb} F_{jb} = \omega F_{ia} \tag{1.42}$$

where the matrix A is defined as:

$$A_{ia,jb} = (\epsilon_a - \epsilon_i)\delta_{ij}\delta_{ab} + 2\sqrt{(\epsilon_a - \epsilon_i)(\epsilon_b - \epsilon_j)}K_{ia,jb} \tag{1.43}$$

TD-DFT, including its TDA variant, is computationally efficient and provides a good balance between accuracy and computational cost, making it suitable for large systems. The accuracy of TD-DFT depends on the choice of the exchange-correlation

functionals. Standard functionals can struggle with charge-transfer and Rydberg excitations.[67,68] The TDA, while reducing computational cost, can sometimes lead to less accurate results for certain types of excitations.[69] We will go into more detail related to charge transfer excitations in the next chapter.

1.4 Fundamentals of UV-Visible Spectroscopy

Spectroscopy techniques such as infrared, ultraviolet-visible (UV-vis), and femtosecond electronic spectroscopy are widely used to study the electronic behavior of various chemical systems and molecular reactions in the condensed phase.[70–76] These techniques help us understand phenomena like charge transfer, electronic excitation, Coulombic coupling, and excitation energy transfer. For instance, UV-visible spectroscopy allows us to examine the spectroscopic properties of molecules occurring in the 200 - 800 nm wavelength range. This type of spectroscopy involves the coupling of vibrational degrees of freedom with electronic excitations and is also known as vibronic spectroscopy. We can gain insights into their electronic structure by measuring how molecules interact with ultraviolet and visible light. This interaction occurs when photons are absorbed, promoting electrons from their ground states to excited states. Analyzing the specific wavelengths of light absorbed provides valuable information about electronic transitions and chemical environments within a sample. In Chapter 4, we will go through the computation of UV-visible spectra of molecules in both implicit and explicit solvent environments.

UV-vis spectroscopy has wide-ranging applications. In quantitative analysis, the characteristic absorption bands of a molecule can be used to determine its concentration in a solution based on the Beer-Lambert Law. This technique finds application in various fields, including biochemistry for quantifying proteins and DNA and environmental science for monitoring pollutants.

1.4.1 Fermi's Golden Rule

The Fermi golden rule[77,78] in quantum mechanics describes the transition probability between quantum states due to an external perturbation. Specifically, it focuses on the rate of transitions from an initial state to a final state caused by the interaction with an external field (such as light). The rule is particularly relevant in spectroscopy, which explains the absorption and emission of electromagnetic radiation by atoms and molecules.

At its core, the Fermi golden rule relies on the concept of time-dependent perturbation theory.[79] When an external field (e.g., a photon) interacts with a quantum system, it induces transitions between energy levels. The probability of such transitions depends on the strength of the perturbation, the energy difference between the initial and final states, and the density of states available for the transition. Mathematically, the Fermi golden rule is expressed as:

$$W_{i\to f} = \frac{2\pi}{\hbar}|V_{if}|^2\rho(E_f) \tag{1.44}$$

where: $W_{i\to f}$ represents the transition rate from the initial state i to the final state f. V_{if} is the matrix element of the perturbing interaction between the states. $\rho(E_f)$ denotes the density of final states at the energy E_f.

The Fermi Golden Rule has several important implications:

1. Absorption and Emission Spectra: In UV-Vis spectroscopy, the rule explains the absorption and emission spectra observed when molecules absorb or emit photons. The intensity of spectral lines depends on the transition probabilities governed by the Fermi Golden Rule.

2. Lifetime of Excited States: The rule provides insights into the lifetime of excited states. Short-lived states (with high transition rates) correspond to fast decay processes, while long-lived states exhibit slower decay.

3. Rate Equations: The Fermi Golden Rule is foundational in rate equations for chemical reactions. It connects the microscopic quantum world to the macroscopic observable.

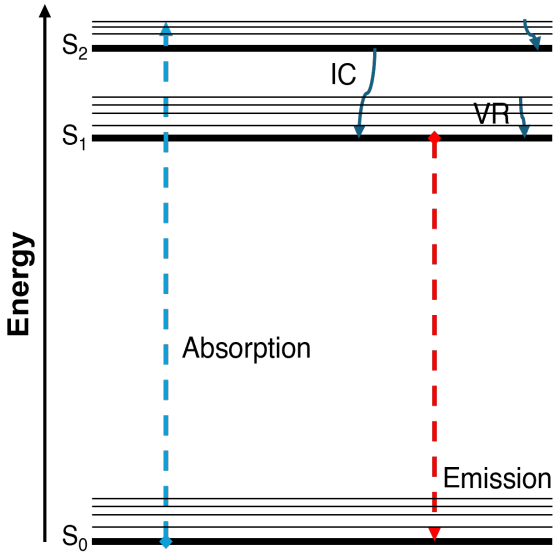

Figure 1.2: One form of Jablonski diagram showing absorption, internal crossing (IC), vibrational relaxation(VR), and emission processes

The Fermi Golden Rule bridges quantum mechanics and spectroscopy, allowing us to understand the dynamics of transitions and the behavior of quantum systems under external influences.

1.4.2 The Jablonski Diagram

The Jablonski diagram, see Figure 1.2, is a visual representation that illustrates the process of light absorption and emission.[80] The diagram displays the ground state (S_0) and the first two excited states (S_1 and S_2) of a molecule. When the molecule absorbs light, its electrons are excited to higher vibrational states of the excited state, shown by vertical transition lines. Following initial excitation, the electron undergoes rapid electronic transitions, including internal crossing (IC) from a higher excited state to the first excited state, as well as vibrational relaxation (VR) and reorganization processes. These transitions occur in incredibly short time frames, measured in attoseconds and femtoseconds, during which the nuclei remain essentially fixed. This concept is known as the Franck-Condon principle,[81] which will be further discussed in Chapter 3 and Chapter 4. Once the molecule reaches the lowest excited state, it reaches thermal equilibrium with its surroundings. After

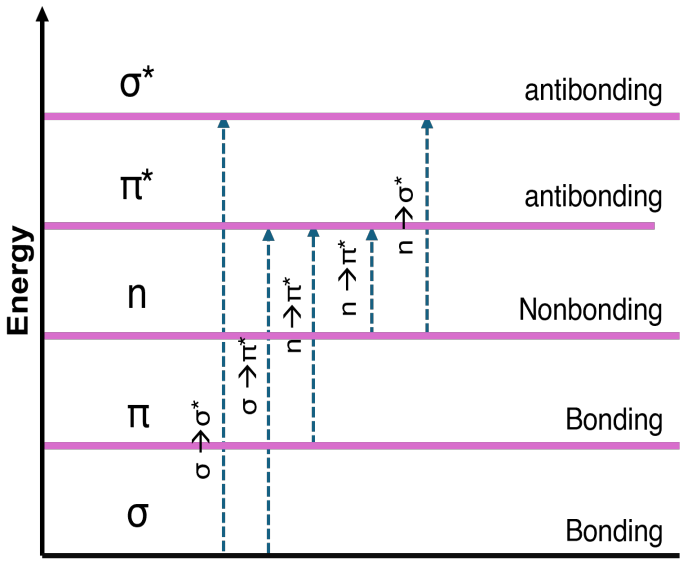

Figure 1.3: Electronic Transitions

equilibration, the emission process occurs, and according to Kasha's rule,[82] 99% of the emission comes from the S_1 excited state. It's important to note that there are other processes, such as non-radiative energy transfer, quenching, and luminescence, that are not covered here. The Jablonski diagram is a simple yet important tool for illustrating the interaction between light and matter.

1.4.3 Electronic Transitions

The electronic transitions mainly involve exciting electrons from the highest occupied molecular orbital (HOMO) to the lowest unoccupied molecular orbital (LUMO). These transitions can be grouped into $\pi \rightarrow \pi^*$, $n - \pi^*$, and $\sigma \rightarrow \sigma^*$ transitions, shown in figure 1.3. The difference in energy between these orbitals determines the absorbed light's wavelength. The Laporte selection rule[83] for UV-visible spectroscopy states that electronic transitions between two symmetric states are forbidden; however, they are allowed between unsymmetric states. For a transition to be allowed, it must cause a change in the molecular dipole moment. This is why molecules without a permanent dipole moment, such as homonuclear diatomic molecules, do not absorb light in the UV-visible region.

1.4.4 The Stokes Shift

When examined closely, the Jablonski diagram shows that emission/fluorescence spectra occur at lower energies than absorption spectra. Sir G. G. Stokes first discovered this energy shift,[84] which is now known as the Stokes shift (SS). The SS is a feature of fluorescence spectra, particularly in solution.

$$SS = \lambda_{Emi}^{max} - \lambda_{Abs}^{max} \tag{1.45}$$

It is usually measured as the difference between the molecule's absorption and emission maximum peaks. Vibrational relaxation (VR) is one common cause of the Stokes shift, but factors like solvent polarity and energy transfer processes can also influence the value. Fluorophores have an intriguing characteristic - they are sensitive to changes in the polarity of their surrounding environment. As a result, the Stokes shift significantly depends on the interaction between the molecules and the surrounding environment. This sensitivity is often utilized to determine structural and pH changes in a protein environment in various bio-imaging applications by analyzing fluorophores' emission spectral shape and intensities. The definition of Stokes shift can be challenging when there are multiple maximum peaks in either the absorption or emission spectra. In Chapter 4, we will address how to calculate the Stokes shift in such scenarios.

1.4.5 The Mirror-Image Rule

Due to rapid vibrational relaxation, excitation energies typically do not affect emission spectra. Generally, both absorption and emission spectra are mirror images of each other because they involve the same vibronic transitions. Figure 1.4 shows mirror image absorption and emission spectra of anthracene.[85] In most fluorophores, the energy levels are local excitations and are not significantly altered by electron redistribution during or after excitation. However, some molecules have emissions from an S_2 state,[86] or the molecule exists in two ionization states,[87] violating Kasha's rule. These situations are not common in the molecules used in most fluorescence-based applications. Polynuclear aromatic hydrocarbons typically exhibit well-matched absorption and emission spectra.

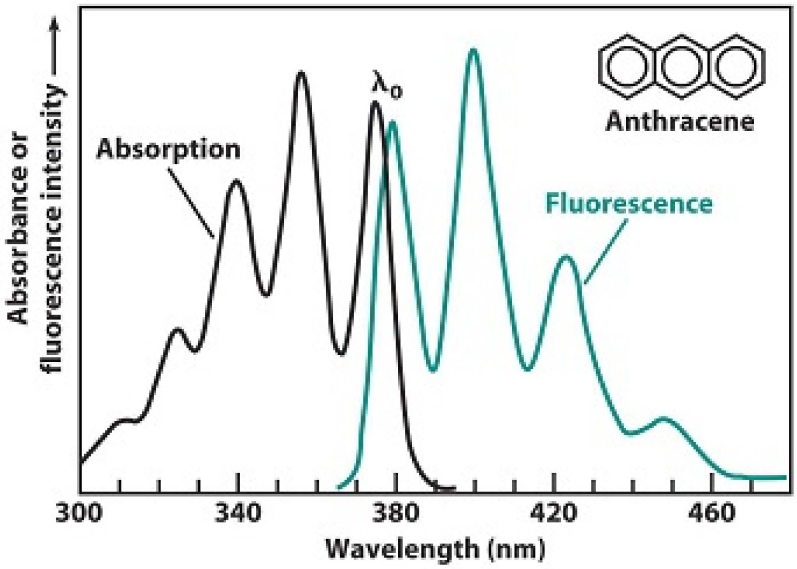

Figure 1.4: Absorption and emission spectra of anthracene showing mirror image relation. Adapted from Byron, C.M. and Werner, T.C., *J. Chem. Ed.*, 1991, 68, 433.[85]

1.4.6 Environmental Influence

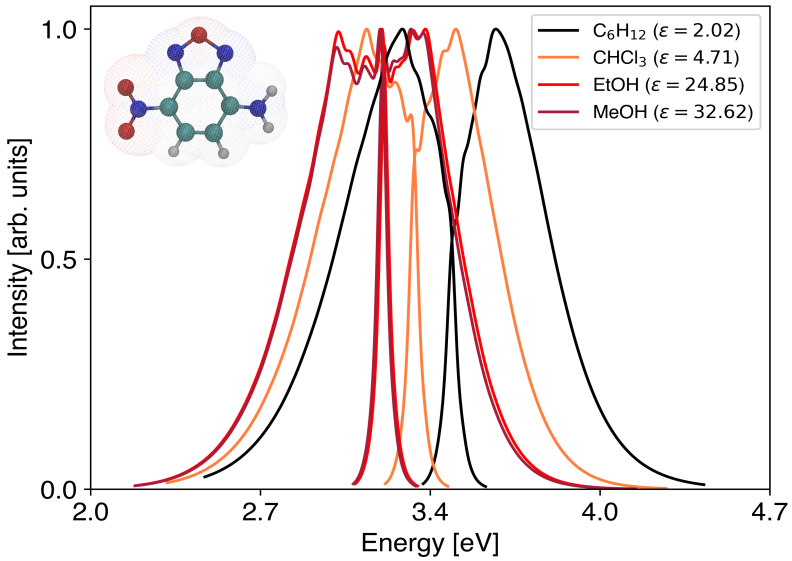

Figure 1.5: Absorption and fluorescence lineshape spectra of NBD in various implicit solvents of increasing dielectric constant. The level of theory used is TDA/CAM-B3LYP/6-31G(d) with IEFPCM solvent model

The environment around the chromophore can have profound effects on its atomic

and electronic properties. The effects of the environment are multifaceted in nature and could result from the following reasons:

1. Multiple excitation and deexcitation pathways
2. Planar and twisted charge transfer pathways
3. Solvent polarity and viscosity
4. Molecular conformational changes

Relative to absorption spectra, the fluorescence properties of the molecule are much more sensitive to environmental fluctuations. The excited state, from which fluorescence occurs, is more reactive to its surroundings than the ground state involved in absorption, allowing for more interactions with the environment.[88,89] The longer timescale of fluorescence also enables solvent molecules to reorient around the excited fluorophore, affecting the energy of emitted photons and resulting in spectral shifts. Fluorophores with large excited-state dipole moments can exhibit significant spectral shifts in response to changes in solvent polarity, particularly in emission spectra.[90,91] The environmental effects such as spatial confinement, where chromophores embedded in protein environments may alter the spectral properties due to restricted movement and specific interactions.[92–96] Moreover, molecules in an open system can experience environmental effects akin to a thermal bath, where the surrounding medium can induce or relax electronic excited states, thereby affecting the absorption and emission spectra.[97–99]

Solvatochromism,[100] the phenomenon where solvent polarity changes the energy levels of molecular electronic states, thus shifting the absorption or fluorescence spectra,[101–105] further exemplifies the profound impact of the environment on spectroscopic behavior. A typical example of solvent effects on the absorption and fluorescence spectra of NBD in implicit solvents of varying dielectric constant is shown in Figure1.5. Additionally, the synergy between the molecule and its environment can result in complex behaviors such as enhanced fluorescence[106] or quenching,[107] dependent on the intricate balance of intermolecular interactions and the physicochemical properties of the surroundings. These interactions underscore the necessity of considering

the environmental context when interpreting spectroscopic data, as they can significantly modulate the spectral signatures of molecules, offering deeper insights into their behavior in diverse settings.

In the next chapter, we will revisit some fundamental aspects of DFT functionals. Following that, I will present my work benchmarking how these functionals impact the absorption and emission spectra of molecules in implicit and explicit solvent environments. These examples will offer guidance on how to navigate the zoo of DFT functionals and make informed decisions when selecting one for studies of optical spectroscopy of chromophores in solution.

Chapter 2

Benchmark of Density Functionals for Vibronic Spectra

This chapter provides a benchmark study of density functionals for modeling vibronic spectra for molecules in solution. It contains an overview of Density Functional Theory (DFT) and approximate density functionals, categorizing functionals into the famous Jacob's ladder and examining their efficacy in modeling excited state properties. The performance of various functionals in implicit and explicit solvent environments is compared using three dyes (Nile Red, NBD, and 7MC). The findings highlight the limitations of some functionals and the improved performance of hybrid and long-range corrected hybrid functionals. The chapter underscores the necessity of informed functional selection for reliable spectral predictions, advocating for comprehensive benchmarking to guide the choice of DFT functionals for vibronic absorption and fluorescence spectra.

2.1 Introduction

Density Functional Theory (DFT) functionals are frequently benchmarked to evaluate their performance across various properties.[108–122] Runge and Gross first introduced Time-Dependent Density Functional Theory (TD-DFT) in 1984 as an extension of DFT into the time domain.[61] TD-DFT has since become a popular method for modeling excited state energies, structures, and properties. In 1995, Casida developed the linear response formalism for TD-DFT, which has been widely used for studying excited state properties.[63] Currently, most TD-DFT functional benchmarks make use

of the vertical approximation, which calculates excited state energies and properties based on the optimized ground-state geometry without fully exploring the ground state or excited state potential energy surfaces.[123–126] While this method allows for calculations on large systems using a single-point TD-DFT calculation, it is not suitable for comparing vertical transition energies to experimental measurements of λ_{max}, which involve frequency dependence.[127–131]

Our work focuses on the accurate modeling of excited state properties, particularly those with significant charge-transfer character. Accurate modeling of vibronic spectra necessitates the determination of functionals that not only yield precise excitation energies but also faithfully represent ground and excited state potential energy surfaces. The motivation behind benchmarking density functionals for vibronic spectra lies in the need to achieve reliable theoretical predictions that can complement and guide experimental studies. Vibronic spectra, which incorporate both electronic and vibrational transitions, are crucial for understanding molecules' photophysical and photochemical properties. The accurate simulation of these spectra is essential for developing fluorescent dyes, organic photovoltaic materials, and other optoelectronic devices.[132–136]

In this chapter, we dive into the intricacies of DFT considerations, focusing on selecting appropriate functionals for modeling charge-transfer excitations – a topic that has garnered significant attention in the field.[137–145] Charge-transfer excitations are particularly challenging to model due to the need to accurately represent both the donor and acceptor states and the coupling between them. The choice of functional can significantly influence the predicted spectra, making it imperative to perform comprehensive benchmarks.

Through extensive benchmarking of density functionals, we aim to identify those that provide the most accurate vibronic lineshapes for systems of interest. I will present results comparing the performance of various functionals for three solvated dyes, emphasizing the importance of choosing the right functional for accurate predictions. The benchmarks include comparisons of vibronic absorption lineshapes of

Nile Red in implicit solvent, published in 146, as well as vibronic absorption and fluorescence lineshapes for three dyes in explicit solvent environments, published in 147.

This chapter begins with a brief introduction to density functionals using Jacob's ladder, setting the stage for a detailed discussion on functional selection for modeling charge-transfer excitations. The subsequent sections will build on this foundation, presenting our benchmark results and highlighting the strengths and limitations of different functionals. By providing a thorough benchmark of density functionals for vibronic spectra, we aim to offer insights that will guide the computational studies conducted in chapters 3 and 4 and improve the reliability of theoretical predictions in computational UV-visible spectroscopy.

2.2 Jacob's Ladder of Density Functional Theory

A unique challenge in developing density functional theory is the inability to improve density functionals systematically. Unlike other theories, adding more components to meet stricter constraints or provide more flexible functional forms does not guarantee overall improvement across all types of interactions. This sets DFT apart from wave functional theory, as wave function-based methods benefit from a clear hierarchy that allows for the creation of systematically improvable models. Perdew and Ruzsinszky introduced the concept of systematically categorizing density functional approximations based on their level of sophistication and intended accuracy.[148] The Jacob's Ladder is a metaphorical classification scheme that organizes the hierarchy of approximations in exchange-correlation (XC) functionals used in DFT to calculate the electronic structure of molecules and solids.

Each rung represents a progressively more complex and accurate approximation to the true, unknown XC functional. Below, I categorize each rung and its associated advantages and disadvantages:

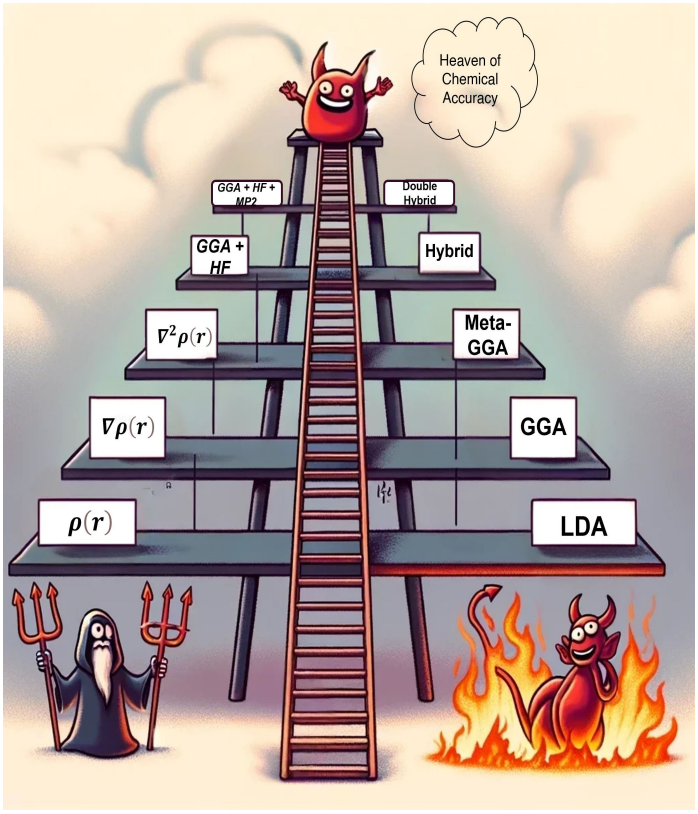

Figure 2.1: The Jacob's Ladder

2.2.1 Rung 1: Local Density Approximation (LDA)

The simplest XC functional only depends on the electron density, as shown in equation 2.1. This first rung, also known as the local spin-density approximation (LSDA), treats each point in space as though it were part of a uniform electron gas, neglecting how changes in density might alter electron interactions. The XC energy using only the density can simply be obtained as

$$\begin{aligned} E_{xc} &= \int \rho(r)\epsilon_{xc}(\rho(r))d\mathbf{r}, \\ \epsilon_{xc} &= E_x + E_c \\ \epsilon_x &= \sum_{\sigma}^{\alpha,\beta} \int_{\alpha,\beta} \epsilon_{x,\sigma}^{UEG} d\mathbf{r} = -\frac{3}{2}\left(\frac{3}{4\pi}\right)^{\frac{1}{3}} \sum_{\sigma}^{\alpha,\beta} \int \rho_{\sigma}^{\frac{4}{3}} d\mathbf{r}. \end{aligned} \tag{2.1}$$

The analytical expression of the correlation, ϵ_c, is unknown and can be solved numerically via quantum Monte Carlo methods.[149] Some popular density functionals

associated with this rung are SVWN[150] (Slater exchange + Vosko-Wilk-Nusair correlation), PZ81,[151] and PW92.[152] LDA's severe assumptions lead to the overbinding of molecules, inaccurate bond lengths, and poor vibrational frequencies.[153,154] While overly simplistic for most molecules, LSDA remains surprisingly useful for certain metallic systems[155] and provides a theoretical reference point for testing higher-rung functionals. The SVWN/SVWN5 functionals have been used to calculate absorption maxima, oscillator strengths,[156,157] vertical excitation energies,[158] and vibrational frequencies.[153,159] However, their accuracy in computing vibronic lineshapes has remained limited.[160,161]

2.2.2 Rung 2: Generalized Gradient Approximation (GGA)

The distribution of electrons in most molecules is not uniform, which poses a challenge for LDA functionals. GGAs address this issue by considering the electron density gradient $\Delta\rho(r)$, which gives insight into how quickly the electron density changes in space.[162–165] This consideration helps to capture some of the non-local aspects of how electrons interact with each other. The exchange-correlation energy depends on both the density and its derivative and can be obtained as

$$E_{xc} = \int \rho(r)\epsilon_{xc}(\rho(r), \Delta\rho(r))d\mathbf{r}, \tag{2.2}$$

where ϵ_{xc} now relies on both density and how rapidly it's changing in space. This method was initially called non-local DFT due to the higher-order derivative expansion formalism. However, the term "gradient approximation" is more fitting, as the first derivative of any function at a single point is inherently local. PBE[162] and BLYP[166,167] are widely used GGA functionals, and numerous variations and refinements are available. Empirical parameter-free GGA functionals have been developed based on rational function expansions of the reduced gradient, such as B86,[166,168–170] and PBE.[162]

The GGA functionals show improved capability in modeling molecular geometries, bond strengths, and reaction barriers compared to the LDA and can be applied to a wide range of materials. However, GGA functionals often experience self-interaction

errors due to incomplete cancellation of Coulomb and exchange energies for one-electron densities.[171–175] Additionally, they do not accurately describe weaker, long-range interactions such as Van der Waals forces.[176–178]

2.2.3 Rung 3: Meta-Generalized Gradient Approximation (mGGA)

Meta-generalized gradient approximation (mGGAs) density functionals aim for increased accuracy by incorporating more information, including the kinetic energy density $\tau(r)$ and potentially the Laplacian of the density $\Delta^2\rho(r)$ reflecting density curvature.[179,180] The XC energy of a mGGA functional can be represented as

$$E_{xc} = \int \rho(r)\epsilon_{xc}(\rho(r), \Delta\rho(r), \tau(r), ...)d\mathbf{r}. \tag{2.3}$$

Commonly used standard mGGA functionals like TPSS,[181] SCAN,[165] and revTPSS[182,183] are often employed in describing solids, surfaces, and systems where weaker long-range interactions are significant. mGGAs are specifically designed to enhance the accuracy of these descriptions. Despite being comparable in cost to GGA calculations, mGGAs are more challenging to parameterize due to their increased complexity[184–186] and may not universally improve all properties, sometimes trading off the robustness of GGAs for specific advantages. Unlike the LDA functional, GGA and mGGA functionals have been routinely used to compute the λ_{max}, oscillator strength,[187] and nuclear ensemble spectra.[188]

2.2.4 Rung 4: Hybrid Functionals

Hybrid functionals, located on the third level of Jacob's Ladder, mix a part of precise HF exchange with DFT approximate exchange and correlation energy. This combination aims to reduce the inherent errors in pure DFT approximations by using the more accurate, albeit computationally expensive, HF exchange. This approach reintroduces physics that the earlier rungs approximated due to relying solely on the density. The adiabatic connection approach[189–192] allows the majority of global hybrid functionals to be represented by a form described in equation 2.4.

$$E_{xc}^{GH} = \alpha E_x^{HF} + (1-\alpha)E_x^{GGA/mGGA} + E_c^{GGA/mGGA}. \tag{2.4}$$

By fitting three linear parameters for atomization energies, Becke developed the first global hybrid functional, B3PW91.[193] Another widely used DFT functional, B3LYP, is similar to B3PW91, but with the correlation energy portion replaced from PW91 and PW92 to VWN1RPA[194] and LYP. Most global hybrid functionals contain a consistent 20 to 25 percent exact Hartree-Fock exchange. Some of the celebrated examples include B3LYP, PBE0, and M06. Hybrid functionals often deliver excellent accuracy for thermochemistry,[193,195,195–201] reaction barriers,[202–204] and electronic excitations.[111,140,188,205,206] We will employ hybrid functionals and some of their categories in section 2.3.2.

2.2.5 Rung 5: Double-Hybrid Functionals

As we move up to the fourth level, we come across double hybrid functionals, which add another layer of complexity. Double hybrids not only include a portion of exact HF exchange but also integrate a corrective element from second-order Moller-Plesset (MP2) theory.[207,208] By accounting for electron correlation effects from MP2, a more thorough treatment of electronic interactions is achieved, enhancing accuracy for a wider variety of chemical systems. The XC energy using double hybrid functional can be obtained using equation 2.5.

$$E_{xc}^{DH} = \alpha E_x^{HF} + (1-\alpha)E_x^{GGA/mGGA} + \beta E_c^{\mathrm{MP2}} + (1-\beta)E_c^{GGA/mGGA} \tag{2.5}$$

There are several popular double hybrid functionals used in computational chemistry, such as B2PLYP,[209] DSD-BLYP,[210] and PWPB95,[115] which have demonstrated superior performance in capturing non-covalent interactions, reaction energies, and spectroscopic properties.[211] These functionals aim to achieve high accuracy in solving complex problems, especially those involving strong correlation and non-covalent interactions. However, they are computationally demanding, and the choice of parameters can greatly affect their performance.

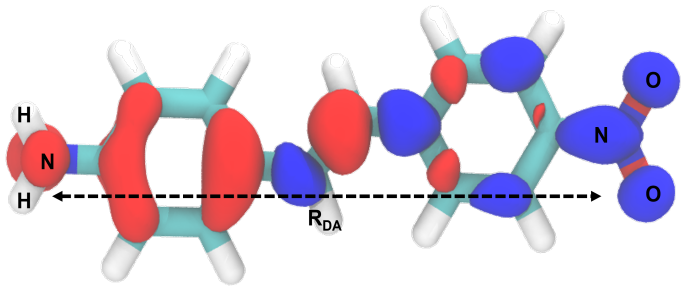

Figure 2.2: The density difference plot of 4Amino-4'Nitrostilbene push-pull electron system

For a more comprehensive analysis of DFT functionals, we recommend that readers refer to the works of Goerigk and Mehta,[55,212] as well as Becke[53] and Mardirossian and Gordon.[54]

2.3 Charge Transfer (CT) Excitations

If a system consists of electron donor and electron acceptor groups, typically, the excitation process resembles charge transfer excitation. Most of the molecules used in fluorescence spectroscopy involve charge transfer excitation, generally of a $\pi \rightarrow \pi^*$ nature. One of the failures of TD-DFT using LDA or GGA functionals, and even hybrid functionals, comes from its failure to describe CT accurately.[68,140,142,144,213–217]

Figure 2.2 shows a typical example of push-pull electron systems, where NH_2 is the donor group and NO_2 is the acceptor group with trans-stilbene acting as a π-spacer. In fluorescence spectroscopy, most molecules exhibit charge transfer excitation, often of a $\pi \rightarrow \pi^*$ nature. One limitation of traditional TD-DFT is its failure to describe charge transfer accurately.

In the limit of large electron-hole distance, R_{DA}, the exact characterization of the CT energy can be obtained via:

$$E_{CT}^{exact} = E_d - E_a - \frac{1}{R_{DA}}, \tag{2.6}$$

where E_d is the ionization energy of the donor required to remove its electron, E_a is the electron affinity of the acceptor, and $\frac{1}{R_{DA}}$ is the Coulombic interaction between

the newly generated electron-hole pair.

Typically, a local excitation is localized on the electron-withdrawing group, n $\rightarrow \pi*$, in a molecule, whereas a charge transfer excitation, $\pi \rightarrow \pi*$, often involves migration of charge from the donor to the acceptor region.[218,219] Due to this difference in the excitation character, both excitations generally occur on different energy scales. Using the single-pole approximation (SPA),[220–223] we can obtain the CT energy as:

$$E_{CT}^{SPA} = \Delta\epsilon + K(\Delta\epsilon) \tag{2.7}$$

where $\Delta\epsilon = \epsilon_{LUMO}^{A} - \epsilon_{HOMO}^{D}$ is the difference between the KS eigenvalue of the lowest unoccupied molecular orbital (LUMO) and highest occupied orbital (HOMO) of the acceptor and donor systems. K is a correction given by:

$$K(\Delta\epsilon) = 2\mathcal{R}\int d^3r \int d^3r' \phi_{LUMO}^{A}(r)\phi_{HUMO}^{d}(r) f_{Hxc}(r, r', \Delta\epsilon)\phi_{LUMO}^{A}(r')\phi_{HUMO}^{d}(r'), \tag{2.8}$$

At a large distance, due to the exponentially vanishing overlap, $K(\Delta E)$ goes to zero. For traditional TD-DFT, rung 1 to run 2, E_{CT}^{SPA} becomes equal to the difference of eigenvalues:

$$E_{CT}^{SPA} = \Delta\epsilon \tag{2.9}$$

As we can see, we are missing the $-1/R_{DA}$ component of E_{CT}^{exact}. In practical applications, traditional TD-DFT often yields KS eigenvalues lower than expected and fails to capture the discontinuity, Δ_{xc}^{a}. This limitation is fundamentally why traditional TDDFT struggles to describe charge transfer excitations accurately. One way to improve upon this limitation of TDDFT is to use the exact Hartree-Fock exchange (EXX).

2.3.1 The Role of Exact Hartee-Fock Exchange

When using time-dependent Hartree-Fock (TDHF) instead of TDDFT, specifically in the TDA approach, the CT energy at large distances is expressed as:

$$E_{CT}^{TDHF} = \epsilon_{LUMO}^{A,HF} - \epsilon_{HOMO}^{D,HF} - \int d^3r \int d^3r' \frac{\phi_{LUMO}^{A}(r)\phi_{HOMO}^{d}(r)\phi_{LUMO}^{A}(r')\phi_{HOMO}^{d}(r')}{|r - r'|} \tag{2.10}$$

The inclusion of the exchange integral, the third term in the equation 2.10, restores the $-1/R_{DA}$ dependency. Furthermore, Koopman's theorem[224,225] implies that $\epsilon^{A,HF}_{LUMO} - \epsilon^{D,HF}_{HOMO}$ is approximately equal to $E_d - E_a$. This indicates that TDHF theory accurately predicts the CT excitation energy at large separations. Hence, it is recommended to use hybrid XC functionals, which incorporate a portion of EXX, as they enhance the traditional TDDFT approach in effectively describing the charge transfer process.

Traditional DFT methods, LDA, GGAs, and meta-GGAs, aim to model the exchange-correlation energy, which governs electron interactions. Although these methods are computationally efficient, they introduce inaccuracies such as self-interaction errors and the underestimation of long-range effects. Hartree-Fock theory calculates the exchange energy (part of the electron-electron interaction) by considering the exact way the wave function of one electron changes due to the presence of all other electrons. This captures non-local effects more accurately than DFT approximations alone.

2.3.2 Range-separated/long-range hybrid functionals

Hybrid functionals incorporate a portion of exact HF exchange into DFT approximations. The idea behind this approach is to offset the errors in DFT exchange-correlation with the more accurate but computationally expensive HF exchange. This is typically done through a mixing parameter:

$$E_{xc} = \alpha E_x^{HF} + (1-\alpha) E_{xc}^{GGA/mGGA}, \tag{2.11}$$

Range-separated and long-range corrected hybrid functionals further refine this approach by splitting exchange interactions into short-range and long-range components. A portion of exchange interaction is handled by a GGA or meta-GGA functional, which performs well locally. For long-range corrected functionals, the contribution from the Hartree-Fock exchange increases smoothly, addressing non-local interactions that lower-rung DFT methods miss. This division of labor allows for a more nuanced treatment of electron interactions.

Incorporating EXX into traditional TDDFT methods enhances various aspects of computational chemistry. It leads to improved thermochemical predictions,[193,195,195–198] more accurate heats of formation,[226,227] better reaction energy calculations,[228] and spectral lineshapes.[229] Additionally, it provides more accurate electronic excitation energies, reduces self-interaction errors, and improves the description of charge-transfer processes and weakly bound systems. Range-separated and long-range hybrids, such as ωB97X, CAM-B3LYP, and LC-ωPBE, offer improved descriptions of properties significantly impacted by long-range interactions.

Choosing the optimal separation parameter often requires balancing computational cost and the system's specific needs. Some limitations include selecting the fraction of HF exchange, which is system-dependent and non-trivial. Despite their strengths, these functionals can still struggle with very complex electron interactions, particularly in strongly correlated systems.

2.4 Hybrid DFT Functionals for Vibronic Spectra

Over the years, due to improvements in the computational power and efficient implementation of derivatives for many hybrid functionals in popular electronic structure packages, many excited state studies have been conducted benchmarking vertical excitation energies,[56,110,113,230–235] λ_{max},[109,236,237] and $0 \rightarrow 0$ transitions.[129,238,239] Hybrid DFT functionals that contain a flat percentage of the EXX are considered global hybrids. If the EXX is divided over short-range (SR) and long-range (LR) as shown in equation2.12, considered range-separated hybrid functionals and functionals that contain zero percent EXX at short range and one hundred percent EXX at long-range are considered long-range hybrids functionals.

$$\frac{1}{r_{12}} = \underbrace{\frac{1-(\alpha+\beta)(1-\mathbf{erfc}(\omega r_{12}))}{r_{12}}}_{SR} + \underbrace{\frac{\alpha+\beta(1-\mathbf{erfc}(\omega r_{12}))}{r_{12}}}_{LR} \tag{2.12}$$

where $1/r_{12}$ divides the DFT and HF EXX, α and β are mixing parameters. With $\alpha \neq 0$ and $\beta = 0$ representing global hybrids, $\alpha \neq 0$ and $\beta \neq 0$, range-separated

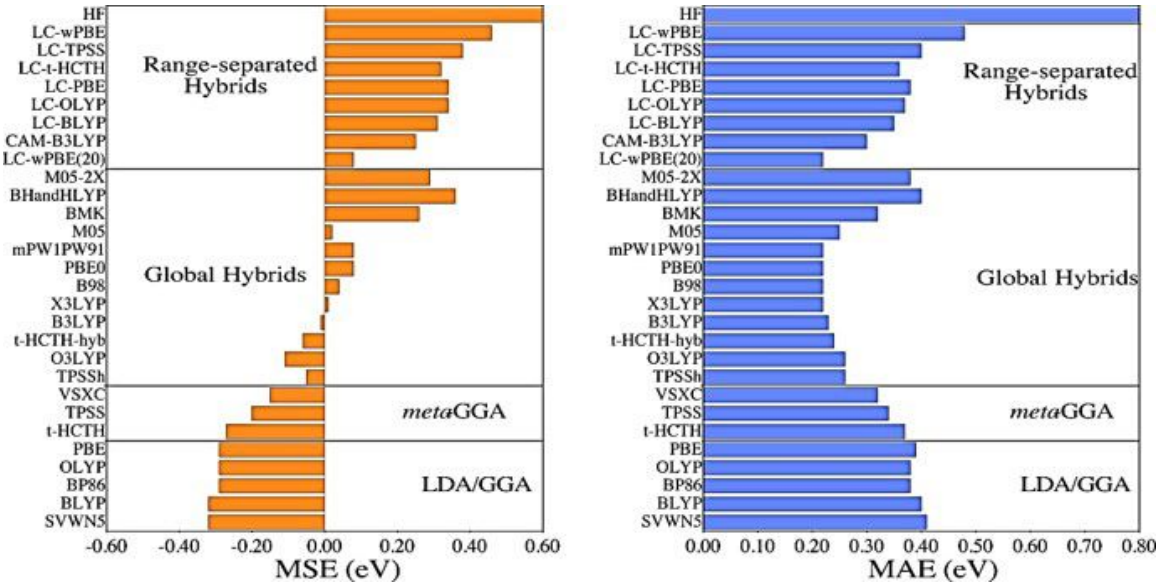

Figure 2.3: Mean absolute and mean signed error relative to experimental λ_{max} and vertical excitation energies. The figure is reproduced from article[230] with permission obtained from the International Journal of Quantum Chemistry

hybrids, and $\alpha = 0$ and $\beta \neq 0$ representing LR hybrid DFT functionals. The **erfc** is the error function, and ω is the tuning parameter, which has been shown to affect the properties of molecules.[240,241]

As seen in Figure 2.3, global hybrid functionals have performed exceptionally well for excitation energies, while long-range corrected and range-separated functionals overestimate the excitation energies, and LDA and mGGA functionals underestimate them. The overestimation arises due to the large percentage of EXX used in these functionals.

There have been few recent studies that have focused on comparing the vibronic spectra of molecules using DFT functionals.[161] Most of these studies have been carried out in an implicit solvent environment, with a focus on exploring the excited state[229,242,243] or using vertical approximations such as vertical gradient, vertical Hessian, or adiabatic shift.[244–248] Recently, there has been a growing number of studies on vibronic absorption spectra in explicit solvent environments.[146,249–262,262–268] However, there are still limited studies that explore fluorescence spectra[269–278] in explicit solvent environments and even more limited for vibronic fluorescence spectra.[279]

In the following section, I discuss how the selection of functionals impacts the lineshape of absorption and fluorescence vibronic spectra in implicit and explicit environments. These studies will provide the basis for choosing functionals when calculating vibronic spectra for chromophores with significant charge transfer characteristics.

2.4.1 Benchmark Study: Effect of Density Functional on Spectral Lineshapes

To determine the effect of various density functionals on the absorption and fluorescence lineshape, we selected three dyes, namely Nile red (NR), 7-nitrobenz-2-oxa-1,3-diazol-4-yl (NBD), and 7-methoxy coumarin-4-acetic acid, in various solvents, see Figure 2.4. These fluorophores are commonly used as fluorescent probes to label biological substrates.[280–285] The experimental absorption and emission data for NBD and NR were sourced from,[286] while spectra for 7MC in methanol were retrieved from the PhotochemCAD database.[287,288]

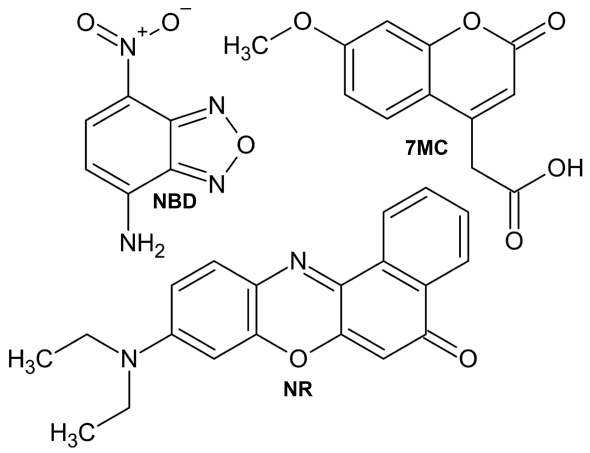

Figure 2.4: Chemical structures of the three chromophores used as benchmarks in this chapter: 7-nitrobenz-2-oxa-1,3-diazol-4-yl (NBD), Nile red (NR), and 7-methoxy coumarin-4-acetic acid (7MC).

In this study, we compared the performance of various functionals from the rungs described above, analyzing the spectral lineshapes. The functionals used can be categorized into the following categories:

1. GGA: BLYP, PBE
2. Hybrid Functionals:
   (a) Global: B3LYP(20%), B3PW91(20%), HSEH1PBE/HSE06(25%), M06(28%), M06-2X(54%), and MPW1PW91(25%), and PBE0(25%)
   (b) Range Separated: ωB97XD (SR: 19.57%, LR=100%, $\omega = 0.30$), and CAM-B3LYP (SR: 20%, LR=65%, $\omega = 0.33$)
   (c) Long Range Corrected: ωB97 (SR: 0%, LR=65%, $\omega = 0.11$) and LC-ωHPBE(SR: 0%, LR=100%, $\omega = 0.25$)

Our analysis here is focused on understanding how different types of functionals influence the spectral shape and intensity. We here perform benchmark studies of vibronic lineshapes for two different cases: (i) Nile Red with an implicit solvent model for water and cyclohexane using a large range of functionals and (ii) three dyes in explicit solvent, focusing on three high-performing functionals.

2.4.2 Computational Details

For all electronic structure calculations, we used the 6-31G(d) basis set, and for spectra in explicit solvent, we used empirical dispersion accounted via the D3 version of Grimmes dispersion.[289] Because the Tamm-Dancoff approximation provides similar excitation energies and, to some extent, comparable vibronic lineshapes to full TDDFT at a lower computational cost, we decided to use the TDA for our excited state calculations instead of full TD-DFT.[290] In Chapter 4, we will also compare the differences in the vibronic lineshapes that result from this choice. For the spectra generated in implicit solvent, we provide details of all functionals in the results and discussion section. For the explicit solvent lineshapes, we focus on the absorption and fluorescence vibronic lineshapes and provide comparisons for FC spectra using CAM-B3LYP,[291] LC-ωHPBE,[292–294] and M06-2x[295] density functionals in both implicit and explicit solvents.

For geometry optimization in explicit QM solvent, the 2020 development version of TeraChem[296] was used. Frequency calculations in frozen QM solvent and vibronic

spectra calculations were carried out using a developmental version of Gaussian16.[297] The integral equation formalism for the polarizable continuum model (PCM)[298–302] as implemented in Gaussian16 was used for modeling solvent effects on implicit solvent Franck-Condon (FC) absorption and emission spectra.

For all vibronic FC spectra, for both implicit and explicit solvent environments, the time-dependent implementation of one photon absorption and emission procedure[303–316] was employed with the default adiabatic Hessian model as implemented in the development version of the Gaussian16 electronic structure program. A temperature of 300 K was used for the finite temperature FC spectra. Two advantages of the time-dependent FC implementation are that zero temperature spectra are obtained along with finite temperature spectra at no additional computational cost, and no approximations are made when summing over contributions for combination modes.[317] The Gaussian16 default half width half maximum (HWHM) value of 135 cm^{-1} was used as the FC broadening factor.

For explicit solvent lineshapes, average FC lineshapes were generated using five randomly selected snapshots and aligning their 0-0 transitions. To compare the spectra equivalently, we transformed the experimental and simulated spectra into energy-independent lineshapes. Additionally, configurations were sampled using AIMD simulation; please refer to Chapter 4 for more details. Here, only the first excited state is considered since it is the bright state of interest.

2.4.3 Nile Red in Water and Cyclohexane: Implicit Solvent Models

The solvent polarity strongly influences NR's fluorescence. In polar solvents, NR is almost nonfluorescent; however, it undergoes fluorescence enhancement and significant absorption and emission blue shift in nonpolar solvents.[318–320] The experimental absorption spectra of NR in water and cyclohexane are shown in Figure 2.5. Two notable observations are that as the polarity of the solvent changes, there is a solvatochromic shift, and we also observe the emergence of distinct vibronic peaks in

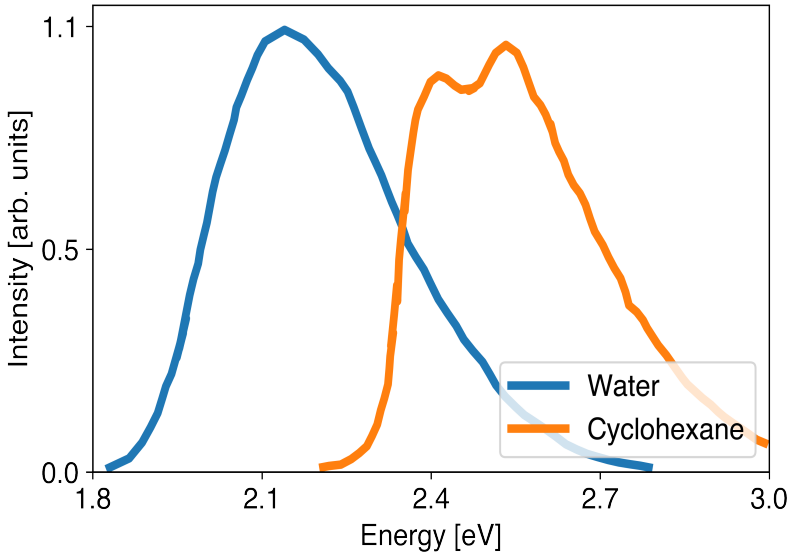

Figure 2.5: Experimental absorption spectra of NR in water and cyclohexane. The experimental data was extracted using the WebPlot digitizer from article[326]

.

cyclohexane. Some earlier studies have shown the charge transfer character of the excitation is responsible for driving the fluorescence properties of NR.[321–323] Previous implicit solvent studies showed the crucial role of vibronic coupling on the absorption spectra of NR.[324,325] Here, I will demonstrate the impact of density functional on the absorption spectra of NR in implicit water and cyclohexane solvents.

Figure 2.6 shows our simulated finite temperature Franck-Condon (FTFC) vibronic absorption spectra of NR in water obtained from various density functionals. Note that all the spectra here are aligned with their maxima such that the 0-0 transition is at the origin. The BLYP and PBE functionals (see inset) contain no EXX, and with their low intensity and multiple peaks clearly provide a less effective description of vibronic transitions compared to other functionals, showing that GGAs do not perform well for NR.

Among the global hybrid functionals with a similar percentage of EXX, M06 produces the highest initial peak with subsequent peaks of decreasing intensity. B3LYP also displays a high initial peak with broader subsequent peaks of moderate inten-

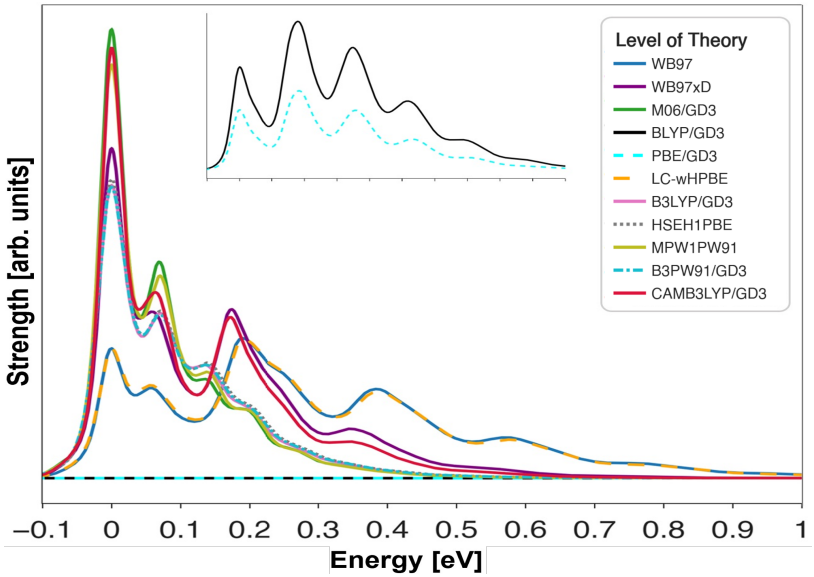

Figure 2.6: Nile Red in Water: Density functional comparison for FTFC absorption spectra in an implicit water solvent. The level of theory used here is TDA/6-31G and the IEFPCM implicit solvent model was used for solvent effects. The spectra are reproduced with permission from the Journal of Chemical Physics found in the SI of article[146]

sity. B3PW91 is similar to B3LYP but shows slight differences in peak positions and intensities. HSEH1PBE (HSE06) presents a high initial peak followed by smaller, smoother peaks. MPW1PW91 exhibits a high initial peak followed by moderate intensity peaks, similar to B3LYP and B3PW91.

The range-separated hybrid functionals WB97XD and CAM-B3LYP show high initial peaks, well-separated secondary peaks of moderate intensity, and overall very similar vibronic spectra to each other. The long-range hybrid functionals WB97 and LC-wHPBE exhibit high initial peaks with moderate-intensity secondary peaks. Relative to both global and range-separated hybrids, long-range hybrid functionals show equally pronounced vibronic peak spectra with a much broader global width.

When comparing the FTFC absorption spectra of NR in implicit water with experimental spectra, GGA functionals with no EXX clearly fail to capture the shape of the absorption spectra. Global hybrids perform similarly, along with wB97XD and CAM-B3LYP. LC-wHPBE and wB97 show similar features as with the global hybrid

for the first three peaks; however, the intensities of all peaks show significant variability. In implicit solvent, none of the functionals are able to reproduce single-peak broad absorption spectra, as seen in the experimental spectra. Next, we compare the role of these functionals on the lineshape when the polarity of the solvent is decreased substantially.

Figure 2.7 shows our simulated FTFC absorption spectra of NR in cyclohexane using an implicit solvent model. In cyclohexane, BLYP and PBE functionals again show overly low intensity, indicating consistently poor performance across different solvent environments. For the global hybrid functionals, MPWPW91 yields a high initial peak with smooth, clear peak separations relative to other global hybrids. B3LYP produces a high initial peak with broader subsequent peaks of moderate intensity. B3PW91 displays a similar pattern to B3LYP, with slight peak positions and intensities variations. HSEH1PBE (HSE06) shows a high initial peak followed by smaller, smoother peaks. M06 shows the lowest intensity for the first two peaks among all and has a less well-defined third peak.

Range-separated hybrid functionals WB97XD and CAM-B3LYP/GD3, just as in water, exhibit high initial peaks with well-defined secondary peaks, reinforcing their consistent performance across different solvent environments. Long-range hybrid functionals WB97 and LC-wHPBE maintain their characteristic high initial peaks with minor variations in secondary peak intensities between water and cyclohexane. WB97 is similar to WB97XD without dispersion corrections. LC-wHPBE shows more defined peaks than GGA.

Our analysis of the vibronic absorption spectra for NR in implicit solvent reveals that global hybrid functionals such as B3LYP, B3PW91, and MPW1PW91 exhibit consistent spectral shapes in both solvents, characterized by high initial and moderate-intensity secondary peaks. Range-separated hybrids WB97XD and CAMB3LYP also show similar spectral features in both environments, with high initial peaks and well-defined secondary peaks. However, some differences are observed:

1. The intensity and sharpness of the peaks vary slightly between the two solvents,

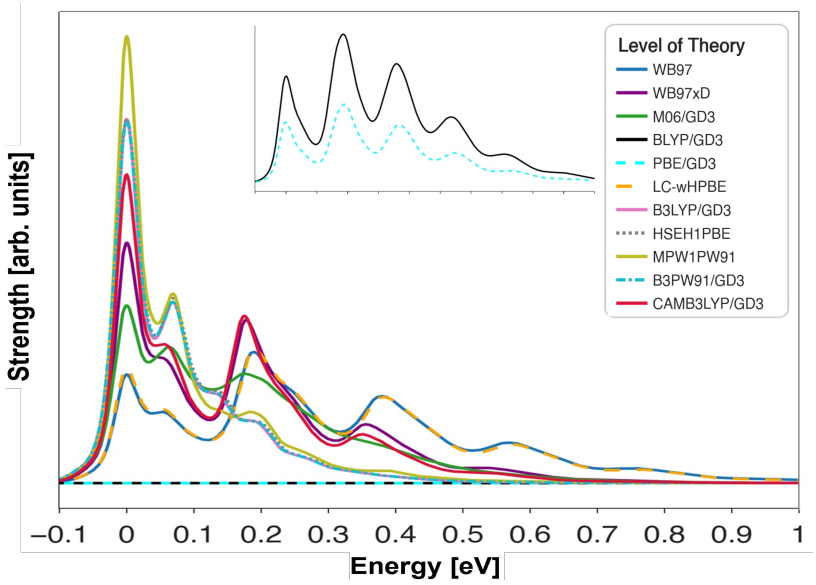

Figure 2.7: Nile Red in cyclohexane: Density functional comparison for FTFC absorption spectra in an implicit cyclohexane solvent. The level of theory used here is TDA/6-31G and the IEFPCM implicit solvent model was used for solvent effects. The spectra are reproduced with permission from the Journal of Chemical Physics found in the SI of article[146]

reflecting differences in solvent interactions. For example, the width of the first peak is slightly narrower in cyclohexane than in water. The intensity of the first peak also increases in cyclohexane, which could explain why NR is more fluorescent in non-polar environments than polar.

2. Long-range hybrids WB97 and LC-wHPBE maintain their characteristic high initial peaks but show minor variations in the shoulder's intensities and sharpness between water and cyclohexane.

Our comparison here examines how different density functionals affect the vibronic absorption spectra of Nile red in water and cyclohexane. Global hybrids consistently and reliably describe vibronic transitions, while range-separated and long-range hybrids increase peak definition and intensity. Our analysis emphasizes the importance of considering solvent effects and functional choices in UV-visible spectroscopy.

In experiments, the condensed phase spectra include explicit solvent interactions, resulting in featureless spectra without pronounced vibronic peaks due to contributions

from inhomogeneous broadening. This difference occurs because vibronic features tend to diminish when averaged over an explicit environment, and the final spectra result from the average of numerous molecular configurations, leading to smooth spectra with single peaks. In the next section, we will explore how explicit solvent environments affect the resulting vibronic spectra.

2.4.4 Vibronic Spectra in Explicit Solvent Environment

In the last two case studies, we observed the impact of density functional on absorption line shapes when employing an implicit solvent model. Implicit solvent models lack important interactions such as hydrogen bonding, $\pi - \pi$ interactions, and dispersion. In the upcoming study, we will focus on three hybrid functionals: global M06-2x, range-separated CAM-B3LYP, and range-corrected LC-wHPBE with a 6-31G(d) basis set. We aim to benchmark their effectiveness in replicating experimental absorption and fluorescence line shapes.

We first carry out an AIMD sampling procedure and randomly select five snapshots separated by 200 fs. These snapshots are divided into three layers. The dye is unrestrained and treated with QM, 5Å of frozen solvent treated with the same QM, and 27Å of MM point charge environment. We optimized the dye in its ground and excited state with the frozen QM solvent surrounded and then again performed normal mode calculations in the same environment. We selected three dyes for this case study: Nile Red and NBD in DMSO and 7MC in methanol. The vibronic lineshapes are generated again using the same adiabatic Hessian approach. From all 5 snapshots, an average FTFC absorption and fluorescence lineshape is obtained and compared with the experimental lineshape. For further details on the AIMD sampling, spectrum to lineshape transformation, and averaging scheme, please refer to the computational details section in Chapter 4.

Nile Red in DMSO

Figure 2.8 shows the simulated vibronic absorption and fluorescence lineshapes of Nile Red in the implicit (inset) and explicit DMSO solvent environment.

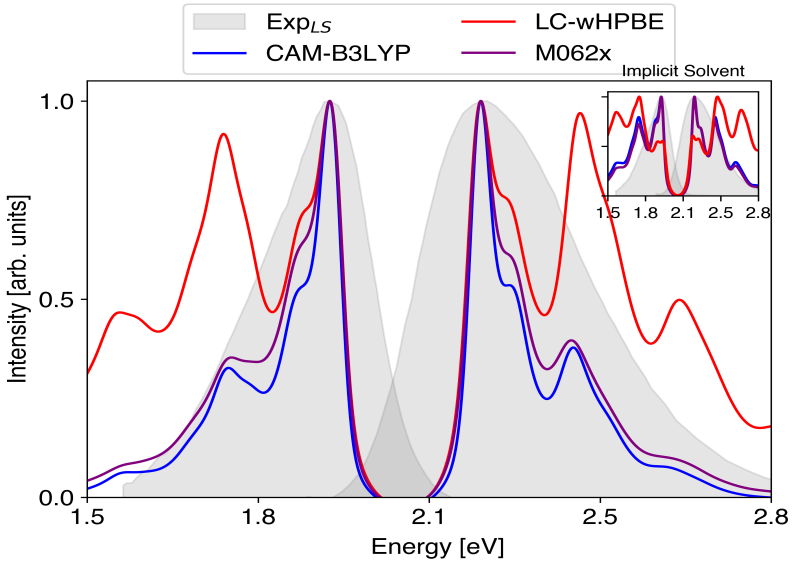

Figure 2.8: Comparison of average FTFC lineshape with experimental lineshape for NR in DMSO obtained from CAM-B3LYP, LC-wHPBE, and M06-2X. The average FTFC lineshape is generated using 5 snapshots for both absorption and emission spectra. The inset plot shows absorption and emission spectra generated with the implicit solvent model. All spectra are generated using the adiabatic Hessian approach with the TDA/6-31G* level of theory.

Because fluorescence spectra are relatively low in intensity compared to absorption spectra, the intensity (y-axis) is normalized to unity for comparison of both lineshapes. Each lineshape shown is an average of five different vibronic lineshapes obtained from molecular configurations of Nile red in slightly different explicit DMSO environments; refer to Chapter 4 for more details of the lineshape averaging procedure. The experimental lineshapes are shown in gray for comparison.

CAM-B3LYP and M06-2X functionals generate similar vibronic lineshapes with a high-intensity initial peak and multiple well-separated peaks. This similarity could be attributed to both having a similar percentage of Hartree-Fock exchange (65 and

56, respectively) to describe the charge transfer character. The emission spectrum shows a strong correlation with the experimental lineshape, a bit more so for M06-2X, highlighting M06-2X's effectiveness in capturing vibronic features in explicit solvent.

The LC-wHPBE functional, on the other hand, produces a lineshape with multiple pronounced peaks at high intensity. The absorption lineshape shows peaks at higher intensities compared to CAM-B3LYP and M06-2X but still captures the main features observed experimentally. The emission lineshape aligns fairly well with experimental lineshapes, indicating LC-wHPBE's capability to model the potential of NR in the presence of explicit solvent accurately.

The inset of the figure 2.8 compares the lineshapes obtained using implicit solvent models for each functional. The implicit solvent lineshapes show more pronounced vibronic features compared to the experimental spectra. This discrepancy arises because the explicit solvent model affects the shape of the ground and excited state potentials, leading to spectra that more closely resemble the experiment.

NBD in DMSO

The NBD molecule is a push-pull system with strong electron-donating and withdrawing groups. Therefore, there is significant charge transfer within the molecule during excitation and deexcitation. For NBD in DMSO, implicit solvents provide a bit more vibronic and narrow lineshapes than experimental lineshapes. This suggests that the inclusion of explicit solvent interactions is needed to get an improved agreement with experimental lineshapes.

As shown in Figure 2.9, the absorption lineshape from all three functionals demonstrate an excellent agreement with the experimental absorption spectrum, particularly in capturing the full width at half maximum (FWHM). The lineshape from LC-wHPBE, while having slight vibronic features, maintains good agreement with experiment, suggesting that all three functionals perform well for absorption.

Regarding the fluorescence lineshape, CAM-B3LYP and M062x provide broader but

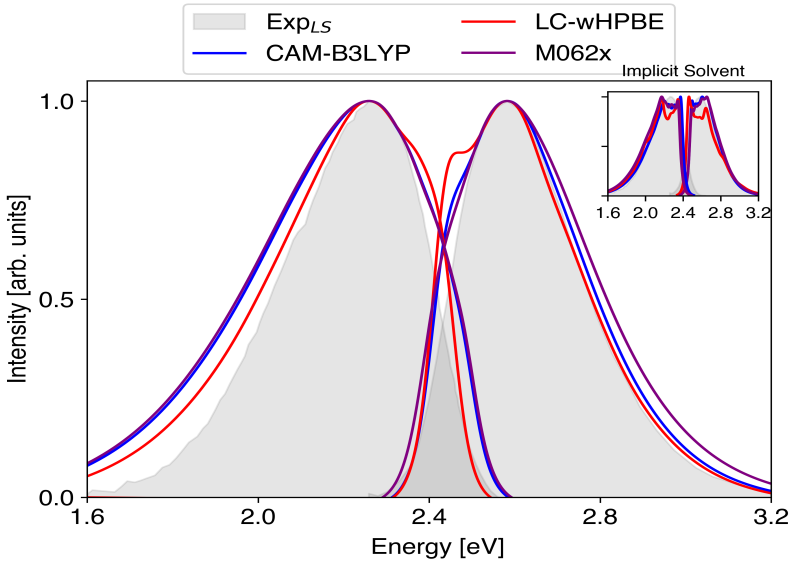

Figure 2.9: Comparison of average FTFC lineshape with experimental lineshape of NBD in DMSO obtained from CAM-B3LYP, LC-ωHPBE, and M06-2X. The average FTFC lineshape is generated using 5 snapshots for both absorption and emission lineshape. The inset plot shows absorption and emission lineshapes generated with the implicit solvent model. All lineshapes are generated using the adiabatic Hessian approach with the TDA/6-31G* level of theory.

similar spectra, while LC-wHPBE offers a slightly more narrow spectrum that shows better agreement with the experimental spectrum. This difference is explored in more detail in Chapter 4. In summary, the reason for the poorer performance for fluorescence is that an overly flat excited state potential energy surface is predicted by both CAM-B3LYP and M06-2x, and a slightly more harmonic and rigid excited state potential is predicted by LC-wHPBE.

Overall, any of the three functionals chosen here can be chosen to achieve good agreement with the experimental spectra. It's important to note that in this context, all of the spectra and lineshapes are reported with TDA. We also compare the role of TDA versus full TD on the vibronic lineshapes, and more details about this can be found in Chapter 4.

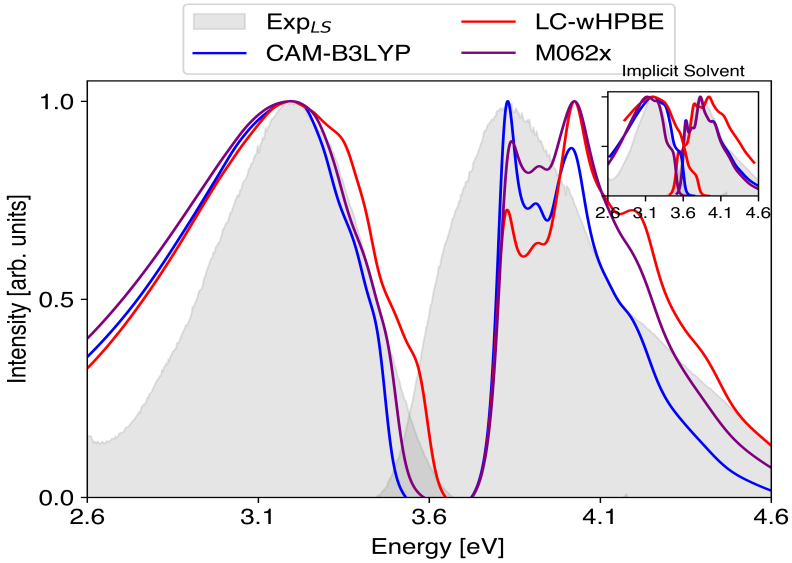

Figure 2.10: Comparison of average FTFC lineshape with experimental spectra of 7MC in methanol obtained from CAM-B3LYP, LC-wHPBE, and M06-2X. The average FTFC lineshape is generated using 5 snapshots for both absorption and emission spectra. The inset plot shows absorption and emission spectra generated with the implicit solvent model. All spectra are generated using the adiabatic Hessian approach with TDA/6-31G* level of theory.

7MC in Methanol

The last example for our benchmark study shows the comparison of FTFC lineshapes with experimental lineshapes of 7MC in methanol solvent. The 7MC FTFC lineshapes produced by all three functionals, see Figure 2.10, are similar in both implicit and explicit solvent models, which is aligned with our previous observations with the push-pull electron system NBD. None of the functionals accurately replicate the broadening and lineshape characteristics seen in the experimental lineshapes. The simulated absorption lineshapes display distinct vibronic features that are absent in the experimental lineshapes. For emission, the simulated spectra are too wide.

While it may seem that none of the functionals offer good agreement with the experiment, there are additional issues beyond an average vibronic lineshape to consider. Among the three dyes examined here, 7MC is the most flexible molecule, leading to non-harmonic vibrational modes that violate the harmonic approximation used in the

FC method to generate the vibronic lineshapes. This is explored in more detail in Chapter 4.

2.5 Conclusions

We here provided a benchmark comparison of density functionals for absorption and fluorescence vibronic spectra for three different dyes in solution. Our analysis shows that GGA functionals such as BLYP perform poorly, having very low intensity, for these conjugated dye molecules that have significant charge transfer excited state character. Functionals with large percentages of exact HF exchange and long-range correction provide improved vibronic lineshapes. The larger degree of exact exchange, as in LC-wHPBE, tends to increase the vibronic structure, leader to wider spectra. However, our study did not provide a single clear top-performing functional for simulating vibronic lineshapes.

The test cases shown here serve as a cautionary tale, reminding us that choosing the right functional for studying vibronic lineshapes is not a simple task. It's important to tread carefully and avoid selecting a functional based solely on its popularity. Instead, it's more advisable to make an informed choice by gathering prior information about the atomic and electronic structure of the molecules. For instance, in systems where charge transfer is significant, starting with global hybrids and long-range corrected hybrids should be a clear priority.

Certainly, these limited case studies do not represent a comprehensive benchmark for various fluorophores in which the absorption and fluorescence properties are influenced by charge transfer excitations. A thorough benchmark study of vibronic lineshapes in both implicit and explicit solvents is necessary to establish a trend that can help in selecting DFT functionals. Our group is already working on efforts in this direction, which will be included in future studies.

Chapter 3

Ensemble Franck-Condon Methods For Absorption and Fluorescence Spectroscopy

This chapter presents computational approaches for modeling UV-visible spectra, emphasizing the importance of accurately capturing solvent effects and vibronic features. It gives background on various methods that underlie our combined ensemble-Franck-Condon approaches, including classical force field molecular dynamics (FFMD), ab initio molecular dynamics (AIMD), vertical excitation energy (VEE) approach, nuclear ensemble approach, and Franck-Condon (FC) approach. The chapter provides the details of recently developed Ensemble Franck-Condon (E-FC) methods, which integrate ensemble sampling with FC lineshapes, offering improved accuracy by explicitly considering solvent interactions and vibronic contributions. As part of this dissertation work, we have extended and generalized the E-FC methods for the first time to compute the fluorescence spectra of molecules in an explicit solvent environment. The chapter concludes by highlighting the advantages of E-FC methods and their potential applications in calculating absorption and fluorescence spectra of chromophores in explicit solvent environments.

3.1 Introduction

Spectroscopy remains a powerful technique in elucidating the molecular structure[327–329] in complex environments, probing the electronic behaviour[330,331] and reaction mechanism[332–335] of many complex phenomena , excitation energy[336–338] and charge trans-

fer[339–341] processes, proton transfer[93,95] and many others. Theoretical spectroscopy methods that provide accurate modeling of experimental spectra bridge the experimental findings with electronic level understanding and allow predicting photochemistry. Many existing and newly developed computational spectroscopy methods have explored absorption spectroscopy with and without environmental effects. These methods have provided accurate mathematical models linking the computed and observed experimental spectra. However, computational emission spectroscopy remained relatively unexplored compared to absorption spectroscopy, especially in an explicit environment. Existing studies have explored traditional methods such as vertical excitation energy calculations (aka λ_{max} approach) and the ensemble approach, where the solvent effects are included either through the continuum models or the electrostatic charge environment. A thorough study of emission spectra with explicit environmental interactions remains a long-standing challenge for theoreticians to model.

The complexity in modeling emission spectra arises from many factors: higher sensitivity of excited state properties to the fluctuations in the environment compared to ground state properties, non-availability of excited state forcefield even for small molecules, non-trivial methods for the parameterizing excited state force field, and correctly describing the right excited state without conical intersection problems. Recent studies have explored excited state force fields for small molecules with low-lying electronic states using quantum mechanical calculations such as QUantum mechanical BEspoke (QUBE) force field,[342–345] and others have proposed excited state empirical force fields such as electron force field4 and interpolated mechanics/molecular mechanics (IM/MM).[346]

3.2 Environmental Effect on Molecular Spectra

Some of the most exciting chemical phenomena occur in a complex solvent environment, such as exciplex formation,[348–350] solvent-mediated electron[351–353] and proton transfer reactions.[354–357] A solvent environment around a molecule greatly tunes the

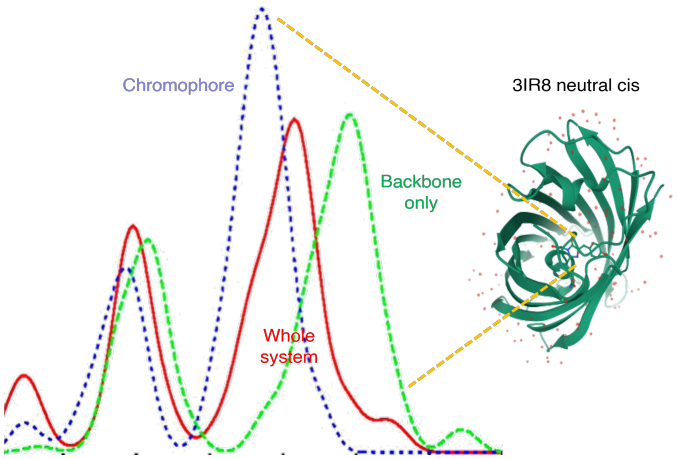

Figure 3.1: Effect of the expanding protein environment of the absorption spectra of Fluorescent Protein mKeima. Adapted from Marc Nadal-Ferret et al., J. Chem. Theory Comput. 2013, 9, 3, 17311742[347]

properties of the molecules through various types of interactions, such as explicit hydrogen bonding and polarization. An example of such effect is shown in figure 3.1, where different protein environment is accounted for, leading to changes in both the intensity, shape, and position of the absorption spectra of chromophore.[347]

Environmental effects that affect the width of the lineshape are typically categorized as homogeneous broadening and inhomogeneous broadening.[358,359] Homogeneous broadening occurs when all the atoms in a molecule are affected similarly. This means that all the atoms in the chromophore experience identical external influences, like temperature, pressure, or an electric field, leading to consistent energy level changes and identical transition energies. If a slightly different local environment surrounds the chromophores, the environmental broadening leads to inhomogeneous broadening. Inhomogeneous broadening results from each local environment affecting the frequencies differently. The frequency difference causes the lineshape to broaden unevenly, leading to an irregular or asymmetric shape. The type of broadening observed in a spectrum depends on the time scale of the measurement and is often determined by the lineshape of the transition. Gaussian lineshapes are associated with inhomogeneous broadening, while Lorentzian lineshapes are linked to homogeneous broadening.

Accurately modeling these broadening mechanisms, especially in explicit environments, remains a long-standing, challenging task for theoreticians. Modeling properties such as absorption and fluorescence spectra of molecules in solution reveals the underlying physics that governs their optoelectronic properties and the energy transfer mechanisms, such as Forster Resonance Energy Transfer (FRET) in light-harvesting systems.

Since experimental spectra are ensemble averages of several molecular configurations present in slightly different environments, theoretical methods need to properly account for these locally different environmental configurations by sampling molecular configurations from molecular dynamics simulation methods. In the next section, we will talk about some of the common sampling techniques used to explore the configuration landscape and explore my chromophores embedded in the explicit solvent environment.

3.3 Configuration Sampling Techniques

The molecular configuration space in an explicit solvent environment can be explored in two ways: classical all-atom force field molecular dynamics (FFMD) and ab initio molecular dynamics (AIMD). All-atom FFMD simulations are a powerful computational tool for studying molecular systems at the atomic level.[360,361] These simulations use predefined force fields, which are mathematical models that describe the forces between atoms in a molecule using parameterized equations to predict interactions. The parameterization is based on empirical data and quantum mechanical calculations, allowing faster computations to handle larger systems over longer time scales. A typical example of an all-atom force field is the generalized amber force field (GAFF),[362,363] which uses a combination of bonded and non-bonded terms to model molecular interactions. The mathematical form of the force field in GAFF can

be expressed as:

$$V_{\text{total}} = \sum_{\text{bonds}} k_b(r - r_0)^2 + \sum_{\text{angles}} k_\theta(\theta - \theta_0)^2 + \sum_{\text{torsions}} \sum_{n} V_n \left[1 + \cos(n\phi - \gamma)\right] + \sum_{\text{i,j}} \left(\frac{A_{ij}}{r_{ij}^{12}} - \frac{B_{ij}}{r_{ij}^{6}} \right). \tag{3.1}$$

where, k_b and k_θ are the force constants for bond stretching and angle bending, respectively, with r_0 and θ_0 representing the equilibrium bond length and angle. The torsion term involves a sum over all torsional angles, with V_n being the torsion potential amplitude, n the periodicity, and γ the phase shift. The non-bonded interactions are modeled using the Lennard-Jones potential, represented by the A_{ij} and B_{ij} parameters, which describe the repulsive and attractive forces, respectively, between atom pairs at a distance r_{ij}.

One of the primary advantages of FFMD is its efficiency. By utilizing parameterized force fields, these simulations can cover much larger timescales and system sizes than ab initio methods, which are computationally more demanding. This efficiency makes all-atom force field MD particularly useful in studying complex biological processes such as protein folding,[364–366] ligand-receptor interactions,[367,368] and membrane dynamics.[369,370] Moreover, the availability of various specialized force fields allows researchers to tailor simulations to specific types of molecules and interactions, enhancing the accuracy and relevance of the results. However, it's crucial to note that the success of all-atom force field MD hinges on the quality and accuracy of these force fields, underscoring the importance of meticulous parameterization. The simulation results may not accurately reflect real-world phenomena if the force fields are not well-parameterized for a specific type of interaction or molecular system.[371] Moreover, these simulations generally do not explicitly account for electronic polarization effects or changes in electronic structure, which can be critical for specific chemical reactions and in the study of reactive biological systems.

The AIMD procedure is a relatively more accurate way of sampling molecular configurations by incorporating electronic effects into the sampling processes. AIMD simulations provide a rigorous approach to studying molecular systems by explicitly

calculating real-time electronic structures.[372–374] Unlike FFMD, which relies on predefined parameterized equations to model interactions, AIMD uses principles from quantum mechanics to dynamically compute the interactions between atoms. This method directly integrates the Schrödinger's equation into molecular dynamics simulations, allowing the system's electronic structure to evolve naturally with atomic positions. Consequently, AIMD can accurately capture molecules' electronic properties and chemical reactions under various conditions without the need for empirical parameters.

AIMD simulations can be further divided into QM and MM regions using the hybrid QM/MM[375] embedding methods to simulate molecular systems, allowing for an efficient yet detailed analysis where quantum mechanics is applied to the area of interest (usually the active site) and the surrounding environment is treated with molecular mechanics.[376] Three of such methods are:

1. **Mechanical Embedding (ME)**: ME treats the QM and MM regions almost independently, with the MM part providing a static structural environment. The interactions between the QM and MM regions are typically limited to non-bonded van der Waals and electrostatic interactions, with the MM atoms modeled as point charges that do not affect the electronic structure of the QM region. The energy in ME can be represented as,

$$E_{\text{total}} = E_{\text{QM}}(\mathbf{r}_{\text{QM}}) + E_{\text{MM}}(\mathbf{r}_{\text{MM}}) + E_{\text{non-bonded}}(\mathbf{r}_{\text{QM}}, \mathbf{r}_{\text{MM}}) \tag{3.2}$$

2. **Electrostatic Embedding (EE)[377]**: EE allows the MM region's electrostatic effects to influence the electron density of the QM region. This method captures the electrostatic interaction between the QM and MM atoms, enhancing the realism of the simulation by considering how charges within the MM region affect the quantum calculations. This is one of the most commonly employed AIMD approaches. The total energy of the system in EE can be obtained as:

$$E_{\text{total}} = E_{\text{QM}}(\mathbf{r}_{\text{QM}}, \{q_j\}) + E_{\text{MM}}(\mathbf{r}_{\text{MM}}) + E_{\text{electrostatic}}(\mathbf{r}_{\text{QM}}, \mathbf{r}_{\text{MM}}) \tag{3.3}$$

3. **Polarizable Embedding (PE)[378,379]**: PE extends electrostatic embedding by incorporating the polarizability of the MM region, allowing the MM atoms

to influence and respond to the electron density changes in the QM region. This dynamic adaptation leads to a more accurate representation of the real interactions but also an increase in the computational cost. The energy can be expressed as:

$$E_{\text{total}} = E_{\text{QM}}(\mathbf{r}_{\text{QM}}, \{q_j, \alpha_j\}) + E_{\text{MM}}(\mathbf{r}_{\text{MM}}, \{\alpha_j\}) + E_{\text{polarizable}}(\mathbf{r}_{\text{QM}}, \mathbf{r}_{\text{MM}}) \quad (3.4)$$

One of AIMD's significant advantages is its ability to model chemical reactions and complex electronic phenomena, such as charge transfer[380] and electronic excitations,[381] that are beyond the reach of traditional force field approaches. This makes AIMD particularly valuable in chemistry and materials science,[382] where understanding the electronic basis of reactions and properties is crucial. Moreover, AIMD can provide insights into the behavior of systems under extreme conditions, such as high pressure and temperature, where the electronic structure may undergo significant changes that affect the material's properties. Additionally, in pharmaceuticals, it allows for the exploration of drug interaction mechanisms[383–385] at an electronic level, potentially leading to the design of more effective drugs with fewer side effects.

For sampling molecular configurations with AIMD simulations, an electrostatic embedding based hybrid QM/MM approach is typically employed since it is computationally affordable and relatively more accurate than mechanical embedding. Within the EE approach, only the dye is generally treated with quantum mechanics, and the rest of the system is treated as a classical point change environment. In Chapter 4, in the computational details, I will provide a more elaborate introduction to preparing AIMD simulations for sampling purposes.

The main limitation of AIMD lies in its computational demand.[386,387] The need to solve the electronic structure problem at each simulation step makes AIMD much more computationally intensive than force field MD. This restricts the size of the systems and the timescales that can be realistically simulated, often limiting studies to smaller molecules or shorter time periods. Additionally, the accuracy of AIMD depends on the level of theory used to describe the electronic structure, which can sometimes lead to inaccuracies if not adequately chosen or implemented. The detailed

insights AIMD provides into the electronic structure and its evolution during chemical processes complement the broader, faster analyses possible with all-atom FFMD. This combination of methods enriches our understanding of molecular dynamics, each addressing different aspects and scales of the phenomena under investigation.

3.4 Vertical Excitation Energy (VEE) Approach

The VEE method is one of the most commonly used approaches for calculating a molecule's absorption spectrum.[388] In this method, the molecule is first optimized in its ground state, and then a single-point excited-state calculation is performed. This calculation provides vertical excitation energy as delta functions, with the height corresponding to the oscillator strength, but no spectral width is provided. The absorption spectrum is then obtained by dressing the excitation energies with a broadening line-shape function such as Gaussian:

$$\sigma^{vert}(\omega) = \frac{4\pi^2\omega_{if}(R_0^i)}{3c}\left|\mu_{if}(R_0^i\right|^2) \times \mathcal{N}(\omega - \omega_{if}(\boldsymbol{R_0^i}; T), s), \tag{3.5}$$

where R_0^{GS} is the optimized reference state, ω_{if} is the vertical energy from electronic reference state i to final state f. μ_{if} is the transition dipole moment at the optimized reference state and $\mathcal{N}$, is centered at ω_{if} with standard deviation s, a parameter that is often used to account for limited sampling.

When studying the behavior of molecules in solutions, implicit solvents such as continuum models (PCM) are often utilized to simulate the impact of the environment on the chromophore's absorption spectra.[389–392] This approach offers the advantage of being computationally efficient and allows for the use of advanced electronic structure methods such as CCSD, CI, and MP2. However, it does not fully capture important effects such as vibronic features of the absorption spectrum, explicit solute-solvent interactions, and solvent-induced inhomogeneous broadening.

3.5 Nuclear Ensemble Approach

In the nuclear ensemble approach,[269,393–401] the electronic spectra are simulated using molecular configurations, here called snapshots, that we sample from different points in time during an MD trajectory at a specified temperature. For absorption, ground state MD is performed, followed by calculations of vertical excitation energy (VEE) and oscillator strength for each snapshot. For emission, excited state MD is performed, with the energy gap calculations on these snapshots representing the vertical de-excitation energy (VDE). To obtain the final optical spectrum, often a Gaussian function dresses the bare vertical energies. The linear absorption and emission cross-sections using the ensemble approach are then obtained as,

$$\begin{aligned}\sigma^{\text{ens}}(\omega;T) \propto & \frac{1}{N_{\text{snaps}}} \sum_{j=1}^{N_{\text{snaps}}} \omega_{if}^{\beta}(\boldsymbol{R_j^i};T)|\mu_{if}(\boldsymbol{R_j^i};T)|^2 \\ & \times \mathcal{N}(\omega-\omega_{if}(\boldsymbol{R_j^i};T),s),\end{aligned} \tag{3.6}$$

where $f_{if} \propto \omega_{if}(\boldsymbol{R_j^i};T)|\mu_{if}(\boldsymbol{R_j^i};T)|^2$ is the oscillator strength, ω_{if} is the vertical excitation/de-excitation energy, $\beta = 1$ for absorption and $\beta = 3$ for emission, and μ_{if} is the transition electric dipole moment between two electronic states of the dye with reference state nuclear configuration $\boldsymbol{R_j^i}$ obtained from an MD trajectory at temperature T. The frequency of the light is given by ω, and N_{snaps} is the number of uncorrelated snapshots from either a ground or excited state MD trajectory. The Gaussian function, $\mathcal{N}$, is centered at ω_{if} with standard deviation s, a parameter that is often used to account for limited sampling. A Python code to perform spectra and lineshapes calculation using the nuclear ensemble approach is provided in Appendix A A.1.1.

The nuclear ensemble approach offers several benefits, including the ability to sample anharmonic regions of the potential, easily include effects from higher-lying excited states, capture inhomogeneous broadening due to explicit interactions with solvent, and account for temperature effects of both the chromophore and solvent via finite temperature MD..[396,402,403] Some nuclear quantum effects on the optical spectra can be included through the MD sampling by employing a path integral formalism.[25–28]

However, the spectra generated from the nuclear ensemble approach lack vibronic features and, thus, generally do not have the correct shape.[140,389]

3.6 The Franck-Condon Approach

The vibronic coupling can be incorporated into the lineshapes by explicitly accounting for the nuclear wavefunctions of ground and excited electronic transitions. Assuming the potential energy surface (PES) to be harmonic[404,405] for both the ground and excited state and employing the Condon approximation where the nuclear configuration does not change during an electronic transition, leading to the Franck-Condon principle. The intensity of the electronic transition is determined from the overlap of the nuclear (vibrational) wave functions of the initial and final electronic states, creating a vibronic spectrum. Within the adiabatic Hessian approach,[313,406,407] the absorption and emission cross-section of a molecule at a finite temperature (FT) can be obtained for the FC approach[303–316,408–410] creating an FTFC spectrum given by,

$$\sigma^{\mathrm{FC}}(\omega;T) \propto \omega^{\beta}|\mu_{if}^{\mathrm{opt}}(\boldsymbol{R}^{\boldsymbol{i},\mathrm{opt}})|^2 \sum_{\nu_f}\sum_{\nu_i} \rho(\nu_i,T)\left|\langle\phi_{\nu_f}|\phi_{\nu_i}\rangle\right|^2 \times \delta\left(\omega_{\nu_f} - \omega_{\nu_i} \pm \omega\right), \quad (3.7)$$

where ω is the frequency of the incident (ω^1) or emitted (ω^3) photon. The Boltzmann distribution of the initial state at temperature T is denoted by $\rho(\nu_i,T)$, and $\phi_{\nu_i},\phi_{\nu_f}$ are the nuclear vibrational wave functions of the electronic state i and f, and the delta function is placed at the energy of absorption or emission, with + used for absorption and − for emission. The delta function is usually replaced by a Gaussian function, $\mathcal{N}\left(\omega_{\nu_f} - \omega_{\nu_i} \pm \omega, s\right)$, where the standard deviation, s, generally represents the solvent-induced broadening, which is usually chosen in an ad-hoc way but can also be estimated by Marcus theory.[411–413] Solvent effects on the optimized geometry and frequencies are frequently included using implicit solvent models such as the polarizable continuum model (PCM).[298,414–418]

Though slightly more computationally expensive than the nuclear ensemble approach, savings in time for computation of the FTFC spectrum can be achieved using the vertical gradient approach that employs only the normal modes of the ground state optimized structure,[244,247,248,311,419] instead of the full adiabatic Hessian that

requires the normal mode computation for both the ground and the excited state optimized structures. Herzberg-Teller effects can also be included in the FC spectral simulations by considering the first-order derivative of the transition dipole moment, which is beyond the Condon approximation.[308,404,420–422]

The FC approach allows for the inclusion of vibronic transition in the lineshapes, but it can still result in narrower lineshapes compared to experimental absorption and fluorescence lineshapes.[413,423] The main drawbacks of the pure FTFC approach are the absence of explicit solvent-solute interactions and the approximation of low-frequency vibrational modes as harmonic.[124,258,424–426]

3.7 Combined Ensemble Franck-Condon (E-FC) Approaches

So far, we have seen the application of the traditional spectroscopy methods. The nuclear ensemble approach accounts for direct solute-solvent interactions but does not include vibronic features in the generated spectra. On the other hand, the standard FC approach includes vibronic features but does not consider the effects of direct solute-solvent interactions. To address these limitations, in our previous work,[146,252,253,258,259] we introduced a family of computational approaches that combine the advantages of the ensemble and the FC approach, which we call E-FC methods. We have described these approaches for combining ensemble sampling of the environment with Franck-Condon lineshapes, outlining methods with varying degrees of computational cost.

Like the ensemble approach, snapshots of chromophore-environment configurations are first obtained at the desired temperature from an MD simulation. Each configuration corresponds to a different local environment; the effects of the environment on the FC lineshape can be captured by freezing the solvent environment and then optimizing the ground and excited state geometry and computing the normal modes of the chromophore. The three E-FC approaches we've developed to incorporate these

local environment effects with vibronic transitions are given in order of decreasing computational cost:

1. Summation of the finite temperature FC (FTFC) spectrum obtained for each snapshot in the ensemble (E-sumFTFC). For the adiabatic Hessian FC approach,[311] this method involves the computationally expensive evaluation of ground and excited state normal modes for each snapshot.

2. Summation of an FTFC lineshape that is used to dress the vertical excitation/de-excitation energies obtained at optimized geometries of the chromophore in the frozen solvent, where we employ an average FTFC lineshape (E_{opt}-avgFTFC), thus avoiding the costly excited state normal mode calculation for many snapshots.

3. Summation of a zero-temperature FC (ZTFC) lineshape that is used to dress the vertical excitation/de-excitation energies obtained at snapshot geometries, where we employ an average ZTFC lineshape (E-avgZTFC), altogether avoiding both the ground state and excited state optimization for many snapshots.

In the following sections, we will outline the theoretical details for each approach. This is the first time we are directly comparing the lineshapes of these approaches and expanding the range of methods used to model fluorescence spectra. We will introduce some slight modifications to our previous expressions to compute the energies of absorption and fluorescence spectra on an equal basis, which will enable us to calculate Stokes shifts.

3.7.1 Summation of an Ensemble of Finite Temperature Franck-Condon Spectra

For the E-sumFTFC approach, an FTFC spectrum is computed for each snapshot, and then all FTFC spectra are summed to generate the final absorption or emission spectrum, see Appendix A.1.2 for the Python program. The inhomogeneous broadening then arises from the different energies of the spectra obtained from the different local environments. The E-sumFTFC absorption and emission spectra are generated

as

$$\sigma_{\text{E-sumFTFC}}(\omega, T) = \frac{1}{N_{\text{snaps}}} \sum_{j}^{N_{\text{snaps}}} \sigma_j^{\text{FC}}(\omega, T; \boldsymbol{R_j^{i,\text{opt}}}; \boldsymbol{R_j^{i,\text{solv}}}), \tag{3.8}$$

where σ_j^{FC} is the FTFC absorption/emission spectrum of each snapshot computed with optimized chromophore geometry, $\boldsymbol{R_j^{i,opt}}$, in a frozen solvent configuration, $\boldsymbol{R_j^{i,solv}}$ for reference electronic state i. Temperature effects of the chromophore are modeled through the population of the vibrational energy levels within the FTFC lineshape function, whereas temperature effects of the solvent are modeled classically using MD.

While straightforward, the E-sumFTFC approach is computationally expensive due to the need for geometry optimization for both ground and excited states, along with the computation of the corresponding normal modes within an adiabatic Hessian approach. The computational can be reduced further by employing some physical intuition-based approximations, which are described in the next section.

3.7.2 Optimized Ensemble Average Finite Temperature Franck Condon Approach

The cost of the E-sumFTFC approach can be reduced by using an average FC lineshape function generated using a small number of snapshots and aligning the lineshape with the VEE/VDEs obtained from the optimized geometries of the chromophore in the frozen solvent. The use of an average FC lineshape is valid if the perturbation introduced by the different local frozen solvent environments present in each snapshot does not significantly alter the shape or displacement of the ground and excited-state potential energy surfaces of the chromophore. The average FTFC lineshape, σ^{avgFTFC}, is derived by aligning the absorption or emission 0-0 energies, ω_{00}, of individual FTFC spectra. We then scale the area of the lineshape for each snapshot according to the square of the transition dipole computed for the optimized geometry. A Python code to compute the average FC lineshape is provided in Appendix A.1.3.

Within the E_{opt}-avgFTFC approach, the vibrational frequencies and a full vibronic spectrum are not calculated for each snapshot, and therefore ω_{00} that measures the energy difference between the zero-point energies of the ground and excited state for each snapshot is not available. The question then arises - How will the placement of the average FC lineshape be determined, given that we only have the VEE/VDEs for each snapshot? Generally, the VEE is higher in energy than ω_{00}, and the VDE energy is lower in energy than ω_{00}.[427–429] For placement of the average FC lineshape for each snapshot at an energy approximating ω_{00} for that snapshot, we determined an energetic shift value as the average value of the difference between the VEE/VDE and ω_{00} for the snapshots used in the average FTFC lineshape calculation: $\overline{(\omega_{if} - \omega_{00})}_{\mathrm{FC}}$. This value is positive for absorption and negative for emission. The average FTFC lineshape is then aligned with its ω_{00} at the value of the vertical excitation/deexcitation energy for each snapshot shifted by $\overline{(\omega_{if} - \omega_{00})}_{\mathrm{FC}}$, and the spectra are summed to create the E_{opt}-avgFTFC spectrum as

$$\sigma_{E_{\mathrm{opt}}-\mathrm{avgFTFC}}(\omega, T) = \omega^{\beta} \frac{1}{N_{\mathrm{snaps}}} \sum_{j}^{N_{\mathrm{snaps}}} \left|\mu_{if}(\boldsymbol{R_j^{i,\mathrm{opt}}}; \boldsymbol{R_j^{i,\mathrm{solv}}})\right|^2 \times \sigma^{\mathrm{avgFTFC}}(\omega - \Delta\omega_{if}, T), \tag{3.9}$$

where here $\Delta\omega_{if} = \omega_{if}(\boldsymbol{R_j^{i,\mathrm{opt}}}; \boldsymbol{R_j^{i,\mathrm{solv}}}) - \overline{(\omega_{if} - \omega_{00})}_{\mathrm{FC}}$, with $\omega_{if}(\boldsymbol{R_j^{i,\mathrm{opt}}}; \boldsymbol{R_j^{i,\mathrm{solv}}})$ the VEE/VDE of snapshot j optimized on reference potential i. By using only a small number of snapshots to generate the average FC lineshape, we only perform the geometry optimization for the reference state for the remaining snapshots, and ground and excited state normal mode calculation for each snapshot can be avoided, thus significantly reducing the computation cost. See Appendix A A.1.4 to the Python code used to compute A Python code to compute E_{opt}-avgFTFC.

3.7.3 Ensemble Average Zero Temperature Franck Condon Approach

A further reduction in the computational cost can be achieved by avoiding geometry optimization of the ensemble of snapshots altogether and instead dressing the shifted VEE/VDEs of the ensemble of solute-solvent configurations directly with an average

zero-temperature (ZT) FC lineshape, see Appendix A.1.4 for the Python code. This E-avgZTFC approach accounts for temperature classically in the vibrational degrees of freedom of both the chromophore and the solvent, as there is no population of the vibrational energy levels in the zero-temperature FC lineshape. The average ZTFC lineshape is generated through the same procedure as the average FTFC lineshape, with the alignment of the 0-0 transitions. The linear optical spectrum using this approach is then obtained as,

$$\sigma_{\text{E-avgZTFC}}(\omega, T) = \omega^{\beta} \frac{1}{N_{\text{snaps}}} \sum_{j}^{N_{\text{snaps}}} \left|\mu_{if}(\boldsymbol{R_j^i}; T)\right|^2 \times \sigma^{\text{avgZTFC}}(\omega - \Delta\omega_{if}, T), \quad (3.10)$$

where here $\Delta\omega_{if} = \omega_{if}(\boldsymbol{R_j^i}) - \overline{(\omega_{if} - \omega_{00})}_{\text{FC}}$, with $\omega_{if}(\boldsymbol{R_j^i})$ the VEE/VDE of unoptimized snapshot j obtained from the MD trajectory on the reference PES i. Although this E-avgZTFC approach is the most computationally affordable of all three E-FC methods, this approach double-counts the zero-point vibrational motion of the chromophore: once from the sampling of vibrational degrees of freedom in the nuclear ensemble and then again in the zero-temperature nuclear wave packet of the ZTFC lineshape. This double-counting may result in overly broad spectra.

3.8 Case Study: Cresyl Violet Cation in Methanol

In the following section, I demonstrate the working of E-FC methods for Cresyl violet cation (CV^+, 9-amino-5-imino-5H-benzo[a]phenoxazine) absorption spectra in methanol solvent. CV^+, like NBD, NR, and 7MC, is a commonly used fluorescent dye used to highlight nuclei, cell membranes, and cytoplasm.[430,431]

The molecular configurations for CV^+ were obtained using AIMD simulations. The Amber-TeraChem interface[389] was used to perform the AIMD simulations. During the AIMD simulations, the electrostatic hybrid QM/MM protocol was used. In this protocol, CV^+ was treated with CAM-B3LYP[291]/6-31(d) level of theory and the environment as point charges. The snapshots from the AIMD simulations were obtained every 200 steps. For more details of the configuration sampling procedure, please refer to.[432] The TeraChem 2020 version[296] was used for geometry optimization and vertical

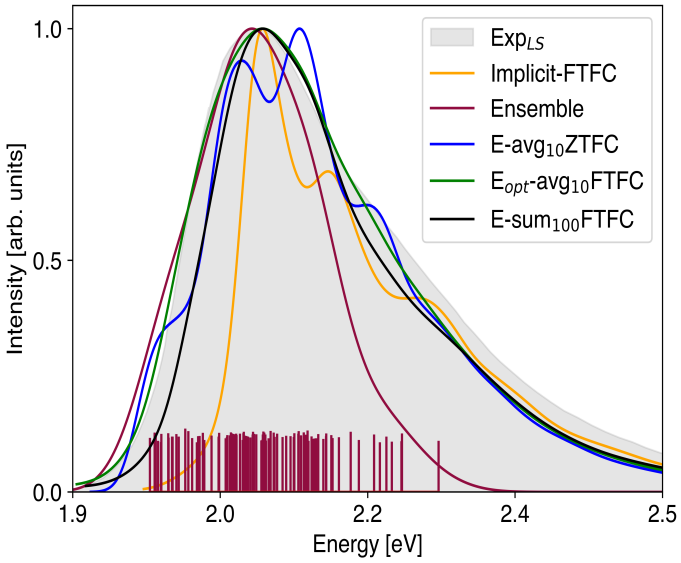

Figure 3.2: Absorption lineshapes of CV^+ in Methanol: Filled gray spectra are experimental lineshapes, transformed from Ref.[433] All lineshapes are shifted energetically to align with the experimental lineshape maxima.

excitation energy calculations, and the developmental version of Gaussian16[297] was used for frequency calculations on both ground and excited states. The FC spectra were also obtained using the time-dependent formulation as implemented in Gaussian16. A Gaussian half-width-half-maximum was used for both implicit and explicit solvent spectra. For the implicit solvent effect, the IEFPCM model[299–302] was used.

The experimental spectra of CV^+ in methanol were obtained from reference.[433] The original spectra and all computed vibronic absorption spectra are transformed into lineshapes using the equation 4.2 for better one-to-one comparison between experimental and computed results.

Figure 3.2 shows the absorption lineshapes computed using both traditional and modern hybrid E-FC spectroscopy methods. We see that both ensemble and implicit FTFC lineshape are much narrower than the experimental lineshape; see table 3.1 for FWHMs. The ensemble lineshape, with a Gaussian FWHM broadening of 600 cm^{-1}, has a good on-set; however, they are still more narrow than the experimental spectrum. Relative to the ensemble lineshape, the implicit solvent FTFC spectrum is

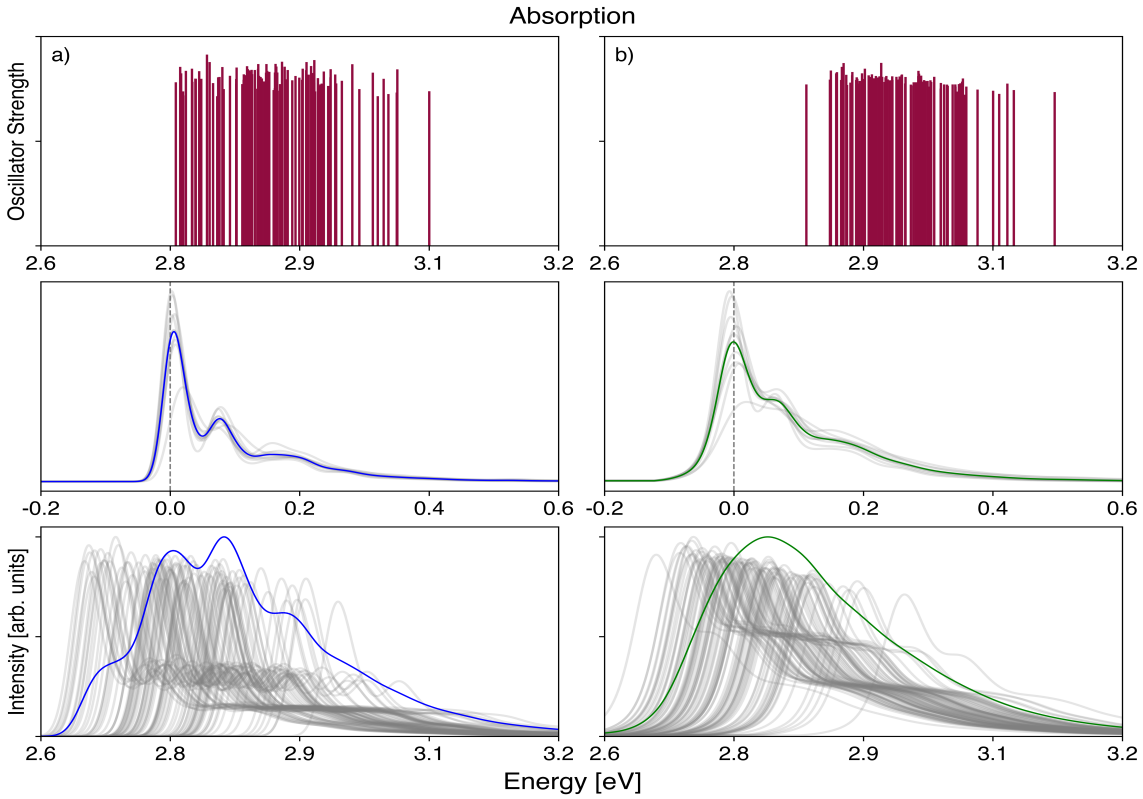

Figure 3.3: Pictorial representation of the E-avg$_{10}$ZTFC and E$_{opt}$-avg$_{10}$FTFC methods for CV^{+} in methanol: The two columns a) and b) absorption. The top row shows the distribution of VEEs from a) unoptimized and b) optimized geometries on the ground state, respectively. The middle row depicts the procedure of generating the average FC lineshape by aligning the $0 \rightarrow 0$ transition energies. The bottom row represents the dressing of the ω_{00} shifted unoptimized and optimized VEEs with avg$_{10}$ZTFC and avg$_{10}$FTFC lineshapes, resulting in E-avg$_{10}$ZTFC and E$_{opt}$-avg$_{10}$FTFC methods, respectively.

more narrow and jagged in nature, implying that local configurations play a crucial role in controlling the global width of the absorption lineshape. Observation from these two lineshapes suggests that proper account needs to be taken of both vibronic coupling and explicit solvent interactions to improve the absorption lineshape.

The absorption lineshapes generated from the hybrid E-FC methods are also shown in Figure 3.2, and a pictorial representation of the approximate methods Eopt-avgFTFC and E-avgZTFC is shown in Figure 3.3.

Table 3.1: CV^+ in Methanol: FWHM, and applied energy shift from experiment, ensemble, implicit FTFC, and E-FC methods for absorption lineshapes. All values are given in eV.

Methods	**FWHM**	**Energy Shift**
Exp_{LS}	0.23809	0.00000
Implicit	0.13287	0.32746
Ensemble	0.16637	0.77803
Ensemble_Opt	0.14479	0.85265
E-avg_{10}ZTFC	0.20280	0.68168
$E_{opt} - avg_\{10\}$$FTFC	0.22300	0.69598
E-sum_{100}FTFC	0.18508	0.68665

All three methods within the E-FC family show a much better improvement over the ensemble and implicit FTFC lineshapes; see Table 3.1. All three methods show good agreement for the absorption lineshape and similar FWHM, though they remain underestimated in width relative to the experimental lineshape. The jaggedness in the E-avg_{10}ZTFC lineshape comes from vibronic lineshapes at zero temperature, which have more pronounced vibronic features due to the absence of temperature contributing to the population of the vibrational energy levels. The smoothness of the E-avg_{10}ZTFC can be improved further if the HWHM used for individual ZTFC lineshapes is increased to a value higher than 135 cm^{-1}; see Chapter 4 for further discussion on the choice of HWHM. Despite similar lineshapes, the E_{opt}-avgFTFC is broader than E-sumFTFC and has better agreement with the experimental lineshape due to large standard deviations in the VEEs.

In the present example, we demonstrate the enhanced performance of hybrid E-FC methods compared to traditional methods. In Chapter 4, we explore the capabilities of these methods for fluorescence lineshapes and evaluate their suitability for three different molecules, encompassing a wide range of chemical compounds commonly used in fluorescence spectroscopy.

3.9 Conclusion

The E-FC method represents a significant improvement over traditional spectroscopy. It offers a deeper understanding of the physics that governs the behavior of molecules by explicitly considering solvent interactions and vibronic contributions. In the upcoming chapters, we will discover that FTFC calculations for all snapshots are not always necessary and that using only ten snapshots can produce spectra that are just as accurate for most molecules.

With prior knowledge of the system in question, the computational cost can be further reduced. For example, using DFTB[434,435] and TD-DFTB[232] methods instead of full electron consideration could lower the cost of both optimization and normal mode calculations, particularly for the excited state. Vertical methods such as adiabatic shift, vertical Hessian, and vertical gradient will also reduce the computational cost.

In Chapter 4, we will apply both traditional spectroscopy methods (ensemble, implicit solvent Franck-Condon) and newly developed E-FC methods to calculate the absorption and fluorescence spectra of chromophores in explicit solvent environments.

Chapter 4

Calculating Absorption and Fluorescence Spectra for Chromophores in Solution with Ensemble Franck-Condon Methods

Accurately modeling absorption and fluorescence spectra for molecules in solution poses a challenge due to the need to incorporate both vibronic and environmental effects, as well as the necessity of accurate excited state electronic structure calculations. Nuclear ensemble approaches capture explicit environmental effects, Franck-Condon methods capture vibronic effects, and recently introduced ensemble-Franck-Condon approaches combine the advantages of both methods. In this study, we present and analyze simulated absorption and fluorescence spectra generated with combined ensemble-Franck-Condon approaches for three chromophore-solvent systems and compare them to standard ensemble and Franck-Condon spectra, as well as to experiment. Employing configurations obtained from ground and excited state ab initio molecular dynamics, three combined ensemble-Franck-Condon approaches are directly compared to each other to assess the accuracy and relative computational time. We find that the approach employing an average finite-temperature Franck-Condon lineshape generates spectra nearly identical to the direct summation of an ensemble of Franck-Condon spectra at one-fourth of the computational cost. We analyze how the spectral simulation method, as well as the level of electronic structure theory, affects spectral lineshapes and associated Stokes shifts for 7-nitrobenz-2-oxa-1,3-diazol-4-yl (NBD) and Nile Red in dimethyl sulfoxide (DMSO), and 7-methoxy coumarin-4-acetic acid (7MC) in methanol. For the first time, our studies showcase the capability of combined ensemble-Franck-Condon methods

for both absorption and fluorescence spectroscopy and provide a powerful tool for simulating linear optical spectra.

4.1 Introduction

Optical spectroscopy plays a pivotal role in understanding the properties of molecules, where absorption and fluorescence spectra act as reporters for local environments and vibronic coupling through their energies, spectral widths, shapes, and Stokes shifts. Simulations of optical spectroscopy serve as a crucial bridge between experimental results and electronic-level understanding of molecular behavior. Developing models that can effectively capture both explicit environmental effects and vibronic contributions remains a critical challenge in linking experimental spectra with molecular properties.

Traditional computational methods for linear spectroscopy simulation have predominantly focused on incorporating vibronic effects through Franck-Condon (FC) spectral simulations[303–316,408–410] using either an adiabatic Hessian[313,406,407] or a vertical gradient approach[311] for efficiency. In practice, harmonic potential energy surfaces are generally assumed within the FC approach as the harmonic oscillator nuclear wave functions are readily available upon geometry optimization and normal mode analysis. The FC methods often model solvent effects implicitly, utilizing polarizable continuum models[298,414–418,436] to approximate the influence of the surrounding medium. This harmonic FC approach works well for rigid molecules or systems with weak solvent interactions. However, the absence of direct solute-solvent interactions and the harmonic treatment of the potential energy surfaces can lead to more narrow spectra than observed experimentally.[252,413]

Explicit solvent effects are traditionally incorporated into spectral simulations by employing a nuclear ensemble approach.[269,393–401] This method involves sampling chromophore-solvent configurations, generally through a molecular dynamics (MD) trajectory, and naturally captures vibrational degrees of freedom of the chromophore. This approach does not incorporate vibronic effects,[407] often leading to poor spectral

shape. The ensemble approach has seen limited application in simulating fluorescence spectra,[269–271,273–275] likely due to the computational demands of performing excited state molecular dynamics to obtain chromophore-solvent configurations on the excited state potential energy surface. There are multiple advantages of the nuclear ensemble approach, such as being able to sample anharmonic regions of the potential, the ease of including effects from higher-lying excited states, capturing inhomogeneous broadening due to explicit interactions with solvent, and accounting for temperature effects of both the chromophore and solvent via finite temperature MD.[396,402,403]

Some recent approaches to simulating absorption spectra have made progress in capturing both specific environmental and vibronic effects through the use of MD sampling of chromophore-environment configurations. For example, employing a cumulant expansion for the ensemble average of the time-ordered exponential of the linear response function[437] treats chromophore vibrational and environmental degrees of freedom on equal footing, allowing vibronic absorption spectra to be generated from energy gap correlation function computed along an MD trajectory.[249–251,254–257,260,263,264,267,268] Molecular dynamics, along with snapshot clustering for unique features, has also been exploited within a variational and perturbative approach to spectroscopy.[261,262,438] An alternative approach based on the separation of classical (soft) and quantum (stiff) nuclear degrees of freedom expresses the absorption spectrum as a conformational integral of vibronic spectra of the stiff coordinates.[265,266] The approach developed by some of the authors of the present work is similar in spirit, where vibronic spectra of the chromophore are generated within a frozen environment in order to combine features of both the ensemble and Franck-Condon approaches, creating hybrid ensemble-Franck-Condon (E-FC) approaches that capture both explicit environment and vibronic effects.[146,252,253,258,259] In previous work,[146] we have outlined variations of the E-FC approach with differing levels of approximation and corresponding computational cost, and shown good agreement with experiment for the simulated absorption spectral shapes of chromophores in various explicit solvent environments.

In this study, we compare three E-FC methods introduced previously and, for the first time, extend these approaches to the simulation of fluorescence spectra. This is

the first study in which these methods have been directly compared to each other and the first in which they have been used to model fluorescence. We employ both ground and excited state ab initio molecular dynamics (AIMD) to sample chromophore-solvent configurations and compare the resulting ensemble, implicit solvent Franck-Condon, and E-FC absorption and fluorescence lineshapes. To showcase the performance of these spectroscopy methods, they are applied to three well-known fluorophores: 7-nitrobenz-2-oxa-1,3-diazol-4-yl (NBD), Nile Red (NR), and 7-methoxy coumarin-4-acetic acid (7MC).

4.2 Computational Details

Our computational strategy for generating implicit solvent FTFC, ensemble, and E-FC spectra is shown pictorially in Figure 4.1. To generate and then align spectra in the combined ensemble-Franck-Condon approach, we follow four steps:

(A) Sampling configurations using AIMD where we treat the chromophore quantum mechanically (with QM) and the solvent with fixed molecular mechanical (MM) point charges

(B) Performing QM/MM electronic structure calculations on AIMD snapshots (computing excitation energies, geometry optimization, and normal modes)

(C) Generating spectra using combined ensemble-Franck-Condon (E-FC) methods

(D) Aligning spectral lineshapes for better comparison with experiment

4.2.1 Sampling Configurations Using Ab Initio Molecular Dynamics

Before running the electrostatic embedding-based AIMD QM/MM simulations using the Amber[439]-TeraChem[296] interface,[389] we set up the initial system as follows:

- For ground state AIMD, we optimized the ground state geometry of the dye with the CAM-B3LYP[291]/6-31G(d)[440,441] level of theory and the IEF-PCM implicit

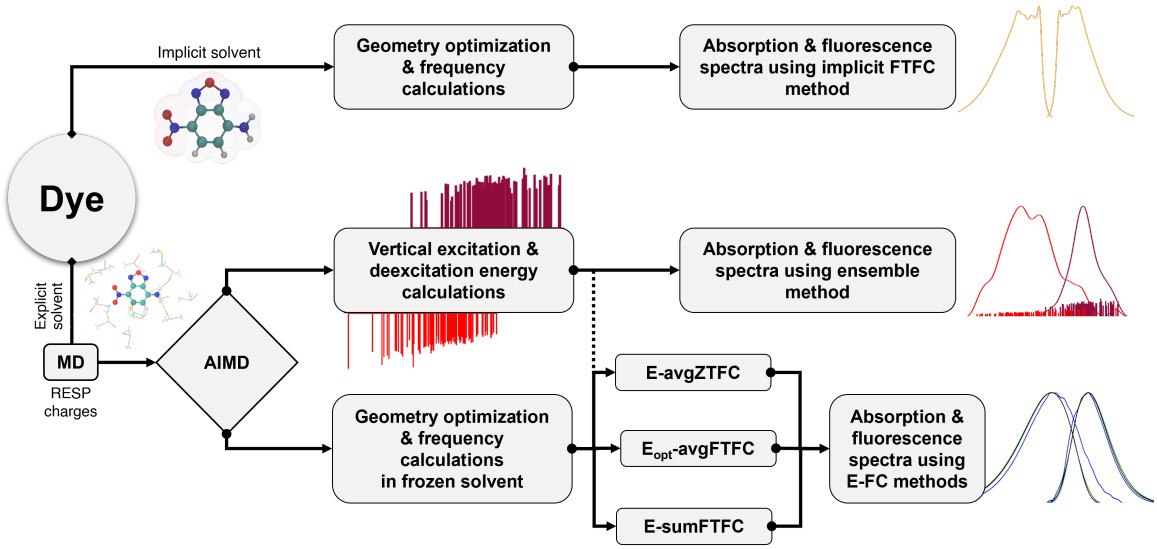

Figure 4.1: Computational procedure for modeling absorption and fluorescence spectra of dyes in an implicit and explicit solvent environment using various spectroscopy methods.

solvent model.[299–302] We then computed the restrained electrostatic potential[442] (RESP) for the dye with the Hartree-Fock/6-31G(d) level of theory and partial atomic charges using the ChelpG[443] scheme as implemented in Gaussian16.[297]

- For excited state AIMD, we optimized the excited state geometry of the dye with TDA[158]-CAM-B3LYP/6-31G(d) and the linear response[444–447] IEF-PCM solvent model. We then obtained the excited state charges with CIS[448–452]/6-31G(d)[440,441] using the same ChelpG population analysis scheme from Gaussian16.

- We optimized the geometry of the solvent molecule in its ground state with the CAM-B3LYP/6-31G* level of theory and used the IEF-PCM solvent model, obtaining CHELPG charges for the solvent using the same population analysis method as used for dyes.

- Using the antechamber tool[453] in AmberTools, the Generalized Amber force field version[363] 2 (GAFF2) was used to develop a molecule-specific force field along with the RESP charges obtained in the above steps. The tLeap program was used to create a droplet of chromophore surrounded by solvent with an

initial radius of ∼37. The force field parameter files (*.inpcrd and *.prmtop) were then generated.

- The whole system was then minimized using 50 steps of the steepest descent method[454,455] and for another ∼35000 steps using the conjugate gradient method.[456,457] Minimization was done without periodic boundary conditions and with a non-bonded cut-off of 999.

- The whole system was equilibrated in two steps; first, the system was initially heated to 300K for 5ps and then a longer equilibration for 50ps with a time step of 0.5fs with a positional restraint weight of 1.0 kcal/mol^2 on the dyes. The Langevin thermostat[458–463] was used, and a value of 2000 steps was used to remove the center of mass motion. Both equilibration steps were carried out in an NVT ensemble at 300 K using the classical force field before switching to AIMD production simulation.

Following the equilibration of the chromophore-solvent system at room temperature, the TeraChem-AMBER interface[389] was used for AIMD QM/MM simulations, wherein only the chromophore is treated with QM, while the solvent is treated with GAFF2,[363] with the MM point charges coupled to the QM region with an electrostatic embedding approach.[464–466] During the AIMD simulations, the temperature of the system was maintained at 300 K using the Berendsen[467] thermostat with a time constant of 1 ps for the heat bath coupling. For ground state AIMD, the CAM-B3LYP range-separated density functional[291] and the 6-31G(d) basis set was used for the chromophore and for the excited state AIMD, we use the Tamm-Dancoff approximation (TDA)[158] to TDDFT[63] with the same level of theory. For both the ground and excited state trajectories, the initial 10 ps of the AIMD QM/MM trajectories were discarded to let the system equilibrate with the new Hamiltonian. After the system was equilibrated, a few snapshots were chosen randomly to act as the starting points for separate independent AIMD simulations. These simulations are used for the production run. From the independent trajectories, a total of 100 uncorrelated snapshots were obtained, separated by at least 200 fs.

4.2.2 Performing Electronic Structure Calculations

Once an ensemble of uncorrelated snapshots was obtained, for each snapshot, we performed calculations of the VEE or VDE, ground or excited state geometry optimization, and corresponding frequencies. Each snapshot is divided into three layers: a central dye that is optimized during the ground or excited state geometry optimizations and is treated with QM, a 5 Å region of frozen solvent from the geometric center of the dye treated with QM but excluded from optimization, and a 27 Å region of MM fixed point charge solvent providing an electrostatic environment to the QM region. Thus, the QM region for all snapshot calculations is the chromophore plus 5 Å of solvent to account for chromophore-solvent polarization and charge transfer fully.

For all electronic structure calculations, we use the CAM-B3LYP/6-31G(d) level of theory with empirical dispersion accounted via the D3 version of Grimmes dispersion.[289] Because the TDA usually provides excitation energy and vibronic lineshapes similar to TDDFT and is computationally cheaper than TDDFT,[290] we use the TDA within TDDFT for the excited state properties. Comparisons between TD and TDA are also showen for each dye. The performance of the various density functionals for excited state properties, including fluorescence, has been evaluated previously, with range-separated hybrid functionals found to be superior.[468] Here we focus on the absorption and fluorescence vibronic lineshapes and provide comparisons for FC spectra using CAM-B3LYP,[291] LC-ωHPBE,[292–294] and M06-2x[295] density functionals in both implicit and explicit solvents. These results are already detailed in section 2.4.4 of chapter 2.

For geometry optimization in explicit QM solvent and VEE/VDE calculations, the 2020 development version of TeraChem[296] was used. Frequency calculations in frozen QM solvent and vibronic spectra calculations were carried out using a developmental version of Gaussian16.[297] The integral equation formalism for PCM[298,300–302] as implemented in Gaussian16 was used for modeling solvent effects on implicit solvent FC absorption and emission spectra.

4.2.3 Generating Spectra Using Combined Ensemble-Franck-Condon (E-FC) Methods

For all vibronic FC spectra, for both implicit and explicit solvent environments, the time-dependent implementation of one photon absorption and emission procedure[303–316] was employed with the default adiabatic Hessian model as implemented in the development version of the Gaussian16 electronic structure program. A temperature of 300 K was used for the finite temperature FC spectra. Two advantages of the time-dependent FC implementation are that zero temperature spectra are obtained along with finite temperature spectra at no additional computational cost, and no approximations are made when summing over contributions for combination modes.[404]

The average FC lineshapes were generated using ten randomly selected snapshots and aligning their 0-0 transitions for avg_{10}FTFC and avg_{10}ZTFC methods. We tested the robustness of the lineshape generated with the randomly selected snapshots, see Figure 4.2, finding ten snapshots to be adequate.

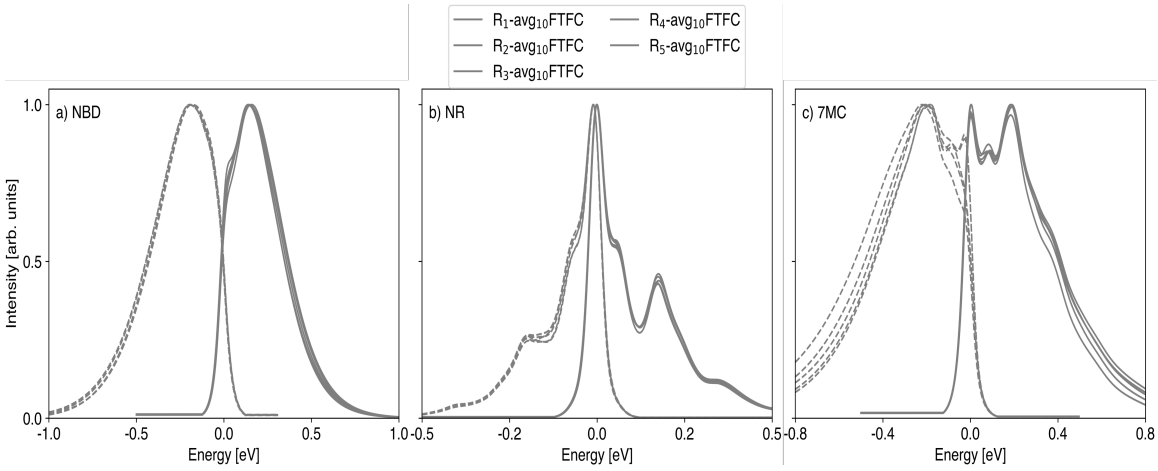

Figure 4.2: Average FTFC lineshapes generated for absorption and emission. The average FTFC lineshapes were computed using 10 random snapshots from 5 sampling procedures

4.2.4 Spectral Simulation Parameters and Alignment

Transformation to an energy-independent lineshape function allows for equivalent comparison of computed and experimental spectra. Because experimental spectra are generally reported in the wavelength domain, the emission spectrum is first scaled to transform to the energy/frequency domain as[89,469–472]

$$\sigma_{ems}(\omega) \propto \lambda^2 \sigma_{ems}(\lambda). \tag{4.1}$$

No such scaling is required for the absorption spectrum as it is measured as the log ratio of the transmitted and incident ray leading to the same absorption cross-section when measured in the wavelength or frequency domain.[469] The spectrum and the energy-independent lineshape are related to each other via:

$$\sigma(\omega) \propto \omega^{\beta} L(\omega), \tag{4.2}$$

where $\beta = 1$ for absorption and $\beta = 3$ for emission.[303,473–476] The lineshape function transformation can therefore be obtained as $L(\omega) \propto \omega^{-1}\sigma(\omega)$ for absorption and $L(\omega) \propto \omega^{-3}\sigma(\omega) \propto \omega^{-5}\sigma(\lambda)$. The Python code to perform this transformation is given in Appendix A B. In practice, we observe minimal differences in the experimental absorption spectra and scaled lineshapes. However, the transformation from wavelength to energy and then to lineshape leads to broader emission spectral lineshapes, and their maxima shift to higher wavelengths / lower energies; see Figure 4.3 see the impact of these transformations. This shift of the maximum will affect the value of the Stokes shift; herein, we report the Stokes shift from the lineshapes after the transformation.

This study aims to compare the computed lineshape generated for a single bright state transition using different spectroscopy methods. Therefore, we have normalized the lineshapes based on their maximum intensities. We also display all computed lineshapes energetically shifted to align with the experimental lineshapes. For the ensemble absorption and emission lineshapes, the average values of the vertical excitation and deexcitation energies are aligned with the experimental lineshape maxima. For vibronic spectra, we aligned the lineshape maxima, except for more jagged spec-

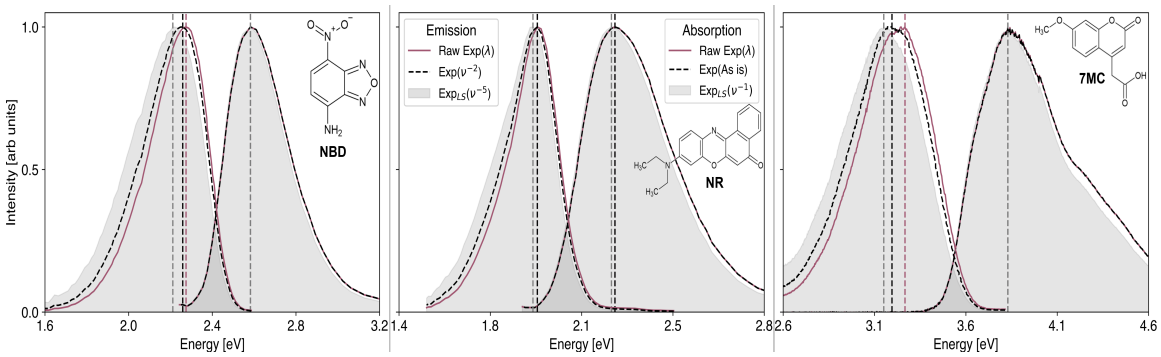

Figure 4.3: Original experimental spectra and lineshape transformation of NBD and NR in DMSO[286] and 7MC in methanol.[287]

tra, where averaged band maxima were used to determine alignment. This averaging procedure selects the peaks within 80% of the first maximum and then computes the average energy of these peaks. For all computed lineshapes, the applied energy shift is given in the main manuscript, and the unshifted lineshapes are shown in Figure 4.4.

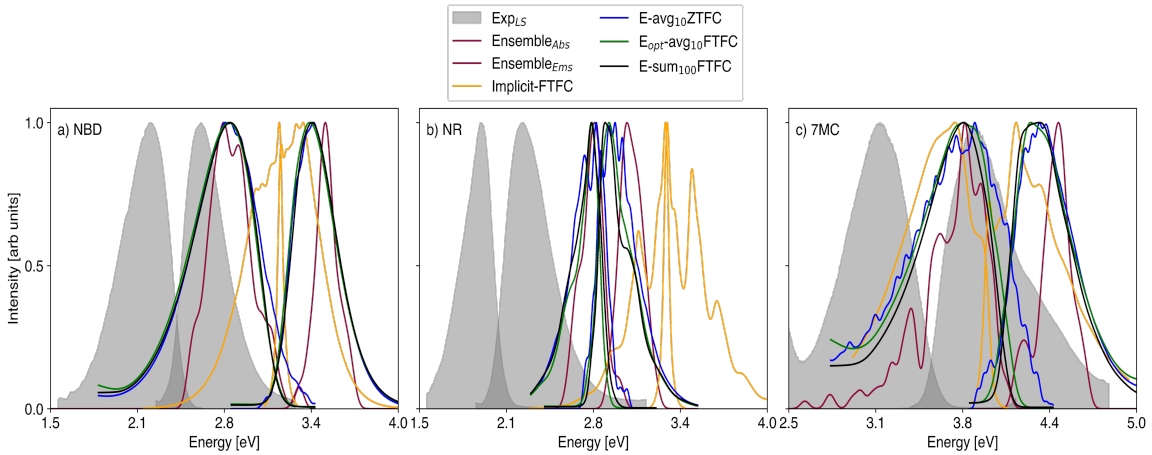

Figure 4.4: Unshifted lineshapes of all three dyes: a) NBD in DMSO, b) NR in DMSO, and c) 7MC in methanol

We also report the full-width-half-maxima (FWHM) of our computed lineshapes to compare with the experiment. This value is dependent on our choice of broadening factor. A Gaussian lineshape function with a broadening factor of 600 cm^{-1} was used to generate the ensemble lineshapes. For both implicit and explicit solvent FTFC

spectra, the Gaussian16 default half width half maximum (HWHM) value of 135 cm^{-1} was used as the FC broadening factor. Although the hybrid E-FC spectroscopy methods include inhomogeneous broadening in the lineshapes, due to the use of a limited number of snapshots to calculate the spectra, the final E-FC lineshapes, especially in zero-temperature spectra, can be noisy. Using 135 cm^{-1} HWHM results in smoother lineshapes while maintaining the overall lineshape width,[27,265] as shown in Figure 4.5.

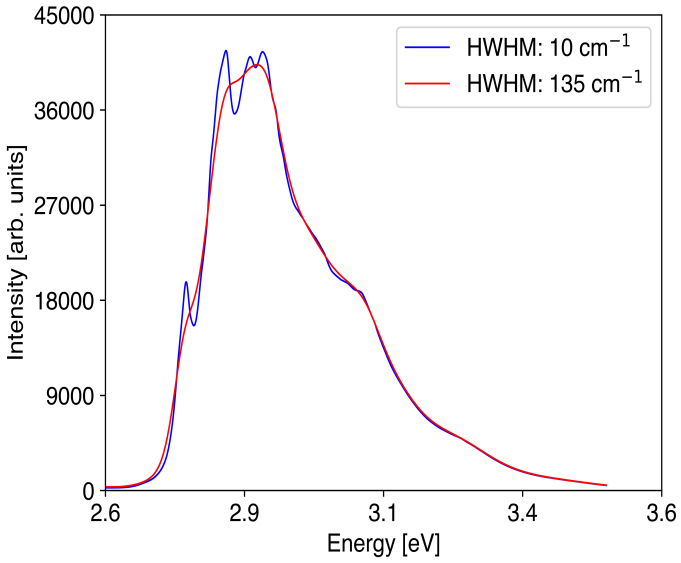

Figure 4.5: E-sum$_{30}$FTFC absorption lineshape of NR in explicit DMSO generated using HWHM of 10 cm^{-1} and 135 cm^{-1} on each FTFC lineshape.

The Stokes shift measures the difference between the energy of excitation and deexcitation at corresponding band maxima. We follow this approach for reporting the Stokes shift using the maxima of the unshifted computed spectra. However, this definition can become inconsistent when dealing with multiple maxima or jagged spectra, complicating the comparison of Stokes shift values.

4.3 Result and Discussion

Our study involves three well-known fluorophores: 7-nitrobenz-2-oxa-1,3-diazol-4-yl (NBD) and Nile Red (NR) in dimethyl sulfoxide (DMSO), and 7-methoxy coumarin-

4-acetic acid (7MC) in methanol; see Figure 4.6 for chromophore structures. These fluorophores are commonly employed as fluorescent probes for labeling biological substrates.[280–285] The experimental absorption and emission data for NBD and NR were obtained from Tosi et al.,[286] whereas spectra for 7MC in methanol were taken from the PhotochemCAD database.[287,288] The experimental spectra and corresponding lineshapes are shown in Figure 4.3. Below, we present simulated spectra for each chromophore, and then we analyze relative computational timings for the E-FC methods. For each chromophore, we consider only the low-lying bright state in our simulated spectra. If two electronic states are nearly degenerate, a dark state can mix with the bright state of interest, and then an approach that accounts for the nonadiabatic coupling between excited states is necessary for simulating the spectra.[23,24]

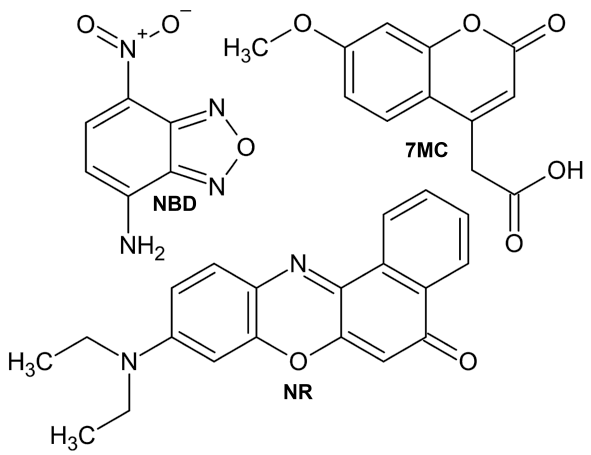

Figure 4.6: Chemical structures of the three chromophores studied in this work: 7-nitrobenz-2-oxa-1,3-diazol-4-yl (NBD), Nile red (NR), and 7-methoxy coumarin-4-acetic acid (7MC).

4.3.1 NBD in DMSO

NBD and its derivatives, due to high sensitivity to the polarity of the environment, are routinely used as fluorescent dyes.[477–481] In aprotic solvents like DMSO, NBD acts as a hydrogen bond donor via the chromophore's NH_2 group, potentially forming two hydrogen bonds with the oxygen atom in the DMSO solvent. For the first excited state, which is also the bright state of interest here, there is a partial intramolecular

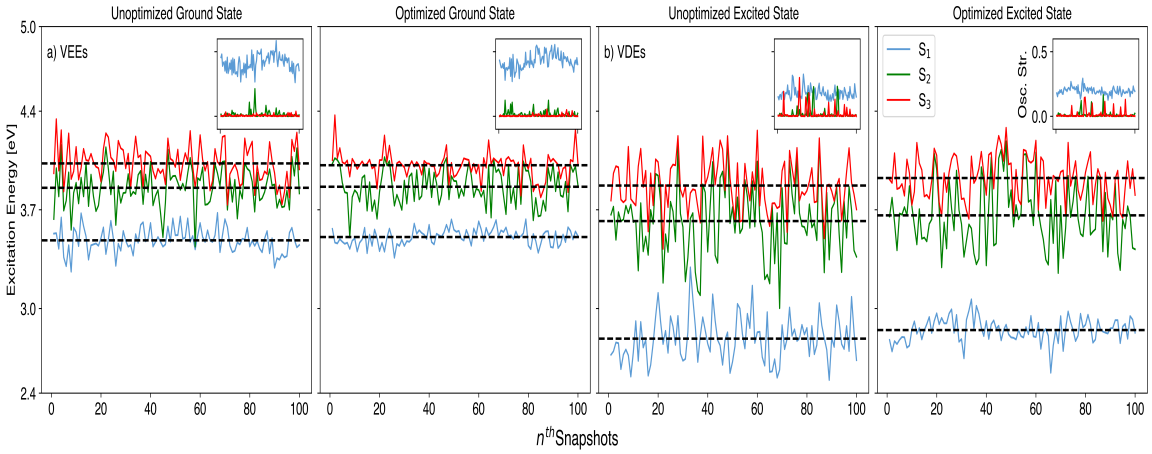

Figure 4.7: NBD in DMSO: Vertical excitation energies obtained from ground state AIMD snapshots and vertical de-excitation energies obtained from excited state AIMD snapshots. Energy gaps are also shown for the same snapshots after geometry optimization in a frozen QM solvent environment. Corresponding oscillator strengths are included as an inset.

charge-transfer character driving the observed fluorescence.[280,482,483]

The FWHM of experimental[286] absorption and emission lineshapes (after the scaling correction discussed in Eqs. 6-7) are 0.341 and 0.400 eV, respectively, suggesting potentially an increase in the flexibility of the molecule in the excited state or an increase in the strength of the chromophore-solvent interactions compared to the ground state. The lineshape Stokes shift is moderate at 0.334 eV.

From the 100 uncorrelated snapshots from the ground and excited state AIMD trajectories, we performed VEE/VDE calculations on these snapshots for use in both ensemble and E-ZTFC spectra calculations. We then checked for potential state mixing between the S_1 state and higher-lying states. Analyzing the VEEs, we observed that the higher-lying excited states S_2 and S_3 are within 0.2-0.5 eV of the bright S_1 state. These electronic states show almost zero oscillator strength, as shown in Figure 4.7 throughout the ground state trajectory, with only one snapshot showing clear state mixing and sharing of oscillator strength between S_1 and S_2. Compared to the VEE calculations, the VDE calculations on excited state AIMD snapshots showed a much larger fluctuation of the energies for all states, along with a decrease in the oscillator strength of the S_0 to S_1 transition and an increase in the oscillator strength

Table 4.1: NBD in DMSO: FWHM, applied energy shift, and Stokes shift from experiment, ensemble, implicit FTFC, and E-FC methods for absorption and emission lineshapes. All values are given in eV.

Methods	**Abs FWHM**	**Ems FWHM**	**Abs Energy Shift**	**Ems Energy Shift**	**Stokes Shift**
Exp_{LS}	0.341	0.400	-	-	0.334
Implicit	0.330	0.381	0.663	0.819	0.123
Ensemble	0.155	0.336	0.901	0.575	0.731
Ensemble_{Opt}	0.154	0.218	0.925	0.636	0.668
E-avg_{10}ZTFC	0.379	0.557	0.810	0.546	0.635
E_{opt}-avg_{10}FTFC	0.380	0.536	0.782	0.573	0.580
E-sum_{100}FTFC	0.370	0.532	0.798	0.582	0.588

of the S_0 to S_3 transition for some snapshots. Despite the large fluctuations, the states are energetically well-separated and do not appear to mix. After optimizing the excited state geometries in the field of the frozen QM solvent, we observe a significant decrease in the energy fluctuations, suggesting that these large fluctuations on the excited state are due to motions of the chromophore degrees of freedom rather than increased strength of chromophore-solvent interactions. Next, we analyze these energies in the context of ensemble absorption and emission spectra.

Figure 4.8 shows the experimental and computed absorption and fluorescence spectral lineshapes for NBD in DMSO. The computed lineshapes are shifted on the energy axis, as discussed in the computational details, for better comparison of lineshapes. Table 4.1 gives the FWHM, applied energy shifts, and Stokes shift values for all lineshapes. See Figure 4.4 for unshifted spectral lineshapes.

The spectra generated using the nuclear ensemble approach, as shown in Figure 4.8a, reveals that the VDEs exhibit larger fluctuations than the VEEs, as discussed above, resulting in an emission spectrum that is significantly broader than the absorption spectrum. This is evidenced by the standard deviation of the energies and the FWHM

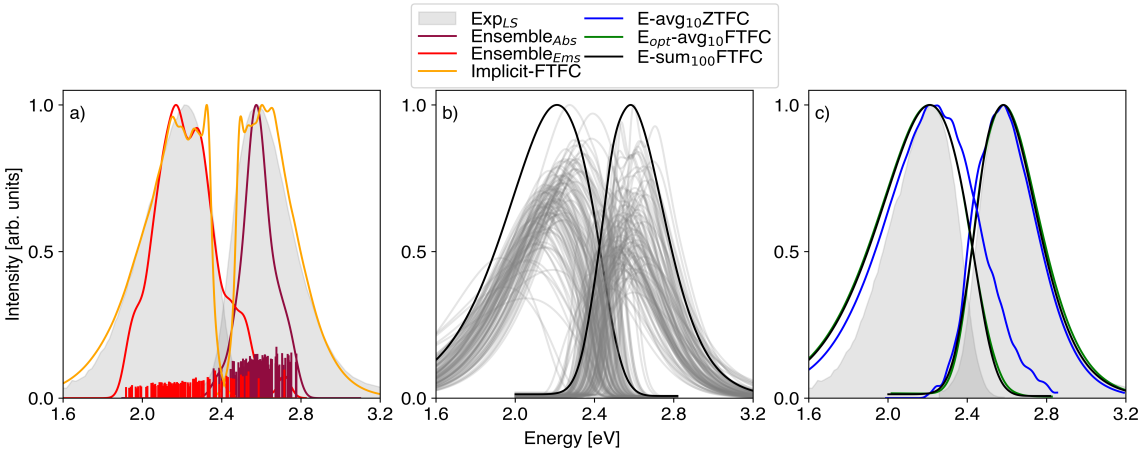

Figure 4.8: Absorption and fluorescence lineshapes of NBD in DMSO: Filled gray spectra are experimental lineshapes, transformed from Ref.286. a) Ensemble and implicit solvent FTFC methods, b) E-sum$_{100}$FTFC and individual FTFC spectra, and c) E-avg$_{10}$ZTFC, E$_{opt}$-avg$_{10}$FTFC, and E-sum$_{100}$FTFC lineshapes. All lineshapes are shifted energetically to align with the experimental lineshape maxima.

of the emission spectrum being almost twice as large as those of the absorption spectrum, see Table 4.1.

To understand how chromophore-only degrees of freedom contribute to spectral broadening, we removed all solvent molecules from the chromophore AIMD configurations, and then we recalculated the VEEs and VDEs. These chromophore-only VEE/VDEs allow us to compare the standard deviation of the energies with and without solvent contributions. The VEEs calculated from the chromophore-only configurations obtained from the ground state AIMD contained a significant amount of mixing of the bright S_1 and dark S_2 states, as shown in Figure 4.9. Therefore, we were unable to make a proper comparison to the distribution of solvated bright S_0 to S_1 VEEs. The VDEs, however, did not display significant state mixing, and the resulting standard deviation of energies decreased from 0.156 (solvated) to 0.128 eV (chromophore-only), see Table 4.2. The standard deviation of the VDEs for the chromophore alone is still larger than the value of the standard deviation of the VEEs of 0.086 eV for the chromophore in explicit solvent, again suggesting that the chromophore degrees of freedom on the exited state are the main contributor to the overly wide distribution of VDEs for the S_1 configurations and correspondingly larger

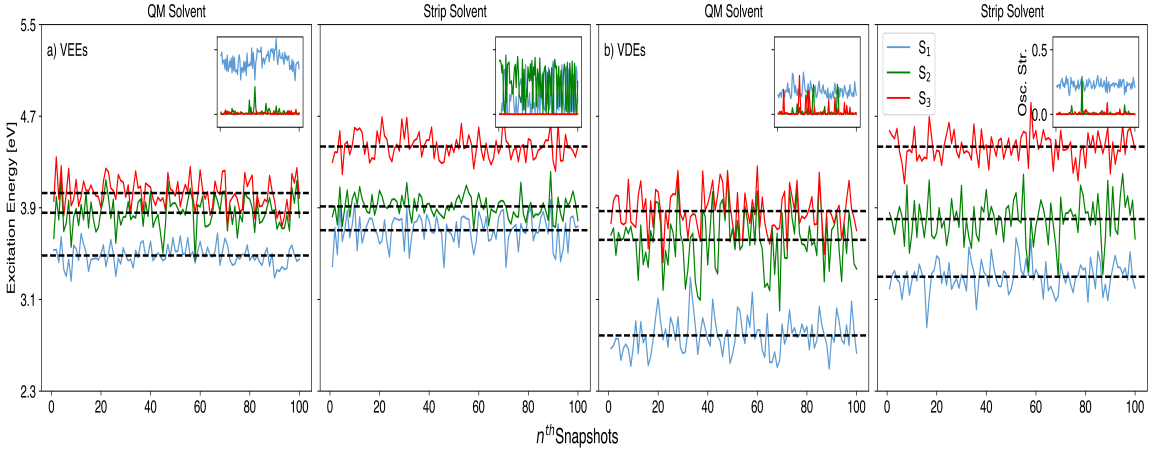

Figure 4.9: NBD in DMSO: a) VEEs computed for ground state AIMD configurations and b) VDEs computed for S_1 excited state AIMD configurations computed for both QM solvent and chromophore-only (strip solvent) configurations.

Table 4.2: NBD VEE/VDE distribution mean, standard deviation, E_{max}, and FWHM for QM, MM solvent (point charges) and chromophore-only (strip solvent) configurations. Sampled from 100 AIMD snapshots. * indicates S_1 and S_2 electronic state mixing

	Mean Abs — Ems (eV)		STD Abs — Ems (eV)		E_{max} Abs — Ems (eV)		FWHM Abs — Ems (eV)	
QM Solvent	3.483	2.786	0.086	0.156	3.476	2.745	0.155	0.336
MM Solvent	3.660	2.864	0.088	0.163	3.642	2.821	0.210	0.338
Strip Solvent	3.850*	3.296	0.101*	0.128	3.832*	3.315	0.236*	0.228

FWHM of the emission ensemble lineshape compared to absorption.

A Stokes shift can be computed from the ensemble of VEE/VDEs, but this value should not be rigorously compared to experimental lineshape maxima as spectra generated from the ensemble approach do not include vibronic contributions, which can affect the position of the maxima. Taking the difference between the ensemble spectral maxima gives a value of 0.731 eV, significantly larger than the experimental lineshape Stokes shift value of 0.334 eV. In contrast, the difference in the VEE at the ground state geometry and the VDE at the excited state geometry, both with implicit solvation for the respective state, is only 0.357 eV, as mentioned previously. We can isolate the origin of this difference by comparing VEE and VDE differences. The

average VEE value from the explicit solvent snapshots is 3.483 eV, and the implicit solvent-optimized geometry VEE value is 3.605 eV, 0.122 eV higher. In contrast, the average VDE value from the explicit solvent snapshots is 2.786 eV and the implicit solvent-optimized geometry VDE value is 3.248 eV, 0.462 eV higher. There is clearly a much larger discrepancy in VDE compared to VEE, suggesting a substantial change in electronic structure for the explicitly solvated excited state AIMD snapshots compared to the implicitly solvated excited state optimized geometry. This shift to lower VDE for the explicitly solvated excited state is responsible for the overly large computed Stokes shift with the ensemble method.

The implicit solvent FTFC spectral lineshapes, shown in Figure 4.8a, display asymmetry from the vibronic tail and show relatively good agreement with the experimental lineshape (FWHM values of 0.330 and 0.381 eV for absorption and emission, respectively), with both absorption and fluorescence being slightly underestimated in width by 0.011 eV and 0.019 eV, respectively. The computed Stokes shift determined from the lineshape spectral maxima is 0.123 eV, thus significantly underestimated compared to the experimental value of 0.334 eV (see Table 4.1). Overall, the implicit solvent model predicts too-narrow spectral lineshapes and underestimates the Stokes shift when we employ the default broadening factor of 135 cm^{-1}.

We now turn to the main focus of this work and the spectra generated with the combined ensemble-Franck-Condon methods. The results obtained from the ensemble and implicit solvent FTFC approaches highlight the significance of explicit environmental interactions and vibronic contributions. The E-FC methods incorporate both of these effects.

Examining lineshapes computed with the E-sumFTFC approach, Figure 4.8b, we note that both absorption and fluorescence spectra are generated using the same one hundred snapshots obtained from the ground and excited state AIMD as in the ensemble spectral simulations but with the ground and excited state geometry optimizations and frequency calculations performed with frozen QM solvent. The individual FTFC spectra (thin gray lines) show a significant degree of variability in the lineshape and

position, confirming the importance of explicit environmental interactions on the resulting vibronic spectrum. The FWHM of individual explicit solvent FTFC spectra, see Figure 4.10, range between 0.260 and 0.780 eV, with an average FWHM value of 0.366 eV for absorption and 0.514 eV for emission. These average values are larger than the FWHM values for the implicit solvent FTFC spectra of 0.354 and 0.458 eV, suggesting that for NBD, the QM explicit solvent environment leads to stronger vibronic coupling than the implicit solvent environment, even more so for fluorescence.

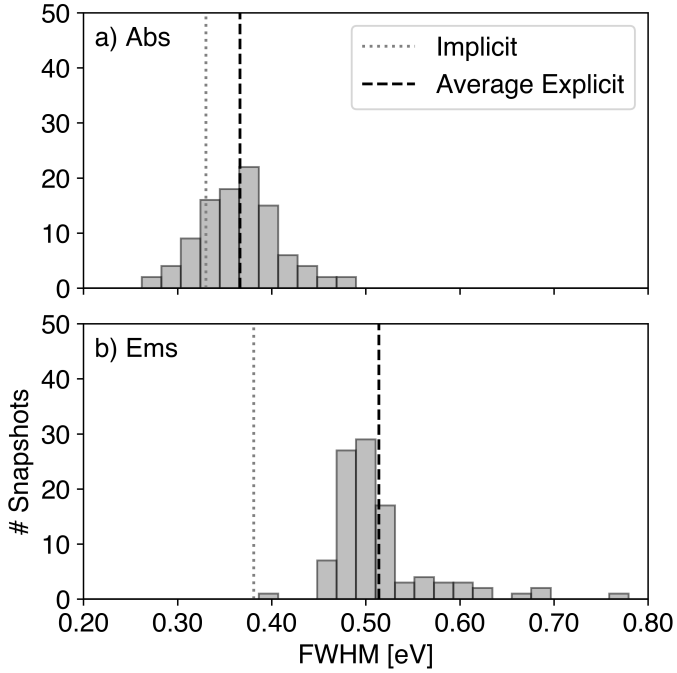

Figure 4.10: Frequency distribution of a) absorption and b) emission vibronic lineshape FWHM values of NBD in DMSO. The dotted gray lines correspond to the FWHM of the implicit solvent FTFC spectra (Abs: 0.330 eV, Ems: 0.381 eV). The dashed black lines represent the average values of the FWHM of the explicit solvent FTFC spectra (Abs: 0.366 eV, Ems: 0.514 eV).

The summed FTFC spectra create the E-sum$_{100}$FTFC absorption and emission spectra, black lines in Figure 4.8b and c, which are broader than their implicit solvent FTFC counterparts, with smoothed-out vibronic features. Overall, the E-sum$_{100}$FTFC absorption lineshape gives good agreement with the experimental absorption lineshape, see Figure 4.8c, with a slight overestimation of the FWHM value.

In contrast, the E-sum$_{100}$FTFC emission lineshape, albeit with a good overall spectral shape for the onset and vibronic tail, is too broad, with an FWHM value that overestimates the experimental value by 0.132 eV. This overestimation is likely due to vibronic contributions, with the vibronic emission spectrum being, on average, overestimated compared to absorption for single snapshots, see Fig.4.10. The E-sum$_{100}$FTFC method also produces an overly large Stokes shift value of 0.588 eV, which is 0.254 eV larger than the experimental value, indicating that the overestimation of the emission spectral width may also be due to environmental contributions.

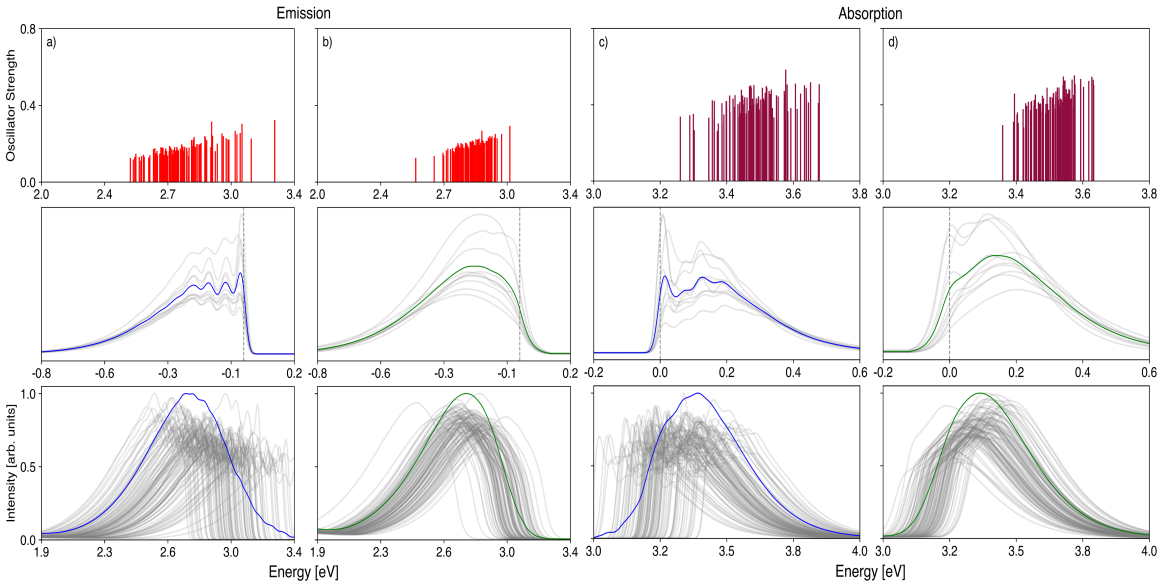

Figure 4.11: Pictorial representation of the E-avg$_{10}$ZTFC and E$_{opt}$-avg$_{10}$FTFC methods for NBD in DMSO: The first two columns a) and b) represent emission, and the columns c) and d) represent absorption. The top row shows the distribution of VDEs from a) unoptimized and b) optimized geometries and VEEs from c) unoptimized and d) optimized geometries on the excited and ground state PESs, respectively. The middle row depicts the procedure of generating the average FC lineshape by aligning the $0 \rightarrow 0$ transition energies. The bottom row represents the dressing of the ω_{00} shifted unoptimized and optimized VDEs and VEEs with avg$_{10}$ZTFC and avg$_{10}$FTFC lineshapes, resulting in E-avg$_{10}$ZTFC and E$_{opt}$-avg$_{10}$FTFC methods, respectively.

The spectra generated using the more cost-effective E$_{opt}$-avg$_{10}$FTFC and E-avg$_{10}$ZTFC methods are shown in Figure 4.8c, with the individual components of both approaches shown in Figure 4.11. Upon optimization of the chromophore, we see that the ensemble of VEE/VDEs narrows, Figure 4.11 top row, as expected, as thermal energy of

the chromophore is removed at the minimum energy geometry within the frozen QM solvent environment. In particular, for the VDEs (top of columns a and b), we see that some of the higher energy transitions at ∼3.1 - 3.3 eV that were energetically separated from the ensemble are no longer present at these high energies.

We also depict in the middle row of Figure 4.11 the average ZTFC and FTFC lineshapes from ten randomly chosen snapshots generated from energetically aligned individual vibronic FC spectra. The optimized VEEs/VDEs and unoptimized VEEs/VDEs, shifted[427] using the average 0-0 transition values from the same snapshots that generate the average FC lineshape, are combined with the average FTFC and ZTFC lineshapes and then summed to produce the E_{opt}-avg$_{10}$FTFC and E-avg$_{10}$ZTFC spectra, respectively, shown in the bottom row of Figure 4.11. For NBD in DMSO, we see that the absorption spectra generated using all three E-FC approaches are in excellent agreement with each other and with the experimental absorption lineshape. In contrast, the emission spectra from all E-FC methods are broader than experiment. The E_{opt}-avg$_{10}$FTFC and the E-sum$_{100}$FTFC methods are in impressively good agreement with each other, showing that the use of average FC lineshape can be representative for most snapshots while presenting significant computational savings. The E-avg$_{10}$ZTFC emission spectrum shows additional over-broadening due to the presence of the high-energy outlier VDEs.

Although the broader emission spectra likely contain contributions from overly strong chromophore-solvent interactions in the excited state, which may contribute to the overestimation of the Stokes shift values, see Table 4.1, they likely also originate from the CAM-B3LYP density functional within the TDA predicting an overly flat excited state potential in explicit QM solvent. This overly flat potential would manifest in both a wider distribution of chromophore configurations sampled during the excited state AIMD and a wider vibronic spectrum, as we see in our average FC lineshapes. This explanation is supported by the much more narrow spectrum generated by a vertical gradient compared to adiabatic Hessian Franck-Condon lineshape (see Figure 4.12) as well as going beyond the TDA to employing the full TDDFT matrix, which leads to a slight broadening of the absorption spectrum and narrowing of the

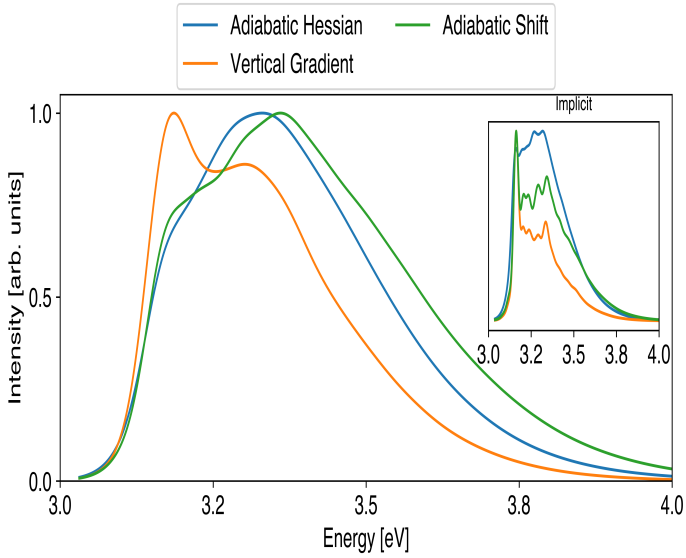

Figure 4.12: NBD in DMSO: Comparison of FC methods, including adiabatic Hessian, vertical gradient, and adiabatic shift with the TDA/CAM-B3LYP/6-31G* level of theory.

emission spectrum (see Figure 4.13).

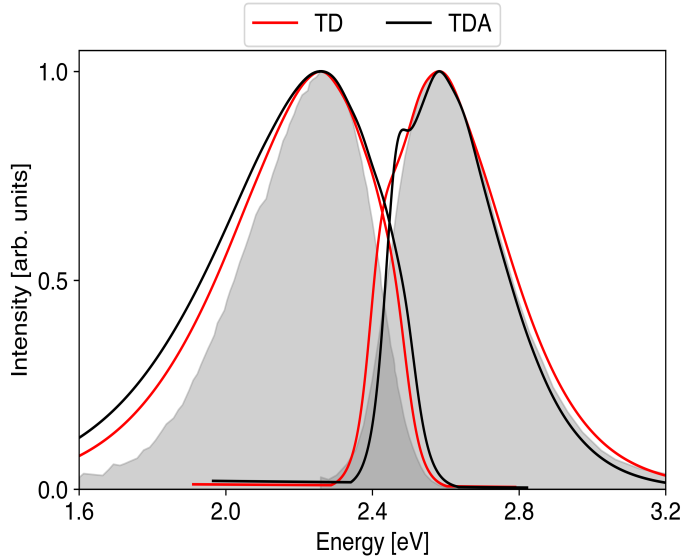

Figure 4.13: Comparison of average FTFC vibronic lineshape generated using five randomly selected explicit solvent snapshots using TD and TDA for NBD in DMSO using CAM-B3LYP/6-31G* level of theory.

The difference in absorption and emission spectral width also shows some mild dependence on the choice of functional, with LC-ωPBE yielding a more narrow fluorescence spectrum as shown in Figure 2.9.

In summary, the E-FC methods capture both specific environmental and vibronic effects but are susceptible to errors in the description of the electronic structure, which for NBD in DMSO at the TDA/CAM-B3LYP level of theory appears to yield an overly flat description of the excited state potential.

4.3.2 Nile Red in DMSO

Like NBD, NR is also used as a fluorescence emitter[282,283,484–486] and its spectral properties are sensitive to the environment.[286,487] The experimental absorption lineshape is broader than the fluorescence lineshape, with FWHM values of 0.365 eV and 0.252 eV, respectively.[286] Unlike NBD, there are no hydrogen bonds between NR and DMSO molecules, and the resulting Stokes shift is noticeably smaller, being 0.290 eV for NR (compared to 0.334 eV for NBD).

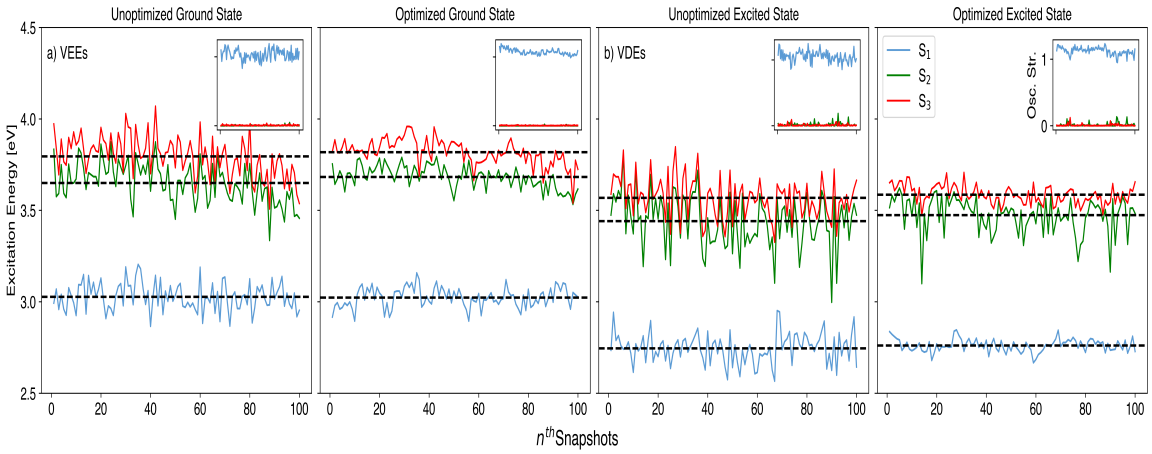

Figure 4.14: NR in DMSO: Vertical excitation energies obtained from ground state AIMD snapshots and vertical de-excitation energies obtained from excited state AIMD snapshots. Energy gaps are also shown for the same snapshots after geometry optimization in a frozen QM solvent environment. Corresponding oscillator strengths are included as an inset.

From the AIMD simulations, we obtained one hundred uncorrelated snapshots on both the ground and excited state potentials and computed the VEEs and VDEs. We here focus only on the low-lying bright state of charge transfer character; higher-lying excited states are energetically well separated from the first excited state, and no state mixing was observed. Both S_2 and S_3 excited states have near-zero oscillator strength across the snapshots, as shown in Figure 4.14.

Fig. 4.15a shows both absorption and fluorescence lineshapes for NR in DMSO obtained using the standard ensemble and implicit solvent FTFC approaches, with corresponding spectral values given in Table 4.3. For the VEEs and VDEs contributing to the ensemble spectra, the standard deviation is only 0.08 eV due to the rigid structure of NR. The computed FWHM for absorption and emission ensemble spectral lineshapes are 0.210 and 0.179 eV, respectively. These values are underestimated compared to experimental lineshapes, see Table 4.3, which could be due to overly weak interactions of NR in DMSO or due to the missing vibronic contributions. The Stokes shift determined from the ensemble lineshapes is also underestimated at 0.234 eV.

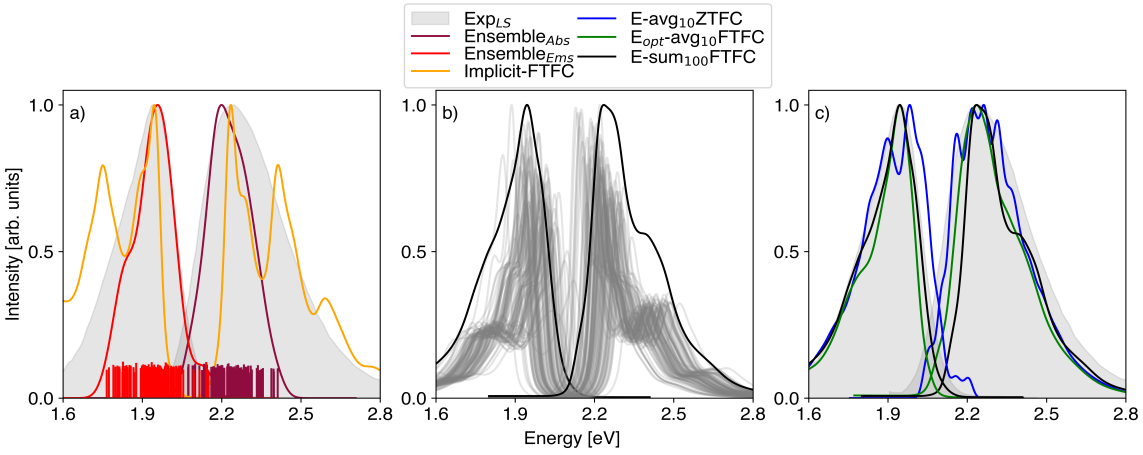

Figure 4.15: Absorption and fluorescence lineshapes of NR in DMSO: Filled gray spectra are experimental lineshapes, transformed from Ref.286. a) Ensemble and implicit solvent FTFC methods, b) E-sum$_{100}$FTFC and individual FTFC spectra, and c) E-avg$_{10}$ZTFC, E$_{opt}$-avg$_{10}$FTFC, and E-sum$_{100}$FTFC lineshapes. All lineshapes are shifted energetically to align with the experimental lineshape maxima.

Table 4.3: NR in DMSO: FWHM, applied energy shift, and Stokes shift from experiment, ensemble, implicit FTFC, and E-FC methods for absorption and emission lineshapes. All values are given in eV.

Methods	**Abs FWHM (eV)**	**Ems FWHM (eV)**	**Abs Energy Shift (eV)**	**Ems Energy Shift (eV)**	**Stokes Shift (eV)**
Exp_{LS}	0.365	0.252	-	-	0.290
Implicit	0.114	0.289	1.046	1.323	0.013
Ensemble	0.210	0.179	0.792	0.801	0.234
$Ensemble_{Opt}$	0.148	0.109	0.788	0.816	0.261
E-avg_{10}ZTFC	0.300	0.267	0.644	0.788	0.136
E_{opt}-avg_{10}FTFC	0.268	0.166	0.627	0.795	0.123
E-sum_{100}FTFC	0.256	0.228	0.599	0.791	0.098

To examine the effect of solvent-induced broadening on the ensemble spectra, the solvent surrounding NR was removed, and the VEEs/VDEs were recomputed. Unlike for NBD, the S_1 state of NR remained the bright state, and all higher-lying electronic states remained energetically separate and dark, except for one snapshot where S_2 gained considerable oscillator strength during excitation from the ground state, see Figure 4.16. The chromophore-only ensemble VEEs indicate a significant impact from solvent broadening, with the chromophore-only VEE standard deviation decreasing from 0.077 to 0.052 eV and the FWHM decreasing from 0.210 to 0.102 eV, see Table 4.3 and Table 4.4. Surprisingly, upon removal of the solvent environment, the change in the standard deviation of the ensemble of VDEs is negligible, with a slight increase produced in the FWHM. This observation suggests that the excited state of NR weakly interacts with DMSO and doesn't have a significant impact on the distribution of VDEs.

To improve the comparison between the simulated and experimental spectral shape and FWHM, it is necessary to include the missing vibronic contributions. Previous implicit solvent studies by Kostjukova et al.[325] and Boldrini et al.[324] have confirmed the crucial role of vibronic contributions in the absorption spectra of NR. The implicit solvent FTFC simulated absorption and fluorescence spectral lineshapes, see

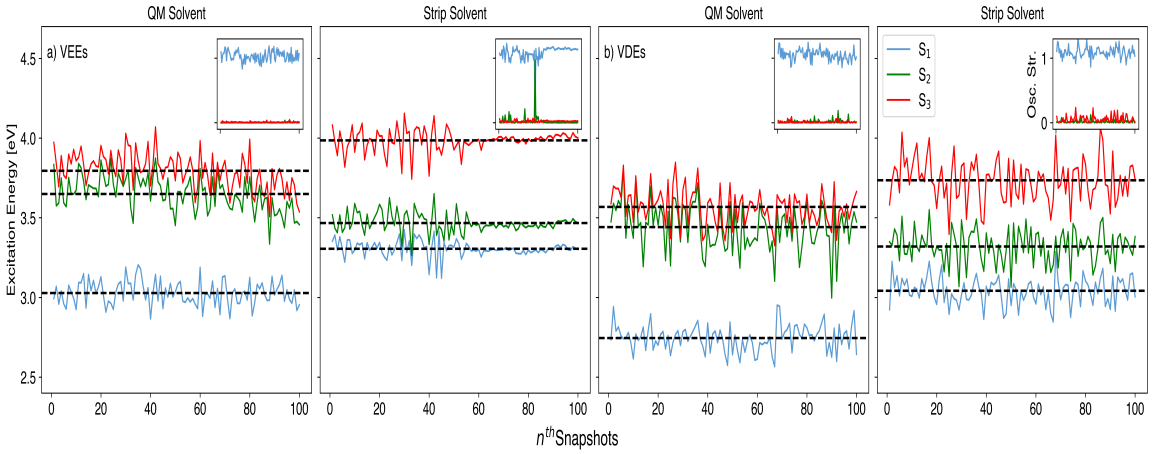

Figure 4.16: NR in DMSO: a) VEEs and b) VDEs trend across the snapshots in QM and chromophore-only (strip solvent) configurations.

Table 4.4: NR VEE/VDE distribution mean, standard deviation, E_{max}, and FWHM for QM solvent, MM solvent, and chromophore-only configurations. Sampled from 100 AIMD snapshots.

	Mean Abs (eV)	Mean Ems (eV)	STD Abs (eV)	STD Ems (eV)	E_{max} Abs (eV)	E_{max} Ems (eV)	FWHM Abs (eV)	FWHM Ems (eV)
QM Solvent	3.027	2.746	0.077	0.082	2.992	2.758	0.210	0.179
MM Solvent	3.186	2.893	0.084	0.079	3.169	2.887	0.236	0.196
Strip Solvent	3.306	3.042	0.052	0.086	3.302	3.079	0.102	0.198

Figure 4.15a, do not show the smooth spectral lineshapes of the experiment, with FWHM values that are under and over-estimated at 0.114 and 0.289 eV, respectively; both of these values include the second main vibronic peak. The calculated Stokes shift using the corresponding maxima is 0.013 eV, which is severely underestimated due to the small distance between the 0-0 peaks that dominate the lineshape maxima. Thus, we find that both the ensemble and implicit solvent FTFC methods fail to describe the experimental absorption and emission spectra of NR in DMSO adequately. Combining an explicit description of the solvent environment with vibronic coupling is essential for an improved description of both absorption and fluorescence spectra.

Next, we compare spectral lineshapes generated with the E-FC methods. The pictorial representation of the working of E-FC methods for NR in DMSO is shown in

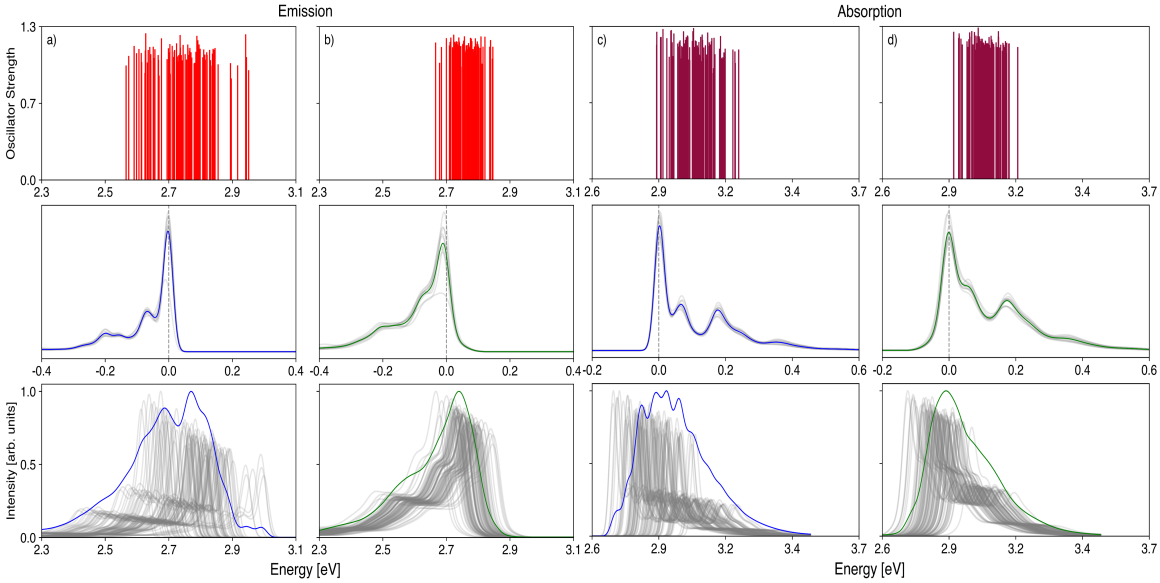

Figure 4.17: Pictorial representation of the E-avg$_{10}$ZTFC and E$_{opt}$-avg$_{10}$FTFC methods for NR in DMSO: The first two columns from the left represent emission lineshape spectra, and the remaining two columns represent absorption lineshape spectra. The top row shows the distribution of VDEs and VEEs from unoptimized and optimized geometries on the excited and ground state PES, respectively. The middle row depicts the procedure of generating the average FC lineshape by aligning the $0 \rightarrow 0$ transition energies. The bottom row represents the dressing of the zero-point transition energy corrected unoptimized and optimized VDEs and VEEs with avg$_{10}$ZTFC and avg$_{10}$FTFC lineshape resulting in E-avg$_{10}$ZTFC and E$_{opt}$-avg$_{10}$FTFC, respectively.

Figure 4.17. The individual FTFC spectra and resulting E-sum$_{100}$FTFC lineshape are shown in Fig. 4.15b. The individual FTFC spectra computed in the explicit solvent environment are quite similar to each other across configurations and they do not show the same intensity in the second vibronic peak as is seen with the implicit solvent FTFC spectra. The FWHM values for the individual spectra do not usually account for the contributions from the second vibronic peak, leading to very small values. Therefore, in Figure 4.18, we instead plot the full-width half-half max (FWHHM), taking the width at 25% of the lineshape maximum. At 25% of the maximum, we observe broadening primarily from two vibronic peaks in both absorption and emission lines. However, there are some single-peak outliers in both FWHHM distributions. For absorption, widths below 0.20 eV originate from a single peak, which in Figure 4.18a, we represent by light blue bars. For emission, widths below 0.20 eV are due to a combination of both single and double peaks; in Figure 4.18b, these values are

colored light blue with gray stripes. We computed the average value of this FWHHM using only the spectra for which there are two vibronic peaks contributing to the FWHHM value, which we determined to be 0.274 for absorption and 0.264 eV for fluorescence. These values are smaller than the corresponding implicit solvent FWHHM values of 0.452 and 0.470 eV taken at the 25% intensity value, showing decreased vibronic coupling in explicit solvent. The summation of the E-sum$_{100}$FTFC method washes out the pronounced vibronic nature of the peaks, providing relatively smooth absorption and fluorescence lineshapes, as observed in the experimental lineshapes.

The E_{opt}-avg$_{10}$FTFC and E-avg$_{10}$ZTFC spectra are shown in Fig. 4.15c. In contrast to the NBD results, for NR, the E-sum$_{100}$FTFC and E_{opt}-avg$_{10}$FTFC fluorescence spectra agree in width and shape with the experiment, whereas the absorption spectrum is predicted to be too narrow by both methods. For the E-avg$_{10}$ZTFC method, the lineshapes remain a bit jagged, and there is an increase in lineshape width, leading to an overly broad fluorescence lineshape. We also see for fluorescence that there are clearly a few high-energy outlier VDEs that lead to an unphysical high-energy fluorescence spectral onset. The Stokes shift predicted by all three methods, see Table 4.3, remains underestimated compared to the experiment. Overall, the more affordable E_{opt}-avg$_{10}$FTFC method is again in good agreement with the E-sum$_{100}$FTFC method, with the E-avg$_{10}$ZTFC showing more of a discrepancy with some unphysical jaggedness remaining in the spectrum.

The electronic structure method is undoubtedly one source of potential error for the missing spectral width for NR in DMSO. When we examined the effect of the TDA versus the full solution of the TDDFT equations on five snapshots, we found that the second vibronic peak gains significant intensity in both absorption and emission spectra (see Figure 4.19), which would lead to a considerable broadening of the simulated absorption and emission spectra of the TDDFT lineshape was used instead of the TDA lineshape.

Additionally, benchmarking FTFC lineshapes against two other density functionals showed that although the M06-2X method gives good agreement with the CAM-

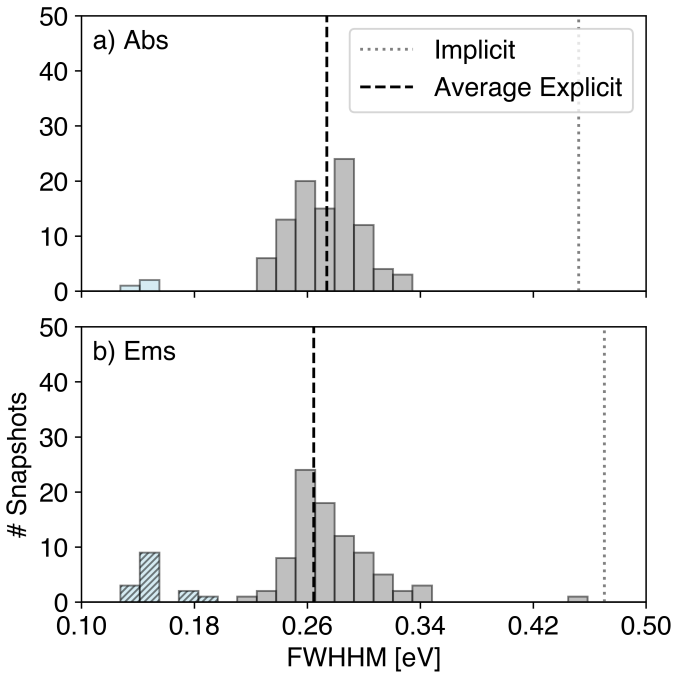

Figure 4.18: Frequency distribution of a) absorption and b) emission vibronic lineshape widths computed at 25% intensity, Full Width at Half-Half Maximum (FWHHM), of NR in DMSO. The dotted gray lines correspond to the FWHHM value of the implicit solvent FTFC spectra (Abs: 0.452 eV, Ems: 0.470 eV), which includes the second main vibronic peak. The dashed black lines represent the average values of the FWHHM of the explicit solvent FTFC spectra that include the second main vibronic peak (Abs: 0.274 eV, Ems: 0.264 eV).

B3LYP lineshapes, the LC-ωHPBE functional produces FTFC spectra that are substantially broader than the other two functionals (Figure 2.8). Thus, by changing the electronic structure method to one with broader vibronic spectra, we can expect improved agreement with the experimental absorption spectrum; however, the emission spectrum would also gain additional broadening and become broader than the experimental spectrum. Overall, the vibronic broadening appears underestimated with TDA-CAM-B3LYP for Nile Red in DMSO. This underestimated vibronic broadening may also be responsible for the underestimated Stokes shifts, as the increased intensity of the second vibronic peak may change the position of the spectral maxima and increase the energy between the maxima of the absorption and emission spectra.

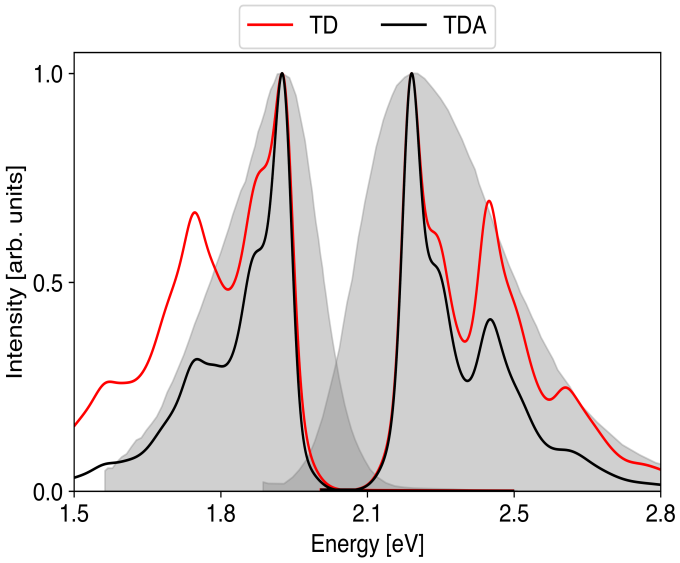

Figure 4.19: Comparison of average FTFC vibronic lineshape spectra generated using five randomly selected explicit solvent snapshots using TD and TDA for NR in DMSO using CAM-B3LYP/6-31G* level of theory.

4.3.3 7MC in Methanol

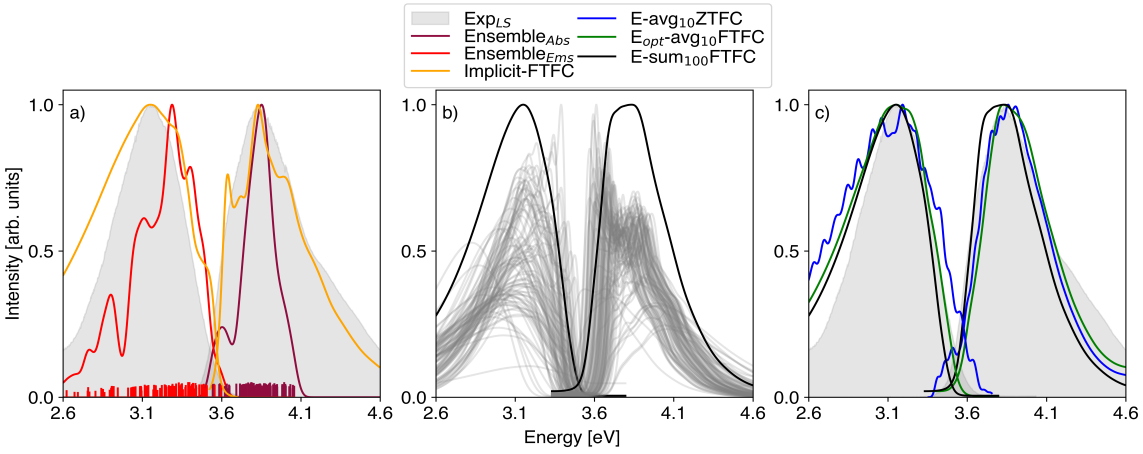

Figure 4.20: Absorption and fluorescence lineshapes of 7MC in methanol: Filled gray spectra are experimental lineshapes, transformed from Ref.287,288. a) Ensemble and implicit solvent FTFC methods, b) E-sum$_{100}$FTFC and individual FTFC spectra, and c) E-avg$_{10}$ZTFC, E$_{opt}$-avg$_{10}$FTFC, and E-sum$_{100}$FTFC lineshapes. All lineshapes are shifted energetically to align with the experimental lineshape maxima.

7-Methoxycoumarin-4-acetic acid (7MC), like NBD, is a push-pull electron system

and is used as a fluorescent probe in various cell biology applications.[284,285,488] 7MC shows the largest conformational changes and the largest number of hydrogen bonds of all three dyes studied here. Due to the carboxylic acid group and the carbonyl bond, 7MC acts as both an acceptor and donor of hydrogen bonds in methanol. The experimental FWHM values are 0.563 and 0.539 eV for absorption and emission lineshapes, indicating similar potential energy surfaces for ground and excited states with a Stokes shift of 0.683 eV, the largest among all three dyes studied here.

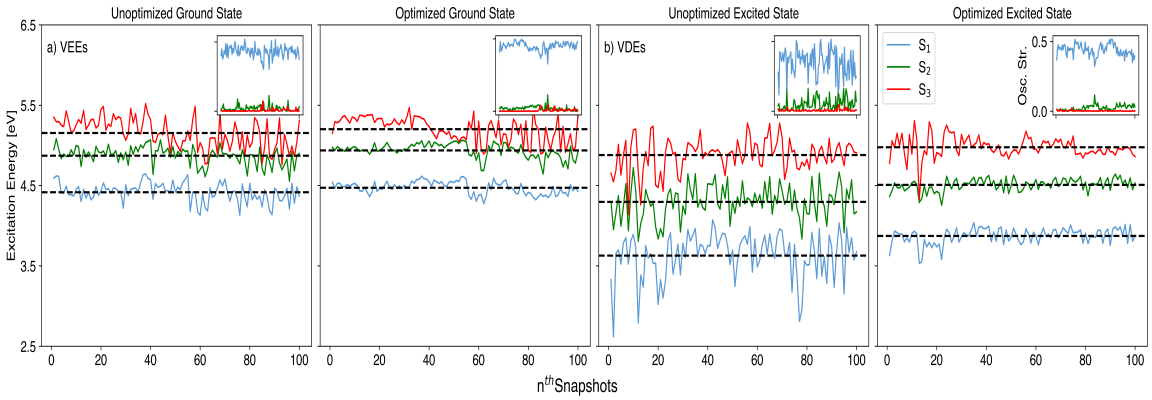

Figure 4.21: 7MC in methanol: Vertical excitation energies obtained from ground state AIMD snapshots and vertical de-excitation energies obtained from excited state AIMD snapshots. Energy gaps are also shown for the same snapshots after geometry optimization in a frozen QM solvent environment. Corresponding oscillator strengths are included as an inset.

Like the other two dyes, we extracted 100 snapshots from the ground and excited state AIMD simulations and performed VEE and VDE calculations. The higher-lying states are well separated from S_1 during the ground state dynamics; see Figure 4.21. However, during the excited state S_1 dynamics, a few of the snapshots show shared oscillator strength between S_1 and S_2. Once the chromophore is optimized in the frozen QM solvent, the S_2 and S_3 states show negligible oscillator strength and remain energetically separated from the S_1 state. Upon analyzing the geometrical changes throughout the dynamics, we observed a considerable increase in the flexibility in the excited state, particularly around the pyrone ring. Consequently, the value of the standard deviation of the energy gap distribution more than doubles, going from 0.119 eV for VEEs to 0.285 eV for VDEs, see Table 4.5. However, once the geometries

Table 4.5: 7MC VEE/VDE distribution mean, standard deviation, E_{max}, and FWHM for QM and MM solvent, and chromophore-only configurations. Sampled from 100 AIMD snapshots.

	Mean Abs — Ems (eV)		STD Abs — Ems (eV)		E_{max} Abs — Ems (eV)		FWHM Abs — Ems (eV)	
QM Solvent	4.416	3.629	0.119	0.285	4.439	3.766	0.203	0.445
MM Solvent	4.525	3.718	0.102	0.291	4.493	3.882	0.229	0.425
Strip Solvent	4.532	3.812	0.096	0.293	4.545	3.986	0.244	0.452

are optimized in frozen QM solvent, the standard deviation values decrease to 0.077 and 0.097, respectively.

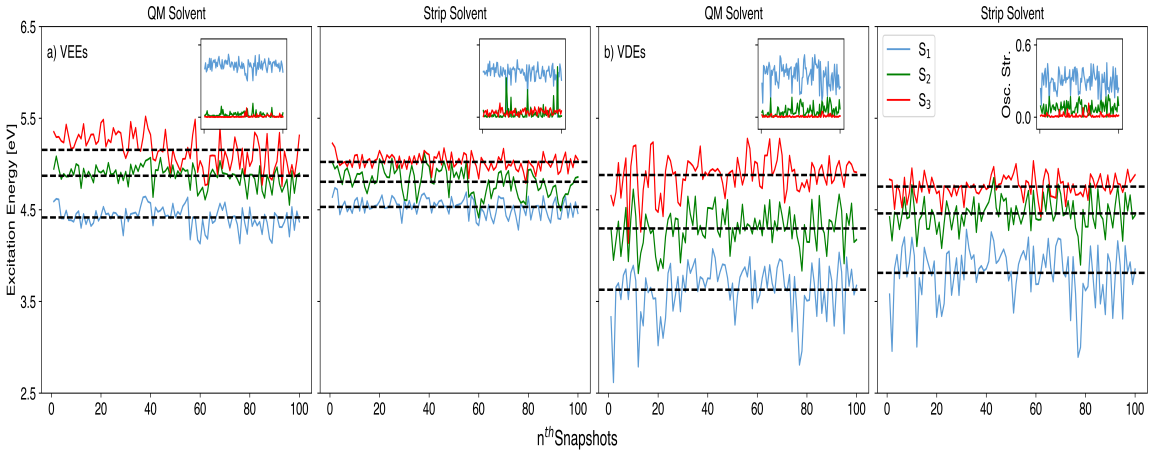

Figure 4.22: 7MC in methanol: a) VEEs and b) VDEs for QM solvent and chromophore-only (strip solvent) configurations.

Figure 4.20a shows lineshapes generated using the ensemble and implicit solvent FTFC approaches. Although the ensemble absorption spectral lineshape is too narrow compared to the experiment, the ensemble emission lineshape is twice as broad as absorption, nearing the experimental spectral width and giving a FWHM value of 0.445 eV, see Table 4.6. The difference in absorption and emission spectral width correlates to the standard deviation computed for the VEEs and VDEs. The effect of the explicit solvent interactions on chromophore energy gaps was analyzed by computing VEEs and VDEs of the chromophore-only configurations. The results show that solvent interactions have minimal impact on the energy distributions, as depicted in

Table 4.6: 7MC in methanol: FWHM, applied energy shift, and Stokes shift from experiment, ensemble, implicit FTFC, and E-FC methods for absorption and emission lineshapes. All values are given in eV.

Methods	**Abs FWHM (eV)**	**Ems FWHM (eV)**	**Abs Energy Shift (eV)**	**Ems Energy Shift (eV)**	**Stokes Shift (eV)**
Exp_{LS}	0.563	0.539	-	-	0.683
Implicit	0.539	0.766	0.303	0.380	0.602
Ensemble	0.203	0.445	0.587	0.478	0.673
Ensemble_{Opt}	0.229	0.235	0.642	0.722	0.582
E-avg_{10}ZTFC	0.494	0.779	0.444	0.646	0.464
E_{opt}-avg_{10}FTFC	0.490	0.653	0.412	0.604	0.484
E-sum_{100}FTFC	0.480	0.585	0.468	0.605	0.546

Figure 4.22 and Table 4.5, suggesting that the chromophore configurations dominate the majority of the energy fluctuations and ensemble spectral linewidth.

The implicit FTFC absorption lineshape displays distinct vibronic peaks, whereas the emission lineshape appears smoother and broader. The FTFC computed FWHM values are 0.539 eV and 0.766 eV, respectively, with a Stokes shift of 0.602 eV. Thus, similar to NBD, both the ensemble and the implicit solvent FTFC approaches predict a wider emission spectral lineshape than absorption, contrary to the experiment, suggesting an overly flat excited state potential at this level of theory.

Next, we compare the spectra generated with the E-FC family of approaches. The pictorial representation of the working of E-FC methods for 7MC in methanol is shown in Figure 4.23. The individual explicit solvent FTFC absorption and fluorescence lineshapes of 7MC in methanol, along with the resulting E-sum_{100}FTFC spectra, are shown in Figure 4.20b. We find that there is a large degree of variability in the features of the individual FTFC lineshapes, but the trend of the FWHM values is consistent with the wider emission predicted by implicit solvent, with average values of 0.416 eV for the absorption lineshape and 0.630 eV for the emission lineshape, see FWHM distribution in Figure 4.24. Both of these values are smaller than those

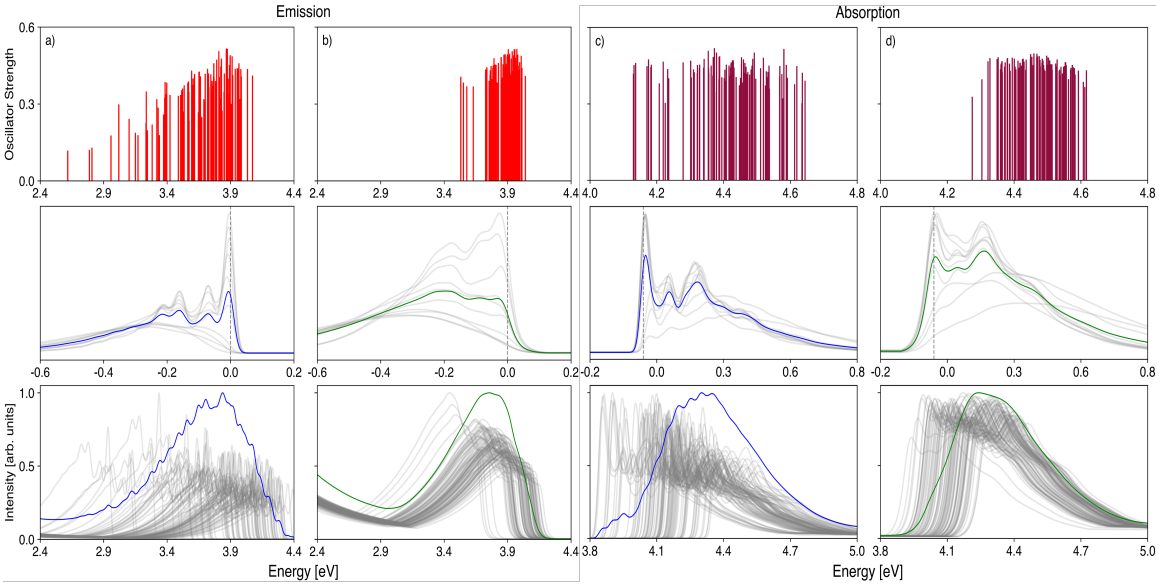

Figure 4.23: Pictorial representation of the working of computational efficient E-avg$_{10}$ZTFC and E$_{opt}$-avg$_{10}$FTFC methods for 7MC in methanol: The first two columns from the left represent emission lineshape spectra, and the remaining two columns represent absorption lineshape spectra. The top row shows the distribution of VDEs and VEEs from unoptimized and optimized geometries on the excited and ground state PES, respectively. The middle row depicts the procedure of generating the average FC lineshape by aligning the $0 \rightarrow 0$ transition energies. The bottom row represents the dressing of the zero-point transition energy corrected unoptimized and optimized VDEs and VEEs with avg$_{10}$ZTFC and avg$_{10}$FTFC lineshape resulting in E-avg$_{10}$ZTFC and E$_{opt}$-avg$_{10}$FTFC, respectively.

predicted by the implicit solvent approach, suggesting that for 7MC, the explicit solvent decreases the vibronic coupling compared to the implicit solvent model, opposite of what we see with NBD.

Although it is difficult to separate the role of individual factors affecting the lineshape, our analysis suggests that the most important geometrical change is associated with the planarity of the pyrone ring. For spectra with no vibronic features, the ring remains out-of-plane after optimization. For emission, we observe three distinct categories: spectra with the first peak as the maximum, spectra with the second peak as the maximum, and only one maximum but overly broad. Following the same procedure as with the other dyes, we chose random snapshots for generating the average FC lineshape, and found that there is minimal variation after ten vibronic spectra

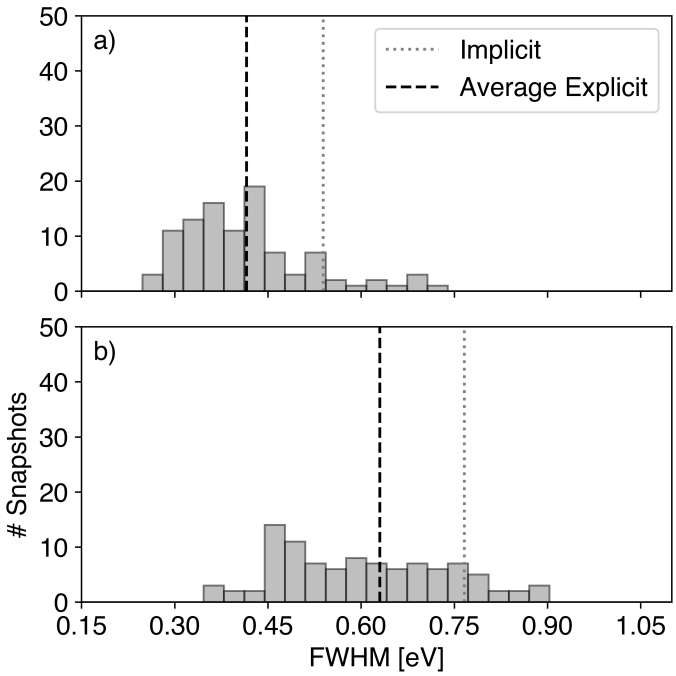

Figure 4.24: Frequency distribution of a) absorption and b) emission vibronic lineshape FWHM values of 7MC in methanol. The dotted gray lines correspond to the FWHM of the implicit solvent FTFC spectra (Abs: 0.539 eV, Ems: 0.766 eV). The dashed black lines represent the average values of the FWHM of the explicit solvent FTFC spectra (Abs: 0.416 and Ems: 0.630 eV).

are included in the averaging procedure. Given the variability of lineshapes, a more sophisticated averaging scheme could be envisioned that weights the lineshape based on the percentage of particular configurations, but here, we choose not to explore this direction.

Figure 4.20c compares the absorption and emission lineshapes generated using the three E-FC methods. All three methods show good agreement for the absorption lineshape and similar FWHM (∼0.490 eV) but remain underestimated in width relative to the experiment. For the emission lineshapes, both E_{opt}-avg$_{10}$FTFC and E-sum$_{100}$FTFC show good agreement with each other, with E-sum$_{100}$FTFC producing a more narrow spectrum (FWHM is 0.585 eV for E-sum$_{100}$FTFC, 0.653 eV for E_{opt}-avg$_{10}$FTFC), whereas the emission spectrum of the E-avg$_{10}$ZTFC method is wider and jagged because of the large distribution of VDEs, leading to an overly large

FWHM value of 0.779 eV. Unlike NBD, this overly large broadening appears to be completely dominated by chromophore flexibility. About 33% of emission lineshapes have an FWHM of more than 0.7 eV, and these are the snapshots where the pyrone ring is no longer planar. As shown in Table 4.6, the predicted Stokes shift is underestimated by all three methods.

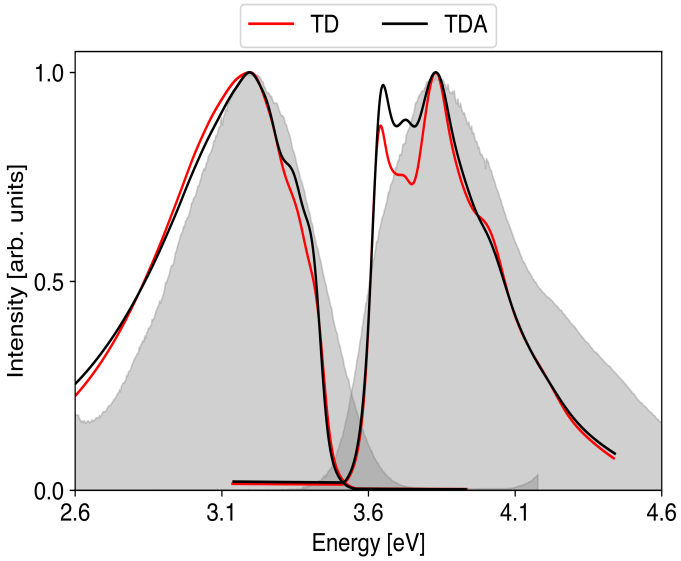

Figure 4.25: Comparison of average FTFC vibronic lineshape spectra generated using five randomly selected explicit solvent snapshots using TD and TDA for 7MC in methanol using CAM-B3LYP/6-31G* level of theory.

Unlike the other two chromophores, the 7MC spectral lineshape differences from full TD-DFT and TDA are minimal for both absorption and emission, as shown in Figure 4.25. Compared to CAM-B3LYP, both M06-2X and LC-ωHPBE predict broader lineshapes for absorption and slightly broader FTFC spectra for emission, as shown in Figure 2.10. This comparison suggests that CAM-B3LYP may underestimate the vibronic progression for absorption, leading to a more narrow absorption lineshape. As the wide distribution of VDEs suggests a potentially flat and anharmonic excited state S_1 surface, we also compared our vibronic lineshape computed with the adiabatic Hessian approach, the lineshape generated with the vertical gradient and adiabatic shift approaches, finding that for planar configurations there is good agreement between methods, whereas for more bent chromophore configurations the adia-

batic Hessian produces a broader lineshape, see Figure 4.26. This broader lineshape supports that the excited state potential is indeed anharmonic at this geometry for this flexible degree of freedom, leading to a breakdown of the harmonic approximation and contributions from overly broad lineshape within the adiabatic Hessian approach.

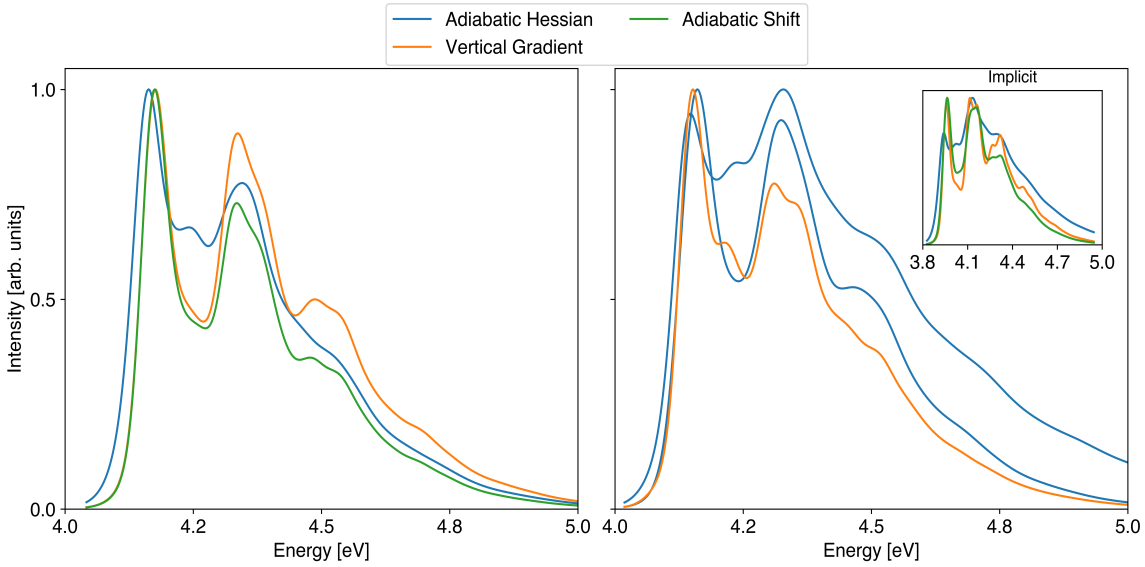

Figure 4.26: 7MC in Methanol: Comparison of FC methods for two explicit solvent snapshots with a) planar and b) non-planar optimized excited state geometries, including adiabatic Hessian, vertical gradient, and adiabatic shift with the TDA/CAM-B3LYP/6-31G* level of theory.

Ultimately, we see similar trends for E-FC approaches with 7MC as with the other dyes, where E-sum$_{100}$FTFC and E$_{opt}$-avg$_{10}$FTFC are in good agreement, but E-avg$_{10}$ZTFC is generally too broad and jagged with the 135 cm^{-1} broadening factor used here.

4.3.4 Relative Computational Cost of E-FC Methods

We next show the computational cost associated with the various ensemble and E-FC spectroscopy methods, accounting for the electronic structure calculations on the MD snapshots. We do not consider the computational cost from the QM/MM AIMD sampling, which is substantial, and could be accelerated with recent approaches of

machine learning interatomic potentials.[489–494] The chart depicted in Figure 4.27 illustrates the relative computational wall time required for the various spectroscopy methods, with average results given for simulating absorption and fluorescence lineshapes. For the corresponding relative costs for emission, which is similar to absorption but has an increased computational cost for excited state geometry optimization for the E_{opt} approach. Relative times are averaged over the three dyes investigated in this study. The geometry optimization and excitation energies were performed using TeraChem on a dual NVIDIA Tesla A100 PCIe v4 40GB HBM2 Passive Single GPU setup. Frequency calculations for the ground and excited states of NBD in DMSO, as well as 7MC in methanol, were carried out utilizing Gaussian16 on two Intel 28-core Xeon Gold 6330 processors, equipped with 256GB and 1TB of RAM, respectively, with the latter configuration used for the NR dye in DMSO.

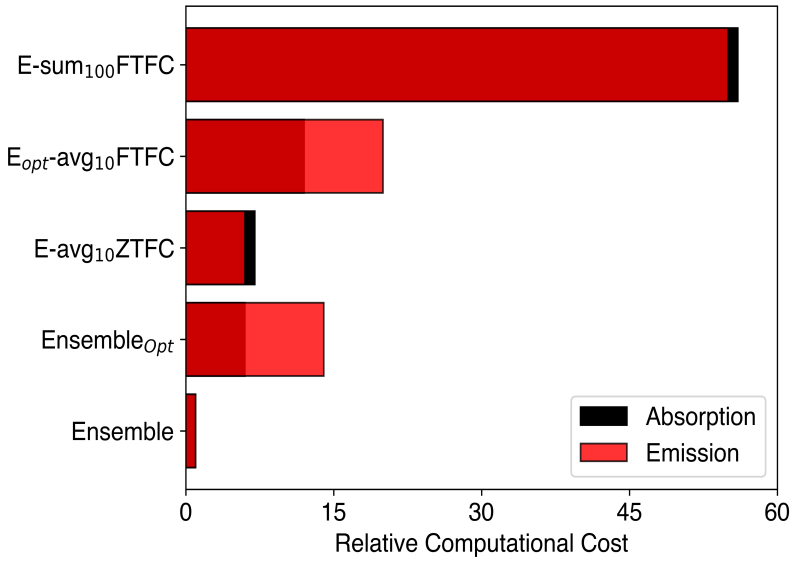

Figure 4.27: The average relative computational cost of all explicit solvent absorption spectroscopy methods for all three dyes.

The E-sum$_{100}$FTFC method is by far the most computationally demanding, taking 56.2× as long as the ensemble approach alone. Note that due to the larger QM region size for NR in DMSO, the frequency calculations are more computationally expensive, leading to a larger relative cost for the E-sum$_{100}$FTFC approach. There is a substantial reduction in computational cost achieved through the use of more

approximate methods, with the E_{opt}-avg$_{10}$FTFC method taking only 11.6× and the E-avg$_{10}$ZTFC method taking only 6.7× as long as the ensemble approach. For the E_{opt}-avg$_{10}$FTFC approach, this decrease in computational cost comes with nearly the same accuracy as the E-sum$_{100}$FTFC method, underscoring the efficiency of this approach and making it our recommended E-FC method for spectroscopic simulations.

4.4 Conclusions

In this study, we compared the simulated absorption and fluorescence lineshapes computed with three combined ensemble-Franck-Condon methods that account for both explicit environmental effects and vibronic effects. The explicit solvent is modeled through QM/MM AIMD trajectories performed on the ground state and the excited state. The vibronic effects are captured through the simulation of Franck-Condon spectra for the chromophore embedded in a frozen QM solvent shell. These E-FC methods are used to generate spectral lineshapes for three different chromophore-solvent systems and are compared to the more standard ensemble and implicit solvent Franck-Condon approaches.

We find that for both absorption and fluorescence, the E_{opt}-avg$_{10}$FTFC approach matches very well with the more expensive E-sum$_{100}$FTFC approach, generating very similar spectra at approximately 25% of the computational cost, and this, therefore, is our recommended approach for capturing vibronic and environmental effects for spectral lineshapes. The main approximation of the E_{opt}-avg$_{10}$FTFC approach is the assumption of an average FTFC lineshape, which we find here works very well with an average over ten individual lineshapes generated in explicit QM solvent. The E-avg$_{10}$ZTFC approach shows some over-broadening due to outliers from the MD sampling and jaggedness in the spectra but presents a reasonable alternative for 12.5% of the computational cost of the E-sumFTFC method.

One way to assess the extent of vibronic coupling is by measuring the width of the spectra before accounting for environmental broadening. Compared to FTFC spectra computed with implicit solvent, the FTFC spectra computed in explicit solvent

showed stronger vibronic coupling (larger average FWHM) for NBD but weaker vibronic coupling for NR and 7MC. Errors in the simulated lineshape FWHM values can be traced to the underlying electronic structure methods and the extent of vibronic coupling for each method. We find here that the choice of density functional theory affects the lineshape, with more exact exchange tending to lead to stronger vibronic coupling and broader spectra NR but slightly weaker coupling for NBD. We also find that the use of the TDA, compared to full TDDFT, can lead to more narrow vibronic spectral lineshapes in some cases.

Our study of computed absorption and emission lineshapes showcases the ability of a variety of spectroscopy simulation methods to capture vibronic and environmental effects. Advances in computational power, particularly GPUs, now allow ground and excited state explicit solvent interactions and vibronic contributions to be incorporated into molecules' absorption and fluorescence spectra, paving the way for accurate simulations of full spectral lineshapes. However, many challenges remain, including determining an accurate level of electronic structure theory and incorporating nonadiabatic and nuclear quantum effects. Many efforts along these fronts are underway, broadening the ability of simulation to connect with complex spectroscopic experiments.

Chapter 5

Going Beyond Förster Theory: Resonance Energy Transfer Processes in Explicit Environment

The goal of this chapter is to provide an analysis of how to best compute the coupling between donor and acceptor molecules involved in the excitation energy transfer processes in an implicit and explicit solvent environment. The chapter starts by providing some background on existing literature and studies in the field, including the methods used to compute the coupling using isolated dyes and a supramolecular diabatization approach. The Coulomb coupling methods include coupling via transition dipole moments, transition charges, and transition densities. The chapter compares results obtained with these various methods and then extends them to implicit and explicit solvent environments.

5.1 Introduction

Resonance energy transfer (RET) is a naturally occurring phenomenon where the energy from an excited donor molecule (D) transfers to an acceptor molecule (A) through a non-radiative process.[495] This transfer can be observed in processes like photosynthesis, where sunlight is absorbed by light-harvesting antennas such as chlorophyll (D), then transferred to the reaction centers (A), and ultimately utilized to drive chemical reactions.[496,497]

The first formulation for the rate of RET was put forward by Förster in 1948.[498] By invoking assumptions such as the ideal point dipole approximation (IPD), the rate of vibrational relaxation is faster than the rate of RET, and the energy transfer is incoherent. Based on this assumption, Förster put forward an elegant and versatile equation that, since its inception, has been used as a "spectroscopic ruler"[499,500] in many experiments, including protein-protein distances,[501] enzymatic reactions,[502] and bioimaging experiments.[503] Using this approximation and assumptions, the conclusion of Förster's theory can be conveniently written as the following set of three equations:

$$E = \frac{k_T}{k_T + \frac{1}{\tau_D}} = \frac{R_0^6}{R_0^6 + R_{DA}^6} \tag{5.1}$$

$$k_T = \frac{1}{\tau_D}\left(\frac{R_0^6}{R_{DA}^6}\right) \tag{5.2}$$

$$R_0^6 = \frac{9(ln10)\kappa^2\phi_D J_{DA}}{128\pi^5 n^4 N_A}, \tag{5.3}$$

where k_T is the rate of energy transfer, τ_D is the donor's excited state lifetime in the absence of the acceptor, R_{DA} is the distance between D and A, R_0 is the Förster radius, E is the efficiency of transfer, J_{DA} is the spectral overlap integral between D and A, κ^2 is the orientation factor, ϕ_D is the quantum yield of the donor in the absence of the acceptor and n is the refractive index.

Though FRET is a powerful and versatile tool used as a molecular yardstick and for studying the structure and dynamics of large molecules in the condensed phase, the fundamental RET process is still poorly understood at the atomic and electronic levels. For example, RET still occurs even when the ideal dipole approximation fails.[504–506] When the distance between the donor and acceptor molecule is too small, the Coulombic coupling could become grossly exaggerated, giving RET rate values that are orders of magnitude higher than the correct value.[504] In those instances, transition dipole moment vectors are insufficient to provide an accurate value of the Coulombic coupling. At a close distance, a complete transition density description is needed to describe the coupling values correctly.[507]

Similarly, the dependence on the orientation factor between the TDMs of donor and acceptor is unclear.[508,509] The orientation factor that affects the Coulombic coupling describes the relationship between the alignment of the transition dipole vector of the donor and acceptor. The value of the orientation factor can be obtained using

$$\kappa^2 = \cos\theta_T - 3\cos\theta_D \cos\theta_A, \tag{5.4}$$

where θ_T is the angle between the transition dipole moment vector of D and A, θ_D and θ_A are the angles donor and acceptor making with the line connecting the TDM vector.

A simple inspection of the orientation factor reveals that its value can range from 0 to 4. However, a value of 2/3 is generally used as this parameter is not easily accessible from experiments. The value of 2/3 remains valid as long as there is an equal probability of orientations that the donor and acceptor molecules could adopt during the lifetime of the excited donor state; however, either due to restricted rotation or slow rotation of the transition dipole moment vectors compare to the deexcitation process, this value of 2/3 becomes invalid. The correct value of the orientation factor then needs to be calculated either from steady-state confocal microscopy[510] or from an accurate MD simulation.[511–514]

Similar to the effects of absorption and fluorescence spectra by various solute-solvent explicit interactions, the overlap integral, which is an overlap between the donor's emission spectra and the acceptor's absorption spectra, may affect the overall observed FRET rate. A detailed mechanistic investigation should be carried out to understand FRET and to generalize the RET process in the condensed phase beyond Förster's assumptions.

In this study, we examine the assumption of the 2/3 orientation factor, and we compare methods for calculating the Coulombic coupling, such as transition density, transition charges, and transition dipole moment, analyzing the situations where the ideal point dipole approximation breaks down. We also examine the impact of dye distance on these couplings in implicit and explicit solvents. We utilized two pairs of donor and acceptor dyes: the heterodimer 7-nitrobenz-2-oxa-1,3-diazol-4-y (NBD)

and Nile red (NR) in implicit and explicit solvent models of DMSO and the homodimer cresyl violet cation (CV+) in a vacuum and implicit solvent model for water. For NBD-NR, we perform MD simulations to sample donor-acceptor geometries with solvent configurations, also analyzing the orientation factor and the validity of the 2/3 value. Results for the CV+ dimer system were generated by Sayan Adhikari, a contributor to this project.

5.2 Theoretical Details

5.2.1 The Spectral Overlap Integral

The rate of RET can be calculated as:

$$k_T = \frac{1}{\hbar^2 c} V_{DA}^2 J_{DA} \tag{5.5}$$

where $\hbar$ is Plank's constant, c is the speed of light, J_{DA} overlap-integral, is also known as the Franck-Condon factor of the weighted density of states (FCWD), and V_{DA} is the Coulombic coupling between the donor and acceptor. Using equation 4.1, J_{DA} can be easily obtained from experimental data and used for computing the rate; however, it can also be obtained using computational methods assuming Gaussian lineshapes.[515,516] The overlap integral is an essential factor for calculating the rates of RET and can be derived from the spectral overlap between the donor emission and acceptor absorption normalized lineshapes. Mathematically, it can be obtained as:

$$J_{DA} = \int_{-\infty}^{+\infty} \sigma_D^{Ems}(\omega) \sigma_A^{Abs}(\omega) d\omega \tag{5.6}$$

where $\sigma_D^{Ems}(\omega)$ and $\sigma_A^{Abs}(\omega)$ represent the fluorescence of the donor and absorption cross-section of the acceptor, respectively, which account for the vibronic states populated upon electronic excitation. It measures the resonance condition necessary for efficient energy transfer, incorporating the overlap of electronic states modified by vibrational interactions. It's important to accurately estimate the donor-acceptor energy difference when computing the J_{DA} functions from Franck-Condon calculations. Spectral overlaps can be highly sensitive to this difference, and even a small deviation in the excitation energies can lead to a large error in the computed rate.[517]

5.2.2 Coupling Methods

The total excitonic coupling for singlet excitation energy transfer is composed of Coulombic, exchange, and overlap contributions as shown in the equation 5.7.

$$V^{Total} = V^{Coul} + V^{Exch} + V^{Ovlp} \tag{5.7}$$

The V^{Exch} denotes the Dexter[518]-type excitonic coupling, which decays exponentially and much faster than Coulomb at large distances between the donor and acceptor. The overlap coupling[519] arises from the overlap between donor and acceptor orbitals and is often overlooked[520–522] in its contribution to the total coupling. The primary contribution to the total excitonic coupling comes from the Coulombic contribution. Below, we provide a brief overview of some commonly used methods for computing the Coulombic coupling, where the coupling can be determined from separate electronic structure calculations on each of the monomers, allowing for scaling to large, multi-chromophore systems.

5.2.3 Transition Densities

The transition densities are readily available from the solution of TDDDFT matrix equations (using the eigenvectors). Transition density methods calculate electronic couplings based on the Coulomb integral of transition densities of the donor and acceptor molecules,[507,519,523] as shown below:

$$V_{DA}^{TD} = \int\int \rho_D^T(\mathbf{r}) \frac{1}{|\mathbf{r} - \mathbf{r}'|} \rho_A^T(\mathbf{r}') d\mathbf{r} d\mathbf{r}' \tag{5.8}$$

The transition density cube methods[507] are some of the earliest attempts to compute the Coulombic coupling using the transition densities of isolated donor and acceptor molecules, where the transition density is represented on a grid (cube), transforming the Coulomb integration to a sum over grid point values. This approach captures the unscreened Coulomb interaction between the charge distributions associated with the electronic transitions, making it suitable for short- and long-range interactions. Transition density methods are particularly useful for systems where the dipole approximation is insufficient, such as in closely spaced chromophores or when dealing with higher multipole moments.[505,524,525] For typical dyes in RET processes, a value of 125000 grid points is typically used to generate the transition density cube files.

5.2.4 Transition Charges

The cost of computing the coupling from the transition densities can grow significantly with the system's size, as many grid points need to be included in the summation to approximate the coupling integral. Transition charge (TrCh) methods simplify the calculation of electronic couplings by approximating the transition density as a set of discrete charges.[526–528] The change in the electron density in the transition is then represented by point charges located at specific atomic positions, and the coupling is calculated as the electrostatic interaction between these charges,

$$V_{DA}^{TrCh} = \sum_{i,j} \frac{q_D^i q_A^j}{|\mathbf{R}_i - \mathbf{R}_j|} \tag{5.9}$$

where q_D^i and q_A^j are the transition charges of the donor and acceptor, respectively, and $\mathbf{R}_i$ and $\mathbf{R}_j$ are their atomic positions, see Appendix C.1.1 for the Python code. The most commonly used method to compute the transition charges is Mulliken population analysis.[529–533] A more accurate form of the transition charges can be obtained by fitting them to the electrostatic potential obtained from the transition densities(TrEsp).[526,528] The transition charge method provides a computationally efficient way to estimate couplings, particularly for systems where full transition density coupling calculations may be impractical. However, the accuracy of this method depends on the proper assignment of transition charges and their positions[534,535] and may fall short in accuracy at short distances.[536,536]

5.2.5 Transition Dipoles

The transition dipole moment coupling method is based on IPD approximation, where the dipole-dipole interaction between the donor and acceptor molecules accounts for the coupling between them. The coupling between two transition dipoles μ_D and μ_A is given by the Förster resonance energy transfer (FRET) formula:

$$\begin{aligned} V_{DA}^{DD} &= \left(\frac{\mu_D \cdot \mu_A}{R_{DA}^3} - \frac{3(\mu_D \cdot \mathbf{R_{DA}})(\mu_A \cdot \mathbf{R_{DA}})}{R_{DA}^5} \right) \\ V_{DA} &= \frac{1}{4\pi\epsilon_0} \frac{\kappa |\mu_D||\mu_A|}{R_{DA}^3} \end{aligned} \tag{5.10}$$

$$\kappa = \cos\theta_{DA} - 3\cos\theta_D \cos\theta_A \tag{5.11}$$

where $\mathbf{R_{DA}}$ is the vector connecting the donor and acceptor, and κ is the orientation factor between the donor and acceptor's transition dipole moments. θ_{DA} is the angle between μ_D and μ_A, whereas θ_D and θ_A is the angle between transition dipole and the R_{DA}, see Appendix C.1.2 for the Python code. This method is suited well for long-range interactions where the IPD approximation holds. It is widely used due to its simplicity; note that the dipole vector is often approximated based on atomic positions and the availability of experimental dipole moments. It is also the cheapest computational method compared to the transition densities and transition charge methods. At closer distances, the IDP approximation starts to break down, and the accuracy of coupling values starts to decrease.[504–506,508]

5.2.6 Diabatization

Diabatization methods[524,537,538] can be used to compute excitonic couplings in molecular aggregates. These methods involve transforming adiabatic excited states (those computed from electronic structure methods such as TDDFT on supramolecular dimer systems) into diabatic states that resemble non-interacting isolated molecular excitations as closely as possible. The transformation is accomplished using an orthogonal matrix, $\mathbf{C}$, which connects the adiabatic Hamiltonian $\mathbf{H}^{Adia}$ to the diabatic Hamiltonian $\mathbf{H}^{Dia}$:

$$\mathbf{H}^{Dia} = \mathbf{C}\mathbf{H}^{Adia}\mathbf{C}^{\dagger}, \tag{5.12}$$

here, $\mathbf{H}^{Adia}$ is a diagonal matrix with elements corresponding to the adiabatic excited state energies E_1^{Adia} and E_2^{Adia} of the dimer. The off-diagonal elements of $\mathbf{H}^{Dia}$ represent the excitonic coupling V, while the diagonal elements are the diabatic energies E_1^{Dia} and E_2^{Dia}.

The diabatic states $\psi_1^{Dia}, \psi_2^{Dia}$ are constructed to maximize their similarity to the excited states of isolated molecules. This involves solving the orthogonal Procrustes problem[539] to find the best transformation matrix $\mathbf{C}$:

$$\mathbf{C} = \text{argmin}_{\mathbf{R}} \, \|\mathbf{R}\boldsymbol{\mu}^{Adia} - \boldsymbol{\mu}^{\text{ISO}}\|_F \tag{5.13}$$

where $|\cdot\|_F$ denotes the Frobenius norm, $\boldsymbol{\mu}^{Adia}$ are the adiabatic transition dipole moments, and $\boldsymbol{\mu}^{\text{ISO}}$ are the transition dipole moments of the isolated molecules. The

solution to this problem is given by:

$$\mathbf{C} = \mathbf{U}\mathbf{V}^T \tag{5.14}$$

with $\mathbf{U}$ and $\mathbf{V}$ obtained from the singular value decomposition of $\mathbf{M} = \boldsymbol{\mu}^{Adia}(\boldsymbol{\mu}^{\mathrm{ISO}})^T$. Once $\mathbf{C}$ is determined, the excitonic coupling V can be calculated from the off-diagonal elements of $\mathbf{H}^{Dia}$, see Appendix C.1.3 for the Python code. Because full molecular coupling (including polarization, exchange, and correlation) via a dimer calculation is encoded in this diabatization procedure, these coupling values can serve as the ground truth for comparing coupling values computed using other methods.

5.2.7 Environmental Factors

Environmental interactions play a crucial role in controlling the coupling in molecular systems embedded in a condensed phase environment. The environment can directly affect the transition density of each molecule and also act to screen the molecules from each other, thus affecting the strength and nature of the interactions between the transition densities/charges/dipoles of the molecules involved in energy transfer.

Traditionally, Förster theory employs a simple model to account for environmental effects, using a dielectric screening factor derived from the refractive index of the medium. Specifically, the coupling V_{DA}^{Env} in Förster theory is given by:

$$V_{DA}^{Env} \approx \frac{1}{n^2} V_{DA}^{DD}, \tag{5.15}$$

where n is the refractive index of the environment, which is related to the frequency-dependent optical dielectric constant via $\epsilon_{opt} = n^2$. V_{DA}^{DD} is the Coulombic coupling via point dipole-dipole interaction term. This approach assumes a homogeneous and isotropic environment, leading to a constant screening effect of $\sqrt{2}$.[540] While this approximation works reasonably well for simple systems, it often fails to capture the complexity of biological environments where the dielectric properties can vary significantly at different spatial scales and orientations.[519]

Modern approaches incorporate detailed models of the environment to achieve more accurate coupling calculations.[519] One such method is the polarizable continuum

model (PCM),[299,300,302,541] which treats the solvent or surrounding medium as a polarizable dielectric continuum. This model accounts for the induced polarization of the medium in response to the electronic states of the donor and acceptor, providing a more nuanced description of the screening effect.[542] The coupling in the presence of a PCM is given by:

$$V_{PCM}^{TD} = \sum_k \int \rho_D^T(r') \frac{1}{|r' - s_k|} q_{PCM}^A(\rho_A^T(\mathbf{r})) d\mathbf{r} d\mathbf{r}', \tag{5.16}$$

where ρ_D^T is the transition density of the donor, q_{PCM}^A are the surface charges induced on the molecular cavity by the acceptor's transition density, and s_k are points on the cavity surface.

Another technique involves using polarizable molecular mechanics (MMPol) embeddings, where the environment is modeled atomistically with fixed charges and polarizable sites.[543–545] This approach allows for the explicit inclusion of environmental heterogeneity, capturing local variations in dielectric properties and providing a detailed picture of how the environment modulates the electronic coupling. The MMPol method calculates the coupling as follows:

$$V_{MMPol} = -\sum_l \int \rho_D^T(r') \frac{(r - r_l)}{|r - r_l|^3} \mu_{MMPol}^A(\rho_A^T(\mathbf{r})) d\mathbf{r} d\mathbf{r}', \tag{5.17}$$

where μ_{MMPol}^A are the dipoles induced by the acceptor's transition density at polarizable sites r_l.

5.3 Computational Details

Initial results are presented here from sampling chromophore-solvent configurations for the NR-NBD system, where we perform two kinds of MD sampling as described below.

5.3.1 Configuration Sampling

Fixed Chromophores with Solvent Dynamics

We performed a series of fixed-orientation molecular dynamics (MD) simulations to investigate how explicit solvent molecules impact the computed coupling. Figure 5.1 shows the selected orientations for three fixed chromophore MD simulations. In orientation A, the donor NBD is aligned perpendicular to the plane containing the acceptor NR. In orientations B and C, both donor and acceptor molecules are parallel to each other. However, in orientation B, the NH_2 and $N(CH_2CH_3)_2$ groups and the ring oxygen atoms face each other while they are flipped for orientation C. In resonance energy transfer conditions, the energy levels of the excited state of NBD closely match the ground state energy of the NR molecule, making them a perfect donor-acceptor pair. In these simulations, the dyes were individually optimized and then positioned at fixed distances from each other. To set up the initial system, we used Amber's GAFF2 forcefield to optimize the dyes and solvents in an implicit solvent environment. During the MD trajectory, a strong restraint was applied to the coordinates of these dyes to keep them fixed while the solvent was allowed to move freely.

The dyes were positioned in a pre-equilibrated box, so the minimization step was omitted. The system was gradually heated at a rate of 10K per 1000 steps until it reached 300K. Following the heating, we performed a pressure equilibration process until the system reached a density equilibration and an average pressure of 1 atm. The production run was conducted in the NVT ensemble and a Langevin thermostat with a collision frequency of 3 ps^{-1} was used throughout the dynamics to maintain the temperature.

No Restraint Ab initio Molecular Dynamics

We conducted another molecular dynamics simulation in which the donor and acceptor molecules were placed together starting at a distance of 5 Åbut were allowed to move freely. The initial equilibration process was similar to the first approach. However, for the production run, we employed an ab initio molecular dynamics

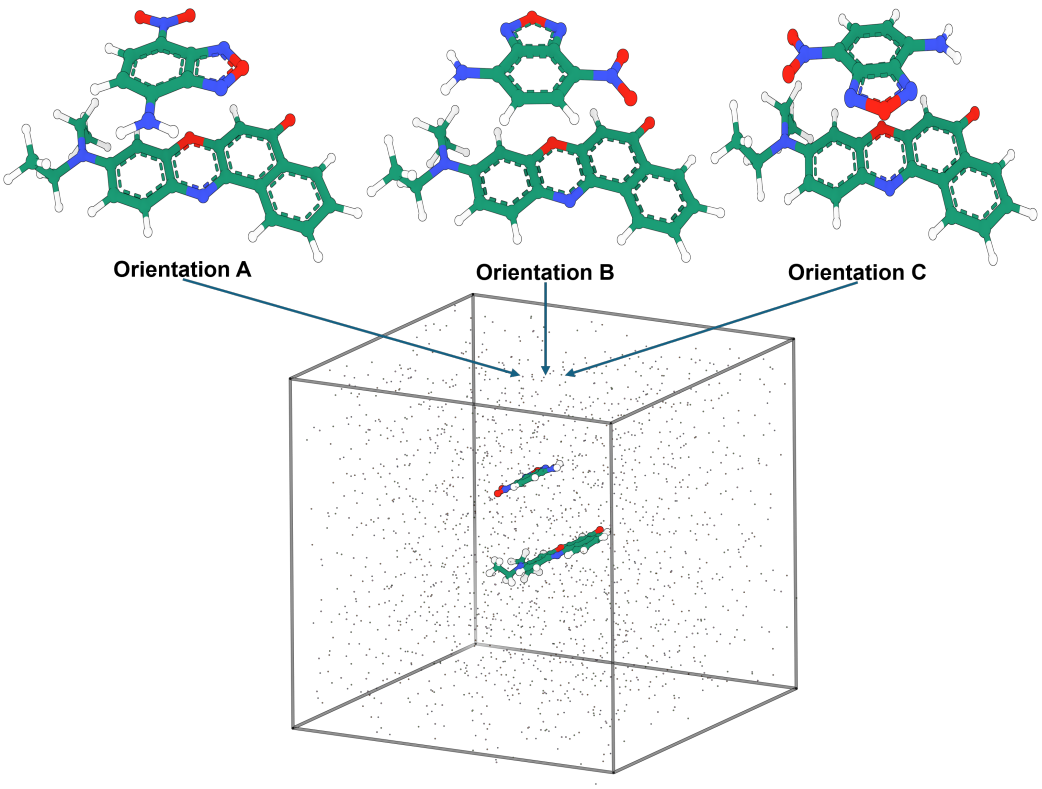

Figure 5.1: Pictorial representation of three fixed orientation dynamic solvent MD simulations

(AIMD) simulation where both donor and acceptor molecules were treated quantum-mechanically using the CAM-B3LYP method and 6-31G(d) basis set. This approach did not account for the dispersion interactions. However, dispersion interactions are one of the key interactions in the NBD-NR dyad. We plan to compare the effect of this crucial interaction with AIMD simulations where the dispersion interactions are included with a standard Grimme D2/D3 approach. The solvent molecules were treated with molecular mechanics via an electrostatic embedding approach. We discarded the first 10 ps of the trajectory to allow the system to equilibrate and then used the remaining trajectory to extract uncorrelated snapshots, separated by 250 fs. These snapshots were used for computing the orientation factor between the donor and acceptor molecule.

5.3.2 Electronic Structure Calculations

For vertical excitation energies, transition densities, transition dipole moments, and transition charges with both Mulliken population analysis and restrained electrostatic potentials (RESP), we used Gaussian16. The Merz-Kollman (MK) and ChelpG schemes were used to compute the transition charges between the ground and the S_1 excited state. To model implicit solvent effects on resonance energy transfer, the integral equation formalism for the polarization continuum model (IEFPCM)[298–302] was used as implemented in Gaussian16.[297]

5.4 Preliminary Results and Discussion

In the next section, we show the value of the orientation factor computed for each snapshot obtained from the no-restrains AIMD simulation. Additionally, we compare the Coulombic coupling values computed using the transition density, charge, and dipole methods. We show results for the NBD-NR system in an implicit and explicit DMSO solvent environment and the CV^+ dimer in a vacuum and implicit water solvent.

5.4.1 Orientation Factor from the AIMD simulation for NBD-NR in DMSO

The orientation factor, if determined incorrectly, could affect the rate of energy transfer by at least a magnitude, especially in systems where the chromophores are embedded in protein cavities and likely have restricted rotations. Both NBD and NR were placed in the same box and allowed to rotate freely during the AIMD. The uncorrelated snapshots were obtained at a time separation of 250 fs. Instead of calculating the transition dipole moments for each snapshot, Atoms N_1 and N_4 in NBD and C_{21} and C_{31} in NR were selected as proxies for the transition dipole moments(see Figure 5.2). This choice was based on the observation that the transition dipole moment is parallel to the vector connecting these atoms when visualized. Figure 5.2 displays the resulting orientation factor throughout the trajectory. We observe that during the first 60 snapshots (corresponding to ∼6.0 ps), the orientation factor increases,

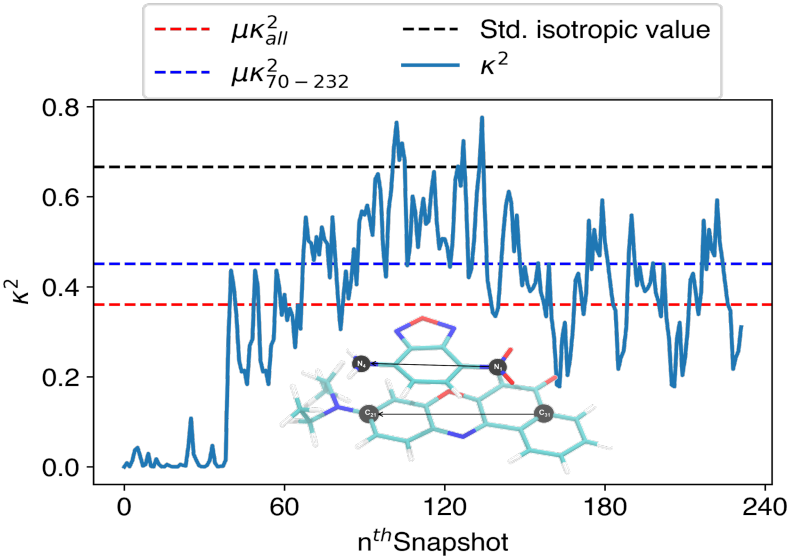

Figure 5.2: Distribution of the orientation factor between NBD and NR in DMSO solvent. The atoms in N_1 and N_2 in NBD and C_{21} and C_{31} in NR are chosen as proxies for the transition dipole moments. The dashed-blacked line represents the standard isotropic value of the orientation factor; the red dashed line represents the average value computed from the snapshots along the entire trajectory; the blue dashed line represents the average value computed after the 70^{th} snapshot.

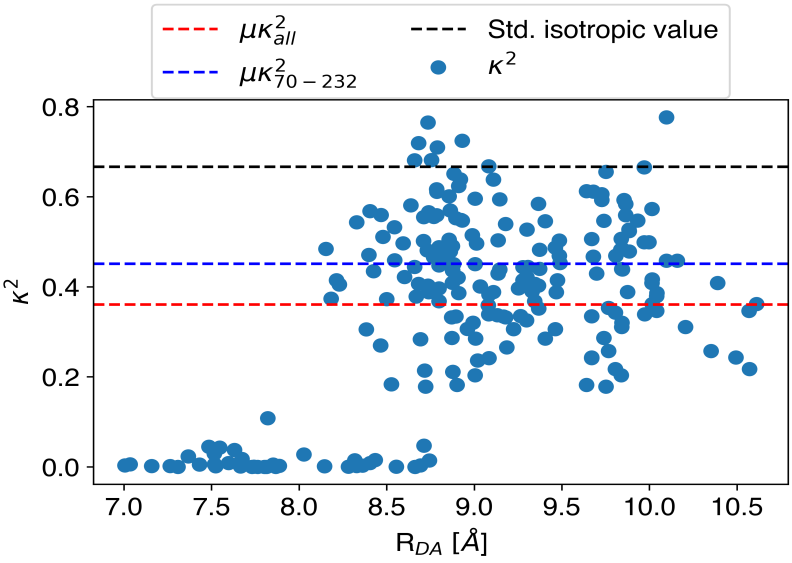

Figure 5.3: Distribution of the orientation factor between NBD and NR in DMSO solvent as a function of distance.

leveling off and oscillating after 70 snapshots. Upon analyzing the trajectory, we see that during the first part of the trajectory, the NR and NBD chromophores drift away from each other, going from ∼7.0 Å to ∼8.0 Å by the 70th snapshot, see Figure 5.3. Computing the average value of the orientation factor for the entire trajectory gives a value of just over 0.36, less than the traditionally assumed value of 2/3. However, if we compute the average value over snapshots 70-230, we obtain a value of 0.45, a bit closer to the 2/3 value. This work shows that if chromophores are at closer distances, their interaction with each other affects their relative orientation, resulting in a value that does not agree with the value obtained in an isotropic limit. Thus, our work shows that the assumption of the 2/3 value may not hold below inter-chromophore distances of ∼8.0 Åand likely breaks down. However, as the dyes start to drift away from each other, we see an increase in the orientation factor value, potentially reaching the isotropic value with sufficient sampling. The distance at which the chromophores no longer interact is likely dependent on the magnitude of their transition dipoles and the ability of the environment to screen them from each other.

Given our analysis here of the orientation factor, it would be interesting to compare our findings to an MD simulation of the same system with dispersion interactions included in the MD Hamiltonian. The orientation factor may also vary with the strength of the solvent interaction, which may be another interesting direction to examine.

5.4.2 Coupling between NBD-NR in DMSO

We next analyze the coupling between NBD and NR in DMSO solvent. Using optimized structures, we use orientation B across various distances from the donor's geometric center to the acceptor's geometric center. Note, for the NBD-NR system, we were unable to calculate the couplings in a vacuum as the first excited state (S_1) of NBD is dark in a vacuum but becomes bright when the chromophore is solvated. We examine both implicit and explicit solvent models of DMSO. The implicit solvent is simulated using the IEFPCM solvent model, whereas our explicit solvent configurations are obtained from our fixed orientation chromophore MD simulations. For the explicit solvent calculations, when computing the excited state properties of one dye

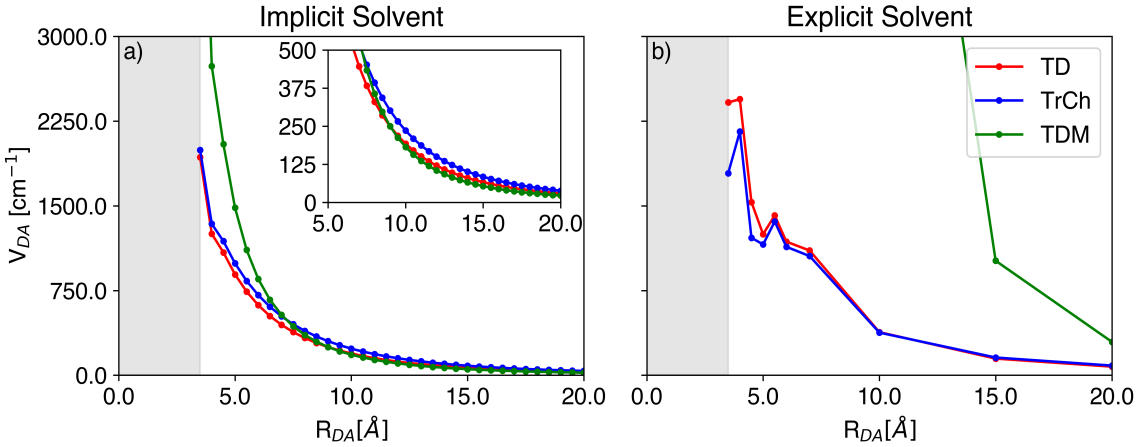

Figure 5.4: Comparison of Coulombic coupling calculated using the transition densities cube, Mullliken transition charges, and transition dipole moment methods for orientation B of NBD-NR in a) implicit and b) explicit QM/MM DMSO solvent.

with QM, the other dye and the solvent molecules are included in the QM calculation as electrostatically embedded fixed MM point charges. Note that only the donor position changes as the distance varies. The transition densities, Mulliken transition charges, and transition dipole moments are computed from the isolated molecules, with either the PCM model or the MM point charge model for the environment. The transition charges are multiplied by a factor of $\sqrt{2}$ so that the transition dipole can be reproduced and a proper comparison between the coupling values can be made.

In Figure 5.4 a), we show the computed coupling values for NBD-NR in DMSO implicit solvent using three different methods for the Coulombic coupling. As the distance exceeds 10 Å, the coupling rapidly decreases, and all three methods predict similar coupling values approaching zero. We observe that the ideal point dipole approximation breaks down at distances closer than 7 Å. At these shorter distances, coupling values obtained from the transition dipole moments are significantly overestimated compared to those from more accurate transition density cube and transition charge methods.

The strong agreement between the transition charge method and the transition density cube method indicates that the atomic charge representation of transition den-

sities produces similar results as if they were derived from the transition densities themselves. This agreement remains even at the closest distance of 3.3 Å. With this good agreement and the lower computational cost of evaluating the coupling compared to using transition densities, these transition charges present a promising way forward.

Next, we compare the Coulombic coupling values computed in the explicit point charge solvent environment for MD snapshots for NR-NBD in orientation B at different distances for the geometric center between the dyes, see Figure 5.4 b). For these initial results, the coupling values are computed from the last snapshot obtained from the MD simulations for a given distance (future work will sample over multiple snapshots to ascertain the range of values obtained across different solvent configurations). We computed the excited state properties of each dye by employing a QM/MM model, where the excited state properties of one dye are treated with QM and we consider the other dye and the solvent as fixed MM point charges. Unlike the implicit solvent coupling, here we only compute the coupling for a few distances because each data point is a separate MD simulation, making it a relatively expensive calculation. However, these data points are varied enough to provide the effect of distance on the coupling values for dyes embedded in the point charge environment.

Figure 5.4 b) compares the coupling values computed using the same three Coulomb interaction methods. We once again observe a closer match between the coupling values calculated using the transition density cube and transition charge methods. Comparing the coupling values to those obtained in an implicit solvent, it's evident that the implicit solvent coupling values are much smaller than the values computed with the explicit solvent environment with point charges. This large difference could be attributed to the presence of mutual polarization in the PCM models but missing in an electrostatic embedding environment.

We find that the coupling values calculated using the QM/MM transition dipole moments are significantly overestimated even up to a distance of 15 Å in the explicit point charge environment. At distances smaller than 15 Å, the values are excessively

large, on the order of 10^6 cm^{-1}, and consequently, they are not displayed alongside the smaller coupling values predicted using transition densities and transition charges. The very large discrepancy between the transition dipole and transition charge/density methods suggests that the dipole representation is no longer accurate within the point charge environment and that higher-order moments must be considered to compute a reasonable coupling.

Analyzing the couplings for the transition charge and density methods, we see that the decrease in the coupling values is not as smooth as a function of distance as was observed in the implicit solvent. Upon investigation of the positions of solvent molecules around the chromophore, we attribute the lack of decrease to the absence of solvent between the NBD and NR molecules. The DMSO solvent is relatively bulky, and throughout the simulation, where NBD and NR are fixed at 7.0 Å , we do not observe any DMSO molecules between them. Due to the missing interaction from neighboring dye and DMSO solvent, the molecules are partly solvated and partly exposed to the vacuum. This issue leads to a change in the oscillator strength, transition dipole moments, and transition charges of both dyes and is the likely reason why the decrease in the coupling values is not smooth. We plan to investigate this issue with the solvent molecule geometries to resolve this discrepancy in the expected coupling behavior.

Another issue we potentially face when two chromophores are in the vicinity of each other is charge transfer and polarization-induced state mixing/swapping. Figure 5.5 a) and b) track the oscillator strength of NBD and NR in the QM/MM point charge environment as a function of distance, respectively. Additionally, Table 5.1 tracks the changes in oscillator strength and vertical excitation energies of both molecules in comparison to the values of the isolated molecules in an implicit DMSO solvent. For NR, the S_1 state is the bright state of interest for distances up to 8 Å and after 8 Å, thus it can be used for calculating the properties of the excited state. However, at 8Å, the bright state swaps to S_2. We also see that there is substantial state swapping for NBD. Although S_1 remains an allowed transition, other states either become equally bright through intensity borrowing or have more oscillator strength

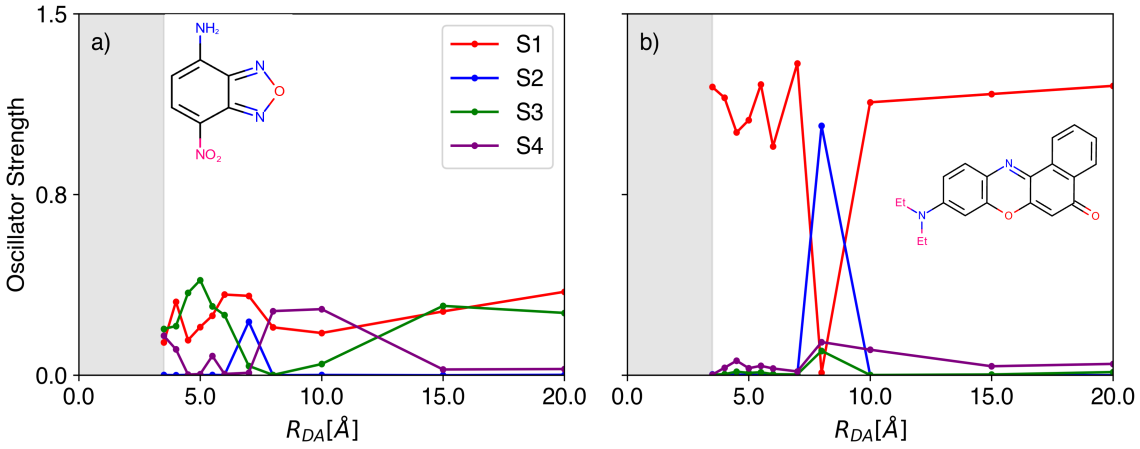

Figure 5.5: Oscillator strength of the first four excited states of a) NBD and b) NR as a function of distance in MM point charge environment

than S_1. Thus, the default procedure of choosing the lowest energy excited state can be quite problematic with state swapping, motivating the development of a more rigorous approach to choosing the bright state of interest, which we are planning to explore in the near future.

5.4.3 Coupling between CV+ dimer

Author Contribution: The results of the Coulombic coupling for the CV+ dimer were obtained by Sayan Adhikari, who is a contributor to the current project. I am utilizing these findings to showcase the effectiveness of various coupling methods for a charged system and to compare their relative performance.

Similar to our analysis of the Coulombic couplings of NR-NBD, we next analyze the couplings for the CV+ dimer at various distances using the same level of theory, where the total system has a charge of +2. Unlike NBD, CV+ retains its bright state in both vacuum and solution, allowing a comparison of the method in both vacuum and implicit solvent environments.

Figure 5.6 shows the comparison between Coulombic coupling values for CV+ dimer in a stacked configuration (shown in the plot inset) in vacuum and implicit water sol-

Table 5.1: The trend of oscillator strength and vertical excitation energies of NBD and NR as a function of distance in a QM/MM point charge environment

Distance RDA [A]	**NBD Osc. Str**	**NBD Ex. Energy [eV]**	**NR Osc. Str**	**NR Ex. Energy [eV]**
3.5	0.1366	3.0560	1.1962	2.9864
4.0	0.3048	3.3834	1.1521	2.9870
4.5	0.1458	2.9226	1.0077	3.1398
5.0	0.2002	3.2957	1.0588	3.0567
7.0	0.3294	3.3542	1.2940	2.8519
8.0	0.1988	3.3656	0.0102	2.9839
10.0	0.1752	3.0395	1.1326	2.8455
15.0	0.2648	3.2237	1.1669	3.0059
20.0	0.3463	3.3233	1.2009	2.8858

vent. A quick comparison between coupling values from the transition dipole moments in both vacuum and implicit shows that at distances less than 10 Å, the coupling values are overestimated more so in the implicit solvent as compared to the transition density cube and transition charges methods. This observation shows that the IDP approximations breakdown at those distances, leading to unphysically large coupling values.

When comparing coupling values obtained from the transition density cube and transition charge-based methods, we observe that the coupling values are slightly lower in vacuum compared to implicit solvent, indicating that the polarization provided by the solvent environment increases the coupling. For both environments, we see that for distances less than 10 Å, the coupling values are slightly different for the two methods, with the transition charge method predicting slightly higher values than the transition density cube method. This contrasts with the trend observed for the NBD-NR system in DMSO, where there was very good agreement for the transition charge and transition density cube method. We hypothesize that the reason for the poor agreement is the quality of transition charges for a charged system.

Charges obtained by fitting them to the electrostatic potentials (ESP) through ac-

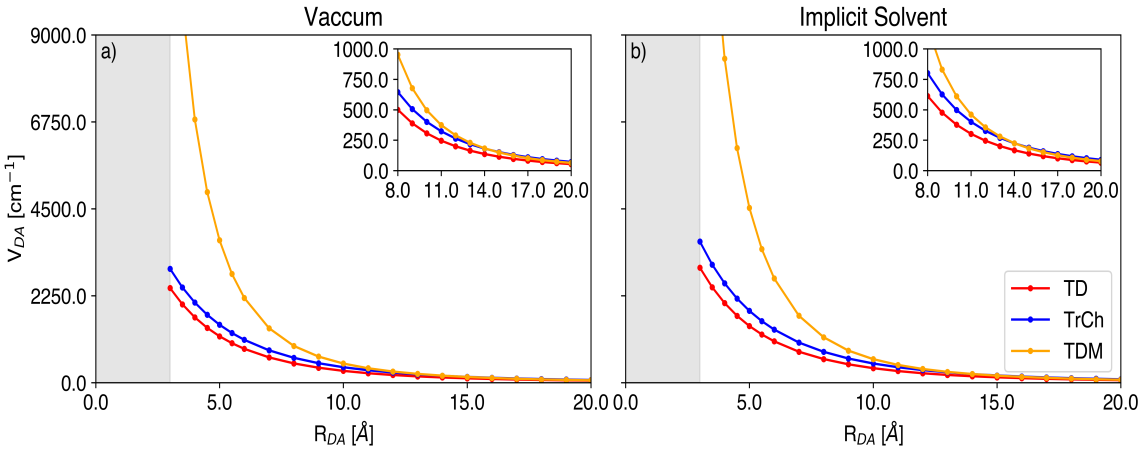

Figure 5.6: Comparison of Coulombic coupling calculated using the transition densities cube, Mulliken transition charges, and transition dipole moment methods for a parallel orientation CV+ dimer in a) vacuum and b) implicit water solvent.

curate Merz-Kollman and ChelpG schemes provide an avenue for improving charge accuracy. These schemes are commonly used for force field parameterization. Currently, these schemes are not implemented in standard codes for use with charged systems. We plan to address this limitation by fitting the charges on the ESP while ensuring the total transition charge is zero and we are currently working on developing this computational procedure.

Based on the analysis of the two systems in this chapter, we found similar performance of the transition density cube and transition charge-based methods. For NBD-NR, the transition charge-based method offers reduced computational cost without significantly sacrificing accuracy. The coupling values computed using the transition dipoles for both systems are significantly overestimated at closer distances, leading to the breakdown of the IPD approximation. Future work where we account for solvent screening may improve the IPD approximation.

5.5 Next Steps

In the upcoming analysis, we intend to incorporate the coupling values obtained from the diabatization approach and compare them with the results obtained from

implicit and explicit solvent simulations.

Furthermore, we will expand our calculations of the coupling values for the CV+ dimer system to explicit solvent conditions. For the NBD-NR system, we will also determine the coupling values in acetonitrile and chloroform solvents to examine the influence of different solvents on the coupling values and extend our analysis to A and C chromophore orientations. Finally, we plan to calculate the coupling values from restraint-free AIMD simulations, averaging over multiple configurations, and compare the relative accuracy of these methods with each other and with supramolecular methods.

5.6 Conclusion

The results presented in this chapter pertain to the NBD-NR and CV+ dimer systems. We examined the influence of local configuration on the orientation factor. While the average orientation factor closely resembles the isotropic value for larger NBD-NR distances, our analysis emphasizes the impact of the local environment and relative chromophore distance on the energy transfer between these molecules.

We also investigated the impact of implicit solvent and point charge explicit solvent models on the Coulombic coupling values derived from various methods. In comparison to the explicit solvent, the implicit solvent predicts lower Coulombic coupling values, albeit at distances greater than 10 Å, where the values align. For NR-NBD, Coulombic coupling values computed using the Mulliken transition charges closely match those computed using computationally expensive transition density cube methods in both explicit and implicit solvents at a fraction of the computational cost. However, at shorter distances of less than 5 Å, the coupling values from the TDC and TrCh methods begin to diverge, as the localized atomic charge point misses the interaction from the three-dimensional transition densities at close distances.

Additionally, the Coulombic coupling values computed using the transition dipole moments of the molecules exhibit significant exaggeration, particularly when com-

puted in an explicit MM solvent environment. Beyond 10 Å, the Coulombic coupling calculated from the transition dipole begins to follow the trends observed in the TrCh and TDC methods. At distances exceeding 10 Å, the point dipole approximation becomes valid, and the transition dipoles yield results similar to those obtained from the transition charges or transition densities.

5.7 Future Outlook

This project is still ongoing, and we anticipate more results in the near future. We are committed to getting this project to publication.

Chapter 6

Uncharted Frontier for Relative Binding Free Energy Using Hybrid QM/MM Methods

This chapter explores the application of hybrid QM/MM methods for predicting ligand binding affinities to Brutons Tyrosine Kinase (BTK). It investigates various computational approaches and compares their effectiveness against experimentally determined inhibition constants (Ki). The study assesses three QM/MM regions with varying extents of quantum mechanical treatment and finds that including a more significant portion of the protein environment in QM calculations significantly improves prediction accuracy. The chapter concludes that hybrid QM/MM methods hold great potential for predicting ligand binding affinities. Still, careful consideration of QM/MM boundaries and the inclusion of a substantial region of the protein environment are crucial for achieving accurate and reliable results. The insights gained from this study provide a foundation for future work, emphasizing the need for comprehensive models that account for the complex interactions within the protein-ligand binding site.

6.1 Introduction

Bruton's Tyrosine Kinase (BTK) is a crucial enzyme in the immune system's signaling routes, playing a vital role in the growth and functioning of B-cells.[546,547] It belongs to the Tec family of non-receptor tyrosine kinases and is required for B-cell receptor (BCR) signaling, impacting various aspects of B-cell growth, differentiation,

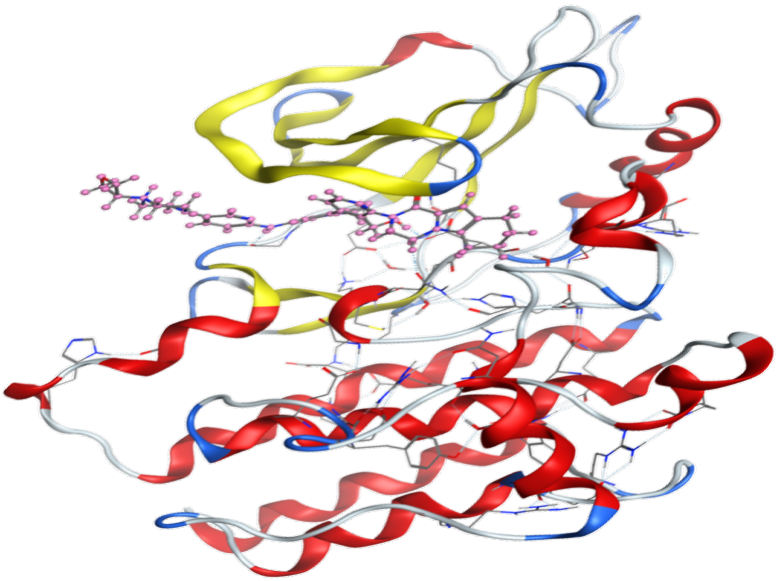

Figure 6.1: Bruton's tyrosine kinase (BTK) with GDC-0853

and response.[548–550] Irregularities in BTK signaling can lead to immune deficiencies or contribute to the development of autoimmune diseases and cancers. BTK malfunction is closely connected to several hematologic malignancies, including Chronic Lymphocytic Leukemia (CLL)[551,552] and Mantle Cell Lymphoma (MCL).[553,554] Overactivity or unregulated activity of BTK can contribute to the survival and multiplication of malignant B cells, making it a focus of interest in targeted therapies for immune disorders and malignancies.

Over the years, several BTK inhibitors have been developed, offering new therapeutic options.[555–562] Ibrutinib, a first-generation inhibitor, has shown efficacy against various B-cell malignancies.[555,563] Following this, more selective and potent inhibitors like Acalabrutinib[564] and Zanubrutinib[565] have been developed, aiming for better efficacy and fewer side effects.

It is important to understand the thermodynamic characteristics of how a drug binds to its molecular target in order to develop new treatments. This process aims to deter-

mine the way the drug binds and to calculate the energy involved in the binding. Experimental techniques, such as measuring dissociation constant, inhibition constant, EC50, IC50, Ki, and kinetic rate, can provide this information, but they are often time-consuming and expensive. Computational methods offer a valuable alternative for calculating binding free energies, providing a less labor-intensive option compared to traditional experimental approaches. These methods vary in computational cost and complexity and include single-structure approaches, endpoint methods, and alchemical transformation methods.[566–568]

The single structure approach, which incorporates quantum mechanics (QM) calculations, is one of the simplest methods.[569–572] This approach uses single structures obtained from crystal structures, docking, or geometry optimization.[573] Although approximate, it is computationally efficient and does not require extensive conformational sampling. Endpoint methods, such as MM/PBSA and MM/GBSA,[574–576] perform conformational sampling of the protein-ligand complex, the isolated protein, and the ligand, potentially leading to improved free energy estimations compared to single-structure approaches.

Typically, single structure and endpoint methods serve as initial filtration stages to discard less potent compounds. Once a subset of lead compounds is identified, more computationally expensive methods can be employed. Alchemical methods, like Free Energy Perturbation (FEP)[577,578] and Thermodynamic Integration (TI),[579–581] offer more accurate relative free energy calculations by morphing two similar compounds through multiple intermediate steps. These methods reduce the entropic cost of calculating binding energies, leveraging the state-function nature of free energy to choose efficient intermediate steps. The free energy from these two methods can be obtained as:

$$\begin{aligned} \Delta G_{BA}^{FEP} &= G_B - G_A = -k_B T ln \frac{\iint e^{-H_B/K_B T}}{\iint e^{-H_A/K_B T}} \\ \Delta G_{BA}^{TI} &= \int_0^1 \frac{dG(\lambda)}{d\lambda} \end{aligned} \tag{6.1}$$

When using single-structure methods to calculate binding free energies, the accuracy

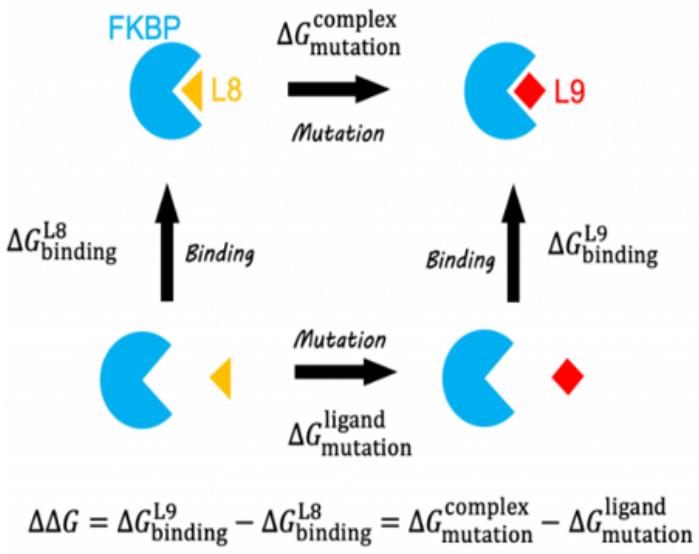

Figure 6.2: Pictorial representation on how to calculate relative binding free energies. The image is adapted from Relative protein-ligand binding free energy Website

can be compromised due to the lack of consideration for conformational sampling.[571] These methods rely on the choice of theory, either molecular mechanics (MM) or quantum mechanics (QM), to compute relative energy terms. One way to improve accuracy is to use hybrid QM/MM methods.[375,582] These methods are considered reliable for accurately modeling and studying complex system.[583] They are effective for studying ligand binding,[584–586] structural mechanisms,[587] reaction mechanisms,[588,589] and spectroscopic properties.[147,590,591]

In this study, we use a hybrid QM/MM-based single-structure method to compute the ligand binding free energy of BTK inhibitors. These computational results are then compared with experimentally determined inhibition constants (Ki) from a recent study by Crawford et al. at Genentech on GDC-0853 inhibitors.[592] GDC-0853, a promising non-covalent BTK inhibitor, is highlighted for its specificity and favorable pharmacokinetic properties in treating oncological and autoimmune diseases.

6.2 Theoretical Details

The ligand-binding free energy is the difference between the bound and unbound protein-ligand complex and can be computed using the equation 6.2. If the relative geometrical difference (number of rotatable bonds, for example) between ligands is minimal, generally, the entropic term, ΔS in the equation 6.4, is assumed to be zero. This assumption allows us to calculate the relative free energy, which is the free energy difference between the free energy of two ligands bound to the same protein, as seen in the pictorial representation 6.2.

$$\Delta G = \Delta H - T\Delta S \tag{6.2}$$

if $\Delta S = 0$, equation 6.2 reduces to:

$$\Delta G = \Delta H = \Delta E \tag{6.3}$$

$$ddG = dG_{LigA} - dG_{LigB} \tag{6.4}$$

Since our computation of relative free energies is from a single structure QM/MM procedure, we will be computing free energies as a sum of strain, interaction, and solvation energies as shown in equation 6.5,

$$ddG = ddG_{solv} + ddG_{strain} + ddG_{int} \tag{6.5}$$

where ddG_{solv}, ddG_{strain}, and ddG_{int} are the relative solvation energy, ligand strain energy, and protein-ligand interaction energy, respectively. We can obtain the values of these energies using equation 6.6, 6.7, and 6.8, respectively.

$$ddG_{solv} = ddG^{gas}_{Lig_{opt}} - ddG^{solvent}_{Lig_{opt}} \tag{6.6}$$

$$ddG_{strain} = ddG^{complex}_{Lig_{opt}} - ddG^{gas}_{Lig} \tag{6.7}$$

$$ddG_{int} = ddG^{complex}_{Lig_{opt}} - ddG^{solvent}_{Lig_{opt}} \tag{6.8}$$

where, $ddG^{gas}_{Lig_{opt}}$ is the energy of the locally optimized ligand in vacuum, $ddG^{solvent}_{Lig_{opt}}$ is the energy of the optimized ligand in solvent phase, and $ddG^{complex}_{Lig_{opt}}$ is the energy of the optimized docked ligand bound to the protein.

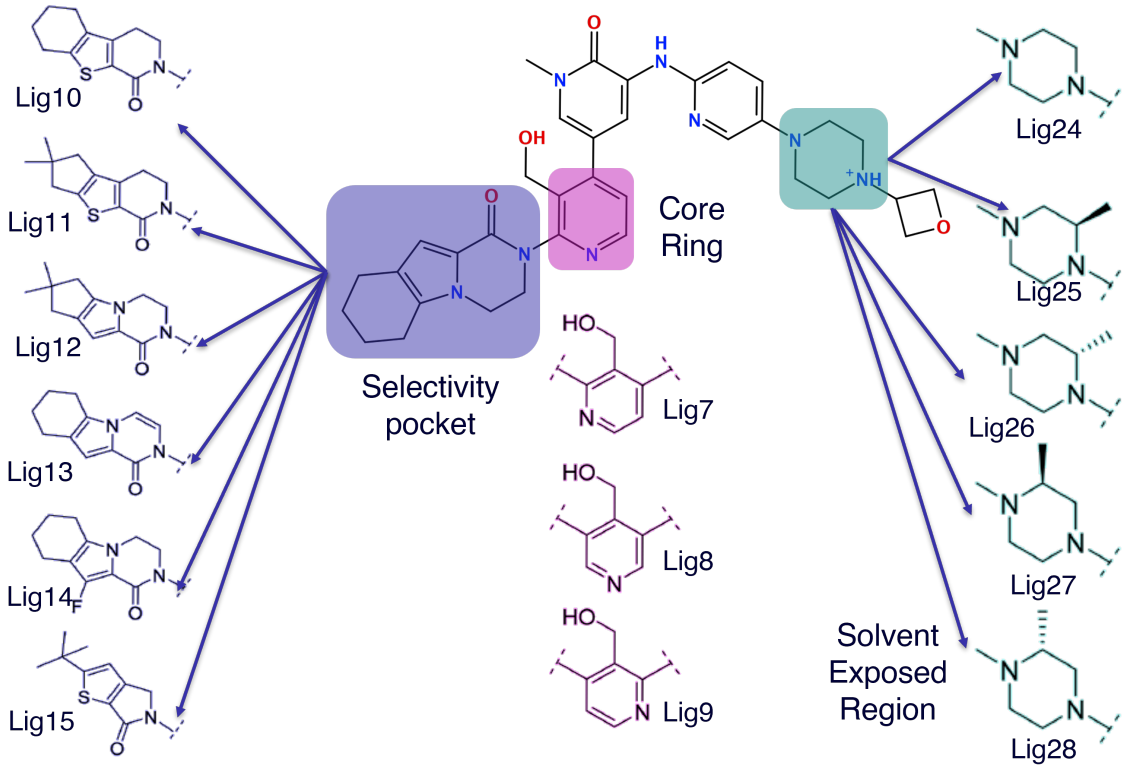

Figure 6.3: BTK inhibitors selected for computing the ligand binding relative free energy calculations

6.3 Computational Details

6.3.1 PDB Structure preparation and Docking

The X-ray crystal structure of the BTK protein with PDB-id: 5VFI bound to ligand GDC-0853 was obtained from the RCSB protein data bank. The protein structure is shown in Figure 6.1. The initial cleaning and preparation of the protein structure were carried out using the Molecular Operating Environment (MOE) structure preparation tool.[593] To conduct relative ligand binding free energy calculations, we selected 14 ligands from the 34 potent ligands listed in the study by Crawford et al.[592] These chosen ligands were modified to adjust nonbonded interactions in the protein pocket, enhance hydrogen bonding between the core ring and protein residues, and have stereochemical influence from modifying the solvent-exposed region, see Figure 6.3.

The ligands were modeled into the protein cavity using MOE. Each ligand was modified manually, and then the geometry was relaxed using the MMFF94 forcefield[594] with generalized Born solvation model.[595]

6.3.2 MD Simulations with OpenMM

Molecular dynamics (MD) simulations were performed to study the interactions between BTK protein (PDB ID: 5VFI) and its potent, selective, and noncovalent inhibitors. The simulations were carried out using the OpenMM molecular simulation toolkit,[596] leveraging GPU acceleration for enhanced computational efficiency. The initial protein-ligand complex was prepared based on the crystal structure of BTK bound to GDC-0853 (PDB ID: 5VFI). The AMBER force field. ff14sb,[597] was employed for the protein, while the GAFF[363] force field was used for ligands. The system was solvated using the TIP3P water model[598] with a cubic box of dimensions 7 X 8 X 7 nm. Counter-ions were added to neutralize the system, and physiological salt concentration was maintained.

The MD simulation protocol consisted of several stages: energy minimization, heating, equilibration, and production. All simulations used periodic boundary conditions with a non-bonded cutoff of 10.0 A. The Particle Mesh Ewald (PME)[599] method was employed to treat long-range electrostatic interactions, with an error tolerance of 0.0005. Hydrogen bonds were constrained using the SHAKE algorithm,[600] allowing for a time step of 1 femtosecond throughout the simulation. The system underwent energy minimization for up to 10,000 steps or until the root-mean-square deviation (RMSD) of energy converged to 10^{-3}. This step was crucial to remove any unfavorable contacts and to relax the system to a lower energy state.

Following minimization, the system was gradually heated from 5 K to 300 K over a period of 60 picoseconds in the NVT ensemble. This slow heating process, divided into 60 steps with temperature increments of 5 K each, allowed for proper system equilibration to the rising temperature. A Langevin thermostat with a default friction coefficient of $2.0ps^{-1}$ was used to control the temperature. After heating, the

system was equilibrated at constant pressure (1 bar) and temperature (300 K) in the NPT ensemble for 100 ps. The pressure was regulated using a Monte Carlo barostat. This step allowed the system to adjust its volume and reach the appropriate density under physiological conditions. The production MD simulation was conducted in the NVT ensemble at 300 K for a total of 1 nanosecond. The simulation employed the same Langevin thermostat[601] as in the heating phase. Trajectory data was saved every 1 ps, resulting in 1000 frames for subsequent analysis.

Throughout the simulation, various properties were monitored and recorded, such as Energy components (total, potential, and kinetic energy), temperature, and pressure. These data were collected at intervals of 1 picosecond and saved in CSV format for further analysis. The simulations were performed using CUDA-enabled GPUs to accelerate computations. The CUDA precision was set to mixed precision to balance accuracy and performance. Checkpoint files were saved at regular intervals to ensure the continuity of simulations and safeguard against potential hardware failures. These files contain all the necessary information to restart the simulation from the last saved point if needed.

6.3.3 QM/MM Optimization and Energy Calculations with OpenMM-Terachem

After completing the MD simulations, we obtain a final snapshot of the equilibrated system. This snapshot is then used to calculate relative free energies, solvation energies, and strain energies. To energy and optimize the geometry, we used the OpenMM-TeraChem[296] interface. We employed density functional theory with the ωPBE functional[602,602,603] and a 6-31G(d) basis set with dispersion correction. ωPBE DFT functional was chosen to mitigate the charge transfer problems present in the traditional DFT. For the solvent effect, we used the COSMO[604,605] implicit water model as implemented in TeraChem and obtained the solvation energies as described in equation 6.6.

To carry out a systematic analysis of the impact of the protein region on the free

energies, we divided the protein and ligand region into three categories; a pictorial representation of the selection process is shown in Figure 6.4. The regions were carved out in a way that avoids disrupting conjugation between atoms. The single bonds that were then chopped after carving the region of interest were capped using the hydrogen atoms.:

1. Region-1: In this selection, we only treat the ligand with quantum mechanics, and the remainder of the system is treated as a point charge environment. The point charges for the protein and water molecules are derived from the ff19sb Amber force field and TIP3P water model.

2. Region-2: In this selection, the ligand, the protein residues, and water molecules making the hydrogen bond with the ligand are treated quantum mechanically, and the remainder of the system is still a point-charge environment.

3. Region-3: In this selection, we go a little further and include around 10A of the surrounding environment; however, geometry optimization is done with the MMFF94 force field, and energies are computed using QM. However, no other region of the protein was added.

6.4 Preliminary Results and Discussion

In this section, we will discuss some preliminary free energy results from all four regions and compare them with the associated inhibitory constant, K_i. We will examine how the environment around the ligands affects their potency and, in the end, will provide some recommendations and conclusions.

6.4.1 Impact of QM Region on Free Energies

Region 1: QM Ligand and Point Charge Environment

In region-1, see Figure 6.5; our goal was to evaluate the effectiveness of 14 different ligands in binding to BTK by calculating their relative binding free energies (RBFEs) using a hybrid QM/MM approach. This analysis focused on the first region, where

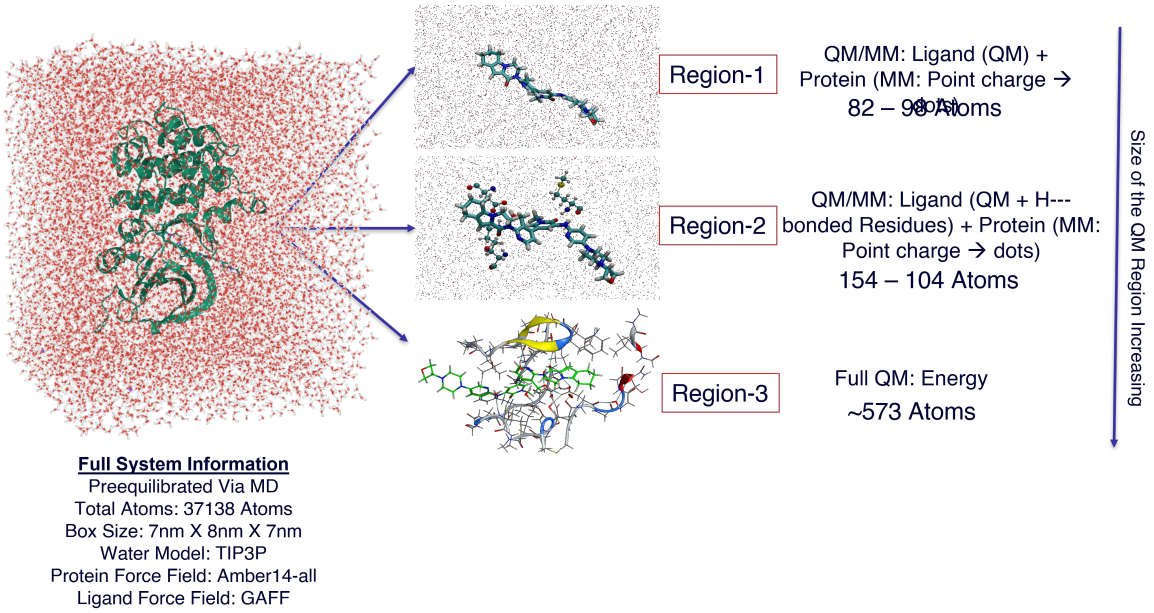

Figure 6.4: Pictorial representation of the selection process for choosing the protein-ligand environment region for calculating relative binding free energy. Each region represents a part of the system treated with QM (quantum mechanics) and MM (molecular mechanics). The size and complexity of the selected region increase as we move from region 1 to region 2.

only the ligand was treated quantum mechanically (QM), and the rest of the system was represented by a point charge environment. We compared these RBFEs with experimentally determined inhibitory constants (Log Ki) to assess whether computational methods can effectively screen for ligand binding affinity. We obtained a final equilibrated snapshot for each ligand from the all-atom MD simulation. We optimized the geometry using the Terachem-OpenMM interface with the wPBE density functional theory (DFT) functional, 6-31G(d) basis set, and Grimme's D3 dispersion correction. We also computed solvation, interaction, and strain energies using the same level of theory.

Figure 6.6 shows the R^2 value of 0.245 indicates no correlation between the com-

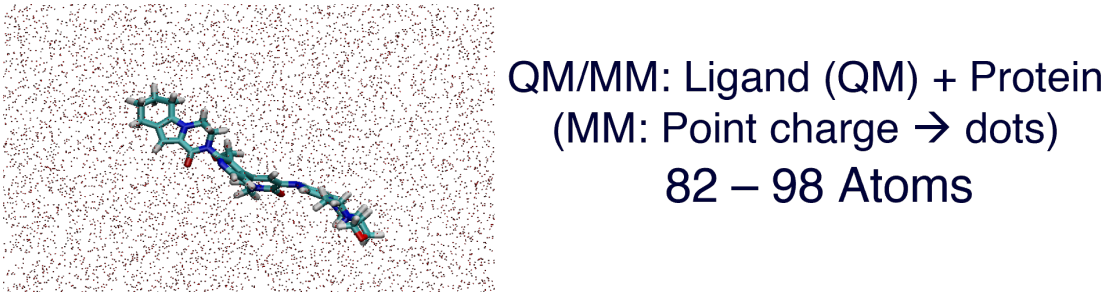

Figure 6.5: Region-1: Only the ligand is treated using quantum mechanics, while the rest of the system is treated as a point-charge environment.

putationally derived RBFEs and the experimentally determined Log Ki values. This suggests that the current QM treatment of the ligand within a point charge environment is not adequate for accurately predicting ligand binding affinities. The wide scatter of data points, significant deviations from the regression line, and the low R value highlight that predicting ligand binding affinities is more complex than what this simplistic model can capture. The model does not account for these complexities, resulting in poor predictive performance. This suggests that the current model oversimplifies the system by treating the protein and surrounding water as mere point charges. Such electrostatic interactions alone cannot sufficiently represent the complexity of the binding environment, leading to inaccurate predictions. It implies that more comprehensive models that include significant portions of the protein and explicit solvent interactions are required for better prediction accuracy.

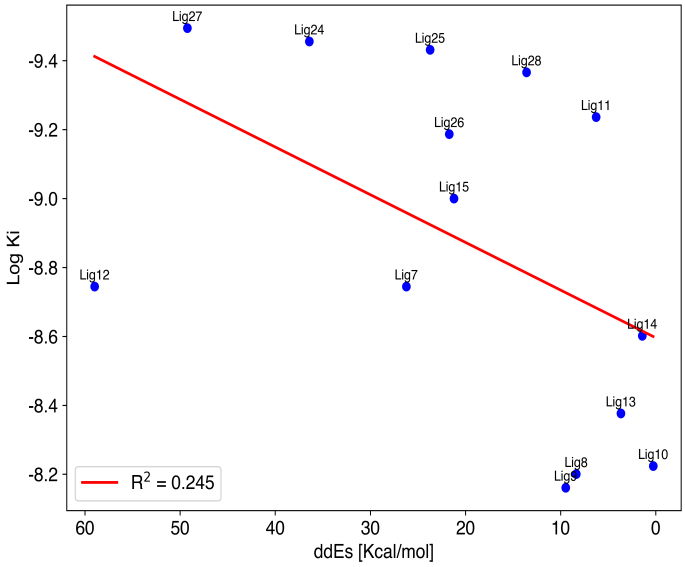

Figure 6.6: Region 1: Correlation of inhibitory activity with ligand binding free energies when only the chromophore is treated quantum mechanically and the remainder of the system is treated like a point charge environment

Region 2: QM Ligand plus hydrogen-bonded residues with Point Charge Environment

Figure 6.7 shows the second region, the ligand, protein residues, and water molecules that form hydrogen bonds with the ligand are treated quantum mechanically (QM), while the rest of the system is in a point-charge environment. The same level of theory was used as in Region 1.

The R^2 value of 0.0376, as shown the Figure 6.8 indicates an even weaker correlation

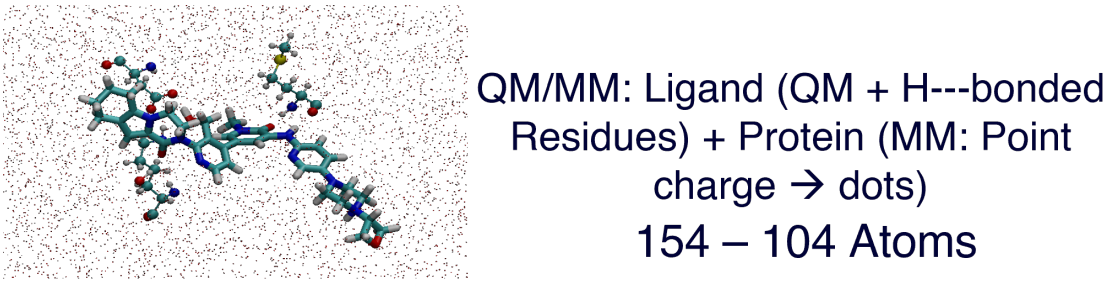

Figure 6.7: Region-2: The ligand and hydrogen-bonded residues are treated using quantum mechanics, the remaining system as point-charge environment.

between the computationally derived RBFEs and experimentally determined Log Ki

values compared to Region 1. This suggests that even with the inclusion of hydrogen-bonding interactions, the model does not significantly improve predictive accuracy. Despite including hydrogen-bonded residues and water molecules in the QM region, the predictive capability did not improve significantly. Hydrophobic and Van der Waals interactions likely play a more significant role in binding affinity, as the inner pocket of the protein only stabilizes the ligand via pi-pi stacking and non-bonded interactions. The current model's simplicity fails to encapsulate the diverse range of interactions influencing ligand binding. A more comprehensive approach considering additional protein regions and explicit solvent interactions is necessary.

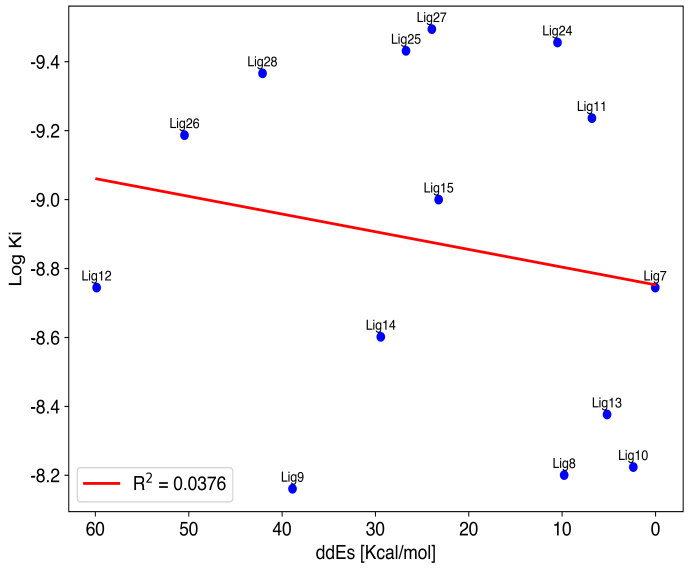

Figure 6.8: Region 2: Correlation of inhibitory activity with ligand binding free energies when the chromophore and the hydrogen bonding protein residues are treated quantum mechanically and the remaining system is treated like a point charge environment

Region 3: QM Ligand plus residues within 10A and salt bridges with Point Charge Environment

The final part of our study on BTK binding affinities includes a larger QM region, encompassing approximately 10 of the surrounding environment without including any other region of the protein environment, see Figure 6.9. However, we use the MMFF94 force field for geometry optimization and compute energies using the

wPBE/6-31G(d)/DE level of theory.

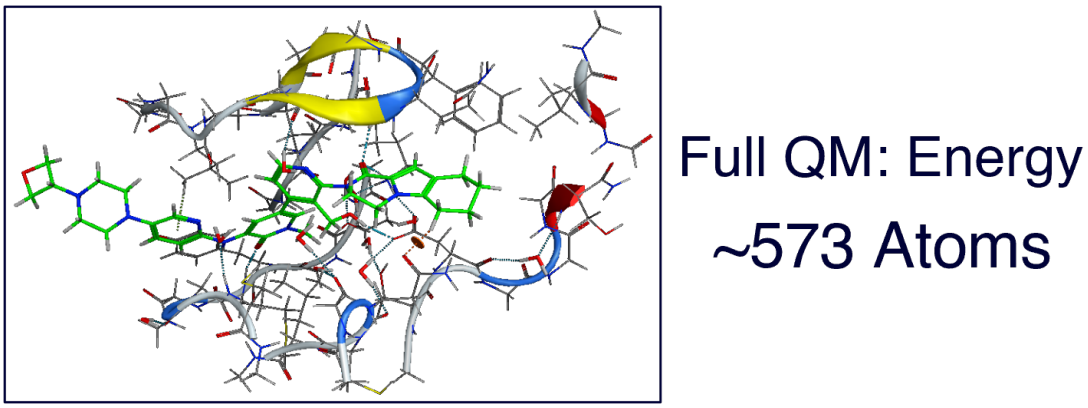

Figure 6.9: Region-3: An area of 10A region within the geometric center of the ligand is treated quantum mechanically for relative binding free energy calculations, and the rest of the system was discarded

The R^2 value of 0.669 significantly improves the correlation between the computationally derived RBFEs and experimentally determined Log Ki values compared to the previous regions. This indicates that including a larger QM region and choosing a specific geometry optimization method have positively impacted the accuracy of the model. Generally, RBFEs are highly sensitive to the positions of the coordinates and their local minima. Without proper QM optimization, the results are prone to inaccuracies due to the static nature of a single snapshot. Using a single snapshot fails to account for conformational flexibility and dynamic interactions. Implementing conformational sampling and averaging over multiple configurations would likely yield more reliable and convergent RBFEs.

Conducting QM energy evaluations on the x-ray crystal structure without QM optimization has demonstrated a more straightforward yet effective approach. However, the success of the method also highlights the importance of selecting an appropriate QM region. This selection of the QM region can serve as a benchmark for accurate RBFE calculations.

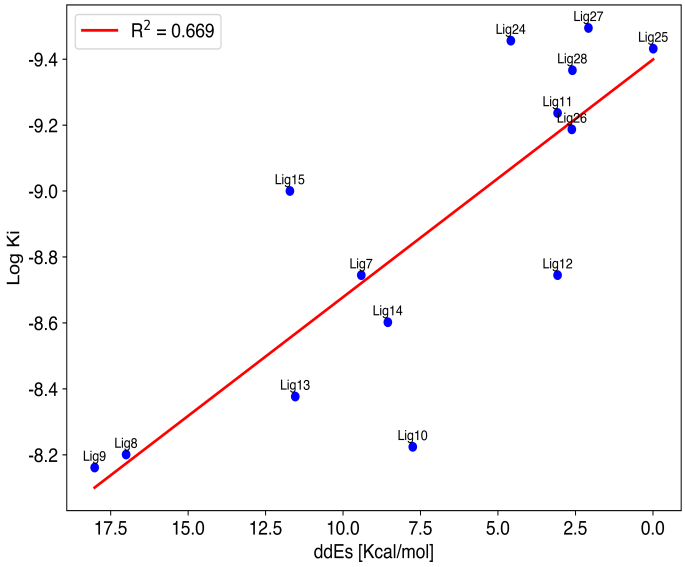

Figure 6.10: Region 3: Correlation of inhibitory activity with ligand binding free energies when the chromophore and about 10 Angstrom of protein regions are treated quantum mechanically and the remaining system is treated like a point charge environment

Affinity Ranking

Using the results obtained from Region 3, we generated an affinity ranking plot, see Figure 6.11, showing the contributions of different energy terms to the total free energy (ddE) for each ligand. The plot helps identify which interactions significantly influence the relative binding free energies (RBFEs) and provides a means to rank-order the ligands based on their predicted binding affinities.

The plot displays the contributions of four energy terms:

1. Strain Energy ddE_{Strain}: The energy cost of distorting the ligand to fit into the binding site computed using equation 6.7. The orange bars indicate the strain energy contributions. Generally, these contributions are relatively small compared to the other energy terms. This suggests that the ligands do not undergo significant distortion upon binding, implying that the binding site is accommodating to the ligands' conformations.

2. Solvation Energy ddE_{Solv}: The change in solvation energy upon binding com-

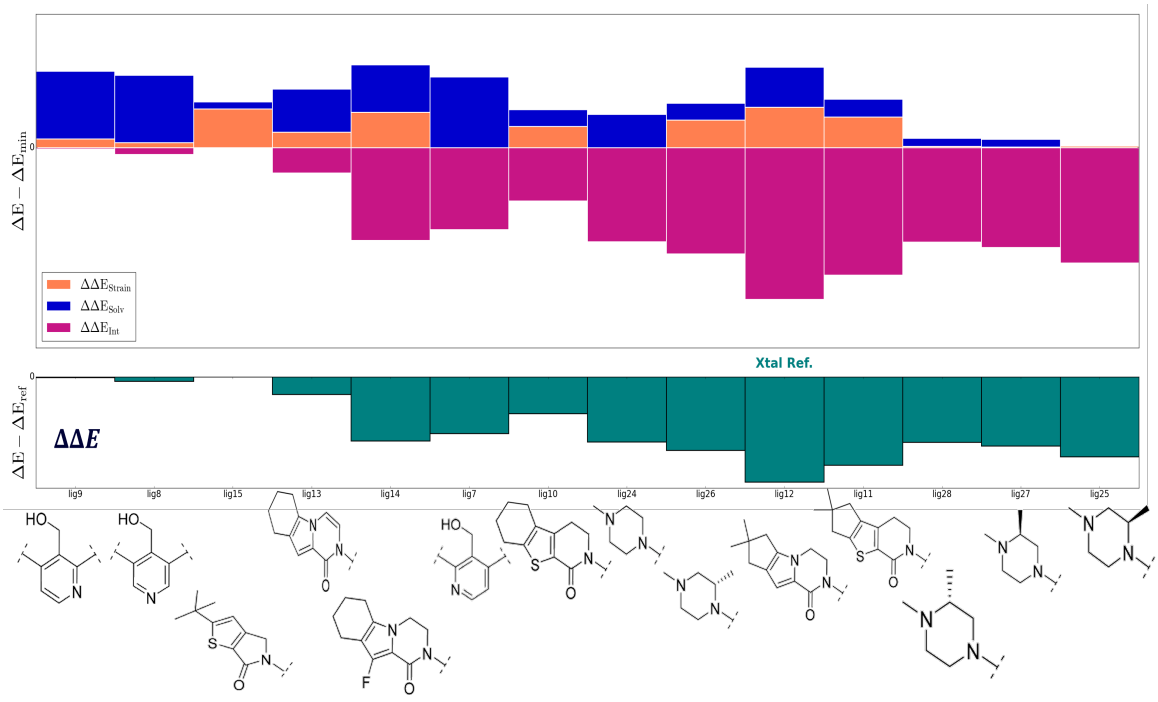

Figure 6.11: Affinity ranking of ligands: The blue histograms display the ordering of ligands based on their relative solvation energies. The orange histograms represent the ordering of the relative strain energy of ligands. The purple histogram illustrates the relative interaction energies, while the dark green histogram shows the relative binding free energies of the ligands. For the relative rank ordering, ligand 12 was chosen as the reference due to its higher potency.

puted using equation 6.6. The blue bars represent the solvation energy contributions. These contributions vary across ligands but are significant in determining the binding affinity. Ligands with more favorable (negative) solvation energies, such as Lig9, Lig8, and Lig15, indicate that desolvation upon binding contributes positively to their binding affinities.

3. Interaction Energy ddE_{Int}: The direct interaction energy between the ligand and the protein computed using equation 6.8. The magenta bars show the interaction energy contributions. This term has the most considerable variation and impact on the total free energy. Ligands such as Lig14, Lig7, and Lig13 exhibit large negative interaction energies, indicating strong favorable interactions with the protein binding site. These ligands are likely to be among the most potent based on their strong interactions. The ligand interactions are tuned more by the hydrophobic interaction present in the inner pocket of the protein.

4. Total Free Energy (ddE): The bottom part of the plot shows the total free energy relative to a reference (dE_{Ref}). Ligands such as Lig14, Lig7, and Lig13, with the most negative total free energies, are ranked highest in terms of binding affinity. This suggests that they are the most potent ligands in the set. Ligands like Lig9, Lig8, and Lig15, which show higher total free energies, are ranked lower, indicating less binding affinity compared to the others.

The affinity ranking plot from Region 3 provides several critical insights into the binding affinities of the ligands. The interaction energy (ddE_{Int})) is the most significant determinant of binding affinity, with strong interactions leading to higher binding potency. The relatively small strain energy contributions suggest that the ligands fit well into the binding site without significant distortion. The solvation energy contributions vary but play an essential role in modulating binding affinity. Favorable desolvation energies enhance the binding affinity of certain ligands.

The plot effectively rank-orders the ligands based on their total free energies, providing a clear indication of the most potent ligands. This computational pipeline, therefore, demonstrates its utility in predicting and ranking ligand binding affinities,

potentially guiding design efforts toward the most promising compounds.

Overall, the Region-3 approach, which includes a larger QM region and accounts for key energy contributions, proves to be a robust method for accurately predicting and rank-ordering ligand binding affinities. This insight can be valuable for drug discovery and development processes, where computational predictions can streamline the identification of lead compounds.

6.5 Conclusion

In this study, we explored the effectiveness of hybrid QM/MM methods for predicting ligand binding affinities to BTK. We assessed the computationally derived RBFEs against experimentally determined inhibitory constants (Log Ki) across three different QM/MM regions. Each region varied in the extent of the system treated with QM.

In Region 1, we treated only the ligand with QM while representing the rest of the system with a point charge environment. The R^2 value of 0.245 indicated no correlation between RBFEs and Log Ki values, demonstrating that this approach failed to capture the complex interactions driving binding affinities. This highlighted the limitations of a model that treats only the ligand with QM and the rest of the system too simplistically.

For Region 2, we expanded the QM treatment to include the ligand, protein residues, and water molecules making hydrogen bonds with the ligand. However, the R^2 value of 0.0376 showed an even weaker correlation than Region 1. This indicated that while hydrogen bonding is important, it alone is insufficient for accurately determining binding affinities. The model's failure here pointed to the significant roles played by hydrophobic and Van der Waals interactions, which were not adequately captured in this setup.

In Region 3, we included a larger region (approximately 10) around the ligand in the QM treatment, using the MMFF94 force field for geometry optimization and QM

for energy evaluations. This approach yielded a much higher R^2 value of 0.669, representing a significant improvement in the correlation between RBFEs and Log Ki values. This result suggests that including a larger portion of the protein environment in the QM calculations is crucial for accurately predicting binding affinities. The enhanced correlation underscores the importance of accounting for the extended protein environment's interactions.

Our comprehensive analysis across the three regions provides several key insights into the use of hybrid QM/MM methods for predicting ligand binding affinities. Firstly, hybrid QM/MM methods are highly sensitive to the boundaries between the QM and MM regions. The choice of which parts of the system to treat quantum mechanically significantly impacts the accuracy of the predictions. This sensitivity highlights the need for careful selection and justification of the QM and MM boundaries in computational studies.

Secondly, the results indicate that QM treatment of the ligand only, as seen in Region 1, is not advisable. This approach fails to account for the complex and diverse interactions within the protein-ligand binding site, resulting in poor predictive performance. The inadequate correlation observed in Region 1 underscores the necessity of including more of the protein environment in the QM treatment to capture essential binding interactions accurately.

Thirdly, our findings demonstrate that for better results, a larger portion of the protein environment should be treated with QM. As demonstrated in Region 4, including more of the protein environment in the QM calculations leads to a significant improvement in the correlation between RBFEs and Log Ki values. This suggests that the interactions within the extended protein environment are critical for accurately determining binding affinities. The success of Region 4 emphasizes the value of expanding the QM region to encompass significant portions of the surrounding environment.

Additionally, the affinity ranking plot from Region 4 provided critical insights into

the contributions of different energy terms to the total free energy. Interaction energy was found to be the most differentiating factor, while moderate strain energies and variable solvation effects also played essential roles. The plot effectively rank-ordered the ligands, showcasing the computational pipeline's potential in guiding experimental efforts.

In addition to these insights, it is essential to perform calculations over multiple configurations and consider conformational sampling to achieve more reliable RBFEs. This approach will ensure convergence and better account for the dynamic nature of protein-ligand interactions. Future studies should balance computational efficiency with accuracy by exploring different levels of QM optimization across multiple snapshots. This balance will help in achieving a comprehensive understanding of the binding affinities and improving the reliability of the predictions.

In conclusion, while hybrid QM/MM methods hold great potential for predicting ligand binding affinities, careful consideration of the QM/MM boundaries and the inclusion of a substantial protein environment in the QM treatment are crucial for achieving accurate and reliable results. The insights gained from this study provide a foundation for future work, emphasizing the need for comprehensive models that account for the complex interactions within the protein-ligand binding site.

Appendix A

Chapter 3 Supplemental Information

A.1 Combined Ensemble Franck Condon Code

A.1.1 Generating The Nuclear Ensemble Spectra

```
#############################################################
#                  Nuclear Enemble Spectra                  #
#                <-------------------------->               #
# A Python Program To Generate Nuclear Ensemble Sepctra     #
# From DFT and TDDFT Vertical Excitation/De-excitation      #
# Calculations                                              #
#                                                           #
#                                                           #
# Developer: Ajay Khanna                                    #
# Place: UC Merced | Isborn Lab                             #
# Project: Fluorescence Resonance Energy Transfer           #
# Date: Aug.15.2019                                         #
#############################################################

import logging
import argparse
import numpy as np
from scipy import integrate
```

```
19
20 # Initialize logging
21 logging.basicConfig(level=logging.INFO, format="%(levelname)s: %(
       message)s")
22
23 # Constant and Conversion Factors
24 INVCM_TO_EV = float(0.00012398)
25
26
27 # --------------------
28 # Required Functions
29 # --------------------
30 def load_excitation_energies_transition_dipole_moments(filename: str
       ) -> np.array:
31     """
32     This function loads excitation energies and
33     transition dipole moments from a file.
34
35     :param filename: The filename parameter is a string that
       represents the name of the file from which
36     the data will be loaded
37     :type filename: str
38     :return: two arrays: the excitation energies and the transition
       dipole moments.
39     """
40     try:
41         data = np.loadtxt(filename, delimiter=",")
42         return data[:, 0], data[:, 1:]
43     except FileNotFoundError:
44         print(f"Error: File {filename} not found.")
45         exit()
46     except Exception as e:
47         print(f"An error occurred: {e}")
48         exit()
49
50
51 def calculate_ensemble_spectra(
52     omega: int,
```

```
    excitation_energies: np.array,
    transition_dipole_moments: np.array,
    energy_grid: np.array,
    gaussian_width: float,
) -> np.array:
    """
    Calculates the ensemble spectra for a given set of excitation energies and transition dipole moments.

    Parameters:
    omega (int): Energy scaling factor, where 1 indicates absorption and 3 indicates emission.
    excitation_energies (np.array): Array of excitation or de-excitation energies.
    transition_dipole_moments (np.array): Array of transition dipole moments.
    energy_grid (np.array): Energy grid or window over which intensities are calculated.
    gaussian_width (float): Width of the Gaussian distribution.

    Returns:
    np.array: Calculated ensemble spectra as a 1D numpy array.
    """
    spectra = np.zeros(len(energy_grid))
    for energy, tdm in zip(excitation_energies, transition_dipole_moments):
        scaled_energy = energy**omega
        gaussian_factor = np.exp(
            -((energy_grid - energy) ** 2.0) / (2.0 * gaussian_width**2.0)
        )
        spectra += scaled_energy * tdm**2 * gaussian_factor

    area_ensemble = integrate.simps(spectra, energy_grid)
    normalized_ens = spectra / area_ensemble

    return normalized_ens

```

```
84
85 def transform_computed_spectra_to_lineshape(
86     spectrum_x: np.array,
87     spectrum_y: np.array,
88     spectroscopy_type: str = "abs",
89     is_gaussian: bool = True,
90 ) -> np.array:
91     """
92     Transforms a computed spectrum into a lineshape by adjusting the
       y-values.
93
94     Parameters:
95     spectrum_x (np.array): 1D array of x-values (spectrum).
96     spectrum_y (np.array): 1D array of y-values (spectrum).
97     spectroscopy_type (str): Type of spectroscopy, "abs" (absorption
      ) or "ems" (emission). Default is "abs".
98     is_gaussian (bool): If True, apply Gaussian16 transformation.
      Default is True.
99
100    Returns:
101    np.array: Transformed 1D array of y-values (lineshape).
102    """
103    assert len(spectrum_x) == len(
104        spectrum_y
105    ), "x and y arrays must be of the same length."
106
107    if spectroscopy_type == "abs":
108        transformed_y = spectrum_y / spectrum_x
109    elif spectroscopy_type == "ems":
110        power = 4 if is_gaussian else 3
111        transformed_y = spectrum_y / spectrum_x**power
112    else:
113        raise ValueError("Invalid spectroscopy type. Choose 'abs' or
       'ems'.")
114
115    return transformed_y
116
117
```

```
118 def main():
119     parser = argparse.ArgumentParser(description="Nuclear Ensemble
    Spectra Generator")
120     parser.add_argument(
121         "--exictation_energies",
122         type=str,
123         help="Path to the excitation energies and transition files(.
    csv)",
124     )
125     parser.add_argument(
126         "--omega",
127         type=int,
128         default=1,
129         help="Omega value: 1 for absorption, 3 for emission",
130     )
131     parser.add_argument(
132         "--energy_grid",
133         type=float,
134         required=False,
135         nargs="+",
136         help="Energy grid for the spectra (eV)",
137     )
138     parser.add_argument(
139         "--fwhm",
140         type=float,
141         default=600.0,
142         required=False,
143         help="FWHM value for Gaussian Broadening, default is 600.0
    cm-1",
144     )
145     parser.add_argument(
146         "--to_lineshape",
147         type=bool,
148         default=False,
149         required=False,
150         help="Transfer to Lineshape?: False (default)",
151     )
152     args = parser.parse_args()
```

```
153
154     # Load excitation energies and transition dipole moments
155     omega = args.omega
156     gaussian_width = (args.fwhm * INVCM_TO_EV) / (2.0 * np.sqrt(2.0
    * np.log(2.0)))
157     """
158     This line is calculating the standard deviation, often referred
159     to as the 'width', of a Gaussian distribution.
160     The args.fwhm is the Full Width at Half Maximum (FWHM) of the
    Gaussian,
161     which is a measure of the width of the distribution at half of
    its maximum value.
162     The INVCM_TO_EV is a conversion factor that is used to convert
    the units of the FWHM
163     from inverse centimeters to electron volts (eV).
164     The denominator of the equation, 2.0 * np.sqrt(2.0 * np.log(2.0)
    ), is a constant
165     derived from the properties of the Gaussian distribution. It is
    used to convert the
166     FWHM to the standard deviation of the Gaussian.
167     """
168     excitation_energies, transition_dipole_moments = (
169         load_excitation_energies_transition_dipole_moments(args.
    exictation_energies)
170     )
171     energy_grid = (
172         np.linspace(args.energy_grid[0], args.energy_grid[1], 26980)
173         if args.energy_grid
174         else np.linspace(
175             excitation_energies.min() - 0.5, excitation_energies.max
    () + 0.5, 26980
176         )  # 0.5eV For Converged Spectra
177     )
178
179     # Calculate ensemble spectra
180     spectra = calculate_ensemble_spectra(
181         omega,
182         excitation_energies,
```

```
        transition_dipole_moments,
        energy_grid,
        gaussian_width,
    )
    if args.to_lineshape:
        spectroscopy_type = ["abs" if omega == 1 else "ems"]
        spectra_ls = transform_computed_spectra_to_lineshape(
            energy_grid, spectra, spectroscopy_type[0], is_gaussian=
    False
        )

        np.savetxt(
            "nuclear_ensemble_spectra.csv",
            np.column_stack([energy_grid, spectra, spectra_ls]),
            delimiter=",",
            header="Energy (eV), Intensity, Lineshape",
        )
    else:
        np.savetxt(
            "nuclear_ensemble_spectra.csv",
            np.column_stack([energy_grid, spectra]),
            delimiter=",",
            header="Energy (eV), Intensity",
        )


if __name__ == "__main__":
    main()
```

Listing A.1: Python code for generating nuclear ensemble intensity and lineshape spectra

A.1.2 Generating The EsumFTFC Spectra

```
# ------------------------------------------------
# Python Program to Computed The EsumFTFC Spectra
# and Lineshape
# ------------------------------------------------

```

```
import numpy as np
import argparse
import matplotlib.pyplot as plt
from scipy import interp1d
from computed_intensity_lineshape_spectra import
    transform_computed_spectra_to_lineshape

# Conversion Factor
INVCM_TO_EV = 0.00012398

# ---------------------------------------
# Image File Name, Quality and Type
# ---------------------------------------
quality = 600
img_format = "png"
bbox_constrain = "tight"


def print_banner():
    banner = """
    ----------------------------------------
    |                                      |
    |        E-sumFTFC Franck-Condon         |
    |            Spectra Calculator        |
    |                                      |
    ----------------------------------------
    """
    print(banner)


def save_file(
    filename,
    *data_arrays,
    custom_header=False,
):
    """
    Save Data to a CSV file.

```

```
    Parameters:
    - filename: Name of the file to save to.
    - num_snaps: Number of snapshots.
    - data_arrays: Variable list of data arrays to save.

    Returns:
    - None.
    """
    if custom_header:
        header = "Energy(eV),Intensity(arb units),Lineshape"
    else:
        header = "Energy(eV), Intensity(arb units)"
    data = np.column_stack(data_arrays)
    cols = np.shape(data)[1]
    np.savetxt(
        f"./{filename}",
        data,
        fmt=["%1.6f" for i in range(cols)],
        header=header,
        delimiter=",",
    )


def save_img(filename):
    """
    The function saves an image with the specified filename and
    parameters.

    :param filename: The filename is the name of the image file that
    you want to save. It should include
    the file extension (e.g., "image.png")
    """
    plt.savefig(
        f"./{filename}",
        format=img_format,
        dpi=quality,
        bbox_inches=bbox_constrain,
    )
```

```
79
80
81 def generate_esumFTFC_spectra(
82     files: list,
83     energy_grid: np.ndarray,
84     temp_col=2,
85     spec_type: str = "abs",
86     is_gaussian=True,
87 ):
88     sum_allY_cross_section = []
89     sum_allY_lineshape = []
90     for fname in files:
91         data = np.loadtxt(fname, skiprows=7, usecols=(0, temp_col))
92         X = data[:, 0] * INVCM_TO_EV
93         Y = data[:, 1]
94         f1_cs = interp1d(X, Y, kind="nearest", fill_value="
    extrapolate")
95         ynew_cs = f1_cs(energy_grid)
96         Y_LS = transform_computed_spectra_to_lineshape(
97             spectrum_x=X,
98             spectrum_y=Y,
99             spectroscopy_type=spec_type,
100            is_gaussian=is_gaussian,
101        )
102        f1_ls = interp1d(X, Y_LS, kind="nearest", fill_value="
    extrapolate")
103        ynew_ls = f1_ls(energy_grid)
104        sum_allY_cross_section.append(ynew_cs)
105        sum_allY_lineshape.append(ynew_ls)
106
107        plt.plot(energy_grid, ynew_ls, color="grey", alpha=0.2)
108        plt.xlabel("Energy [eV]")
109        plt.ylabel("Intensity [arb. units]")
110
111    sum_ftfc_cs = np.mean(sum_allY_cross_section, axis=0)
112    sum_ftfc_ls = np.mean(sum_allY_lineshape, axis=0)
113
114    plt.plot(
```

```
115         energy_grid,
116         sum_ftfc_ls,
117         color="black",
118         linewidth=2,
119         label="E-sum$_{32}$FTFC",
120     )
121     save_img(
122         "E-sumFTFC_lineshape.png",
123     )
124 
125     save_file(
126         "before_shift_E_sumFTFC_CS_LS.csv",
127         energy_grid,
128         sum_ftfc_cs,
129         sum_ftfc_ls,
130         custom_header=True,
131     )
132 
133 
134 def main():
135     parser = argparse.ArgumentParser(description="EsumFTFC Spectra
    Calculator")
136     parser.add_argument(
137         "--input_files",
138         metavar="input_files",
139         required=True,
140         type=int,
141         nargs="+",
142         help="Input vibronic filenames",
143     )
144     parser.add_argument(
145         "--zero_zero_transitions_file",
146         required=True,
147         metavar="zero_zero_transitions",
148         type=str,
149         help="Zero-zero transitions filename",
150     )
151     parser.add_argument(
```

```
152         "--energy_grid",
153         metavar="energy_grid",
154         required=True,
155         type=float,
156         nargs="+",
157         help="Grid of energy values for interpolation",
158     )
159     parser.add_argument(
160         "--is_gaussian",
161         type=bool,
162         default=True,
163         help="Software: True: Gaussian or False: Other",
164     )
165     parser.add_argument(
166         "--temp_col",
167         metavar="Temperature Cols",
168         type=int,
169         default=2,
170         help="1: ZTFC and 2: FTFC",
171     )
172     parser.add_argument(
173         "--spec_type",
174         metavar="spec_type",
175         type=str,
176         default="abs",
177         help="Type of Spectroscopy: abs: Absorption and ems:
    emission",
178     )
179     parser.add_argument(
180         "--output_file", metavar="output_file", type=str, help="
    Output file name"
181     )
182     args = parser.parse_args()
183
184     print_banner()
185     energy_grid = np.linspace(
186         args.energy_grid[0], args.energy_grid[1], num=26980, dtype=
    float
```

```
    )
    input_files_name = [f"frame{i}_vibronic.dat" for i in args.
    input_files]

    generate_esumFTFC_spectra(
        input_files_name,
        energy_grid,
        temp_col=args.temp_col,
        spec_type=args.spec_type,
        is_gaussian=args.is_gaussian,
    )


if __name__ == "__main__":
    main()
```

Listing A.2: Python code for generating summed finite temperature Franck-Condon intensity and lineshape Spectra

A.1.3 Generating The Average FC Lineshape

```
#-------------------------------------
"""
Python Program to Generate the Average
FC Lineshape
"""
#-------------------------------------

import sys
import logging
import argparse
import numpy as np
import matplotlib.pyplot as plt
from scipy.interpolate import interp1d
from matplotlib.ticker import FormatStrFormatter

# Required Functions
from computed_intensity_lineshape_spectra import
    transform_computed_spectra_to_lineshape
```

```
18
19 # Conversion factors
20 INVCM_TO_EV = 0.00012398
21 NM_TO_EV = 4.135667696e-15 * 2.99792458e08 * 1.0e09
22
23 # Setup logging
24 logging.basicConfig(
25     level=logging.INFO, format="%(asctime)s - %(levelname)s - %(
   message)s"
26 )
27
28
29 def print_banner():
30     banner = """
31     ----------------------------------------
32     |                                      |
33     |         Average Franck-Condon        |
34     |             Spectra Calculator       |
35     |                                      |
36     ----------------------------------------
37     """
38     print(banner)
39
40
41 def load_extract_csv_data(
42     fname: str, temp: float, ev_conv: bool = False, normalize: bool
   = False
43 ) -> tuple[np.ndarray, np.ndarray]:
44     """Loads and extracts data from a CSV file.
45
46     Args:
47         :param fname: File name of the CSV data.
48         :param temp: Temperature (0 for ground state, otherwise
   excited state).
49         :param eV_conv: If True, convert energy units to eV.
50         :param normalize: If True, normalize intensity.
51
52     Returns:
```

```
        Tuple of energy (x) and intensity (y) data.
    """

    try:
        data = np.loadtxt(fname, skiprows=7)
        x = data[:, 0]
        if ev_conv:
            x *= INVCM_TO_EV
        y = data[:, 1] if temp == 0 else data[:, 2]
        if normalize:
            y /= np.max(y)
        return x, y
    except FileNotFoundError:
        logging.error(f"File not found: {fname}")
        raise
    except Exception as e:
        logging.error(f"Error processing file {fname}: {e}")
        raise


def average_franck_condon_spectra(
    input_vibronic_filenames: list[str],
    zero_zero_transitions: np.ndarray,
    energy_grid: np.ndarray,
    temp: float,
    spec_type: str = "abs",
) -> np.ndarray:
    """
    Calculate the average Franck-Condon spectra from input files.

    :param input_vibronic_filenames: List of filenames containing
   vibronic spectra.
    :param zero_zero_transitions: Array of zero-zero transitions.
    :param energy_grid: Energy grid for interpolation.
    :param temp: Temperature for the calculation.
    :param spec_type: Type of spectroscopy (absorption or emission).
    :return: Array of the averaged Franck-Condon spectra.
    """
```

```
    zerod_FC_LS = []
    for idx, file in enumerate(input_vibronic_filenames):
        zerovalx = zero_zero_transitions[:, 1][idx]
        try:
            X, Y = load_extract_csv_data(file, temp, ev_conv=True, normalize=False)
        except Exception as e:
            logging.error(f"Error processing file {file}: {e}")
            continue

        Y_LS = transform_computed_spectra_to_lineshape(
            spectrum_x=X, spectrum_y=Y, spectroscopy_type=spec_type, is_gaussian=True
        )
        X = X - (zerovalx * INVCM_TO_EV)
        f1 = interp1d(X, Y_LS, kind="nearest", fill_value="extrapolate")  # type: ignore
        y_predict = f1(energy_grid)
        zerod_FC_LS.append(y_predict)
        plt.plot(
            energy_grid,
            y_predict,
            color="grey",
            label=f"Frame-{int(zero_zero_transitions[:,0][idx])}",
        )

    avg_FC_LS = np.mean(zerod_FC_LS, axis=0)
    plt.plot(energy_grid, avg_FC_LS, color="black", label="avgFC")
    return avg_FC_LS


def save_file_avgFC(filename, *data_arrays, custom_header=False, input_files_name):
    header = (
        "# Energy(eV),avgFTFC_Int,avgFTFC_LS \n"
        if custom_header
        else "# Energy(eV),avgFTFC_Int"
    )
```

```
124     data = np.column_stack(data_arrays)
125     cols = np.shape(data)[1]
126     comment = f"#{','.join(input_files_name)}\n"
127     np.savetxt(
128         f"./{filename}",
129         data,
130         fmt=["%1.6f" for i in range(cols)],
131         header=header,
132         delimiter=",",
133         comments=comment,
134     )
135
136
137 def save_img(filename: str) -> None:
138     """
139     Save the current matplotlib plot to an image file.
140
141     :param filename: Filename for the image.
142     """
143     plt.savefig(filename, format="png", dpi=600, bbox_inches="tight"
    )
144
145
146 def main():
147     parser = argparse.ArgumentParser(description="Average Franck-
    Condon Spectra")
148     parser.add_argument(
149         "--input_files",
150         metavar="input_files",
151         required=True,
152         type=int,
153         nargs="+",
154         help="Input vibronic filenames",
155     )
156     parser.add_argument(
157         "--zero_zero_transitions_file",
158         required=True,
159         metavar="zero_zero_transitions",
```

```
160         type=str,
161         help="Zero-zero transitions filename",
162     )
163     parser.add_argument(
164         "--energy_grid",
165         metavar="energy_grid",
166         required=True,
167         type=float,
168         nargs="+",
169         help="Grid of energy values for interpolation",
170     )
171     parser.add_argument(
172         "--temperature",
173         metavar="temperature",
174         type=float,
175         default=300,
176         help="Temperature for vibronic spectra calculation",
177     )
178     parser.add_argument(
179         "--spec_type",
180         metavar="spec_type",
181         type=str,
182         default="abs",
183         help="Type of Spectroscopy: abs: Absorption and ems:
    emission",
184     )
185     parser.add_argument(
186         "--output_file", metavar="output_file", type=str, help="
    Output file name"
187     )
188     args = parser.parse_args()
189
190     print_banner()
191     energy_grid = np.linspace(
192         args.energy_grid[0], args.energy_grid[1], num=26980, dtype=
    float
193     )
194     input_files_name = [f"frame{i}_vibronic.dat" for i in args.
```

```
    input_files]
195     transition_00 = np.loadtxt(args.zero_zero_transitions_file,
    delimiter=",")
196     zero_zero_transitions = transition_00[
197         np.isin(transition_00[:, 0], args.input_files)
198     ]
199
200     avgFC_LS = average_franck_condon_spectra(
201         input_vibronic_filenames=input_files_name,
202         zero_zero_transitions=zero_zero_transitions,
203         energy_grid=energy_grid,
204         temp=args.temperature,
205         spec_type=args.spec_type,
206     )
207
208     snaps = "_".join(map(str, zero_zero_transitions[:, 0].astype(int
    )))
209
210     save_file_avgFC(
211         f"avgFC_frames{snaps}_LS.csv",
212         energy_grid,
213         avgFC_LS,
214         input_files_name=input_files_name,
215     )
216
217     plt.xlabel("Energy (eV)")
218     plt.ylabel("Intensity")
219     plt.xticks(np.linspace(energy_grid[0], energy_grid[-1], 5))
220     plt.gca().xaxis.set_major_formatter(FormatStrFormatter("%0.1f"))
221     plt.legend()
222     plt.tight_layout()
223     save_img(f"avgFC_frames{snaps}_LS.png")
224
225
226 if __name__ == "__main__":
227     main()
```

Listing A.3: Python code for generating average Franck-Condon Intensity and Lineshape Spectra

A.1.4 Generating The Approximate EFC Spectra: EoptavgFTFC and EavgZTFC

```
#-------------------------------------
"""
Python Program to Generate the Average
FC Lineshape
"""
#-------------------------------------

import sys
import logging
import argparse
import numpy as np
import matplotlib.pyplot as plt
from scipy.interpolate import interp1d
from matplotlib.ticker import FormatStrFormatter

# Required Functions
from computed_intensity_lineshape_spectra import
    transform_computed_spectra_to_lineshape

# Conversion factors
INVCM_TO_EV = 0.00012398
NM_TO_EV = 4.135667696e-15 * 2.99792458e08 * 1.0e09

# Setup logging
logging.basicConfig(
    level=logging.INFO, format="%(asctime)s - %(levelname)s - %(
    message)s"
)


def print_banner():
    banner = """
    ----------------------------------------
    |                                      |
    |        Average Franck-Condon         |
```

```
    |            Spectra Calculator        |
    |                                       |
    ----------------------------------------
    """
    print(banner)


def load_extract_csv_data(
    fname: str, temp: float, ev_conv: bool = False, normalize: bool = False
) -> tuple[np.ndarray, np.ndarray]:
    """Loads and extracts data from a CSV file.

    Args:
        :param fname: File name of the CSV data.
        :param temp: Temperature (0 for ground state, otherwise excited state).
        :param eV_conv: If True, convert energy units to eV.
        :param normalize: If True, normalize intensity.

    Returns:
        Tuple of energy (x) and intensity (y) data.
    """

    try:
        data = np.loadtxt(fname, skiprows=7)
        x = data[:, 0]
        if ev_conv:
            x *= INVCM_TO_EV
        y = data[:, 1] if temp == 0 else data[:, 2]
        if normalize:
            y /= np.max(y)
        return x, y
    except FileNotFoundError:
        logging.error(f"File not found: {fname}")
        raise
    except Exception as e:
        logging.error(f"Error processing file {fname}: {e}")
```

```
70          raise
71
72
73  def average_franck_condon_spectra(
74      input_vibronic_filenames: list[str],
75      zero_zero_transitions: np.ndarray,
76      energy_grid: np.ndarray,
77      temp: float,
78      spec_type: str = "abs",
79  ) -> np.ndarray:
80      """
81      Calculate the average Franck-Condon spectra from input files.
82
83      :param input_vibronic_filenames: List of filenames containing
    vibronic spectra.
84      :param zero_zero_transitions: Array of zero-zero transitions.
85      :param energy_grid: Energy grid for interpolation.
86      :param temp: Temperature for the calculation.
87      :param spec_type: Type of spectroscopy (absorption or emission).
88      :return: Array of the averaged Franck-Condon spectra.
89      """
90      zerod_FC_LS = []
91      for idx, file in enumerate(input_vibronic_filenames):
92          zerovalx = zero_zero_transitions[:, 1][idx]
93          try:
94              X, Y = load_extract_csv_data(file, temp, ev_conv=True,
    normalize=False)
95          except Exception as e:
96              logging.error(f"Error processing file {file}: {e}")
97              continue
98
99          Y_LS = transform_computed_spectra_to_lineshape(
100             spectrum_x=X, spectrum_y=Y, spectroscopy_type=spec_type,
     is_gaussian=True
101         )
102         X = X - (zerovalx * INVCM_TO_EV)
103         f1 = interp1d(X, Y_LS, kind="nearest", fill_value="
    extrapolate")  # type: ignore
```

```
        y_predict = f1(energy_grid)
        zerod_FC_LS.append(y_predict)
        plt.plot(
            energy_grid,
            y_predict,
            color="grey",
            label=f"Frame-{int(zero_zero_transitions[:,0][idx])}",
        )

    avg_FC_LS = np.mean(zerod_FC_LS, axis=0)
    plt.plot(energy_grid, avg_FC_LS, color="black", label="avgFC")
    return avg_FC_LS


def save_file_avgFC(filename, *data_arrays, custom_header=False,
    input_files_name):
    header = (
        "# Energy(eV),avgFTFC_Int,avgFTFC_LS \n"
        if custom_header
        else "# Energy(eV),avgFTFC_Int"
    )
    data = np.column_stack(data_arrays)
    cols = np.shape(data)[1]
    comment = f"#{','.join(input_files_name)}\n"
    np.savetxt(
        f"./{filename}",
        data,
        fmt=["%1.6f" for i in range(cols)],
        header=header,
        delimiter=",",
        comments=comment,
    )


def save_img(filename: str) -> None:
    """
    Save the current matplotlib plot to an image file.

```

```
    :param filename: Filename for the image.
    """
    plt.savefig(filename, format="png", dpi=600, bbox_inches="tight")


def main():
    parser = argparse.ArgumentParser(description="Average Franck-Condon Spectra")
    parser.add_argument(
        "--input_files",
        metavar="input_files",
        required=True,
        type=int,
        nargs="+",
        help="Input vibronic filenames",
    )
    parser.add_argument(
        "--zero_zero_transitions_file",
        required=True,
        metavar="zero_zero_transitions",
        type=str,
        help="Zero-zero transitions filename",
    )
    parser.add_argument(
        "--energy_grid",
        metavar="energy_grid",
        required=True,
        type=float,
        nargs="+",
        help="Grid of energy values for interpolation",
    )
    parser.add_argument(
        "--temperature",
        metavar="temperature",
        type=float,
        default=300,
        help="Temperature for vibronic spectra calculation",
```

```
    )
    parser.add_argument(
        "--spec_type",
        metavar="spec_type",
        type=str,
        default="abs",
        help="Type of Spectroscopy: abs: Absorption and ems: emission",
    )
    parser.add_argument(
        "--output_file", metavar="output_file", type=str, help="Output file name"
    )
    args = parser.parse_args()

    print_banner()
    energy_grid = np.linspace(
        args.energy_grid[0], args.energy_grid[1], num=26980, dtype=float
    )
    input_files_name = [f"frame{i}_vibronic.dat" for i in args.input_files]
    transition_00 = np.loadtxt(args.zero_zero_transitions_file, delimiter=",")
    zero_zero_transitions = transition_00[
        np.isin(transition_00[:, 0], args.input_files)
    ]

    avgFC_LS = average_franck_condon_spectra(
        input_vibronic_filenames=input_files_name,
        zero_zero_transitions=zero_zero_transitions,
        energy_grid=energy_grid,
        temp=args.temperature,
        spec_type=args.spec_type,
    )

    snaps = "_".join(map(str, zero_zero_transitions[:, 0].astype(int)))
```

```
209
210     save_file_avgFC(
211         f"avgFC_frames{snaps}_LS.csv",
212         energy_grid,
213         avgFC_LS,
214         input_files_name=input_files_name,
215     )
216
217     plt.xlabel("Energy (eV)")
218     plt.ylabel("Intensity")
219     plt.xticks(np.linspace(energy_grid[0], energy_grid[-1], 5))
220     plt.gca().xaxis.set_major_formatter(FormatStrFormatter("%0.1f"))
221     plt.legend()
222     plt.tight_layout()
223     save_img(f"avgFC_frames{snaps}_LS.png")
224
225
226 if __name__ == "__main__":
227     main()
```

Listing A.4: Python code for generating approximated ensemble Franck-Condon intensity and lineshape spectra: E_{opt}avgFTFC and EavgZTFC

Appendix B

Chapter 4 Supplemental Information

B.1 Intensity to Lineshape Transformations

The following code is used to transform the experimental absorption and fluorescence spectra into experimental lineshapes:

B.1.1 Transforming Experimental Intensity Spectra to Lineshapes

```
python3 experimental_to_lineshape_spectra_transformation.py --input_filename exp_emission.csv --spec_type ems --output_filename transformed
```

Listing B.1: How to Run?

```
import argparse
import numpy as np
from scipy import integrate

"""
The above Python code is a program that transforms experimental spectra, both absorption, and emission, from the wavelength domain to the frequency domain or performs a lineshape
```

```
    transformation based on the spectroscopy type (absorption or
    emission) and saves the transformed data to CSV files.
"""
# Conversion Factor
NM_TO_EV = float(4.135667696e-15 * 2.99792458e08 * 1.0e09)

# Required Functions
def save_file(filename, *data_arrays):
    """
    Save Data to a CSV file.

    Parameters:
    - filename: Name of the file to save to.
    - data_arrays: Variable list of data arrays to save.

    Returns:
    - None.
    """

    header = "Energy(eV), Intensity(arb units)"
    data = np.column_stack(data_arrays)
    np.savetxt(
        f"{filename}",
        data,
        fmt=["%1.6f", "%1.6f"],
        header=header,
        delimiter=",",
    )


def normalization(x, y, kind="max"):
    """
    The function performs normalization on a given dataset using
    either the maximum value or the area under the curve.

    :param x: The parameter `x` represents the x-values of the data
    points.
    :param y: The y parameter represents the array of values that
```

```
    you want to normalize.
41      :param kind: The parameter "kind" is used to specify the type of
        normalization to be performed.
42      :return: The function `normalization` returns the normalized
    values of `y` based on the specified
43      normalization method (`kind`).
44      """
45      if kind == "max":
46          max_y = np.max(y)
47          return np.divide(y, max_y)
48      else:
49          area_y = integrate.simps(y, x)
50          return np.divide(y, area_y)
51
52
53  def exp_Intensity_lambda_to_frequency_domain_Transformation(x, y,
    spec="abs"):
54      """
55      The function transforms intensity data from the wavelength
    domain to the frequency domain, except
56      for absorption spectra where no transformation is required.
57
58      :param x: The parameter 'x' represents the wavelength or
    wavenumber values of the input spectrum.
59      :param y: The parameter 'y' represents the intensity values in
    the wavelength domain
60      :param spec: The parameter 'spec' is a string that specifies the
        type of spectrum.
61      :return: the y values in the frequency domain.
62      """
63      if spec == "abs":
64          print(
65              """
66  No wavenumber transformation for absorption spectra is required
    because the molar absorptivity
67  is defined as the logarithm of the ratio between the transmitted and
        incident intensity for
68  unit length and molar concentration of the sample cell; its integral
```

```
    is, therefore, the same
if one computes it both in the wavelength and in the frequency scale.

References:
1. Insights for an Accurate Comparison of Computational Data to Experimental Absorption and
Emission Spectra: Beyond the Vertical Transition Approximation. dx.doi.org/10.1021/ct301107m
J. Chem. Theory Comput. 2013, 9, 2072-2082
2. Valeur, B. Molecular Fluorescence: Principles and Applications; Wiley-VCH: Weinheim, 2001; pp 5
"""
        )
        y_frequency_domain = y

    else:
        energy_squared_reciprocal = 1.0 / x**2
        y_frequency_domain = energy_squared_reciprocal * y

    return y_frequency_domain


def exp_Lineshape_Transform(x, y, norm="max", spec="abs"):
    """
    The function `exp_Lineshape_Transform` calculates the lineshape transformation of a given spectrum
    based on the specified spectroscopy information.

    :param x: The x parameter represents the energy values of the spectroscopy data.
    :param y: The parameter "y" represents the intensity or amplitude of the spectroscopy signal at each
    energy value
    :param norm: The "norm" parameter specifies the normalization method to be used.
    :param spec: The "spec" parameter in the function "exp_Lineshape_Transform" is used to specify the
```

```
97      type of spectroscopy information.
98      :return: the lineshape transformed data, which is stored in the
    variable y_lineshape.
99      """
100     if spec == "abs":
101         energy_reciprocal = 1.0 / x
102         y_lineshape = energy_reciprocal * y
103 
104     elif spec == "ems":
105         energy_pent_reciprocal = 1.0 / x**5
106         y_lineshape = energy_pent_reciprocal * y
107 
108     else:
109         print("Please choose a valid type of spectroscopy
    information")
110 
111     return y_lineshape
112 
113 
114 def main():
115     parser = argparse.ArgumentParser(description="Transform
    Experimental Spectra")
116     parser.add_argument("input_filename", type=str, help="Input
    filename")
117     parser.add_argument("spec_type", type=str, choices=["abs", "ems"
    ], help="Spectroscopy type: 'abs' or 'ems'")
118     parser.add_argument("output_filename", type=str, help="Output
    filename")
119     args = parser.parse_args()
120 
121     exp_data = np.loadtxt(args.input_filename, delimiter=",")  # X
    in nm, Y in Lambda-Intensity
122     exp_x = NM_TO_EV / exp_data[:, 0]  # nm --> eV Conversion
123     exp_y = exp_data[:, 1]
124 
125     print("Performing Transformation")
126     exp_y_frequency_domain =
    exp_Intensity_lambda_to_frequency_domain_Transformation(
```

```
        exp_x, exp_y, spec=args.spec_type
    )
    exp_y_lineshape = exp_Lineshape_Transform(exp_x, exp_y, spec=
    args.spec_type)

    print("Transformation Complete, Saving Data")
    print(exp_y_frequency_domain)
    print(exp_y_lineshape)
    save_file(f"exp_{args.output_filename}_freq_domain.csv", exp_x,
    exp_y_frequency_domain)
    save_file(f"exp_{args.output_filename}_lineshape.csv", exp_x,
    exp_y_lineshape)
    print("Done!!")

if __name__ == "__main__":
    main()
```

Listing B.2: Python code for transforming experimental spectra to lineshapes

B.1.2 Transforming Computed Intensity Spectra to Lineshapes

Lineshape transformation of absorption and fluorescence spectra generated using computational methods can be obtained via the following code:

```
    python3 experimental_to_lineshape_spectra_transformation.py --
    input_filename exp_emission.csv --spec_type ems --is_gaussian
    True --temp_col FTFC --output_filename transformed
```

Listing B.3: How to Run?

```
# ---------------------------------------
# A Python Program To Transform Computed
# Intensity-Based Spectra to Lineshapes
# ---------------------------------------
import numpy as np
import argparse

# Conversion factor
INVCM_TO_EV = 0.00012398
```

```
10
11 # Intensity to Lineshape Transformation
12 def transform_computed_spectra_to_lineshape(spectrum_x: np.array,
    spectrum_y: np.array, spectroscopy_type: str = "abs", is_gaussian
    : bool = True) -> np.array:
13     """
14     Transforms a computed spectrum into a lineshape by adjusting the
     y-values.
15
16     Parameters:
17     spectrum_x (np.array): 1D array of x-values (spectrum).
18     spectrum_y (np.array): 1D array of y-values (spectrum).
19     spectroscopy_type (str): Type of spectroscopy, "abs" (absorption
    ) or "ems" (emission). Default is "abs".
20     is_gaussian (bool): If True, apply Gaussian16 transformation.
    Default is True.
21
22     Returns:
23     np.array: Transformed 1D array of y-values (lineshape).
24     """
25     assert len(spectrum_x) == len(spectrum_y), "x and y arrays must
    be of the same length."
26
27     if spectroscopy_type == "abs":
28         transformed_y = spectrum_y / spectrum_x
29     elif spectroscopy_type == "ems":
30         power = 4 if is_gaussian else 3
31         transformed_y = spectrum_y / spectrum_x ** power
32     else:
33         raise ValueError("Invalid spectroscopy type. Choose 'abs' or
     'ems'.")
34
35     return transformed_y
36
37
38 # Save Data to a CSV file: Energy(eV), Intensity(arb units),
    Lineshape(arb units)
39 def save_file(filename, *data_arrays, custom_header=False):
```

```
    """
    Save data to a CSV file.

    Parameters:
    filename (str): Name of the file to save to.
    data_arrays: Variable list of data arrays to save.
    custom_header (bool): Whether to use a custom header.

    Returns:
    None.
    """
    if custom_header:
        header = "Energy(eV),Intensity,Lineshape"
    else:
        header = "Energy(eV), Intensity(arb units)"

    data = np.column_stack(data_arrays)
    cols = data.shape[1]
    np.savetxt(f"./{filename}", data, fmt=["%1.6f" for _ in range(cols)], header=header, delimiter=",")


def main():
    parser = argparse.ArgumentParser(description="Transform Computed Spectra")
    parser.add_argument("--input_filename", type=str, help="Input filename")
    parser.add_argument("--spec_type", type=str, default="abs", choices=["abs", "ems"], help="Spectroscopy type: 'abs' or 'ems'")
    parser.add_argument("--is_gaussian", type=bool, default=True, help="Software: True: Gaussian or False: Other")
    parser.add_argument("--temp_col", type=str, default="FTFC", help="FTFC or ZTFC")
    parser.add_argument("--output_filename", type=str, help="Output filename")
    args = parser.parse_args()

    print("Transforming Computed Spectra to Lineshape...")
```

```
71      if args.temp_col == "FTFC":
72          data = np.loadtxt(args.input_filename, delimiter=",",
    usecols=(0, 2), converters={0: lambda x: float(x) * INVCM_TO_EV})
73      elif args.temp_col == "ZTFC":
74          data = np.loadtxt(args.input_filename, delimiter=",",
    usecols=(0, 1), converters={0: lambda x: float(x) * INVCM_TO_EV})
75      else:
76          raise ValueError("Invalid temperature column. Choose 'FTFC'
    or 'ZTFC'.")
77      spectrum_x_energy_eV = data[:, 0]
78      spectrum_y_intenstiy = data[:, 1]
79
80      transformed_y = transform_computed_spectra_to_lineshape(
    spectrum_x_energy_eV, spectrum_y_intenstiy, spectroscopy_type=
    args.spec_type, is_gaussian=args.is_gaussian)
81      print("Transformed Computed Spectra to Lineshape...")
82      save_file(f"comp_{args.output_filename}_lineshape.csv",
    spectrum_x_energy_eV, spectrum_y_intenstiy, transformed_y,
    custom_header=True)
83
84  if __name__ == "__main__":
85      main()
```

Listing B.4: Python code for transforming computed intensity spectra to lineshapes

Appendix C

Chapter 5 Supplemental Information

C.1 Computing Excitonic Couplings Between Chromophores Using Various Methods

C.1.1 Transition Coupling Via Transition Charges

```
#----------------------------------------
# A Python Program For Computing Coulomic
# Using Transition Dipole Moments
#----------------------------------------

import re
import argparse
import numpy as np

def banner(title, char="=", width=80):
    """
    This function prints a banner with the specified title.

    :param title: The title of the banner.
    :param char: The character used to create the border of the
   banner. Default is '='.
```

```
16      :param width: The width of the banner. Default is 80.
17      """
18      print(char * width)
19      print(title.center(width))
20      print(char * width)
21
22
23  # Print the banner
24  banner("Coulombic Coupling Via PDA")
25
26
27  def read_xyz(input_file):
28      """
29      Reads an XYZ file and returns the input geometry as a NumPy
        array.
30
31      :param input_file: The path to the input XYZ file.
32      :return: A NumPy array of shape (natoms, 4) containing the
        atomic
33      symbols (as integers) and the x, y, z coordinates for each atom.
34      """
35      natoms = 0
36      with open(input_file) as f:
37          for line in f:
38              if "NAtoms=" in line:
39                  natoms = int(line.split()[3])
40                  break
41
42          f.seek(0)
43          input_geometry = np.zeros((natoms, 4))
44          for line in f:
45              if "Input orientation:" in line:
46                  # Skip 4 lines after finding "Input orientation:"
47                  for _ in range(4):
48                      next(f)
49                  # Read the next 'natoms' lines for coordinates
50                  for row in range(natoms):
51                      line = next(f).split()
```

```
52                      symb = int(line[1])
53                      x, y, z = map(float, line[3:6])
54                      input_geometry[row] = symb, x, y, z
55                  break  # Exit loop after reading all atoms
56
57      return input_geometry
58
59
60  def extract_atomic_weights(log_file_path):
61      """
62      Reads an input log file and extracts the atomic weights from the
        file.
63
64      :param log_file_path: The path to the input log file containing
    the atomic weights.
65      :return: A NumPy array of the extracted atomic weights.
66      """
67      atomic_weights = []
68      with open(log_file_path, "r") as file:
69          for line in file:
70              if line.startswith(" AtmWgt="):
71                  # Extract all the floating-point numbers from the
    line
72                  weights = re.findall(r"\d+\.\d+", line)
73                  atomic_weights.extend(map(float, weights))
74
75      return np.array(atomic_weights)
76
77
78  def vertical_excitation_energies(file_path, excited_state=1):
79      """
80      Extracts the vertical excitation energy (in eV) for a specified
    excited state from a file.
81
82      :param file_path: The path to the file containing the vertical
    excitation energy information.
83      :param excited_state: The index of the excited state to extract
    the vertical excitation energy for (default is 1).
```

```
84      :return: The vertical excitation energy (in eV) for the
    specified excited state.
85      """
86      with open(file_path, "r") as file:
87          lines = file.readlines()
88
89      # Find the index of the line containing the specified pattern
90      start_index = next(
91          (
92              i
93              for i, line in enumerate(lines)
94              if f"Excited State   {excited_state}:      Singlet-?Sym"
    in line
95          ),
96          None,
97      )
98
99      if start_index is not None:
100         vee_lines = lines[start_index]
101         fields = vee_lines.split()
102         if len(fields) >= 5:
103             vee_eV = fields[4]
104
105     return float(vee_eV)
106
107
108 def extract_TDM_xyz_values(file_path):
109     """
110     Extracts the X, Y, and Z components of the transition dipole
    moment (TDM) from a file.
111
112     :param file_path: The path to the file containing the TDM
    information.
113     :return: A NumPy array containing the X, Y, and Z components of
    the TDM.
114     """
115     with open(file_path, "r") as file:
116         lines = file.readlines()
```

```
117
118     # Find the index of the line containing the specified pattern
119     start_index = next(
120         (
121             i
122             for i, line in enumerate(lines)
123             if "Ground to excited state transition electric dipole
    moments (Au):"
124             in line
125         ),
126         None,
127     )
128
129     # Extract the relevant line
130     if start_index is not None:
131         xyz_line = lines[start_index + 2]
132
133         # Extract the X, Y, and Z values
134         fields = xyz_line.split()
135         if len(fields) >= 6:
136             tdm_x, tdm_y, tdm_z = float(fields[1]), float(fields[2])
    , float(fields[3])
137
138     return np.array([tdm_x, tdm_y, tdm_z])
139
140
141 def center_of_mass(atomic_weights, coordinates):
142     """
143     Calculates the center of mass (COM) of a set of atoms given
    their atomic weights and coordinates.
144
145     :param atomic_weights: A list or NumPy array of atomic weights
    for each atom.
146     :param coordinates: A 2D NumPy array of atom coordinates, where
    each row represents the x, y, z coordinates of an atom.
147     :return: A NumPy array containing the x, y, z coordinates of the
     center of mass.
148     """
```

```
149     assert len(atomic_weights) == len(coordinates)
150     total_mass = np.sum(atomic_weights)
151 
152     weighted_x = np.sum(np.dot(atomic_weights, coordinates[:, 0]))
153     weighted_y = np.sum(np.dot(atomic_weights, coordinates[:, 1]))
154     weighted_z = np.sum(np.dot(atomic_weights, coordinates[:, 2]))
155 
156     x_COM, y_COM, z_COM = (
157         weighted_x / total_mass,
158         weighted_y / total_mass,
159         weighted_z / total_mass,
160     )
161 
162     return np.array([x_COM, y_COM, z_COM])
163 
164 
165 def coupling_via_PDA(TDM_D, TDM_A, COM_D, COM_A):
166     """
167     Calculates the excitonic coupling between two dyes using the
    point-dipole approximation (PDA) method.
168 
169     Parameters:
170         TDM_D (numpy.ndarray): The transition dipole moment (TDM)
    vector of the donor dye.
171         TDM_A (numpy.ndarray): The TDM vector of the acceptor dye.
172         COM_D (numpy.ndarray): The center of mass (COM) vector of
    the donor dye.
173         COM_A (numpy.ndarray): The COM vector of the acceptor dye.
174 
175     Returns:
176         float: The excitonic coupling between the two dyes in eV.
177     """
178     ANGS2BOHR = 1.8897259885789
179     COM_D = COM_D * ANGS2BOHR
180     COM_A = COM_A * ANGS2BOHR
181     R = np.linalg.norm(COM_A - COM_D)
182     return 27.211396132 * (
183         (np.dot(TDM_D, TDM_A) / R**3)
```

```
        - (3 * (np.dot(TDM_D, COM_D) * np.dot(TDM_A, COM_A)) / R**5)
    )


def main():
    parser = argparse.ArgumentParser(description="Process TDM and COM data.")
    parser.add_argument("--dye_1_filename", type=str, help="Filename of dye 1 log file")
    parser.add_argument("--dye_2_filename", type=str, help="Filename of dye 2 log file")
    parser.add_argument("--nAtoms_dye1", type=int, help="Number of atoms in dye 1")
    parser.add_argument("--nAtoms_dye2", type=int, help="Number of atoms in dye 2")
    args = parser.parse_args()

    TDM_D, COM_D = extract_TDM_xyz_values(args.dye_1_filename), center_of_mass(
        extract_atomic_weights(args.dye_1_filename),
        read_xyz(args.dye_1_filename)[0 : args.nAtoms_dye1][:, 1:],
    )
    TDM_A, COM_A = extract_TDM_xyz_values(args.dye_2_filename), center_of_mass(
        extract_atomic_weights(args.dye_2_filename),
        read_xyz(args.dye_2_filename)[0 : args.nAtoms_dye2][:, 1:],
    )

    print(f"NBD TDMs: {TDM_D}")
    print(f"NR TDMs : {TDM_A}")
    print(
        f"Excitonic Coupling via PDA: {coupling_via_PDA(TDM_D, TDM_A, COM_D, COM_A):.5} eV"
    )


if __name__ == "__main__":
```

```
213     main()
```

Listing C.1: Python code for computing Coulombic coupling between chromophores using transition dipole moments

C.1.2 Transition Coupling Via Transition Dipole Moments

```
1  #----------------------------------------
2  # A Python Program For Computing Coulomic
3  # Using Transition Charges
4  #----------------------------------------
5
6  import re
7  import argparse
8  import numpy as np
9
10 def banner(title, char="=", width=80):
11     """
12     This function prints a banner with the specified title.
13
14     :param title: The title of the banner.
15     :param char: The character used to create the border of the
       banner.
16     Default is '='.
17     :param width: The width of the banner. Default is 80.
18     """
19     print(char * width)
20     print(title.center(width))
21     print(char * width)
22
23
24 # Print the banner
25 banner("Coulombic Coupling Via Atomic Transition Charges")
26 ANGS_TO_BOHRS = 1.8897259885789
27 HA_TO_EV = 27.211396132
28
29
30 def read_Zxyzs(input_file: str) -> np.ndarray:
31     """
```

```
    Reads the input geometry from a file and returns a NumPy array
    containing the atomic numbers and coordinates.

    Parameters:
    - input_file (str): The path to the input file containing the
    geometry.

    Returns:
    - input_geometry (np.ndarray): A 2D NumPy array with shape (
    natoms, 4),
    where the first column contains the atomic numbers and the
    remaining three
    columns contain the x, y, and z coordinates for each atom.
    """

    natoms = 0
    with open(input_file) as f:
        for line in f:
            if "NAtoms=" in line:
                natoms = int(line.split()[3])
                break

        f.seek(0)
        input_geometry = np.zeros((natoms, 4))
        for line in f:
            if "Input orientation:" in line:
                # Skip 4 lines after finding "Input orientation:"
                for _ in range(4):
                    next(f)
                # Read the next 'natoms' lines for coordinates
                for row in range(natoms):
                    line = next(f).split()
                    atNum = int(line[1])
                    x, y, z = map(float, line[3:6])
                    input_geometry[row] = atNum, x, y, z
                break

    return input_geometry
```

```
67
68
69 def read_NATOs(g09_file: str, natoms: int, atNums: list) -> np.
   ndarray:
70     """
71     Reads a G09 logfile and returns the atomic-centered Natural
72     Transition Charges (NTO), obtained via the G09 input line:
73     td=(nstates=1) nosymm Pop=NTO Density=(Transition=1)
74
75     Parameters:
76     - g09_file: str
77         Path to the G09 log file.
78     - natoms: int
79         Number of atoms.
80     - atNums: list
81         List of atomic numbers corresponding to each atom.
82
83     Returns:
84     - NATO: np.ndarray
85         Array of NATO charges in order of atomic positions.
86     """
87     NATO = np.zeros(natoms)
88     with open(g09_file) as f:
89         # Skip lines until Mulliken charges are found
90         for line in f:
91             if line.strip():
92                 if " Mulliken charges:" in line:
93                     line = next(f)
94                     line = next(f)
95                     # Read charges for each atom
96                     for i in range(natoms):
97                         charge_line = line.split()
98                         charge = float(charge_line[2])
99                         NATO[i] = float(atNums[i]) - charge
100                        line = next(f)
101        f.close()
102    return NATO
103
```

```python

def coupling_via_TC(
    NATO_1: np.ndarray,
    NATO_2: np.ndarray,
    coordinates_1: np.ndarray,
    coordinates_2: np.ndarray,
) -> float:
    """
    Calculates the CATC exciton coupling J based on the Coulomb interaction
    between Atomic Transition Charges in two molecules.

    Parameters:
    - NATO_1: np.ndarray[float]
        List of NATO charges for molecule 1.
    - NATO_2: np.ndarray[float]
        List of NATO charges for molecule 2.
    - coordinates_1: np.ndarray
        Nx3 array of x, y, z coordinates for molecule 1.
    - coordinates_2: np.ndarray
        Nx3 array of x, y, z coordinates for molecule 2.

    Returns:
    - J: float
        Exciton coupling.
    """
    coordinates_1 = coordinates_1 * ANGS_TO_BOHRS
    coordinates_2 = coordinates_2 * ANGS_TO_BOHRS

    J = 0
    for i in range(len(NATO_1)):
        for j in range(len(NATO_2)):
            J += (NATO_1[i] * NATO_2[j]) / (
                np.linalg.norm(coordinates_2[j] - coordinates_1[i])
            )

    return J

```

```
141
142 def main():
143     parser = argparse.ArgumentParser(description="Process TDM and
    COM data.")
144     parser.add_argument("--dye_1_filename", type=str, help="Filename
     of dye 1 log file")
145     parser.add_argument("--dye_2_filename", type=str, help="Filename
     of dye 2 log file")
146     parser.add_argument("--nAtoms_dye1", type=int, help="Number of
    atoms in dye 1")
147     parser.add_argument("--nAtoms_dye2", type=int, help="Number of
    atoms in dye 2")
148     args = parser.parse_args()
149
150     dye1_coords = read_Zxyzs(args.dye_1_filename)
151     dye2_coords = read_Zxyzs(args.dye_2_filename)
152
153     dye1_NATOs = read_NATOs(args.dye_1_filename, args.nAtoms_dye1,
    dye1_coords[:, 0])
154     dye2_NATOs = read_NATOs(args.dye_2_filename, args.nAtoms_dye2,
    dye2_coords[:, 0])
155
156     print(
157         f"Excitonic Coupling via Transition Charges: {
    coupling_via_TC(dye1_NATOs, dye2_NATOs, dye1_coords[:,1:],
    dye2_coords[:,1:]) * HA_TO_EV:.5} eV"
158     )
159
160
161 if __name__ == "__main__":
162     main()
```

Listing C.2: Python code for computing Coulombic coupling between chromophores using transition dipole moments

C.1.3 Transition Coupling Via Diabatization

```
1 #----------------------------------------
2 # A Python Program For Computing Supra Molecular
```

```
# Coulomic Using the Diabatization Approach
#----------------------------------------

import argparse
import numpy as np

# Conversion Factors
ANGS_2_BOHR = 1.8897259885789
HA_2_EV = 27.211396132


def print_banner(title, char="=", width=80):
    """
    Print a banner with the specified title.

    Args:
        title (str): The title of the banner.
        char (str, optional): The character used to create the border of the banner. Default is '='.
        width (int, optional): The width of the banner. Default is 80.
    """
    print(char * width)
    print(title.center(width))
    print(char * width)


# Print the banner
print_banner("Coulombic Coupling Via Diabatization")


def extract_vertical_excitation_energy(file_path, excited_state=1):
    """
    Extract the vertical excitation energy for a specified excited state from a file.

    Args:
        file_path (str): The path to the file containing the
```

```
    vertical excitation energy data.
38          excited_state (int, optional): The index of the excited
    state for which to extract
39              the vertical excitation energy. Default is 1.
40
41      Returns:
42          float: The vertical excitation energy in electron volts (eV)
     for the specified excited state,
43              or None if the excited state is not found.
44      """
45      with open(file_path, "r") as file:
46          lines = file.readlines()
47
48      # Find the index of the line containing the specified pattern
49      start_index = next(
50          (
51              i
52              for i, line in enumerate(lines)
53              if f"Excited State   {excited_state}:      Singlet-?Sym"
     in line
54          ),
55          None,
56      )
57
58      if start_index is not None:
59          vee_line = lines[start_index]
60          fields = vee_line.split()
61          if len(fields) >= 5:
62              vee_eV = float(fields[4])
63              vee_hartree = vee_eV / HA_2_EV
64              return vee_hartree
65
66      return None
67
68
69  def extract_tdm_xyz_values(file_path, excited_state=1, max_states
    =10):
70      """
```

```
    Extract the transition electric dipole moment (TDM) values for a specified excited state from a file.

    Args:
        file_path (str): The path to the file containing the TDM data.
        excited_state (int, optional): The index of the excited state for which to extract the TDM values.
            Default is 1.

    Returns:
        list[float] or str: A list of the x, y, and z components of the TDM for the specified excited state,
            or an error message if the pattern or excited state is not found.
    """
    with open(file_path, "r") as file:
        lines = file.readlines()

    # Find the index of the pattern
    pattern = "Ground to excited state transition electric dipole moments (Au):"
    start_index = next((i for i, line in enumerate(lines) if pattern in line), None)

    if start_index is None:
        return f"Pattern '{pattern}' not found in the file."

    # Extract the required rows
    data_lines = lines[start_index + 2 : start_index + max_states]

    # Find the row with the specified excited state
    for line in data_lines:
        row = line.split()
        try:
            if int(row[0]) == excited_state:
                return [float(value) for value in row[1:4]]
        except ValueError:
```

```
102             continue
103
104     return f"Excited state {excited_state} not found in the expected
        rows."
105
106
107 def diabatize(dims1, dims2, mon_a, mon_b, e1, e2):
108     """
109     Compute the diabatic coupling (J) between the first two excited
        states of a dimer
110     molecule using the transition dipole moments (TDMs) of the
        monomer states.
111
112     Note: Units of both TDMs and energies should be in atomic units.
113
114     Args:
115         dims1 (numpy.ndarray): TDMs of the s1 state of the dimer.
116         dims2 (numpy.ndarray): TDMs of the s2 state of the dimer.
117         mon_a (numpy.ndarray): TDMs of the s1 state of monomer A.
118         mon_b (numpy.ndarray): TDMs of the s1 state of monomer B.
119         e1 (float): Energy of the s1 state of the dimer.
120         e2 (float): Energy of the s2 state of the dimer.
121
122     Returns:
123         float: The diabatic coupling (J) between the first two
        excited states of the dimer.
124     """
125     dimer = np.concatenate((dims1, dims2)).reshape(2, len(dims1))
126     monomer = np.concatenate((mon_a, mon_b)).reshape(2, len(mon_a))
127
128     m = np.dot(dimer, monomer.T)
129
130     U, _sigMA, V_T = np.linalg.svd(m)
131
132     C_best = (np.dot(U, V_T)).transpose()
133
134     mat_VEE = np.matrix(([e1, 0], [0, e2]))
135
```

```
136     H = np.dot(np.dot(C_best, mat_VEE), C_best.transpose())
137     J = H[0, 1]
138     return J
139 
140 
141 def main():
142     parser = argparse.ArgumentParser(description="Supramolecular
    coupling calculation")
143     parser.add_argument("--dimer_filename", type=str, help="Dimer
    log file")
144     parser.add_argument(
145         "--excited_states", type=int, nargs="+", help="Excited
    states to consider"
146     )
147     parser.add_argument("--donor_filename", type=str, help="Donor
    log file")
148     parser.add_argument("--acceptor_filename", type=str, help="
    Acceptor log file")
149     parser.add_argument("--max_states", type=int, default=10,
    required=False, help="Maximum nstates=N")
150     args = parser.parse_args()
151 
152     acceptor_file = args.acceptor_filename
153     donor_file = args.donor_filename
154     dimer_file = args.dimer_filename
155     excited_states = args.excited_states
156     max_states = args.max_states
157 
158     dimer_tdm_1 = extract_tdm_xyz_values(dimer_file, excited_state=
    excited_states[0], max_states=max_states)
159     e1 = extract_vertical_excitation_energy(dimer_file,
    excited_state=excited_states[0])
160     dimer_tdm_2 = extract_tdm_xyz_values(dimer_file, excited_state=
    excited_states[1], max_states=max_states)
161     e2 = extract_vertical_excitation_energy(dimer_file,
    excited_state=excited_states[1])
162     acceptor_tdm = extract_tdm_xyz_values(acceptor_file,
    excited_state=1, max_states=max_states)
```

```
163     donor_tdm = extract_tdm_xyz_values(donor_file, excited_state=1,
    max_states=max_states)
164 
165     if isinstance(dimer_tdm_1, str) or isinstance(dimer_tdm_2, str)
    or isinstance(acceptor_tdm, str) or isinstance(donor_tdm, str):
166         print("Error occurred while extracting TDM values.")
167         return
168 
169     if e1 is None or e2 is None:
170         print("Error occurred while extracting vertical excitation
    energies.")
171         return
172 
173     print(f"Dimer TDM-1: {dimer_tdm_1}, Dimer E1: {e1 * HA_2_EV :.4f
    } eV")
174     print(f"Dimer TDM-2: {dimer_tdm_2}, Dimer E2: {e2 * HA_2_EV :.4f
    } eV")
175     print(f"Acceptor TDM: {acceptor_tdm},\nDonor TDM: {donor_tdm}")
176 
177     coupling = diabatize(dimer_tdm_1, dimer_tdm_2, acceptor_tdm,
    donor_tdm, e1, e2)
178     print(f"The Coupling From Diabatization is: {coupling * HA_2_EV
    :.4f} eV")
179 
180 
181 if __name__ == "__main__":
182     main()
```

Listing C.3: Python code for computing Coulombic coupling between chromophores using supra molecular diabatization approach

Bibliography

[1] E. Schrdinger. An undulatory theory of the mechanics of atoms and molecules. *Physical Review*, 28(6):10491070, 1926.

[2] Andrew J. Pounds. Introduction to quantum mechanics: A time-dependent perspective (david j. tannor). *Journal of Chemical Education*, 85(7):919, 2008.

[3] THEODORE LYMAN. An extension of the spectrum in the extreme ultra-violet. *Nature*, 93(2323):241241, 1914.

[4] J. J. Balmer. Notiz ber die spectrallinien des wasserstoffs. *Annalen der Physik*, 261(5):8087, 1885.

[5] F. Paschen. Zur kenntnis ultraroter linienspektra. i. (normalwellenlngen bis 27000 .e.). *Annalen der Physik*, 332(13):537570, 1908.

[6] C. J. H. Schutte. An elementary approach to the wave-mechanical harmonic oscillator. *Journal of Chemical Education*, 45(9):567, 1968.

[7] Harvey F. Blanck. Introduction to a quantum mechanical harmonic oscillator using a modified particle-in-a-box problem. *Journal of Chemical Education*, 69(2):98, 1992.

[8] Michael Messina. A heuristic derivation of the linear harmonic oscillator energy levels. *Journal of Chemical Education*, 77(4):492, 2000.

[9] S. Keith Dunn. Variational method applied to the harmonic oscillator. *Journal of Chemical Education*, 79(11):1378, 2002.

[10] Theresa Julia Zielinski. Exploring the harmonic oscillator wave functions. *Journal of Chemical Education*, 84(7):1232, 2007.

[11] Acadmie des sciences (France) and Centre national de la recherche scientifique (France). *Comptes rendus hebdomadaires des sances de l'Acadmie des sciences*, volume t.58 (1864). Paris, publis avec le concours du Centre national de la recherche scientifique par MM. les secrtaires perptuels, -1965, 1864. https://www.biodiversitylibrary.org/bibliography/4466.

[12] M. Born and R. Oppenheimer. Zur quantentheorie der molekeln. *Annalen der Physik*, 389(20):457484, 1927.

[13] Sebastian Spicher and Stefan Grimme. Single-point hessian calculations for improved vibrational frequencies and rigid-rotor-harmonic-oscillator thermodynamics. *Journal of Chemical Theory and Computation*, 17(3):17011714, 2021.

[14] Leila Zeidabadinejad and Maryam Dehestani. Effects of displacementdistortion of potential energy surfaces on nonadiabatic electron transfers via conical intersections: Application to so2 and trans-1,3,5-hexatriene. *The Journal of Physical Chemistry A*, 120(26):44314446, 2016.

[15] Enrico Tapavicza, Filipp Furche, and Dage Sundholm. Importance of vibronic effects in the uvvis spectrum of the 7,7,8,8-tetracyanoquinodimethane anion. *Journal of Chemical Theory and Computation*, 12(10):50585066, 2016.

[16] Simone Pisana, Michele Lazzeri, Cinzia Casiraghi, Kostya S. Novoselov, A. K. Geim, Andrea C. Ferrari, and Francesco Mauri. Breakdown of the adiabatic bornoppenheimer approximation in graphene. *Nature Materials*, 6(3):198201, 2007.

[17] Adam W. Bushmaker, Vikram V. Deshpande, Scott Hsieh, Marc W. Bockrath, and Stephen B. Cronin. Direct observation of bornoppenheimer approximation breakdown in carbon nanotubes. *Nano Letters*, 9(2):607611, 2009.

[18] Igor Rahinov, Russell Cooper, Daniel Matsiev, Christof Bartels, Daniel J. Auerbach, and Alec M. Wodtke. Quantifying the breakdown of the bornoppenheimer approximation in surface chemistry. *Physical Chemistry Chemical Physics*, 13(28):12680, 2011.

[19] Alexei Stuchebrukhov. Tunneling time and the breakdown of bornoppenheimer approximation. *The Journal of Physical Chemistry B*, 120(8):14081417, 2015.

[20] M Ben-Nun and Todd J Martnez. Photodynamics of ethylene: ab initio studies of conical intersections. *Chemical Physics*, 259(23):237248, 2000.

[21] Benjamin G. Levine and Todd J. Martnez. Isomerization through conical intersections. *Annual Review of Physical Chemistry*, 58(1):613634, 2007.

[22] Barak Hirshberg, Valerio Rizzi, and Michele Parrinello. Path integral molecular dynamics for bosons. *Proceedings of the National Academy of Sciences*, 116(43):2144521449, 2019.

[23] Tammie R. Nelson, Alexander J. White, Josiah A. Bjorgaard, Andrew E. Sifain, Yu Zhang, Benjamin Nebgen, Sebastian Fernandez-Alberti, Dmitry Mozyrsky, Adrian E. Roitberg, and Sergei Tretiak. Non-adiabatic excited-state molecular dynamics: Theory and applications for modeling photophysics in extended molecular materials. *Chemical Reviews*, 120(4):22152287, 2020.

[24] Angus J. Dunnett, Duncan Gowland, Christine M. Isborn, Alex W. Chin, and Tim J. Zuehlsdorff. Influence of non-adiabatic effects on linear absorption spectra in the condensed phase: Methylene blue. *The Journal of Chemical Physics*, 155(14):144112, 10 2021.

[25] Yu Kay Law and Ali A. Hassanali. Role of quantum vibrations on the structural, electronic, and optical properties of 9-methylguanine. *The Journal of Physical Chemistry A*, 119(44):1081610827, 2015.

[26] Subrahmanyam Sappati, Ali Hassanali, Ralph Gebauer, and Prasenjit Ghosh. Nuclear quantum effects in a hiv/cancer inhibitor: The case of ellipticine. *The Journal of Chemical Physics*, 145(20), 2016.

[27] Tim J. Zuehlsdorff, Joseph A. Napoli, Joel M. Milanese, Thomas E. Markland, and Christine M. Isborn. Unraveling electronic absorption spectra using nuclear quantum effects: Photoactive yellow protein and green fluorescent protein chromophores in water. *J. Chem. Phys.*, 149(2):024107, 2018.

[28] YK Law and AA Hassanali. The importance of nuclear quantum effects in spectral line broadening of optical spectra and electrostatic properties in aromatic chromophores. *J. Chem. Phys.*, 148(10):102331, 2018.

[29] Attila Szabo and Neil S. Ostlund. *Modern Quantum Chemistry: Introduction to Advanced Electronic Structure Theory*. Dover Publications, first edition, 1996.

[30] Michael Messina. The hartree-fock self-consistent field: An allegorical connection using two coupled harmonic oscillators. *Journal of Chemical Education*, 76(10):1439, 1999.

[31] Kevin V. Murphy, Justin M. Turney, and Henry F. Schaefer. Student-friendly guide to molecular integrals. *Journal of Chemical Education*, 95(9):15721578, 2018.

[32] J. C. Slater. The theory of complex spectra. *Physical Review*, 34(10):12931322, 1929.

[33] L. Pietronero and F. Zirilli. Limitations and validity of the hartree-fock method. *Il Nuovo Cimento B Series 11*, 24(1):5762, 1974.

[34] J. A. Pople and R. K. Nesbet. Self-consistent orbitals for radicals. *The Journal of Chemical Physics*, 22(3):571572, 1954.

[35] Carlos A. Jimnez-Hoyos, Thomas M. Henderson, and Gustavo E. Scuseria. Generalized hartreefock description of molecular dissociation. *Journal of Chemical Theory and Computation*, 7(9):26672674, 2011.

[36] Chr. Mller and M. S. Plesset. Note on an approximation treatment for many-electron systems. *Physical Review*, 46(7):618622, 1934.

[37] J. A. Pople, R. Seeger, and R. Krishnan. Variational configuration interaction methods and comparison with perturbation theory. *International Journal of Quantum Chemistry*, 12(S11):149163, 2009.

[38] Ji ek. On the correlation problem in atomic and molecular systems. calculation of wavefunction components in ursell-type expansion using quantum-field theoretical methods. *The Journal of Chemical Physics*, 45(11):42564266, 1966.

[39] Ji ek. On the use of the cluster expansion and the technique of diagrams in calculations of correlation effects in atoms and molecules. *Advances in Chemical Physics*, page 3589, 1969.

[40] J. iek and J. Paldus. Correlation problems in atomic and molecular systems iii. rederivation of the coupledpair manyelectron theory using the traditional quantum chemical methodst. *International Journal of Quantum Chemistry*, 5(4):359379, 1971.

[41] Wolfram Koch and Max C Holthausen. *A chemist's guide to density functional theory*. John Wiley & Sons, 2015.

[42] Brian B. Laird, Richard B. Ross, and Tom Ziegler. *Density-Functional Methods in Chemistry: An Overview*. American Chemical Society, 1996.

[43] Tanja van Mourik, Michael Bhl, and Marie-Pierre Gaigeot. Density functional theory across chemistry, physics and biology. *Philosophical Transactions of the Royal Society A: Mathematical, Physical and Engineering Sciences*, 372(2011):20120488, 2014.

[44] Hajime Hirao, Nandun Thellamurege, and Xi Zhang. Applications of density functional theory to iron-containing molecules of bioinorganic interest. *Frontiers in Chemistry*, 2, 2014.

[45] Naike Ye, Zekai Yang, and Yuchen Liu. Applications of density functional theory in covid-19 drug modeling. *Drug Discovery Today*, 27(5):14111419, 2022.

[46] Ewa Napirkowska, Katarzyna Milcarz, and ukasz Szeleszczuk. Review of applications of density functional theory (dft) quantum mechanical calculations to study the high-pressure polymorphs of organic crystalline materials. *International Journal of Molecular Sciences*, 24(18):14155, 2023.

[47] P. Hohenberg and W. Kohn. Inhomogeneous electron gas. *Physical Review*, 136(3B):B864B871, 1964.

[48] Walter Ritz. ber eine neue methode zur lsung gewisser variationsprobleme der mathematischen physik. *crll*, 1909(135):161, 1909.

[49] Walter Ritz. Theorie der transversalschwingungen einer quadratischen platte mit freien rndern. *Annalen der Physik*, 333(4):737786, 1909.

[50] A.W. Leissa. The historical bases of the rayleigh and ritz methods. *Journal of Sound and Vibration*, 287(45):961978, 2005.

[51] Ja Hyon Ku. *J.W. Strutt, third Baron Rayleigh, The theory of sound, first edition (18771878)*. Elsevier, 2005.

[52] W. Kohn and L. J. Sham. Self-consistent equations including exchange and correlation effects. *Physical Review*, 140(4A):A1133A1138, 1965.

[53] Axel D. Becke. Perspective: Fifty years of density-functional theory in chemical physics. *The Journal of Chemical Physics*, 140(18), 2014.

[54] Narbe Mardirossian and Martin Head-Gordon. Thirty years of density functional theory in computational chemistry: an overview and extensive assessment of 200 density functionals. *Molecular Physics*, 115(19):23152372, 2017.

[55] Lars Goerigk and Nisha Mehta. A trip to the density functional theory zoo: Warnings and recommendations for the user. *Australian Journal of Chemistry*, 72(8):563, 2019.

[56] Pierre-Franois Loos, Anthony Scemama, and Denis Jacquemin. The quest for highly accurate excitation energies: A computational perspective. *The Journal of Physical Chemistry Letters*, 11(6):23742383, 2020.

[57] C. David Sherrill and Henry F. Schaefer. *The Configuration Interaction Method: Advances in Highly Correlated Approaches*. Elsevier, 1999.

[58] John F. Stanton, Jrgen Gauss, Naoto Ishikawa, and Martin Head-Gordon. A comparison of single reference methods for characterizing stationary points of excited state potential energy surfaces. *The Journal of Chemical Physics*, 103(10):41604174, 1995.

[59] So Hirata, Martin Head-Gordon, and Rodney J. Bartlett. Configuration interaction singles, time-dependent hartreefock, and time-dependent density functional theory for the electronic excited states of extended systems. *The Journal of Chemical Physics*, 111(24):1077410786, 1999.

[60] Miguel A.L. Marques Neepa T. Maitra Fernando M.S. Nogueira E.K.U. Gross and Angel Rubio. *Fundamentals of Time-Dependent Density Functional Theory*. Springer Berlin Heidelberg, 2012.

[61] Erich Runge and E. K. U. Gross. Density-functional theory for time-dependent systems. *Physical Review Letters*, 52(12):9971000, 1984.

[62] Ryogo Kubo. Statistical-mechanical theory of irreversible processes. i. general theory and simple applications to magnetic and conduction problems. *Journal of the Physical Society of Japan*, 12(6):570586, 1957.

[63] MARK E. CASIDA. Time-dependent density functional response theory for molecules. In *Recent Advances in Density Functional Methods*, pages 155–192. WORLD SCIENTIFIC, November 1995.

[64] Boris M. Bolotovskii, Victor Ya. Frenkel, and Rudolf Peierls, editors. *Selected Papers*. Springer Berlin Heidelberg, 1991.

[65] S. M. Dancoff. Non-adiabatic meson theory of nuclear forces. *Physical Review*, 78(4):382385, 1950.

[66] Andreas Dreuw and Martin Head-Gordon. Single-reference ab initio methods for the calculation of excited states of large molecules. *Chemical Reviews*, 105(11):40094037, 2005.

[67] David J. Tozer, Roger D. Amos, Nicholas C. Handy, Bjorn O. Roos, and Luis Serrano-ANDRES. Does density functional theory contribute to the understanding of excited states of unsaturated organic compounds? *Molecular Physics*, 97(7):859868, 1999.

[68] Andreas Dreuw and Martin Head-Gordon. Failure of time-dependent density functional theory for long-range charge transfer excited states: The zincbacteriochlorin bacteriochlorin and bacteriochlorophyll spheroidene complexes. *Journal of the American Chemical Society*, 126(12):40074016, 2004.

[69] Stefan Grimme and Maja Parac. Substantial errors from timedependent density functional theory for the calculation of excited states of large π systems. *ChemPhysChem*, 4(3):292295, 2003.

[70] Norman Wright. Application of infrared spectroscopy to industrial research. *Industrial Engineering Chemistry Analytical Edition*, 13(1):18, 1941.

[71] Frank S. Parker. *Applications of Infrared Spectroscopy in Biochemistry, Biology, and Medicine*. Springer US, 1971.

[72] Krzysztof B. Be, Justyna Grabska, and Christian W. Huck. Biomolecular and bioanalytical applications of infrared spectroscopy - a review. *Analytica Chimica Acta*, 1133:150177, 2020.

[73] Tamer A. Addissouky, Ibrahim El Tantawy El Sayed, Majeed M. A. Ali, and Mahmood Hasen Shuhata Alubiady. Optical insights into fibrotic livers: Applications of near-infrared spectroscopy and machine learning. *Archives of Gastroenterology Research*, 5(1):110, 2024.

[74] Faizan Ur Rahman, Shahab Khan, Maooz Ur Rahman, Rukhsana Zaib, Mudassir Ur Rahman, Riaz Ullah, Muhammad Zahoor, and Abdul Waheed Kamran. Effect of ionic strength on dnadye interactions of victoria blue b and methylene green using uvvisible spectroscopy. *Zeitschrift fr Physikalische Chemie*, 238(1):173186, 2023.

[75] Jacy K. Conrad, Harry W. Rollins, Dean R. Peterman, and Robert V. Fox. Design of a high-temperature cell for cobalt-60 irradiations of aqueous solutions with in situ uvvisible spectroscopy. *Review of Scientific Instruments*, 95(2), 2024.

[76] Pedro H.M. Andrade, Christophe Volkringer, Thierry Loiseau, Antonio Tejeda, Matthieu Hureau, and Alain Moissette. Band gap analysis in mof materials: Distinguishing direct and indirect transitions using uvvis spectroscopy. *Applied Materials Today*, 37:102094, 2024.

[77] The Royal Society of Lonndon. Papers of a mathematical and physical character. *Proceedings of the Royal Society of London. Series A, Containing Papers of a Mathematical and Physical Character*, 114(767):243265, 1927.

[78] J. Orear, E. Fermi, A.H. Rosenfeld, and R.A. Schluter. *Nuclear Physics: A Course Given by Enrico Fermi at the University of Chicago*. Committee on publications in the physical sciences / the University of Chicago. University of Chicago Press, 1950.

[79] Rainer Dick. *Time-Dependent Perturbations in Quantum Mechanics*, pages 265–310. Springer International Publishing, Cham, 2020.

[80] Gold Victor. *The IUPAC Compendium of Chemical Terminology*. International Union of Pure and Applied Chemistry (IUPAC), 2014.

[81] Wikipedia contributors. Franckcondon principle — Wikipedia, the free encyclopedia, 2024. [Online; accessed 9-June-2024].

[82] Michael Kasha. Characterization of electronic transitions in complex molecules. *Discussions of the Faraday Society*, 9:14, 1950.

[83] Otto Laporte and William F. Meggers. Some rules of spectral structure*. *Journal of the Optical Society of America*, 11(5):459, 1925.

[84] George Gabriel Stokes. On the change of refrangibility of light. *Philosophical Transactions of the Royal Society of London*, 142:463562, 1852.

[85] Colleen M. Byron and T. C. Werner. Experiments in synchronous fluorescence spectroscopy for the undergraduate instrumental chemistry course. *Journal of Chemical Education*, 68(5):433, May 1991.

[86] Alexander P. Demchenko, Vladimir I. Tomin, and Pi-Tai Chou. Breaking the kasha rule for more efficient photochemistry. *Chemical Reviews*, 117(21):1335313381, 2017.

[87] Joseph R. Lakowicz and Aleksander Balter. Analysis of excited-state processes by phase-modulation fluorescence spectroscopy. *Biophysical Chemistry*, 16(2):117132, 1982.

[88] A. B. P. LEVER. Excited states and reactive intermediates: Photochemistry, photophysics, and electrochemistry. *ACS Symposium Series*, 1986.

[89] Joseph R. Lakowicz, editor. *Principles of Fluorescence Spectroscopy*. Springer US, 2006.

[90] Jangwon Seo, Sehoon Kim, and Soo Young Park. Strong solvatochromic fluorescence from the intramolecular charge-transfer state created by excited-state intramolecular proton transfer. *Journal of the American Chemical Society*, 126(36):1115411155, 2004.

[91] Ignacio Fdez. Galvn, M. Elena Martn, Aurora Muoz-Losa, and Manuel A. Aguilar. Solvatochromic shifts on absorption and fluorescence bands ofn,n-dimethylaniline. *Journal of Chemical Theory and Computation*, 5(2):341349, 2009.

[92] Alexander P. Demchenko. *Spectroscopic Properties of Protein Chromophores*, page 526. Springer Berlin Heidelberg, 1986.

[93] Deborah Stoner-Ma, Andrew A Jaye, Pavel Matousek, Michael Towrie, Stephen R Meech, and Peter J Tonge. Observation of excited-state proton transfer in green fluorescent protein using ultrafast vibrational spectroscopy. *Journal of the American Chemical Society*, 127(9):2864–2865, 2005.

[94] Karin Nienhaus, Fabiana Renzi, Beatrice Vallone, Jörg Wiedenmann, and G. Ulrich Nienhaus. Chromophore-protein interactions in the anthozoan green fluorescent protein asfp499. *Biophysical Journal*, 91(11):42104220, December 2006.

[95] Chong Fang, Renee R Frontiera, Rosalie Tran, and Richard A Mathies. Mapping gfp structure evolution during proton transfer with femtosecond raman spectroscopy. *Nature*, 462(7270):200–204, 2009.

[96] Daria M Shcherbakova and Vladislav V Verkhusha. Chromophore chemistry of fluorescent proteins controlled by light. *Current Opinion in Chemical Biology*, 20:6068, June 2014.

[97] Gottfried Kohler and K. Rechthaler. Solvent effects on excited state relaxation phenomena. *Pure and Applied Chemistry*, 65(8):16471652, January 1993.

[98] Kasper S. Kjær, Kristjan Kunnus, Tobias C. B. Harlang, Tim B. Van Driel, Kathryn Ledbetter, Robert W. Hartsock, Marco E. Reinhard, Sergey Koroidov, Lin Li, Mads G. Laursen, Elisa Biasin, Frederik B. Hansen, Peter Vester, Morten Christensen, Kristoffer Haldrup, Martin M. Nielsen, Pavel Chabera, Yizhu Liu, Hideyuki Tatsuno, Cornelia Timm, Jens Uhlig, Villy Sundstöm, Zoltán Németh, Dorottya Sárosiné Szemes, Éva Bajnóczi, György Vankó, Roberto Alonso-Mori, James M. Glownia, Silke Nelson, Marcin Sikorski, Dimosthenis Sokaras, Henrik T. Lemke, Sophie E. Canton, Kenneth Wärnmark, Petter Persson, Amy A. Cordones, and Kelly J. Gaffney. Solvent control of charge transfer excited state relaxation

pathways in [fe(2, 2′-bipyridine)(cn)4]2-. *Physical Chemistry Chemical Physics*, 20(6):42384249, 2018.

[99] Palas Roy, Faisal Al-Kahtani, Andrew N. Cammidge, and Stephen R. Meech. Solvent tuning excited state structural dynamics in a novel bianthryl. *The Journal of Physical Chemistry Letters*, 14(1):253259, January 2023.

[100] Alberto Marini, Aurora Muñoz Losa, Alessandro Biancardi, and Benedetta Mennucci. What is solvatochromism? *The Journal of Physical Chemistry B*, 114(51):1712817135, December 2010.

[101] Shota Tsuru, Bikramjit Sharma, Masanari Nagasaka, and Christof Hättig. Solvent effects in the ultraviolet and x-ray absorption spectra of pyridazine in aqueous solution. *The Journal of Physical Chemistry A*, 125(33):71987206, August 2021.

[102] Kifah S. M. Salih. Solvent influence on absorption spectra and tautomeric equilibria of symmetric azomethine-functionalized derivatives: Structural elucidation and computational studies. *ChemistryOpen*, 11(2), February 2022.

[103] Hanna S. Abbo, Chin Hung Lai, and Salam J.J. Titinchi. Substituent and solvent effects on uv-visible absorption spectra of chalcones derivatives: Experimental and computational studies. *Spectrochimica Acta Part A: Molecular and Biomolecular Spectroscopy*, 303:123180, December 2023.

[104] Aravindhan R., Jianping Hu, and M. Ummal Momeen. Role of the solvent polarity on the optical and electronic characteristics of 1-iodoadamantane. *RSC Advances*, 13(42):2948929495, 2023.

[105] Karnambaram Anandhan, Margarita Cerón, Venkatesan Perumal, Paulina Ceballos, Paola Gordillo-Guerra, Enrique Pérez-Gutiérrez, Armando E. Castillo, Subbiah Thamotharan, and M. Judith Percino. Solvatochromism and ph effect on the emission of a triphenylimidazole-phenylacrylonitrile derivative: experimental and dft studies. *RSC Advances*, 9(21):1208512096, 2019.

[106] Yeqing Chen, Gaoyang Xiong, Lina Zhu, Jie Huang, Xueying Chen, Yan Chen, and Mingxuan Cao. Enhanced fluorescence and environmental stability of red-emissive carbon dots via chemical bonding with cellulose films. *ACS Omega*, 7(8):68346842, February 2022.

[107] Joseph R. Lakowicz and Gregorio Weber. Quenching of fluorescence by oxygen. probe for structural fluctuations in macromolecules. *Biochemistry*, 12(21):41614170, October 1973.

[108] Filipp Furche and Reinhart Ahlrichs. Adiabatic time-dependent density functional methods for excited state properties. *The Journal of Chemical Physics*, 117(16):74337447, 2002.

[109] Denis Jacquemin, Eric A. Perpte, Oleg A. Vydrov, Gustavo E. Scuseria, and Carlo Adamo. Assessment of long-range corrected functionals performance for n* transitions in organic dyes. *The Journal of Chemical Physics*, 127(9), 2007.

[110] Mario R. Silva-Junior, Marko Schreiber, Stephan P. A. Sauer, and Walter Thiel. Benchmarks for electronically excited states: Time-dependent density functional theory and density functional theory based multireference configuration interaction. *The Journal of Chemical Physics*, 129(10), 2008.

[111] Michael J. G. Peach, Peter Benfield, Trygve Helgaker, and David J. Tozer. Excitation energies in density functional theory: An evaluation and a diagnostic test. *The Journal of Chemical Physics*, 128(4), 2008.

[112] Jianmin Tao, Sergei Tretiak, and Jian-Xin Zhu. Performance of a nonempirical metageneralized gradient approximation density functional for excitation energies. *The Journal of Chemical Physics*, 128(8), 2008.

[113] Denis Jacquemin, Valrie Wathelet, Eric A. Perpte, and Carlo Adamo. Extensive td-dft benchmark: Singlet-excited states of organic molecules. *Journal of Chemical Theory and Computation*, 5(9):24202435, 2009.

[114] Mary A. Rohrdanz, Katie M. Martins, and John M. Herbert. A long-range-corrected density functional that performs well for both ground-state properties and time-dependent density functional theory excitation energies, including charge-transfer excited states. *The Journal of Chemical Physics*, 130(5), 2009.

[115] Lars Goerigk and Stefan Grimme. Assessment of td-dft methods and of various spin scaled cis(d) and cc2 versions for the treatment of low-lying valence excitations of large organic dyes. *The Journal of Chemical Physics*, 132(18), 2010.

[116] Denis Jacquemin, Eric A. Perpte, Ilaria Ciofini, and Carlo Adamo. Assessment of functionals for td-dft calculations of singlettriplet transitions. *Journal of Chemical Theory and Computation*, 6(5):15321537, 2010.

[117] Marco Caricato, Gary W. Trucks, Michael J. Frisch, and Kenneth B. Wiberg. Electronic transition energies: A study of the performance of a large range of single reference density functional and wave function methods on valence and rydberg states compared to experiment. *Journal of Chemical Theory and Computation*, 6(2):370383, 2010.

[118] Kiet A. Nguyen, Paul N. Day, and Ruth Pachter. Analytical energy gradients of coulombattenuated timedependent density functional methods for excited states. *International Journal of Quantum Chemistry*, 110(12):22472255, 2010.

[119] Narbe Mardirossian, John A. Parkhill, and Martin Head-Gordon. Benchmark results for empirical post-gga functionals: Difficult exchange problems and independent tests. *Physical Chemistry Chemical Physics*, 13(43):19325, 2011.

[120] Kiet A. Nguyen, Paul N. Day, and Ruth Pachter. The performance and relationship among range-separated schemes for density functional theory. *The Journal of Chemical Physics*, 135(7), 2011.

[121] Ke Yang, Roberto Peverati, Donald G. Truhlar, and Rosendo Valero. Density functional study of multiplicity-changing valence and rydberg excitations of p-block elements: Delta self-consistent field, collinear spin-flip time-dependent density functional theory (dft), and conventional time-dependent dft. *The Journal of Chemical Physics*, 135(4), 2011.

[122] Afshan Mohajeri and Mojtaba Alipour. Time-dependent density functional theory benchmarking for the calculations of atomic spectra: efficiency of exc-etdz basis set. *Theoretical Chemistry Accounts*, 131(3), 2012.

[123] Fabrizio Santoro and Denis Jacquemin. Going beyond the vertical approximation with timedependent density functional theory. *WIREs Computational Molecular Science*, 6(5):460486, 2016.

[124] Joseph D. Alia and Joseph A. Flack. Unspecified verticality of franckcondon transitions, absorption and emission spectra of cyanine dyes, and a classically inspired approximation. *RSC Advances*, 10(70):4315343167, 2020.

[125] Amjad Ali, Muhammad Imran Rafiq, Baojing Zhou, and Weihua Tang. Evaluating the nature of the vertical excited states of fused-ring electron acceptors using td-dft and density-based charge transfer. *Physical Chemistry Chemical Physics*, 23(28):1528215291, 2021.

[126] Talapunur Vikramaditya and Shiang-Tai Lin. Accurate prediction of vertical emission from excited-state tuning of range-separated density functional theory. *The Journal of Physical Chemistry C*, 124(33):1796417970, 2020.

[127] Marc Dierksen and Stefan Grimme. The vibronic structure of electronic absorption spectra of large molecules: a time-dependent density functional study on the influence of exact hartreefock exchange. *The Journal of Physical Chemistry A*, 108(46):1022510237, 2004.

[128] Robert Send, Michael Khn, and Filipp Furche. Assessing excited state methods by adiabatic excitation energies. *Journal of Chemical Theory and Computation*, 7(8):23762386, 2011.

[129] Denis Jacquemin, Aurlien Planchat, Carlo Adamo, and Benedetta Mennucci. Td-dft assessment of functionals for optical 00 transitions in solvated dyes. *Journal of Chemical Theory and Computation*, 8(7):23592372, 2012.

[130] Benjamin Lasorne, Joaquim Jornet-Somoza, Hans-Dieter Meyer, David Lauvergnat, Michael A. Robb, and Fabien Gatti. Vertical transition energies vs. absorption maxima: Illustration with the uv absorption spectrum of ethylene.

Spectrochimica Acta Part A: Molecular and Biomolecular Spectroscopy, 119:5258, 2014.

[131] Shuming Bai, Ritam Mansour, Ljiljana Stojanovi, Josene M. Toldo, and Mario Barbatti. On the origin of the shift between vertical excitation and band maximum in molecular photoabsorption. *Journal of Molecular Modeling*, 26(5), 2020.

[132] Jamie Gibson, Andrew P. Monkman, and Thomas J. Penfold. The importance of vibronic coupling for efficient reverse intersystem crossing in thermally activated delayed fluorescence molecules. *ChemPhysChem*, 17(19):29562961, 2016.

[133] Andreas Lehr, Sandra Gmez, Michael A. Parkes, and Graham A. Worth. The role of vibronic coupling in the electronic spectroscopy of maleimide: a multi-mode and multi-state quantum dynamics study. *Physical Chemistry Chemical Physics*, 22(43):2527225283, 2020.

[134] Eric A. Arsenault, Addison J. Schile, David T. Limmer, and Graham R. Fleming. Vibronic coupling in energy transfer dynamics and two-dimensional electronicvibrational spectra. *The Journal of Chemical Physics*, 155(5), 2021.

[135] Wataru Ota, Motoyuki Uejima, and Tohru Sato. Role of vibronic couplings and energy gap in the internal conversion process of a molecule. *Bulletin of the Chemical Society of Japan*, 96(6):582590, 2023.

[136] U. Priyanka, Aishwarya Paul, and T. Mondal. Vibronic coupling and ultrafast relaxation dynamics in the first five excited singlet electronic states of bithiophene. *The Journal of Chemical Physics*, 160(12), 2024.

[137] Tamar Stein, Leeor Kronik, and Roi Baer. Reliable prediction of charge transfer excitations in molecular complexes using time-dependent density functional theory. *Journal of the American Chemical Society*, 131(8):28182820, 2009.

[138] Ruifang Li, Jingjing Zheng, and Donald G. Truhlar. Density functional approximations for charge transfer excitations with intermediate spatial overlap. *Physical Chemistry Chemical Physics*, 12(39):12697, 2010.

[139] Erik Donovan Hedegrd, Frank Heiden, Stefan Knecht, Emmanuel Fromager, and Hans Jrgen Aagaard Jensen. Assessment of charge-transfer excitations with time-dependent, range-separated density functional theory based on long-range mp2 and multiconfigurational self-consistent field wave functions. *The Journal of Chemical Physics*, 139(18), 2013.

[140] Christine M. Isborn, Brendan D. Mar, Basile F. E. Curchod, Ivano Tavernelli, and Todd J. Martnez. The charge transfer problem in density functional theory calculations of aqueously solvated molecules. *The Journal of Physical Chemistry B*, 117(40):1218912201, October 2013.

[141] Gregorio Garca, Carlo Adamo, and Ilaria Ciofini. Evaluating pushpull dye efficiency using td-dft and charge transfer indices. *Physical Chemistry Chemical Physics*, 15(46):20210, 2013.

[142] Stephan Kmmel. Chargetransfer excitations: A challenge for timedependent density functional theory that has been met. *Advanced Energy Materials*, 7(16), 2017.

[143] Marco Campetella, Federica Maschietto, Mike J. Frisch, Giovanni Scalmani, Ilaria Ciofini, and Carlo Adamo. Charge transfer excitations in tddft: A ghosthunter index. *Journal of Computational Chemistry*, 38(25):21512156, 2017.

[144] Neepa T Maitra. Charge transfer in time-dependent density functional theory. *Journal of Physics: Condensed Matter*, 29(42):423001, 2017.

[145] Dvid Mester and Mihly Kllay. Charge-transfer excitations within density functional theory: How accurate are the most recommended approaches? *Journal of Chemical Theory and Computation*, 18(3):16461662, 2022.

[146] Sapana V. Shedge, Tim J. Zuehlsdorff, Ajay Khanna, Stacey Conley, and Christine M. Isborn. Explicit environmental and vibronic effects in simulations of linear and nonlinear optical spectroscopy. *The Journal of Chemical Physics*, 154(8):084116, February 2021.

[147] Ajay Khanna, Sapana Shedge, Tim Zuehlsdorff, and Christine Isborn. Calculating absorption and fluorescence spectra for chromophores in solution with ensemble franck-condon methods. *The Journal of Chemical Physics*, 2024.

[148] John P. Perdew, Adrienn Ruzsinszky, Jianmin Tao, Viktor N. Staroverov, Gustavo E. Scuseria, and Gbor I. Csonka. Prescription for the design and selection of density functional approximations: More constraint satisfaction with fewer fits. *The Journal of Chemical Physics*, 123(6), 2005.

[149] D. M. Ceperley and B. J. Alder. Ground state of the electron gas by a stochastic method. *Physical Review Letters*, 45(7):566569, August 1980.

[150] S. H. Vosko, L. Wilk, and M. Nusair. Accurate spin-dependent electron liquid correlation energies for local spin density calculations: a critical analysis. *Canadian Journal of Physics*, 58(8):12001211, August 1980.

[151] J. P. Perdew and Alex Zunger. Self-interaction correction to density-functional approximations for many-electron systems. *Physical Review B*, 23(10):50485079, May 1981.

[152] John P. Perdew and Yue Wang. Accurate and simple analytic representation of the electron-gas correlation energy. *Physical Review B*, 45(23):1324413249, June 1992.

[153] Ming Wah Wong. Vibrational frequency prediction using density functional theory. *Chemical Physics Letters*, 256(45):391399, 1996.

[154] Kevin E. Riley, Bryan T. Opt Holt, and Kenneth M. Merz. Critical assessment of the performance of density functional methods for several atomic and molecular properties. *Journal of Chemical Theory and Computation*, 3(2):407433, 2007.

[155] G. L. Zhao, D. Bagayoko, and T. D. Williams. Local-density-approximation prediction of electronic properties of gan, si, c, and ruo2. *Physical Review B*, 60(3):15631572, July 1999.

[156] Jan Andzelm, Berend C. Rinderspacher, Adam Rawlett, Joseph Dougherty, Roi Baer, and Niranjan Govind. Performance of dft methods in the calculation of optical spectra of tcf-chromophores. *Journal of Chemical Theory and Computation*, 5(10):28352846, 2009.

[157] Daniele Toffoli, Matteo Quarin, Giovanna Fronzoni, and Mauro Stener. Accurate vertical excitation energies of bodipy/aza-bodipy derivatives from excited-state mean-field calculations. *The Journal of Physical Chemistry A*, 126(40):71377146, 2022.

[158] So Hirata and Martin Head-Gordon. Time-dependent density functional theory within the tamm–dancoff approximation. *Chemical Physics Letters*, 314(3-4):291–299, December 1999.

[159] Xiaoliang Ji and Yue Yang. Density functional theory investigation on the molecular structure and vibrational spectra of triclosan. *Spectroscopy*, page 2332, 2022.

[160] Zheng-Li Cai, Karina Sendt, and Jeffrey R. Reimers. Failure of density-functional theory and time-dependent density-functional theory for large extended systems. *The Journal of Chemical Physics*, 117(12):55435549, 2002.

[161] Denis Jacquemin, Eric Brmond, Aurlien Planchat, Ilaria Ciofini, and Carlo Adamo. Td-dft vibronic couplings in anthraquinones: From basis set and functional benchmarks to applications for industrial dyes. *Journal of Chemical Theory and Computation*, 7(6):18821892, 2011.

[162] John P. Perdew, Kieron Burke, and Matthias Ernzerhof. Generalized gradient approximation made simple. *Physical Review Letters*, 77(18):38653868, 1996.

[163] John P. Perdew. Jacobs ladder of density functional approximations for the exchange-correlation energy. *AIP Conference Proceedings*, 2001.

[164] Roberto Peverati, Yan Zhao, and Donald G. Truhlar. Generalized gradient approximation that recovers the second-order density-gradient expansion with optimized across-the-board performance. *The Journal of Physical Chemistry Letters*, 2(16):19911997, 2011.

[165] Jianwei Sun, Richard C. Remsing, Yubo Zhang, Zhaoru Sun, Adrienn Ruzsinszky, Haowei Peng, Zenghui Yang, Arpita Paul, Umesh Waghmare, Xifan Wu, Michael L. Klein, and John P. Perdew. Scan: An efficient density functional yielding accurate structures and energies of diversely-bonded materials. *arXiv*, 2015.

[166] A. D. Becke. Density-functional exchange-energy approximation with correct asymptotic behavior. *Physical Review A*, 38(6):30983100, 1988.

[167] Chengteh Lee, Weitao Yang, and Robert G. Parr. Development of the colle-salvetti correlation-energy formula into a functional of the electron density. *Physical Review B*, 37(2):785789, 1988.

[168] A. D. Becke. Density functional calculations of molecular bond energies. *The Journal of Chemical Physics*, 84(8):45244529, 1986.

[169] A. D. Becke. On the large-gradient behavior of the density functional exchange energy. *The Journal of Chemical Physics*, 85(12):71847187, 1986.

[170] A. D. Becke. A multicenter numerical integration scheme for polyatomic molecules. *The Journal of Chemical Physics*, 88(4):25472553, 1988.

[171] J. P. Perdew and Alex Zunger. Self-interaction correction to density-functional approximations for many-electron systems. *Physical Review B*, 23(10):50485079, 1981.

[172] Thomas M. Henderson, Benjamin G. Janesko, and Gustavo E. Scuseria. Generalized gradient approximation model exchange holes for range-separated hybrids. *The Journal of Chemical Physics*, 128(19), 2008.

[173] Narbe Mardirossian and Martin Head-Gordon. Exploring the limit of accuracy for density functionals based on the generalized gradient approximation: Local, global hybrid, and range-separated hybrid functionals with and without dispersion corrections. *The Journal of Chemical Physics*, 140(18), 2014.

[174] Monika Vsianska, Martin Frik, and Mojmr ob. A critical comparative review of generalized gradient approximation: the ground state of fe3al as a test case. *Modelling and Simulation in Materials Science and Engineering*, 31(8):085022, 2023.

[175] Priyanka B. Shukla, Prakash Mishra, Tunna Baruah, Rajendra R. Zope, Koblar A. Jackson, and J. Karl Johnson. How do self-interaction errors associated with stretched bonds affect barrier height predictions? *The Journal of Physical Chemistry A*, 127(7):17501759, 2023.

[176] Michael E. Foster and Karl Sohlberg. Empirically corrected dft and semi-empirical methods for non-bonding interactions. *Phys. Chem. Chem. Phys.*, 12(2):307322, 2010.

[177] Biswajit Santra, Ji Klime, Alexandre Tkatchenko, Dario Alf, Ben Slater, Angelos Michaelides, Roberto Car, and Matthias Scheffler. On the accuracy of van der waals inclusive density-functional theory exchange-correlation functionals for ice at ambient and high pressures. *The Journal of Chemical Physics*, 139(15), 2013.

[178] Clemence Corminboeuf. Minimizing density functional failures for non-covalent interactions beyond van der waals complexes. *Accounts of Chemical Research*, 47(11):32173224, 2014.

[179] Carlo Adamo, Matthias Ernzerhof, and Gustavo E. Scuseria. The meta-gga functional: Thermochemistry with a kinetic energy density dependent exchange-correlation functional. *The Journal of Chemical Physics*, 112(6):26432649, 2000.

[180] F. Zahariev, S. S. Leang, and Mark S. Gordon. Functional derivatives of meta-generalized gradient approximation (meta-gga) type exchange-correlation density functionals. *The Journal of Chemical Physics*, 138(24), 2013.

[181] Jianmin Tao, John P. Perdew, Viktor N. Staroverov, and Gustavo E. Scuseria. Climbing the density functional ladder: Nonempirical metageneralized gradient approximation designed for molecules and solids. *Physical Review Letters*, 91(14), 2003.

[182] John P. Perdew, Adrienn Ruzsinszky, Gbor I. Csonka, Lucian A. Constantin, and Jianwei Sun. Workhorse semilocal density functional for condensed matter physics and quantum chemistry. *Physical Review Letters*, 103(2), 2009.

[183] John P. Perdew, Adrienn Ruzsinszky, Gbor I. Csonka, Lucian A. Constantin, and Jianwei Sun. Erratum: Workhorse semilocal density functional for condensed matter physics and quantum chemistry [phys. rev. lett.103, 026403 (2009)]. *Physical Review Letters*, 106(17), 2011.

[184] Jrgen Grfenstein, Dmitry Izotov, and Dieter Cremer. Avoiding singularity problems associated with meta-gga (generalized gradient approximation) exchange and correlation functionals containing the kinetic energy density. *The Journal of Chemical Physics*, 127(21), 2007.

[185] Erin R. Johnson, Axel D. Becke, C. David Sherrill, and Gino A. DiLabio. Oscillations in meta-generalized-gradient approximation potential energy surfaces for dispersion-bound complexes. *The Journal of Chemical Physics*, 131(3), 2009.

[186] Steven E. Wheeler and K. N. Houk. Integration grid errors for meta-gga-predicted reaction energies: Origin of grid errors for the m06 suite of functionals. *Journal of Chemical Theory and Computation*, 6(2):395404, 2010.

[187] Nora-Aydee Sanchez-Bojorge, Luz-Maria Rodriguez-Valdez, Daniel Glossman-Mitnik, and Norma Flores-Holguin. Theoretical calculation of the maximum absorption wavelength for cyanidin molecules with several methodologies. *Computational and Theoretical Chemistry*, 1067:129134, 2015.

[188] Silvia Di Grande, Ilaria Ciofini, Carlo Adamo, Marco Pagliai, and Gianni Cardini. Absorption spectra of flexible fluorescent probes by a combined computational approach: Molecular dynamics simulations and time-dependent density functional theory. *The Journal of Physical Chemistry A*, 126(47):88098817, 2022.

[189] J Harris and R O Jones. The surface energy of a bounded electron gas. *Journal of Physics F: Metal Physics*, 4(8):11701186, 1974.

[190] O. Gunnarsson and B. I. Lundqvist. Exchange and correlation in atoms, molecules, and solids by the spin-density-functional formalism. *Physical Review B*, 13(10):42744298, 1976.

[191] David C. Langreth and John P. Perdew. Exchange-correlation energy of a metallic surface: Wave-vector analysis. *Physical Review B*, 15(6):28842901, 1977.

[192] J. Harris. Adiabatic-connection approach to kohn-sham theory. *Physical Review A*, 29(4):16481659, 1984.

[193] Axel D. Becke. Density-functional thermochemistry. iii. the role of exact exchange. *The Journal of Chemical Physics*, 98(7):56485652, 1993.

[194] S. H. Vosko, L. Wilk, and M. Nusair. Accurate spin-dependent electron liquid correlation energies for local spin density calculations: a critical analysis. *Canadian Journal of Physics*, 58(8):12001211, 1980.

[195] Yan Zhao and Donald G. Truhlar. Hybrid meta density functional theory methods for thermochemistry, thermochemical kinetics, and noncovalent interactions: the mpw1b95 and mpwb1k models and comparative assessments for hydrogen bonding and van der waals interactions. *The Journal of Physical Chemistry A*, 108(33):69086918, 2004.

[196] Yan Zhao and Donald G. Truhlar. A new local density functional for main-group thermochemistry, transition metal bonding, thermochemical kinetics, and noncovalent interactions. *The Journal of Chemical Physics*, 125(19), 2006.

[197] Robert W. Ashcraft, Sumathy Raman, and William H. Green. Ab initio aqueous thermochemistry: application to the oxidation of hydroxylamine in nitric acid solution. *The Journal of Physical Chemistry B*, 111(41):1196811983, 2007.

[198] Yan Zhao and Donald G. Truhlar. The m06 suite of density functionals for main group thermochemistry, thermochemical kinetics, noncovalent interactions, excited states, and transition elements: two new functionals and systematic testing of four m06-class functionals and 12 other functionals. *Theoretical Chemistry Accounts*, 120(13):215241, 2007.

[199] Dmitry G. Gusev. Assessing the accuracy of m06-l organometallic thermochemistry. *Organometallics*, 32(15):42394243, 2013.

[200] Bilal Ahmad Shiekh. Hierarchy of commonly used dft methods for predicting the thermochemistry of rh-mediated chemical transformations. *ACS Omega*, 4(13):1543515443, 2019.

[201] Irena Efremenko and Michael Montag. Revisiting cc and ch bond activation in rhodium pincer complexes: Thermodynamics and kinetics involving a common agostic intermediate. *Organometallics*, 41(17):23792393, 2022.

[202] Benjamin J. Lynch, Patton L. Fast, Maegan Harris, and Donald G. Truhlar. Adiabatic connection for kinetics. *The Journal of Physical Chemistry A*, 104(21):48114815, 2000.

[203] Junwei Lucas Bao, Bradley K. Welch, Inga S. Ulusoy, Xin Zhang, Xuefei Xu, Angela K. Wilson, and Donald G. Truhlar. Predicting bond dissociation energies and bond lengths of coordinatively unsaturated vanadiumligand bonds. *The Journal of Physical Chemistry A*, 124(47):97579770, 2020.

[204] T. Tchakoua, N. Gerrits, E. W. F. Smeets, and G.-J. Kroes. Sbh17: Benchmark database of barrier heights for dissociative chemisorption on transition metal surfaces. *Journal of Chemical Theory and Computation*, 19(1):245270, 2022.

[205] Junyi Gong, Jacky W. Y. Lam, and Ben Zhong Tang. Benchmark and parameter tuning of hybrid functionals for fast calculation of excitation energies of aiegens. *Physical Chemistry Chemical Physics*, 22(32):1803518039, 2020.

[206] Anna-Sophia Hehn, Beliz Sertcan, Fabian Belleflamme, Sergey K. Chulkov, Matthew B. Watkins, and Jrg Hutter. Excited-state properties for extended systems: Efficient hybrid density functional methods. *Journal of Chemical Theory and Computation*, 18(7):41864202, 2022.

[207] Igor Ying Zhang and Xin Xu. Doubly hybrid density functional for accurate description of thermochemistry, thermochemical kinetics and nonbonded interactions. *International Reviews in Physical Chemistry*, 30(1):115160, 2011.

[208] Lars Goerigk and Stefan Grimme. Doublehybrid density functionals. *WIREs Computational Molecular Science*, 4(6):576600, 2014.

[209] Stefan Grimme. Semiempirical hybrid density functional with perturbative second-order correlation. *The Journal of Chemical Physics*, 124(3), 2006.

[210] Sebastian Kozuch, David Gruzman, and Jan M. L. Martin. Dsd-blyp: A general purpose double hybrid density functional including spin component scaling and dispersion correction. *The Journal of Physical Chemistry C*, 114(48):2080120808, 2010.

[211] Lars Goerigk, Jonas Moellmann, and Stefan Grimme. Computation of accurate excitation energies for large organic molecules with double-hybrid density functionals. *Physical Chemistry Chemical Physics*, 11(22):4611, 2009.

[212] Lars Goerigk, Andreas Hansen, Christoph Bauer, Stephan Ehrlich, Asim Najibi, and Stefan Grimme. A look at the density functional theory zoo with the advanced gmtkn55 database for general main group thermochemistry, kinetics and noncovalent interactions. *Physical Chemistry Chemical Physics*, 19(48):3218432215, 2017.

[213] Andreas Dreuw, Jennifer L. Weisman, and Martin Head-Gordon. Long-range charge-transfer excited states in time-dependent density functional theory require non-local exchange. *The Journal of Chemical Physics*, 119(6):29432946, 2003.

[214] Johannes Neugebauer, Oleg Gritsenko, and Evert Jan Baerends. Assessment of a simple correction for the long-range charge-transfer problem in time-dependent density-functional theory. *The Journal of Chemical Physics*, 124(21), 2006.

[215] Tom Ziegler, Michael Seth, Mykhaylo Krykunov, Jochen Autschbach, and Fan Wang. Is charge transfer transitions really too difficult for standard density functionals or are they just a problem for time-dependent density functional theory based on a linear response approach. *Journal of Molecular Structure: THEOCHEM*, 914(13):106109, 2009.

[216] Natalia Kuritz, Tamar Stein, Roi Baer, and Leeor Kronik. Charge-transfer-like * excitations in time-dependent density functional theory: A conundrum and its solution. *Journal of Chemical Theory and Computation*, 7(8):24082415, 2011.

[217] Johanna I. Fuks. Time-dependent density functional theory for charge-transfer dynamics: review of the causes of failure and success*. *The European Physical Journal B*, 89(11), 2016.

[218] Seth Olsen. Locally-excited (le) versus charge-transfer (ct) excited state competition in a series of para-substituted neutral green fluorescent protein (gfp) chromophore models. *The Journal of Physical Chemistry B*, 119(6):25662575, 2014.

[219] Kyungeon Lee and Dongwook Kim. Local-excitation versus charge-transfer characters in the triplet state: Theoretical insight into the singlettriplet energy differences of carbazolyl-phthalonitrile-based thermally activated delayed fluorescence materials. *The Journal of Physical Chemistry C*, 120(49):2833028336, 2016.

[220] Rdiger Bauernschmitt and Reinhart Ahlrichs. Treatment of electronic excitations within the adiabatic approximation of time dependent density functional theory. *Chemical Physics Letters*, 256(45):454464, 1996.

[221] M. Petersilka, U. J. Gossmann, and E. K. U. Gross. Excitation energies from time-dependent density-functional theory. *Physical Review Letters*, 76(8):12121215, 1996.

[222] Raul E. Gutierrez, Ivana Matanovic, Maciej P. Polak, Ryan S. Johnson, Dane Morgan, and Edl Schamiloglu. *Calculation of Secondary Electron Yield of Alloys: Single Pole Approximation*. IEEE, 2021.

[223] Neepa T. Maitra. Double and charge-transfer excitations in time-dependent density functional theory. *Annual Review of Physical Chemistry*, 73(1):117140, 2022.

[224] T Koopmans. ber die zuordnung von wellenfunktionen und eigenwerten zu den einzelnen elektronen eines atoms. *Physica*, 1(16):104113, 1934.

[225] J. C. Phillips. Generalized koopmans theorem. *Physical Review*, 123(2):420424, 1961.

[226] Branko S. Jursic. A density functional theory estimation of the heat of formation for foocl. *The Journal of Chemical Physics*, 106(6):25552556, 1997.

[227] Amin Alibakhshi and Lars V. Schfer. Accurate evaluation of combustion enthalpy by ab-initio computations. *Scientific Reports*, 12(1), 2022.

[228] Yan Zhao and Donald G. Truhlar. Density functional theory for reaction energies: Test of meta and hybrid meta functionals, range-separated functionals, and other high-performance functionals. *Journal of Chemical Theory and Computation*, 7(3):669676, 2011.

[229] Azzam Charaf-Eddin, Aurélien Planchat, Benedetta Mennucci, Carlo Adamo, and Denis Jacquemin. Choosing a functional for computing absorption and fluorescence band shapes with td-dft. *Journal of Chemical Theory and Computation*, 9(6):27492760, May 2013.

[230] Adle D. Laurent and Denis Jacquemin. Td-dft benchmarks: A review. *International Journal of Quantum Chemistry*, 113(17):20192039, 2013.

[231] Yihan Shao, Ye Mei, Dage Sundholm, and Ville R. I. Kaila. Benchmarking the performance of time-dependent density functional theory methods on biochromophores. *Journal of Chemical Theory and Computation*, 16(1):587600, 2019.

[232] Beatrix M. Bold, Monja Sokolov, Sayan Maity, Marius Wanko, Philipp M. Dohmen, Julian J. Kranz, Ulrich Kleinekathfer, Sebastian Hfener, and Marcus Elstner. Benchmark and performance of long-range corrected time-dependent density functional tight binding (lc-td-dftb) on rhodopsins and light-harvesting complexes. *Physical Chemistry Chemical Physics*, 22(19):1050010518, 2020.

[233] Bishwanath Mahato and Aditya N. Panda. Assessing the performance of dft functionals for excited-state properties of pyridine-thiophene oligomers. *The Journal of Physical Chemistry A*, 125(1):115125, 2020.

[234] David Hall, Juan Carlos Sancho-Garca, Anton Pershin, David Beljonne, Eli Zysman-Colman, and Yoann Olivier. Benchmarking dft functionals for excited-state calculations of donoracceptor tadf emitters: Insights on the key parameters determining reverse inter-system crossing. *The Journal of Physical Chemistry A*, 2023.

[235] PierreFranois Loos and Denis Jacquemin. A mountaineering strategy to excited states: Accurate vertical transition energies and benchmarks for substituted benzenes. *Journal of Computational Chemistry*, 45(21):17911805, 2024.

[236] Dominique Guillaumont and Shinichiro Nakamura. Calculation of the absorption wavelength of dyes using time-dependent density-functional theory (td-dft). *Dyes and Pigments*, 46(2):8592, 2000.

[237] Denis Jacquemin, Eric A. Perpte, Ilaria Ciofini, and Carlo Adamo. On the td-dft uv/vis spectra accuracy: the azoalkanes. *Theoretical Chemistry Accounts*, 120(46):405410, 2008.

[238] Denis Jacquemin, Ivan Duchemin, and Xavier Blase. 00 energies using hybrid schemes: Benchmarks of td-dft, cis(d), adc(2), cc2, and bse/gw formalisms for 80 real-life compounds. *Journal of Chemical Theory and Computation*, 11(11):53405359, 2015.

[239] PierreFranois Loos and Denis Jacquemin. Evaluating 00 energies with theoretical tools: A short review. *ChemPhotoChem*, 3(9):684696, 2019.

[240] Corell Halsey-Moore, Puru Jena, and James T. McLeskey. Tuning range-separated dft functionals for modeling the peak absorption of meh-ppv polymer in various solvents. *Computational and Theoretical Chemistry*, 1162:112506, 2019.

[241] Marvin Friede, Sebastian Ehlert, Stefan Grimme, and Jan-Michael Mewes. Do optimally tuned range-separated hybrid functionals require a reparametrization of the dispersion correction? it depends. *Journal of Chemical Theory and Computation*, 19(22):80978107, 2023.

[242] Azzam Charaf-Eddin, Thomas Cauchy, Franois-Xavier Felpin, and Denis Jacquemin. Vibronic spectra of organic electronic chromophores. *RSC Adv.*, 4(98):5546655472, 2014.

[243] Siwar Chibani, Denis Jacquemin, and Adle D. Laurent. Modelling solvent effects on the absorption and emission spectra of constrained cyanines with both implicit and explicit qm/efp models. *Computational and Theoretical Chemistry*, 10401041:321327, 2014.

[244] Peter Macak, Yi Luo, and Hans gren. Simulations of vibronic profiles in two-photon absorption. *Chemical Physics Letters*, 330(34):447456, November 2000.

[245] Anirban Hazra, Hannah H. Chang, and Marcel Nooijen. First principles simulation of the uv absorption spectrum of ethylene using the vertical franck-condon approach. *The Journal of Chemical Physics*, 121(5):21252136, July 2004.

[246] Francisco José Avila Ferrer and Fabrizio Santoro. Comparison of vertical and adiabatic harmonic approaches for the calculation of the vibrational structure of electronic spectra. *Physical Chemistry Chemical Physics*, 14(39):13549, 2012.

[247] Malgorzata Biczysko, Julien Bloino, Fabrizio Santoro, and Vincenzo Barone. Timeindependent approaches to simulate electronic spectra lineshapes: From small molecules to macrosystems, October 2011.

[248] Javier Cerezo and Fabrizio Santoro. Revisiting vertical models to simulate the line shape of electronic spectra adopting cartesian and internal coordinates. *Journal of Chemical Theory and Computation*, 12(10):49704985, September 2016.

[249] Matthew C. Zwier, Justin M. Shorb, and Brent P. Krueger. Hybrid molecular dynamics-quantum mechanics simulations of solute spectral properties in the condensed phase: Evaluation of simulation parameters. *Journal of Computational Chemistry*, 28(9):15721581, March 2007.

[250] Andreana M. Rosnik and Carles Curutchet. Theoretical characterization of the spectral density of the water-soluble chlorophyll-binding protein from combined quantum mechanics/molecular mechanics molecular dynamics simulations. *Journal of Chemical Theory and Computation*, 11(12):58265837, November 2015.

[251] Suryanarayanan Chandrasekaran, Mortaza Aghtar, Stéphanie Valleau, Alán Aspuru-Guzik, and Ulrich Kleinekathöfer. Influence of force fields and quantum chemistry approach on spectral densities of bchl a in solution and in fmo proteins. *The Journal of Physical Chemistry B*, 119(31):999510004, July 2015.

[252] T. J. Zuehlsdorff and C. M. Isborn. Combining the ensemble and franck-condon approaches for calculating spectral shapes of molecules in solution. *The Journal of Chemical Physics*, 148(2):024110, January 2018.

[253] Tim J. Zuehlsdorff and Christine M. Isborn. Modeling absorption spectra of molecules in solution. *International Journal of Quantum Chemistry*, 119(1), September 2018.

[254] Mi Kyung Lee, Pengfei Huo, and David F. Coker. Semiclassical path integral dynamics: Photosynthetic energy transfer with realistic environment interactions. *Annual Review of Physical Chemistry*, 67(1):639668, May 2016.

[255] Daniele Loco and Lorenzo Cupellini. Modeling the absorption lineshape of embedded systems from molecular dynamics: A tutorial review. *International Journal of Quantum Chemistry*, 119(1), September 2018.

[256] D. Loco, S. Jurinovich, L. Cupellini, M. F. S. J. Menger, and B. Mennucci. The modeling of the absorption lineshape for embedded molecules through a polarizable QM/MM approach. *Photochem. Photobiol. Sci.*, 17(5):552–560, 2018.

[257] Francesco Segatta, Lorenzo Cupellini, Marco Garavelli, and Benedetta Mennucci. Quantum chemical modeling of the photoinduced activity of multichromophoric biosystems: Focus review. *Chemical Reviews*, 119(16):93619380, July 2019.

[258] Andrs Zuehlsdorff Tim J., Montoya-Castillo, Markland Thomas E. Napoli, Joseph A., and Isborn Christine M. Optical spectra in the condensed phase: Capturing anharmonic and vibronic features using dynamic and static approaches. *The Journal of Chemical Physics*, 151(7):074111, August 2019.

[259] Sapana V. Shedge, Tim J. Zuehlsdorff, Michael J. Servis, Aurora E. Clark, and Christine M. Isborn. Effect of ions on the optical absorption spectra of aqueously solvated chromophores. *The Journal of Physical Chemistry A*, 123(29):6175–6184, June 2019.

[260] Tim J. Zuehlsdorff, Hanbo Hong, Liang Shi, and Christine M. Isborn. Influence of electronic polarization on the spectral density. *The Journal of Physical Chemistry B*, 124(3):531543, December 2019.

[261] Sara Del Galdo, Marco Fus, and Vincenzo Barone. The oniom/pmm model for effective yet accurate simulation of optical and chiroptical spectra in solution: Camphorquinone in methanol as a case study. *Journal of Chemical Theory and Computation*, 16(5):32943306, 2020.

[262] Giordano Mancini, Sara Del Galdo, Balasubramanian Chandramouli, Marco Pagliai, and Vincenzo Barone. Computational spectroscopy in solution by integration of variational and perturbative approaches on top of clusterized molecular dynamics. *Journal of Chemical Theory and Computation*, 16(9):57475761, 2020.

[263] Tim J. Zuehlsdorff, Hanbo Hong, Liang Shi, and Christine M. Isborn. Nonlinear spectroscopy in the condensed phase: The role of duschinsky rotations and third order cumulant contributions. *The Journal of Chemical Physics*, 153(4), July 2020.

[264] Mattia Bondanza, Lorenzo Cupellini, Filippo Lipparini, and Benedetta Mennucci. The multiple roles of the protein in the photoactivation of orange carotenoid protein. *Chem*, 6(1):187203, January 2020.

[265] Javier Cerezo, Daniel Aranda, Francisco José Avila Ferrer, Giacomo Prampolini, and Fabrizio Santoro. Adiabatic-molecular dynamics generalized vertical hessian approach: A mixed quantum classical method to compute electronic spectra of flexible molecules in the condensed phase. *Journal of Chemical Theory and Computation*, 16(2):1215–1231, 2020. PMID: 31855424.

[266] Alekos Segalina, Javier Cerezo, Giacomo Prampolini, Fabrizio Santoro, and Mariachiara Pastore. Accounting for vibronic features through a mixed quantum-classical scheme: Structure, dynamics, and absorption spectra of a perylene diimide dye in solution. *Journal of Chemical Theory and Computation*, 16(11):7061–7077, 2020. PMID: 33124412.

[267] Tim J. Zuehlsdorff, Sapana V. Shedge, Shao-Yu Lu, Hanbo Hong, Vincent P. Aguirre, Liang Shi, and Christine M. Isborn. Vibronic and environmental ef-

fects in simulations of optical spectroscopy. *Annual Review of Physical Chemistry*, 72(1):165188, April 2021.

[268] Michael S. Chen, Yuezhi Mao, Andrew Snider, Prachi Gupta, Andrés Montoya-Castillo, Tim J. Zuehlsdorff, Christine M. Isborn, and Thomas E. Markland. Elucidating the role of hydrogen bonding in the optical spectroscopy of the solvated green fluorescent protein chromophore: Using machine learning to establish the importance of high-level electronic structure. *The Journal of Physical Chemistry Letters*, 14(29):66106619, July 2023.

[269] Lima Igo T. Sousa Leonardo Freitas Renato da S. Junior Luiz Antonio Ribeiro de Sousa Junior Rafael Timoteo and da Silva Filho Demetrio A. A dft study of a set of natural dyes for organic electronics. *Journal of Molecular Modeling*, 23(12):343, 2017.

[270] Vincenzo Barone, Julien Bloino, Susanna Monti, Alfonso Pedone, and Giacomo Prampolini. Fluorescence spectra of organic dyes in solution: a time dependent multilevel approach. *Phys. Chem. Chem. Phys.*, 13(6):21602166, 2011.

[271] Alessio Petrone, Javier Cerezo, Francisco J. Avila Ferrer, Greta Donati, Roberto Improta, Nadia Rega, and Fabrizio Santoro. Absorption and emission spectral shapes of a prototype dye in water by combining classical/dynamical and quantum/static approaches. *The Journal of Physical Chemistry A*, 119(21):5426–5438, 2015. PMID: 25699575.

[272] Salsabil Abou-Hatab, Vincenzo Carnevale, and Spiridoula Matsika. Modeling solvation effects on absorption and fluorescence spectra of indole in aqueous solution. *The Journal of Chemical Physics*, 154(6), 2021.

[273] Sulejman Skoko, Cosimo Micheletti, Emanuele Grifoni, Franco Egidi, Tommaso Giovannini, Andrea Pucci, and Chiara Cappelli. Towards a cost-effective modeling of fluorescence in the condensed phase. *Dyes and Pigments*, 215:111227, July 2023.

[274] Rachael Youngworth and Benot Roux. Simulating the fluorescence of di-8-anepps in solvents of different polarity. *The Journal of Physical Chemistry B*, 128(1):184192, December 2023.

[275] Rachael Youngworth and Benot Roux. Simulating the fluorescence of the locally excited state of dmabn in solvents of different polarities. *The Journal of Physical Chemistry B*, 128(1):172183, December 2023.

[276] Alfonso Pedone, Julien Bloino, Susanna Monti, Giacomo Prampolini, and Vincenzo Barone. Absorption and emission uv-vis spectra of the tritc fluorophore molecule in solution: a quantum mechanical study. *Phys. Chem. Chem. Phys.*, 12(4):10001006, 2010.

[277] Mario Barbatti and Hans Lischka. Why water makes 2-aminopurine fluorescent? *Physical Chemistry Chemical Physics*, 17(23):1545215459, 2015.

[278] Samuel Frutos-Puerto, M. Jess Coln, Jose C. Corchado, M. Luz Snchez, M. Elena Martn, and Manuel A. Aguilar. Photophysical and photochemical properties of 3-hydroxyflavone in ethanol solution: Implicit vs explicit solvent models. *Journal of Molecular Liquids*, 381:121783, 2023.

[279] Harrison R. Pearce, Byron W. Purse, and Andrew L. Cooksy. Explicit solvation modeling in the accurate td-dft prediction of absorption spectra for natural nucleobases and fluorescent nucleobase analogues. *chemrxiv*, 2024.

[280] Seiichi Uchiyama, Kohki Kimura, Chie Gota, Kohki Okabe, Kyoko Kawamoto, Noriko Inada, Toshitada Yoshihara, and Seiji Tobita. Environment-sensitive fluorophores with benzothiadiazole and benzoselenadiazole structures as candidate components of a fluorescent polymeric thermometer. *Chemistry - A European Journal*, 18(31):9552–9563, July 2012.

[281] Kazuhiro Imai, Sonoko Uzu, and Toshimasa Toyo'oka. Fluorogenic reagents having benzofuran structure in liquid chromatography. *Journal of Pharmaceutical and Biomedical Analysis*, 7(12):1395–1403, January 1989.

[282] Judith Rumin, Hubert Bonnefond, Bruno Saint-Jean, Catherine Rouxel, Antoine Sciandra, Olivier Bernard, Jean-Paul Cadoret, and Gal Bougaran. The use of fluorescent nile red and BODIPY for lipid measurement in microalgae. *Biotechnology for Biofuels*, 8(1), March 2015.

[283] Gibrán S. Alemán-Nava, Sara P. Cuellar-Bermudez, María Cuaresma, Rouke Bosma, Koenraad Muylaert, Bruce E. Ritmann, and Roberto Parra. How to use nile red, a selective fluorescent stain for microalgal neutral lipids. *Journal of Microbiological Methods*, 128:74–79, September 2016.

[284] C. Graham Knight. Stereospecific synthesis of l-2-amino-3-(7-methoxy-4-coumaryl)propionic acid, an alternative to tryptophan in quenched fluorescent substrates for peptidases. *Letters in Peptide Science*, 5(1):1–4, January 1998.

[285] Lindsay E. Yandek, Antje Pokorny, Anders Florén, Kristina Knoelke, Ülo Langel, and Paulo F.F. Almeida. Mechanism of the cell-penetrating peptide transportan 10 permeation of lipid bilayers. *Biophysical Journal*, 92(7):2434–2444, April 2007.

[286] Irene Tosi, Mireia Segado Centellas, Elisa Campioli, Alessandro Iagatti, Andrea Lapini, Cristina Sissa, Laura Baldini, Chiara Cappelli, Mariangela Di Donato, Francesco Sansone, Fabrizio Santoro, and Francesca Terenziani. Excitation dynamics in hetero-bichromophoric calixarene systems. *ChemPhysChem*, 17(11):1686–1706, March 2016.

[287] James M. Dixon, Masahiko Taniguchi, and Jonathan S. Lindsey. PhotochemCAD 2. a refined program with accompanying spectral database for photochemical calculations. *Photochemistry and Photobiology*, 2004.

[288] R. Farinotti, Ph. Siard, J. Bourson, S. Kirkiacharian, B. Valeur, and G. Mahuzier. 4-bromomethyl-6, 7-dimethoxycoumarin as a fluorescent label for carboxylic acids in chromatographic detection. *Journal of Chromatography A*, 269:8190, January 1983.

[289] Stefan Grimme, Jens Antony, Stephan Ehrlich, and Helge Krieg. A consistent and accurate ab initio parametrization of density functional dispersion correction (dft-d) for the 94 elements h-pu. *The Journal of Chemical Physics*, 132(15), April 2010.

[290] Agisilaos Chantzis, Adle D. Laurent, Carlo Adamo, and Denis Jacquemin. Is the tamm-dancoff approximation reliable for the calculation of absorption and fluorescence band shapes? *Journal of Chemical Theory and Computation*, 9(10):45174525, September 2013.

[291] Takeshi Yanai, David P Tew, and Nicholas C Handy. A new hybrid exchange–correlation functional using the coulomb-attenuating method (CAM-b3lyp). *Chemical Physics Letters*, 393(1-3):51–57, July 2004.

[292] Thomas M. Henderson, Artur F. Izmaylov, Giovanni Scalmani, and Gustavo E. Scuseria. Can short-range hybrids describe long-range-dependent properties? *The Journal of Chemical Physics*, 131(4), July 2009.

[293] Oleg A. Vydrov and Gustavo E. Scuseria. Assessment of a long-range corrected hybrid functional. *The Journal of Chemical Physics*, 125(23), December 2006.

[294] Oleg A. Vydrov, Gustavo E. Scuseria, and John P. Perdew. Tests of functionals for systems with fractional electron number. *The Journal of Chemical Physics*, 126(15), April 2007.

[295] Yan Zhao and Donald G. Truhlar. The m06 suite of density functionals for main group thermochemistry, thermochemical kinetics, noncovalent interactions, excited states, and transition elements: two new functionals and systematic testing of four m06-class functionals and 12 other functionals. *Theoretical Chemistry Accounts*, 120(13):215241, July 2007.

[296] Stefan Seritan, Christoph Bannwarth, Bryan S. Fales, Edward G. Hohenstein, Christine M. Isborn, Sara I. L. Kokkila-Schumacher, Xin Li, Fang Liu, Nathan Luehr, James W. Snyder, Chenchen Song, Alexey V. Titov, Ivan S. Ufimtsev, Lee-Ping Wang, and Todd J. Martínez. Terachem: A graphical processing unit-accelerated electronic structure package for large-scale ab initio molecular dynamics. *WIREs Computational Molecular Science*, 11(2), July 2020.

[297] M. J. Frisch, G. W. Trucks, H. B. Schlegel, G. E. Scuseria, M. A. Robb, J. R. Cheeseman, G. Scalmani, V. Barone, G. A. Petersson, H. Nakatsuji, X. Li, M. Caricato, A. V. Marenich, J. Bloino, B. G. Janesko, R. Gomperts, B. Mennucci, H. P. Hratchian, J. V. Ortiz, A. F. Izmaylov, J. L. Sonnenberg, D. Williams-Young, F. Ding, F. Lipparini, F. Egidi, J. Goings, B. Peng, A. Petrone, T. Henderson, D. Ranasinghe, V. G. Zakrzewski, J. Gao, N. Rega, G. Zheng, W. Liang, M. Hada, M. Ehara, K. Toyota, R. Fukuda, J. Hasegawa, M. Ishida, T. Nakajima, Y. Honda, O. Kitao, H. Nakai, T. Vreven, K. Throssell, J. A. Montgomery, Jr., J. E. Peralta, F. Ogliaro, M. J. Bearpark, J. J. Heyd, E. N. Brothers, K. N. Kudin, V. N. Staroverov, T. A. Keith, R. Kobayashi, J. Normand, K. Raghavachari, A. P. Rendell, J. C. Burant, S. S. Iyengar, J. Tomasi, M. Cossi, J. M. Millam, M. Klene, C. Adamo, R. Cammi, J. W. Ochterski, R. L. Martin, K. Morokuma, O. Farkas, J. B. Foresman, and D. J. Fox. Gaussian16 Revision C.01, 2016. Gaussian Inc. Wallingford CT.

[298] E. Cances, B. Mennucci, and J. Tomasi. A new integral equation formalism for the polarizable continuum model: Theoretical background and applications to isotropic and anisotropic dielectrics. *The Journal of Chemical Physics*, 107(8):3032–3041, August 1997.

[299] B. Mennucci, E. Cancs, and J. Tomasi. Evaluation of solvent effects in isotropic and anisotropic dielectrics and in ionic solutions with a unified integral equation method: Theoretical bases, computational implementation, and numerical applications. *The Journal of Physical Chemistry B*, 101(49):1050610517, December 1997.

[300] Eric Cancs and Benedetta Mennucci. New applications of integral equations methods for solvation continuum models: ionic solutions and liquid crystals. *Journal of Mathematical Chemistry*, 23(3/4):309326, 1998.

[301] Giovanni Scalmani and Michael J. Frisch. Continuous surface charge polarizable continuum models of solvation. i. general formalism. *The Journal of Chemical Physics*, 132(11), March 2010.

[302] Benedetta Mennucci. Polarizable continuum model. *WIREs Computational Molecular Science*, 2(3):386404, January 2012.

[303] Bernardo de Souza, Frank Neese, and Róbert Izsák. On the theoretical prediction of fluorescence rates from first principles using the path integral approach. *The Journal of Chemical Physics*, 148(3):034104, January 2018.

[304] Taras Petrenko and Frank Neese. Efficient and automatic calculation of optical band shapes and resonance raman spectra for larger molecules within the independent mode displaced harmonic oscillator model. *The Journal of Chemical Physics*, 137(23):234107, December 2012.

[305] Taras Petrenko and Frank Neese. Analysis and prediction of absorption band shapes, fluorescence band shapes, resonance raman intensities, and excitation profiles using the time-dependent theory of electronic spectroscopy. *The Journal of Chemical Physics*, 127(16):164319, October 2007.

[306] Vincenzo Barone, Julien Bloino, Malgorzata Biczysko, and Fabrizio Santoro. Fully integrated approach to compute vibrationally resolved optical spectra: From small molecules to macrosystems. *Journal of Chemical Theory and Computation*, 5(3):540–554, February 2009.

[307] Julien Bloino, Malgorzata Biczysko, Fabrizio Santoro, and Vincenzo Barone. General approach to compute vibrationally resolved one-photon electronic spectra. *Journal of Chemical Theory and Computation*, 6(4):1256–1274, March 2010.

[308] Alberto Baiardi, Julien Bloino, and Vincenzo Barone. General time dependent approach to vibronic spectroscopy including franck–condon, herzberg–teller, and duschinsky effects. *Journal of Chemical Theory and Computation*, 9(9):4097–4115, August 2013.

[309] Alberto Baiardi, Julien Bloino, and Vincenzo Barone. General formulation of vibronic spectroscopy in internal coordinates. *The Journal of Chemical Physics*, 144(8):084114, February 2016.

[310] Jeffrey R. Reimers. A practical method for the use of curvilinear coordinates in calculations of normal-mode-projected displacements and duschinsky rotation matrices for large molecules. *The Journal of Chemical Physics*, 115(20):9103–9109, November 2001.

[311] Francisco José Avila Ferrer and Fabrizio Santoro. Comparison of vertical and adiabatic harmonic approaches for the calculation of the vibrational structure of electronic spectra. *Physical Chemistry Chemical Physics*, 14(39):13549, 2012.

[312] A. Toniolo and M. Persico. Efficient calculation of franck-condon factors and vibronic couplings in polyatomics. *Journal of Computational Chemistry*, 22(9):968–975, 2001.

[313] Fabrizio Santoro, Roberto Improta, Alessandro Lami, Julien Bloino, and Vincenzo Barone. Effective method to compute franck-condon integrals for optical spectra of large molecules in solution. *The Journal of Chemical Physics*, 126(8):084509, February 2007.

[314] Diana Madsen, Ove Christiansen, Patrick Norman, and Carolin König. Vibrationally resolved emission spectra of luminescent conjugated oligothiophenes from anharmonic calculations. *Physical Chemistry Chemical Physics*, 21(31):17410–17422, 2019.

[315] Daniel W. Silverstein and Lasse Jensen. Vibronic coupling simulations for linear and nonlinear optical processes: Theory. *The Journal of Chemical Physics*, 136(6):064111, February 2012.

[316] Rami Gherib, Scott N. Genin, and Ilya G. Ryabinkin. On the importance of well-defined thermal correlation functions in simulating vibronic spectra. *The Journal of Physical Chemistry A*, 126(24):3947–3956, June 2022.

[317] Fabrizio Santoro, Alessandro Lami, Roberto Improta, Julien Bloino, and Vincenzo Barone. Effective method for the computation of optical spectra of large molecules at finite temperature including the duschinsky and herzbergteller effect: The qx band of porphyrin as a case study. *The Journal of Chemical Physics*, 128(22), June 2008.

[318] Ashim Kumar Dutta, Kenji Kamada, and Koji Ohta. Spectroscopic studies of nile red in organic solvents and polymers. *Journal of Photochemistry and Photobiology A: Chemistry*, 93(1):5764, 1996.

[319] Dan L. Sackett and J. Wolff. Nile red as a polarity-sensitive fluorescent probe of hydrophobic protein surfaces. *Analytical Biochemistry*, 167(2):228234, 1987.

[320] Wulin Teo, Andrew V. Caprariello, Megan L. Morgan, Antonio Luchicchi, Geert J. Schenk, Jeffrey T. Joseph, Jeroen J. G. Geurts, and Peter K. Stys. Nile red fluorescence spectroscopy reports early physicochemical changes in myelin with high sensitivity. *Proceedings of the National Academy of Sciences*, 118(8), 2021.

[321] Nilmoni Sarkar, Kaustuv Das, Deb Narayan Nath, and Kankan Bhattacharyya. Twisted charge transfer processes of nile red in homogeneous solutions and in faujasite zeolite. *Langmuir*, 10(1):326329, 1994.

[322] Ciro A. Guido, Benedetta Mennucci, Denis Jacquemin, and Carlo Adamo. Planar vs. twisted intramolecular charge transfer mechanism in nile red: new hints from theory. *Physical Chemistry Chemical Physics*, 12(28):8016, 2010.

[323] Alexandra Ya. Freidzon, Andrei A. Safonov, Alexander A. Bagaturyants, and Michael V. Alfimov. Solvatofluorochromism and twisted intramolecular charge-transfer state of the nile red dye. *International Journal of Quantum Chemistry*, 112(18):30593067, 2012.

[324] Barbara Boldrini, Enrico Cavalli, Anna Painelli, and Francesca Terenziani. Polar dyes in solution: A joint experimental and theoretical study of absorption and emission band shapes. *The Journal of Physical Chemistry A*, 106(26):62866294, June 2002.

[325] Lyudmila O. Kostjukova, Svetlana V. Leontieva, and Viktor V. Kostjukov. The vibronic absorption spectrum and electronic states of nile red in aqueous solution. *ChemistrySelect*, 6(6):12971304, February 2021.

[326] K. M. C. DAVIS. Solvent effects on charge-transfer fluorescence bands. *Nature*, 223(5207):728–728, August 1969.

[327] Salvatore Chiantia, Jonas Ries, and Petra Schwille. Fluorescence correlation spectroscopy in membrane structure elucidation. *Biochimica et Biophysica Acta (BBA) - Biomembranes*, 1788(1):225–233, 2009.

[328] Mikhail Elyashberg. Identification and structure elucidation by nmr spectroscopy. *TrAC Trends in Analytical Chemistry*, 69:88–97, 2015.

[329] Rivka Maoz, Jacob Sagiv, Detlef Degenhardt, Helmuth Mhwald, and Peter Quint. Hydrogen-bonded multilayers of self-assembling silanes: structure elucidation by combined fourier transform infra-red spectroscopy and x-ray scattering techniques. *Supramolecular Science*, 2(1):9–24, 1995.

[330] Andrew A. Gewirth and Edward I. Solomon. Electronic structure of plastocyanin: excited state spectral features. *Journal of the American Chemical Society*, 110(12):3811–3819, 1988.

[331] K. Jordan, A. Cazacu, G. Manai, S. F. Ceballos, S. Murphy, and I. V. Shvets. Scanning tunneling spectroscopy study of the electronic structure of fe_3o_4 surfaces. *Phys. Rev. B*, 74:085416, 2006.

[332] K. Gerwert. Molecular reaction mechanisms of proteins monitored by time-resolved ftir-spectroscopy. *Chem. Soc. Rev.*, 380(7-8):931–935, 1999.

[333] Lucile Martin, Herv Martinez, Delphine Poinot, Brigitte Pecquenard, and Frdric Le Cras. Comprehensive x-ray photoelectron spectroscopy study of the conversion reaction mechanism of cuo in lithiated thin film electrodes. *The Journal of Physical Chemistry C*, 117(9):4421–4430, 2013.

[334] Christian Zscherp and Andreas Barth. Reaction-induced infrared difference spectroscopy for the study of protein reaction mechanisms. *Biochemistry*, 40(7):1875–1883, 2001.

[335] Teresa Blasco. Insights into reaction mechanisms in heterogeneous catalysis revealed by in situ nmr spectroscopy. *Chem. Soc. Rev.*, 39:4685–4702, 2010.

[336] Frédéric Laquai, Young-Seo Park, Jang-Joo Kim, and Thomas Basché. Excitation energy transfer in organic materials: from fundamentals to optoelectronic devices. *Macromolecular rapid communications*, 30(14):1203–1231, 2009.

[337] J Breton, J-L Martin, A Migus, A Antonetti, and A Orszag. Femtosecond spectroscopy of excitation energy transfer and initial charge separation in the reaction center of the photosynthetic bacterium rhodopseudomonas viridis. *Proceedings of the National Academy of Sciences*, 83(14):5121–5125, 1986.

[338] CD Van der Weij-de Wit, JA Ihalainen, R Van Grondelle, and JP17390231 Dekker. Excitation energy transfer in native and unstacked thylakoid membranes studied by low temperature and ultrafast fluorescence spectroscopy. *Photosynthesis Research*, 93(1):173–182, 2007.

[339] JS Chappell, AN Bloch, WA Bryden, M Maxfield, TO Poehler, and DO Cowan. Degree of charge transfer in organic conductors by infrared absorption spectroscopy. *Journal of the American Chemical Society*, 103(9):2442–2443, 1981.

[340] Bruce S Brunschwig, Carol Creutz, and Norman Sutin. Electroabsorption spectroscopy of charge transfer states of transition metal complexes. *Coordination chemistry reviews*, 177(1):61–79, 1998.

[341] James K McCusker. Femtosecond absorption spectroscopy of transition metal charge-transfer complexes. *Accounts of chemical research*, 36(12):876–887, 2003.

[342] Daniel J. Cole, Jonah Z. Vilseck, Julian Tirado-Rives, Mike C. Payne, and William L. Jorgensen. Biomolecular force field parameterization via atoms-in-molecule electron density partitioning. *Journal of Chemical Theory and Computation*, 12(5):23122323, 2016.

[343] Alice E. A. Allen, Michael C. Payne, and Daniel J. Cole. Harmonic force constants for molecular mechanics force fields via hessian matrix projection. *Journal of Chemical Theory and Computation*, 14(1):274281, 2017.

[344] Joshua T. Horton, Alice E. A. Allen, Leela S. Dodda, and Daniel J. Cole. Qubekit: Automating the derivation of force field parameters from quantum mechanics. *Journal of Chemical Information and Modeling*, 59(4):13661381, 2019.

[345] Chris Ringrose, Joshua T. Horton, Lee-Ping Wang, and Daniel J. Cole. Exploration and validation of force field design protocols through qm-to-mm mapping. *Physical Chemistry Chemical Physics*, 24(28):1701417027, 2022.

[346] Jae Woo Park and Young Min Rhee. Interpolated mechanicsmolecular mechanics study of internal rotation dynamics of the chromophore unit in blue fluorescent protein and its variants. *The Journal of Physical Chemistry B*, 116(36):1113711147, 2012.

[347] Marc Nadal-Ferret, Ricard Gelabert, Miquel Moreno, and Jos M. Lluch. How does the environment affect the absorption spectrum of the fluorescent protein mkeima? *Journal of Chemical Theory and Computation*, 9(3):17311742, 2013.

[348] Ali Hanoon Al-Subi, Marja Niemi, Nikolai V. Tkachenko, and Helge Lemmetyinen. Quantitative analysis of intramolecular exciplex and electron transfer in a double-linked zinc porphyrinfullerene dyad. *The Journal of Physical Chemistry A*, 116(39):96539661, 2012.

[349] Marius Koch, Romain Letrun, and Eric Vauthey. Exciplex formation in bimolecular photoinduced electron-transfer investigated by ultrafast time-resolved infrared spectroscopy. *Journal of the American Chemical Society*, 136(10):40664074, 2014.

[350] Tomoki Ogoshi, Shogo Azuma, Keisuke Wada, Yuko Tamura, Kenichi Kato, Shunsuke Ohtani, Takahiro Kakuta, and Tada-Aki Yamagishi. Exciplex formation by complexation of an electron-accepting guest in an electron-donating pillar[5]arene host liquid. *Journal of the American Chemical Society*, 146(14):98289835, 2024.

[351] I. Read, A. Napper, R. Kaplan, M. B. Zimmt, and D. H. Waldeck. Solvent-mediated electronic coupling: The role of solvent placement. *Journal of the American Chemical Society*, 121(47):1097610986, 1999.

[352] Leonid Sheps, Elisa M. Miller, Samantha Horvath, Matthew A. Thompson, Robert Parson, Anne B. McCoy, and W. Carl Lineberger. Solvent-mediated electron hopping: Long-range charge transfer in ibr-(co2) photodissociation. *Science*, 328(5975):220224, 2010.

[353] Jos Nelson Onuchic and David N. Beratan. A predictive theoretical model for electron tunneling pathways in proteins. *The Journal of Chemical Physics*, 92(1):722733, 1990.

[354] Dale McMorrow and Thijs J. Aartsma. Solvent-mediated proton transfer. the roles of solvent structure and dynamics on the excited-state tautomerization of 7-azaindole/alcohol complexes. *Chemical Physics Letters*, 125(56):581585, 1986.

[355] Simone Morpurgo, Mario Bossa, and Giorgio O. Morpurgo. *Solvent-mediated proton transfer reactions in cytosine: an ab initio study.* Elsevier, 2000.

[356] Boris Ucur, Alan T. Maccarone, Shane R. Ellis, Stephen J. Blanksby, and Adam J. Trevitt. Solvent-mediated proton-transfer catalysis of the gas-phase isomerization of ciprofloxacin protomers. *Journal of the American Society for Mass Spectrometry*, 33(2):347354, 2022.

[357] Yunkai Yu, Jianhao Wang, Nan Fang, Zhen Chen, Dongxu Liu, Yueming Liu, and Mingyuan He. Evidence of solvent-mediated proton transfer during h2o2 activation in titanosilicate-catalyzed oxidation systems. *Physical Chemistry Chemical Physics*, 25(17):1222012230, 2023.

[358] Anne Myers Kelley. *Electronic Spectroscopy*, chapter 8, pages 139–162. John Wiley and Sons, Ltd, 2012.

[359] E. W. Knapp and S. F. Fischer. On the theory of homogeneous and inhomogeneous line broadening. an exactly solvable model. *The Journal of Chemical Physics*, 74(1):8995, 1981.

[360] Josep Gelpi, Adam Hospital, Ramn Goi, and Modesto Orozco. Molecular dynamics simulations: advances and applications. *Advances and Applications in Bioinformatics and Chemistry*, page 37, 2015.

[361] Scott A. Hollingsworth and Ron O. Dror. Molecular dynamics simulation for all. *Neuron*, 99(6):11291143, 2018.

[362] Junmei Wang, Romain M. Wolf, James W. Caldwell, Peter A. Kollman, and David A. Case. Development and testing of a general amber force field. *Journal of Computational Chemistry*, 25(9):11571174, 2004.

[363] Xibing He, Viet H. Man, Wei Yang, Tai-Sung Lee, and Junmei Wang. A fast and high-quality charge model for the next generation general amber force field. *The Journal of Chemical Physics*, 153(11):114502, September 2020.

[364] Isabella Daidone, Andrea Amadei, Danilo Roccatano, and Alfredo Di Nola. Molecular dynamics simulation of protein folding by essential dynamics sampling: Folding landscape of horse heart cytochrome c. *Biophysical Journal*, 85(5):28652871, 2003.

[365] Lili Duan, Xiaona Guo, Yalong Cong, Guoqiang Feng, Yuchen Li, and John Z. H. Zhang. Accelerated molecular dynamics simulation for helical proteins folding in explicit water. *Frontiers in Chemistry*, 7, 2019.

[366] Juan J. Galano-Frutos, Francho Nern-Fonz, and Javier Sancho. Calculation of protein folding thermodynamics using molecular dynamics simulations. *Journal of Chemical Information and Modeling*, 63(24):77917806, 2023.

[367] Wolfgang Swegat, Jrgen Schlitter, Peter Krger, and Axel Wollmer. Md simulation of protein-ligand interaction: Formation and dissociation of an insulin-phenol complex. *Biophysical Journal*, 84(3):14931506, 2003.

[368] Ahmad Abu Turab Naqvi, Taj Mohammad, Gulam Mustafa Hasan, and Md. Imtaiyaz Hassan. Advancements in docking and molecular dynamics simulations towards ligand-receptor interactions and structure-function relationships. *Current Topics in Medicinal Chemistry*, 18(20):17551768, 2018.

[369] E LINDAHL and M SANSOM. Membrane proteins: molecular dynamics simulations. *Current Opinion in Structural Biology*, 18(4):425431, 2008.

[370] Kenneth Goossens and Hans De Winter. Molecular dynamics simulations of membrane proteins: An overview. *Journal of Chemical Information and Modeling*, 58(11):21932202, 2018.

[371] Jacob D Durrant and J Andrew McCammon. Molecular dynamics simulations and drug discovery. *BMC Biology*, 9(1), 2011.

[372] Radu Iftimie, Peter Minary, and Mark E. Tuckerman. Ab initio molecular dynamics: Concepts, recent developments, and future trends. *Proceedings of the National Academy of Sciences*, 102(19):66546659, 2005.

[373] Eric Paquet and Herna L. Viktor. Computational methods for ab initio molecular dynamics. *Advances in Chemistry*, 2018:114, 2018.

[374] Jrg Hutter, Marcella Iannuzzi, and Thomas D. Khne. *Ab Initio Molecular Dynamics: A Guide to Applications*. Elsevier, 2024.

[375] A. Warshel and M. Levitt. Theoretical studies of enzymic reactions: Dielectric, electrostatic and steric stabilization of the carbonium ion in the reaction of lysozyme. *Journal of Molecular Biology*, 103(2):227249, 1976.

[376] Hai Lin and Donald G. Truhlar. Qm/mm: what have we learned, where are we, and where do we go from here? *Theoretical Chemistry Accounts*, 117(2), 2006.

[377] Mattia Bondanza, Michele Nottoli, Lorenzo Cupellini, Filippo Lipparini, and Benedetta Mennucci. Polarizable embedding qm/mm: the future gold standard for complex (bio)systems? *Physical Chemistry Chemical Physics*, 22(26):1443314448, 2020.

[378] Simone Bonfrate, Nicolas Ferr, and Miquel Huix-Rotllant. An efficient electrostatic embedding qm/mm method using periodic boundary conditions based on particle-mesh ewald sums and electrostatic potential fitted charge operators. *The Journal of Chemical Physics*, 158(2), 2023.

[379] Boyi Zhou, Yanzi Zhou, and Daiqian Xie. Accelerated quantum mechanics/molecular mechanics simulations via neural networks incorporated with mechanical embedding scheme. *Journal of Chemical Theory and Computation*, 19(4):11571169, 2023.

[380] Fabian Bauch, Chuan-Ding Dong, and Stefan Schumacher. Dynamics-induced charge transfer in semiconducting conjugated polymers. *Journal of Materials Chemistry C*, 11(38):1299212998, 2023.

[381] J. Patrick Zobel and Leticia Gonzlez. The quest to simulate excited-state dynamics of transition metal complexes. *JACS Au*, 1(8):11161140, 2021.

[382] Joost VandeVondele, Urban Bortnik, and Jrg Hutter. Linear scaling self-consistent field calculations with millions of atoms in the condensed phase. *Journal of Chemical Theory and Computation*, 8(10):35653573, 2012.

[383] Hao Hu and Weitao Yang. Development and application of ab initio qm/mm methods for mechanistic simulation of reactions in solution and in enzymes. *Journal of Molecular Structure: THEOCHEM*, 898(13):1730, 2009.

[384] Alessio Lodola and Marco De Vivo. *The Increasing Role of QM/MM in Drug Discovery*. Elsevier, 2012.

[385] GiovanniMaria Piccini, Mal-Soon Lee, Simuck F. Yuk, Difan Zhang, Greg Collinge, Loukas Kollias, Manh-Thuong Nguyen, Vassiliki-Alexandra Glezakou, and Roger Rousseau. Ab initio molecular dynamics with enhanced sampling in heterogeneous catalysis. *Catalysis Science and Technology*, 12(1):1237, 2022.

[386] Antnio J.R. da Silva, Hsiu-Yao Cheng, Douglas A. Gibson, Kathy L. Sorge, Zhihua Liu, and Emily A. Carter. Limitations of ab initio molecular dynamics simulations of simple reactions: F + h2 as a prototype. *Spectrochimica Acta Part A: Molecular and Biomolecular Spectroscopy*, 53(8):12851299, 1997.

[387] Zhuoqiang Guo, Denghui Lu, Yujin Yan, Siyu Hu, Rongrong Liu, Guangming Tan, Ninghui Sun, Wanrun Jiang, Lijun Liu, Yixiao Chen, Linfeng Zhang, Mohan Chen, Han Wang, and Weile Jia. *Extending the limit of molecular dynamics with ab initio accuracy to 10 billion atoms*. PPoPP 22. ACM, 2022.

[388] Doron Lancet and Israel Pecht. Spectroscopic and immunochemical studies with nitrobenzoxadiazolealanine, a fluorescent dinitrophenyl analog. *Biochemistry*, 16(23):51505157, 1977.

[389] Christine M. Isborn, Andreas W. Götz, Matthew A. Clark, Ross C. Walker, and Todd J. Martínez. Electronic absorption spectra from mm and ab initio qm/mm molecular dynamics: Environmental effects on the absorption spectrum of photoactive yellow proteinn. *Journal of Chemical Theory and Computation*, 8(12):5092–5106, October 2012.

[390] Xiaochuan Ge, Iurii Timrov, Simon Binnie, Alessandro Biancardi, Arrigo Calzolari, and Stefano Baroni. Accurate and inexpensive prediction of the color optical properties of anthocyanins in solution. *The Journal of Physical Chemistry A*, 119(16):38163822, April 2015.

[391] T. J. Zuehlsdorff, P. D. Haynes, F. Hanke, M. C. Payne, and N. D. M. Hine. Solvent effects on electronic excitations of an organic chromophore. *Journal of Chemical Theory and Computation*, 12(4):18531861, March 2016.

[392] T. J. Zuehlsdorff, P. D. Haynes, M. C. Payne, and N. D. M. Hine. Predicting solvatochromic shifts and colours of a solvated organic dye: The example of nile red. *The Journal of Chemical Physics*, 146(12), March 2017.

[393] John P. Bergsma, Peter H. Berens, Kent R. Wilson, Donald R. Fredkin, and Eric J. Heller. Electronic spectra from molecular dynamics: a simple approach. *The Journal of Physical Chemistry*, 88(3):612–619, 1984.

[394] Jeffrey R Reimers, Kent R Wilson, and Eric J Heller. Complex time-dependent wave packet technique for thermal equilibrium systems: Electronic spectra. *J. Chem. Phys.*, 79(10):4749–4757, November 1983.

[395] Rachel Crespo-Otero and Mario Barbatti. Spectrum simulation and decomposition with nuclear ensemble: formal derivation and application to benzene, furan and 2-phenylfuran. *Theoretical Chemistry Accounts*, 131(6), June 2012.

[396] Fábris Kossoski and Mario Barbatti. Nuclear ensemble approach with importance sampling. *Journal of Chemical Theory and Computation*, 14(6):3173–3183, April 2018.

[397] Weixuan Zeng, Shaolong Gong, Cheng Zhong, and Chuluo Yang. Prediction of oscillator strength and transition dipole moments with the nuclear ensemble approach for thermally activated delayed fluorescence emitters. *The Journal of Physical Chemistry C*, 123(15):1008110086, March 2019.

[398] . "Sre, D. Hollas, and P." Slavek. Uv absorption of criegee intermediates: quantitative cross sections from high-level ab initio theory. *Physical Chemistry Chemical Physics*, 20(9):64216430, 2018.

[399] tpn "Sre, Jaroslav Sita, Petr Slavek, Vt Ladnyi, and Dominik" Heger. Limits of the nuclear ensemble method for electronic spectra simulations: Temperature dependence of the (e)-azobenzene spectrum. *Journal of Chemical Theory and Computation*, 16(10):64286438, August 2020.

[400] tpn "Sre and Petr" Slavek. Optimal representation of the nuclear ensemble: Application to electronic spectroscopy. *Journal of Chemical Theory and Computation*, 17(10):63956404, September 2021.

[401] Antonio "Prlj, Emanuele Marsili, Lewis Hutton, Daniel Hollas, Darya Shchepanovska, David R. Glowacki, Petr Slavek, and Basile F. E." Curchod. Calculating photoabsorption cross-sections for atmospheric volatile organic compounds. *ACS Earth and Space Chemistry*, 6(1):207217, December 2021.

[402] Dina Gegiou, K. A. Muszkat, and Ernst Fischer. Temperature dependence of photoisomerization. VI. viscosity effect. *Journal of the American Chemical Society*, 90(1):12–18, January 1968.

[403] Bao-Xin Xue, Mario Barbatti, and Pavlo O. Dral. Machine learning for absorption cross sections. *The Journal of Physical Chemistry A*, 124(35):7199–7210, August 2020.

[404] Fabrizio Santoro, Alessandro Lami, Roberto Improta, Julien Bloino, and Vincenzo Barone. Effective method for the computation of optical spectra of large molecules at finite temperature including the duschinsky and herzbergteller effect: The qx band of porphyrin as a case study. *The Journal of Chemical Physics*, 128(22), June 2008.

[405] Fabrizio Santoro and Denis Jacquemin. Going beyond the vertical approximation with timedependent density functional theory. *WIREs Computational Molecular Science*, 6(5):460486, 2016.

[406] Fabrizio Santoro, Alessandro Lami, Roberto Improta, and Vincenzo Barone. Effective method to compute vibrationally resolved optical spectra of large molecules at finite temperature in the gas phase and in solution. *The Journal of Chemical Physics*, 126(18), May 2007.

[407] Enrico Tapavicza, Filipp Furche, and Dage Sundholm. Importance of vibronic effects in the uvvis spectrum of the 7, 7, 8, 8-tetracyanoquinodimethane anion. *Journal of Chemical Theory and Computation*, 12(10):50585066, September 2016.

[408] J. Franck and E. G. Dymond. Elementary processes of photochemical reactions. *Transactions of the Faraday Society*, 21(February):536, 1926.

[409] Edward Condon. A theory of intensity distribution in band systems. *Physical Review*, 28(6):1182–1201, December 1926.

[410] Peder Thusgaard Ruhoff and Mark A. Ratner. Algorithms for computing franck-condon overlap integrals. *International Journal of Quantum Chemistry*, 77(1):383–392, 2000.

[411] R. A. Marcus. Relation between charge transfer absorption and fluorescence spectra and the inverted region. *The Journal of Physical Chemistry*, 93(8):3078–3086, April 1989.

[412] Robert Zaleśny, N. Arul Murugan, Faris Gel'mukhanov, Zilvinas Rinkevicius, Borys Ośmiałowski, Wojciech Bartkowiak, and Hans Ågren. Toward fully nonempirical simulations of optical band shapes of molecules in solution: A case study of heterocyclic ketoimine difluoroborates. *The Journal of Physical Chemistry A*, 119(21):5145–5152, December 2014.

[413] Javier Cerezo, Francisco J. Avila Ferrer, Giacomo Prampolini, and Fabrizio Santoro. Modeling solvent broadening on the vibronic spectra of a series of coumarin dyes. from implicit to explicit solvent models. *Journal of Chemical Theory and Computation*, 11(12):5810–5825, November 2015.

[414] S. Miertus, E. Scrocco, and J. Tomasi. Electrostatic interaction of a solute with a continuum. a direct utilizaion of AB initio molecular potentials for the prevision of solvent effects. *Chemical Physics*, 55(1):117–129, February 1981.

[415] S. Miertus and J. Tomasi. Approximate evaluations of the electrostatic free energy and internal energy changes in solution processes. *Chemical Physics*, 65(2):239–245, March 1982.

[416] J. L. Pascual-ahuir, E. Silla, and I. Tuñon. GEPOL: An improved description of molecular surfaces. III. a new algorithm for the computation of a solvent-excluding surface. *Journal of Computational Chemistry*, 15(10):1127–1138, October 1994.

[417] Vincenzo Barone and Maurizio Cossi. Quantum calculation of molecular energies and energy gradients in solution by a conductor solvent model. *The Journal of Physical Chemistry A*, 102(11):1995–2001, February 1998.

[418] R. Cammi. Coupled-cluster theories for the polarizable continuum model. II. analytical gradients for excited states of molecular solutes by the equation of motion coupled-cluster method. *International Journal of Quantum Chemistry*, 110(15):3040–3052, August 2010.

[419] Anirban Hazra, Hannah H. Chang, and Marcel Nooijen. First principles simulation of the UV absorption spectrum of ethylene using the vertical franck-condon approach. *The Journal of Chemical Physics*, 121(5):2125–2136, August 2004.

[420] Fabrizio Santoro, Chiara Cappelli, and Vincenzo Barone. Effective time-independent calculations of vibrational resonance raman spectra of isolated and solvated molecules including duschinsky and herzbergteller effects. *Journal of Chemical Theory and Computation*, 7(6):18241839, April 2011.

[421] Francisco J. Avila Ferrer, Vincenzo Barone, Chiara Cappelli, and Fabrizio Santoro. Duschinsky, herzbergteller, and multiple electronic resonance interferential effects in resonance raman spectra and excitation profiles. the case of pyrene. *Journal of Chemical Theory and Computation*, 9(8):35973611, July 2013.

[422] Pan Yang, Min Pang, Wei Shen, Ming Li, and Rongxing He. Vibronic analysis of the 1lb↔s0 transitions of indole and 3-methylindole: The influence of anharmonic, duschinsky, and herzberg–teller contributions. *Journal of Molecular Spectroscopy*, 313:40–48, July 2015.

[423] Francisco J. Avila Ferrer, Mehdi D. Davari, Dmitry Morozov, Gerrit Groenhof, and Fabrizio Santoro. The lineshape of the electronic spectrum of the green fluorescent protein chromophore, part II: Solution phase. *ChemPhysChem*, 15(15):3246–3257, September 2014.

[424] Huan Wang, Chaoyuan Zhu, Jian-Guo Yu, and Sheng Hsien Lin. Anharmonic franck-condon simulation of the absorption and fluorescence spectra for the low-lying s1 and s2 excited states of pyridine. *The Journal of Physical Chemistry A*, 113(52):14407–14414, July 2009.

[425] Valerie Rodriguez-Garcia, Kiyoshi Yagi, Kimihiko Hirao, Suehiro Iwata, and So Hirata. Franck-condon factors based on anharmonic vibrational wave functions of polyatomic molecules. *The Journal of Chemical Physics*, 125(1), 2006.

[426] Joonsuk Huh and Robert Berger. Application of time-independent cumulant expansion to calculation of franckcondon profiles for large molecular systems. *Faraday Discussions*, 150:363, 2011.

[427] Ernest R. Davidson and Andrzej A. Jarzecki. Zero point corrections to vertical excitation energies. *Chemical Physics Letters*, 285(3):155–159, 1998.

[428] Carlo Adamo and Denis Jacquemin. The calculations of excited-state properties with time-dependent density functional theory. *Chem. Soc. Rev.*, 42(3):845856, 2013.

[429] Changfeng Fang, Baswanth Oruganti, and Bo Durbeej. How method-dependent are calculated differences between vertical, adiabatic, and 00 excitation energies? *The Journal of Physical Chemistry A*, 118(23):41574171, June 2014.

[430] Arturo Alvarez-Buylla, Chang-Ying Ling, and John R. Kirn. Cresyl violet: A red fluorescent nissl stain. *Journal of Neuroscience Methods*, 33(23):129133, 1990.

[431] Philip P. Ostrowski, Gregory D. Fairn, Sergio Grinstein, and Danielle E. Johnson. Cresyl violet: a superior fluorescent lysosomal marker. *Traffic*, 17(12):13131321, 2016.

[432] Christopher A. Myers, Shao-Yu Lu, Sapana Shedge, Arthur Pyuskulyan, Katherine Donahoe, Ajay Khanna, Liang Shi, and Christine M. Isborn. Axial h-bonding solvent controls inhomogeneous spectral broadening, while peripheral h-bonding solvent controls vibronic broadening: Cresyl violet in methanol. *The Journal of Physical Chemistry B*, 128(23):56855699, 2024.

[433] Johanna Brazard, Laurie A. Bizimana, Tobias Gellen, William P. Carbery, and Daniel B. Turner. Experimental detection of branching at a conical intersection in a highly fluorescent molecule. *The Journal of Physical Chemistry Letters*, 7(1):1419, 2015.

[434] D. Porezag, Th. Frauenheim, Th. Khler, G. Seifert, and R. Kaschner. Construction of tight-binding-like potentials on the basis of density-functional theory: Application to carbon. *Physical Review B*, 51(19):1294712957, 1995.

[435] M. Elstner, D. Porezag, G. Jungnickel, J. Elsner, M. Haugk, Th. Frauenheim, S. Suhai, and G. Seifert. Self-consistent-charge density-functional tight-binding method for simulations of complex materials properties. *Physical Review B*, 58(11):72607268, 1998.

[436] John M. Herbert. Dielectric continuum methods for quantum chemistry. *WIREs Computational Molecular Science*, 11(4), March 2021.

[437] Shaul Mukamel. *Principles of Nonlinear Optical Spectroscopy*. Oxford University Press, New York, 1995.

[438] Emanuele Falbo, Marco Fus, Federico Lazzari, Giordano Mancini, and Vincenzo Barone. Integration of quantum chemistry, statistical mechanics, and artificial intelligence for computational spectroscopy: The uvvis spectrum of tempo radical in

different solvents. *Journal of Chemical Theory and Computation*, 18(10):62036216, 2022.

[439] D.A. Case, H.M. Aktulga, K. Belfon, I.Y. Ben-Shalom, J.T. Berryman, S.R. Brozell, D.S. Cerutti, T.E. Cheatham, III, G.A. Cisneros, V.W.D. Cruzeiro, T.A. Darden, R.E. Duke, G. Giambasu, M.K. Gilson, H. Gohlke, A.W. Goetz, R. Harris, S. Izadi, S.A. Izmailov, K. Kasavajhala, M.C. Kaymak, E. King, A. Kovalenko, T. Kurtzman, T.S. Lee, S. LeGrand, P. Li, C. Lin, J. Liu, T. Luchko, R. Luo, M. Machado, V. Man, M. Manathunga, K.M. Merz, Y. Miao, O. Mikhailovskii, G. Monard, H. Nguyen, K.A. O'Hearn, A. Onufriev, F. Pan, S. Pantano, R. Qi, A. Rahnamoun, D.R. Roe, A. Roitberg, C. Sagui, S. Schott-Verdugo, A. Shajan, J. Shen, C.L. Simmerling, N.R. Skrynnikov, J. Smith, J. Swails, R.C. Walker, J. Wang, J. Wang, H. Wei, R.M. Wolf, X. Wu, Y. Xiong, Y. Xue, D.M. York, S. Zhao, , and P.A. Kollman. Amber. *University of California, San Francisco*, 2022.

[440] R. Ditchfield, W. J. Hehre, and J. A. Pople. Self-consistent molecular-orbital methods. IX. an extended gaussian-type basis for molecular-orbital studies of organic molecules. *The Journal of Chemical Physics*, 54(2):724–728, January 1971.

[441] Michelle M. Francl, William J. Pietro, Warren J. Hehre, J. Stephen Binkley, Mark S. Gordon, Douglas J. DeFrees, and John A. Pople. Self-consistent molecular orbital methods. XXIII. a polarization-type basis set for second-row elements. *The Journal of Chemical Physics*, 77(7):3654–3665, October 1982.

[442] R.J Woods and R Chappelle. Restrained electrostatic potential atomic partial charges for condensed-phase simulations of carbohydrates. *Journal of Molecular Structure: THEOCHEM*, 527(1-3):149–156, August 2000.

[443] Lisa Emily Chirlian and Michelle Miller Francl. Atomic charges derived from electrostatic potentials: A detailed study. *Journal of Computational Chemistry*, 8(6):894–905, September 1987.

[444] R. Cammi, S. Corni, B. Mennucci, and J. Tomasi. Electronic excitation energies of molecules in solution: State specific and linear response methods for nonequilibrium continuum solvation models. *The Journal of Chemical Physics*, 122(10), March 2005.

[445] S. Corni, R. Cammi, B. Mennucci, and J. Tomasi. Electronic excitation energies of molecules in solution within continuum solvation models: Investigating the discrepancy between state-specific and linear-response methods. *The Journal of Chemical Physics*, 123(13), October 2005.

[446] Ciro A. Guido, Denis Jacquemin, Carlo Adamo, and Benedetta Mennucci. Electronic excitations in solution: The interplay between state specific approaches and a time-dependent density functional theory description. *Journal of Chemical Theory and Computation*, 11(12):57825790, November 2015.

[447] Aleksandr V. Marenich, Christopher J. Cramer, Donald G. Truhlar, Ciro A. Guido, Benedetta Mennucci, Giovanni Scalmani, and Michael J. Frisch. Practical computation of electronic excitation in solution: vertical excitation model. *Chemical Science*, 2(11):2143, 2011.

[448] George B. Bacskay. A quadratically convergent hartree fock qc-scf method: Application to closed shell systems. *Chemical Physics*, 61(3):385–404, October 1981.

[449] Axel D. Becke. A new mixing of hartree–fock and local density-functional theories. *The Journal of Chemical Physics*, 98(2):1372–1377, January 1993.

[450] John C. Burant, Gustavo E. Scuseria, and Michael J. Frisch. A linear scaling method for hartree–fock exchange calculations of large molecules. *The Journal of Chemical Physics*, 105(19):8969–8972, November 1996.

[451] Petr Čársky and Ivan Hubač. Restricted hartree-fock and unrestricted hartree-fock as reference states in many-body perturbation theory: a critical comparison of the two approaches. *Theoretica Chimica Acta*, 80(4-5):407–425, July 1991.

[452] A.B.F. da Silva, H.F.M. da Costa, and M. Trsic. Universal gaussian and slater-type bases for atoms h to xe based on the generator coordinate hartree-fock method. *Molecular Physics*, 68(2):433–445, October 1989.

[453] Junmei Wang, Wei Wang, Peter A. Kollman, and David A. Case. Automatic atom type and bond type perception in molecular mechanical calculations. *Journal of Molecular Graphics and Modelling*, 25(2):247–260, October 2006.

[454] R. Courant. Variational methods for the solution of problems of equilibrium and vibrations. *Bulletin of the American Mathematical Society*, 49(1):1–23, 1943.

[455] BJ Jaidhan. Energy minimization and conformation analysis of molecules using steepest descent method. *International Journal of Computer Science and Information Technologies*, pages 3525–3528, 2014.

[456] M.R. Hestenes and E. Stiefel. Methods of conjugate gradients for solving linear systems. *Journal of Research of the National Bureau of Standards*, 49(6):409, December 1952.

[457] M. C. Payne, M. P. Teter, D. C. Allan, T. A. Arias, and J. D. Joannopoulos. Iterative minimization techniques for ab initio total-energy calculations: molecular dynamics and conjugate gradients. *Reviews of Modern Physics*, 64(4):1045–1097, October 1992.

[458] Xiongwu Wu and Bernard R. Brooks. Self-guided langevin dynamics simulation method. *Chemical Physics Letters*, 381(3-4):512–518, November 2003.

[459] Xiongwu Wu and Bernard R. Brooks. Toward canonical ensemble distribution from self-guided langevin dynamics simulation. *The Journal of Chemical Physics*, 134(13):134108, April 2011.

[460] Xiongwu Wu, Ana Damjanovic, and Bernard R. Brooks. Efficient and unbiased sampling of biomolecular systems in the canonical ensemble: A review of self-guided langevin dynamics. In *Advances in Chemical Physics*, pages 255–326. John Wiley & Sons, Inc., January 2012.

[461] Xiongwu Wu, Bernard R. Brooks, and Eric Vanden-Eijnden. Self-guided langevin dynamics via generalized langevin equation. *Journal of Computational Chemistry*, 37(6):595–601, July 2015.

[462] Xiongwu Wu and Bernard R. Brooks. Force-momentum-based self-guided langevin dynamics: A rapid sampling method that approaches the canonical ensemble. *The Journal of Chemical Physics*, 135(20):204101, November 2011.

[463] Xiongwu Wu, Milan Hodoscek, and Bernard R. Brooks. Replica exchanging self-guided langevin dynamics for efficient and accurate conformational sampling. *The Journal of Chemical Physics*, 137(4):044106, July 2012.

[464] Ljupčo Pejov, Daniel Spångberg, and Kersti Hermansson. Using md snapshots in ab initio and dft calculations: Oh vibrations in the first hydration shell around li+(aq). *The Journal of Physical Chemistry A*, 109(23):5144–5152, May 2005.

[465] G. Andrés Cisneros, Jean-Philip Piquemal, and Thomas A. Darden. Quantum mechanics/molecular mechanics electrostatic embedding with continuous and discrete functions. *The Journal of Physical Chemistry B*, 110(28):13682–13684, June 2006.

[466] Tobias Schwabe, Jógvan Magnus Haugaard Olsen, Kristian Sneskov, Jacob Kongsted, and Ove Christiansen. Solvation effects on electronic transitions: Exploring the performance of advanced solvent potentials in polarizable embedding calculations. *Journal of Chemical Theory and Computation*, 7(7):2209–2217, June 2011.

[467] H. J. C. Berendsen, J. P. M. Postma, W. F. van Gunsteren, A. DiNola, and J. R. Haak. Molecular dynamics with coupling to an external bath. *The Journal of Chemical Physics*, 81(8):36843690, October 1984.

[468] Abhilash Patra, George Baffour Pipim, Anna I. Krylov, and Shaama Mallikarjun Sharada. Performance of density functionals for excited-state properties of isolated chromophores and exciplexes: Emission spectra, solvatochromic shifts, and charge-transfer character. *Journal of Chemical Theory and Computation*, 20(6):25202537, March 2024.

[469] Bernard Valeur. *Characteristics of Fluorescence Emission*. John Wiley and Sons, Ltd, 2001.

[470] S. J. Strickler and Robert A. Berg. Relationship between absorption intensity and fluorescence lifetime of molecules. *The Journal of Chemical Physics*, 37(4):814–822, August 1962.

[471] Takao Itoh. Franck-condon analysis of the absorption and fluorescence spectra of all trans α, ω-diphenylpolyenes with one to seven polyene double bonds. *The Journal of Chemical Physics*, 123(6):064302, August 2005.

[472] Melvin Lax. The franck-condon principle and its application to crystals. *The Journal of Chemical Physics*, 20(11):1752–1760, November 1952.

[473] Francisco Jos Avila Ferrer, Javier Cerezo, Juan Soto, Roberto Improta, and Fabrizio Santoro. First-principle computation of absorption and fluorescence spectra in solution accounting for vibronic structure, temperature effects and solvent inhomogeneous broadening. *Computational and Theoretical Chemistry*, 10401041:328337, July 2014.

[474] Francisco J. Avila Ferrer, Javier Cerezo, Emiliano Stendardo, Roberto Improta, and Fabrizio Santoro. Insights for an accurate comparison of computational data to experimental absorption and emission spectra: Beyond the vertical transition approximation. *Journal of Chemical Theory and Computation*, 9(4):20722082, March 2013.

[475] Yingli Niu, Qian Peng, Chunmei Deng, Xing Gao, and Zhigang Shuai. Theory of excited state decays and optical spectra: Application to polyatomic molecules. *The Journal of Physical Chemistry A*, 114(30):78177831, July 2010.

[476] Koen Veys, Manon H. E. Bousquet, Denis Jacquemin, and Daniel Escudero. Modeling the fluorescence quantum yields of aromatic compounds: Benchmarking the machinery to compute intersystem crossing rates. *Journal of Chemical Theory and Computation*, 19(24):93449357, December 2023.

[477] S. Mazères, V. Schram, J.F. Tocanne, and A. Lopez. 7-nitrobenz-2-oxa-1, 3-diazole-4-yl-labeled phospholipids in lipid membranes: differences in fluorescence behavior. *Biophysical Journal*, 71(1):327–335, July 1996.

[478] Hugo A. L. Filipe, Maria João Moreno, and Luís M. S. Loura. Interaction of 7-nitrobenz-2-oxa-1,3-diazol-4-yl-labeled fatty amines with 1-palmitoyl, 2-oleoyl-sn-glycero-3-phosphocholine bilayers: A molecular dynamics study. *The Journal of Physical Chemistry B*, 115(33):10109–10119, August 2011.

[479] João R. Robalo, J. P. Prates Ramalho, and Luís M. S. Loura. NBD-labeled cholesterol analogues in phospholipid bilayers: Insights from molecular dynamics. *The Journal of Physical Chemistry B*, 117(44):13731–13742, October 2013.

[480] Sean E. Pidgeon, Jonathan M. Fura, William Leon, Morgan Birabaharan, Dmitri Vezenov, and Marcos M. Pires. Metabolic profiling of bacteria by unnatural c-terminated d-amino acids. *Angewandte Chemie International Edition*, 54(21):6158–6162, apr 2015.

[481] Chenyang Jiang, Haojie Huang, Xueying Kang, Liu Yang, Zhen Xi, Hongyan Sun, Michael D. Pluth, and Long Yi. NBD-based synthetic probes for sensing small molecules and proteins: design, sensing mechanisms and biological applications. *Chemical Society Reviews*, 50(13):7436–7495, 2021.

[482] Seiichi Uchiyama, Tomofumi Santa, Takeshi Fukushima, Hiroshi Homma, and Kazuhiro Imai. Effects of the substituent groups at the 4- and 7-positions on the fluorescence characteristics of benzofurazan compounds. *Journal of the Chemical Society, Perkin Transactions 2*, pages 2165–2174, 1998.

[483] Suzanne Fery-Forgues, Jean-Pierre Fayet, and André Lopez. Drastic changes in the fluorescence properties of NBD probes with the polarity of the medium: involvement of a TICT state? *Journal of Photochemistry and Photobiology A: Chemistry*, 70(3):229–243, March 1993.

[484] Yebin Lee, Ilseung Yang, Jung Eun Lee, Sunjin Hwang, Jong Woo Lee, Seung-Soo Um, Thanh Luan Nguyen, Pil J. Yoo, Han Young Woo, Juhyun Park, and Seong Keun Kim. Enhanced photocurrent generation by förster resonance energy transfer between phospholipid-assembled conjugated oligoelectrolytes and nile red. *The Journal of Physical Chemistry C*, 117(7):3298–3307, February 2013.

[485] D. Basting, D. Ouw, and F.P. Schäfer. The phenoxazones: A new class of laser dyes. *Optics Communications*, 18(3):260–262, August 1976.

[486] Richard Plenderleith, Thomas Swift, and Stephen Rimmer. Highly-branched poly(n-isopropyl acrylamide)s with core–shell morphology below the lower critical solution temperature. *RSC Adv.*, 4(92):50932–50937, 2014.

[487] M. M. Davis and H. B. Helzer. Titrimetric and equilibrium studies using indicators related to nile blue a. *Analytical Chemistry*, 38(3):451–461, March 1966.

[488] Alice Ciencialová, Lenka Žáková, Jiří Jiráček, Jana Barthová, and Tomislav Barth. Preparation and characterization of two LysB29 specifically labelled fluorescent derivatives of human insulin. *Journal of Peptide Science*, 10(7):470–478, June 2004.

[489] Frank No, Simon Olsson, Jonas Khler, and Hao Wu. Boltzmann generators: Sampling equilibrium states of many-body systems with deep learning. *Science*, 365(6457), 2019.

[490] Volker L. Deringer, Miguel A. Caro, and Gbor Csnyi. Machine learning interatomic potentials as emerging tools for materials science. *Advanced Materials*, 31(46), 2019.

[491] Stefan Doerr, Maciej Majewski, Adri Prez, Andreas Krmer, Cecilia Clementi, Frank Noe, Toni Giorgino, and Gianni De Fabritiis. Torchmd: A deep learning framework for molecular simulations. *Journal of Chemical Theory and Computation*, 17(4):23552363, 2021.

[492] Raimondas Galvelis, Alejandro Varela-Rial, Stefan Doerr, Roberto Fino, Peter Eastman, Thomas E. Markland, John D. Chodera, and Gianni De Fabritiis. Nnp/mm: Accelerating molecular dynamics simulations with machine learning potentials and molecular mechanics. *Journal of Chemical Information and Modeling*, 63(18):57015708, 2023.

[493] V. Barone, M. Fus, R. Aguado, S. Potenti, I. Len, E. R. Alonso, S. Mata, F. Lazzari, G. Mancini, L. Spada, A. Gualandi, P. G. Cozzi, C. Puzzarini, and J. L. Alonso. Bringing machinelearning enhanced quantum chemistry and microwave spectroscopy to conformational landscape exploration: the paradigmatic case of 4fluorothreonine. *Chemistry A European Journal*, 29(24), 2023.

[494] Vincenzo Barone, Marco Fus, Federico Lazzari, and Giordano Mancini. Benchmark structures and conformational landscapes of amino acids in the gas phase: A joint venture of machine learning, quantum chemistry, and rotational spectroscopy. *Journal of Chemical Theory and Computation*, 19(4):12431260, 2023.

[495] Ewa M. Goldys, editor. *Fluorescence applications in biotechnology and life sciences*. Wiley-Blackwell, Wiley, United Kingdom, 2009.

[496] Rienk van Grondelle, Jan P. Dekker, Tomas Gillbro, and Villy Sundstrom. Energy transfer and trapping in photosynthesis. *Biochimica et Biophysica Acta (BBA) - Bioenergetics*, 1187(1):165, 1994.

[497] Elisabetta Collini, Carles Curutchet, Tihana Mirkovic, and Gregory D. Scholes. *Electronic Energy Transfer in Photosynthetic Antenna Systems*. Springer Berlin Heidelberg, 2009.

[498] Th. Frster. Zwischenmolekulare energiewanderung und fluoreszenz. *Annalen der Physik*, 437(12):5575, 1948.

[499] L Stryer and R P Haugland. Energy transfer: a spectroscopic ruler. *Proceedings of the National Academy of Sciences*, 58(2):719726, 1967.

[500] Ekaterina Sobakinskaya, Marcel Schmidt am Busch, and Thomas Renger. Theory of fret spectroscopic ruler for short distances: Application to polyproline. *The Journal of Physical Chemistry B*, 122(1):5467, 2017.

[501] Benjamin Schuler. Singlemolecule fluorescence spectroscopy of protein folding. *ChemPhysChem*, 6(7):12061220, 2005.

[502] Igor D. Zlotnikov, Alexander A. Ezhov, and Elena V. Kudryashova. Intermolecular fret pairs as an approach to visualize specific enzyme activity in model biomembranes and living cells. *Biophysica*, 4(3):340356, 2024.

[503] Yoshiyuki Arai and Takeharu Nagai. Extensive use of fret in biological imaging. *Microscopy*, 62(4):419428, 2013.

[504] Kim F. Wong, Biman Bagchi, and Peter J. Rossky. Distance and orientation dependence of excitation transfer rates in conjugated systems: Beyond the frster theory. *The Journal of Physical Chemistry A*, 108(27):57525763, 2004.

[505] Aurora Muoz-Losa, Carles Curutchet, Brent P. Krueger, Lydia R. Hartsell, and Benedetta Mennucci. Fretting about fret: Failure of the ideal dipole approximation. *Biophysical Journal*, 96(12):47794788, 2009.

[506] J. Dominik Spiegel, Simone Fulle, Martin Kleinschmidt, Holger Gohlke, and Christel M. Marian. Failure of the ida in fret systems at close inter-dye distances is moderated by frequent low 2 values. *The Journal of Physical Chemistry B*, 120(34):88458862, 2016.

[507] Brent P. Krueger, Gregory D. Scholes, and Graham R. Fleming. Calculation of couplings and energy-transfer pathways between the pigments of lh2 by the ab initio transition density cube method. *The Journal of Physical Chemistry B*, 102(27):53785386, 1998.

[508] Darren B. VanBeek, Matthew C. Zwier, Justin M. Shorb, and Brent P. Krueger. Fretting about fret: Correlation between and r. *Biophysical Journal*, 92(12):41684178, 2007.

[509] Asif Iqbal, Sinan Arslan, Burak Okumus, Timothy J. Wilson, Gerard Giraud, David G. Norman, Taekjip Ha, and David M. J. Lilley. Orientation dependence in fluorescent energy transfer between cy3 and cy5 terminally attached to double-stranded nucleic acids. *Proceedings of the National Academy of Sciences*, 105(32):1117611181, 2008.

[510] Ben Corry, Dylan Jayatilaka, Boris Martinac, and Paul Rigby. Determination of the orientational distribution and orientation factor for transfer between membrane-bound fluorophores using a confocal microscope. *Biophysical Journal*, 91(3):10321045, 2006.

[511] B.W. van der Meer. Kappa-squared: from nuisance to new sense. *Reviews in Molecular Biotechnology*, 82(3):181196, 2002.

[512] Evelyne Deplazes, Dylan Jayatilaka, and Ben Corry. Testing the use of molecular dynamics to simulate fluorophore motions and fret. *Physical Chemistry Chemical Physics*, 13(23):11045, 2011.

[513] Maria Khrenova, Igor Topol, Jack Collins, and Alexander Nemukhin. Estimating orientation factors in the fret theory of fluorescent proteins: The tagrfp-kfp pair and beyond. *Biophysical Journal*, 108(1):126132, 2015.

[514] Kazuhiro J. Fujimoto, Tomoya Miyashita, Takehisa Dewa, and Takeshi Yanai. Determination of fret orientation factor between artificial fluorophore and photosynthetic light-harvesting 2 complex (lh2). *Scientific Reports*, 12(1), 2022.

[515] Ana Damjanovi, Thorsten Ritz, and Klaus Schulten. Energy transfer between carotenoids and bacteriochlorophylls in light-harvesting complex ii of purple bacteria. *Physical Review E*, 59(3):32933311, 1999.

[516] Ana Damjanovi, Thorsten Ritz, and Klaus Schulten. Excitation transfer in the peridinin-chlorophyll-protein of amphidinium carterae. *Biophysical Journal*, 79(4):16951705, 2000.

[517] Zhi-Qiang You and Chao-Ping Hsu. Ab inito study on triplet excitation energy transfer in photosynthetic light-harvesting complexes. *The Journal of Physical Chemistry A*, 115(16):40924100, 2011.

[518] D. L. Dexter. A theory of sensitized luminescence in solids. *The Journal of Chemical Physics*, 21(5):836850, 1953.

[519] Chao-Ping Hsu, Graham R. Fleming, Martin Head-Gordon, and Teresa Head-Gordon. Excitation energy transfer in condensed media. *The Journal of Chemical Physics*, 114(7):30653072, 2001.

[520] Sang-Il Choi, Joshua Jortner, Stuart A. Rice, and Robert Silbey. Charge-transfer exciton states in aromatic molecular crystals. *The Journal of Chemical Physics*, 41(11):32943306, 1964.

[521] Joshua Jortner, Stuart A. Rice, Joseph L. Katz, and Sang-Il Choi. Triplet excitons in crystals of aromatic molecules. *The Journal of Chemical Physics*, 42(1):309323, 1965.

[522] Sharona-Tal Levy and Shammai Speiser. Calculation of the exchange integral for short range intramolecular electronic energy transfer in bichromophoric molecules. *The Journal of Chemical Physics*, 96(5):35853593, 1992.

[523] ZhiQiang You and ChaoPing Hsu. Theory and calculation for the electronic coupling in excitation energy transfer. *International Journal of Quantum Chemistry*, 114(2):102115, 2013.

[524] Alexander A. Voityuk. Interaction of dark excited states. comparison of computational approaches. *The Journal of Physical Chemistry B*, 119(24):74177421, 2014.

[525] Gregory D. Scholes and Graham R. Fleming. *ENERGY TRANSFER AND PHOTOSYNTHETIC LIGHT HARVESTING*, volume 132 of *Advances in Chemical Physics*. "John Wiley and Sons Inc.", 2006.

[526] M. E. Madjet, A. Abdurahman, and T. Renger. Intermolecular coulomb couplings from ab initio electrostatic potentials: Application to optical transitions of strongly coupled pigments in photosynthetic antennae and reaction centers. *The Journal of Physical Chemistry B*, 110(34):1726817281, 2006.

[527] Julian Adolphs, Frank Mh, Mohamed El-Amine Madjet, Marcel Schmidt am Busch, and Thomas Renger. Structure-based calculations of optical spectra of photosystem i suggest an asymmetric light-harvesting process. *Journal of the American Chemical Society*, 132(10):33313343, 2010.

[528] Thomas Renger and Frank Mh. Theory of excitonic couplings in dielectric media: Foundation of poisson-tresp method and application to photosystem i trimers. *Photosynthesis Research*, 111(12):4752, 2011.

[529] R. S. Mulliken. Electronic population analysis on lcaomo molecular wave functions. i. *The Journal of Chemical Physics*, 23(10):18331840, 1955.

[530] Ana Damjanovi, Thorsten Ritz, and Klaus Schulten. Excitation transfer in the peridinin-chlorophyll-protein of amphidinium carterae. *Biophysical Journal*, 79(4):16951705, 2000.

[531] I. A. Howard, F. Zutterman, G. Deroover, D. Lamoen, and C. Van Alsenoy. Approaches to calculation of exciton interaction energies for a molecular dimer. *The Journal of Physical Chemistry B*, 108(50):1915519162, 2004.

[532] C. D. P. Duffy, J. Chmeliov, M. Macernis, J. Sulskus, L. Valkunas, and A. V. Ruban. Modeling of fluorescence quenching by lutein in the plant light-harvesting complex lhcii. *The Journal of Physical Chemistry B*, 117(38):1097410986, 2012.

[533] Kurt A. Kistler, Francis C. Spano, and Spiridoula Matsika. A benchmark of excitonic couplings derived from atomic transition charges. *The Journal of Physical Chemistry B*, 117(7):20322044, 2013.

[534] Kazuhiro J. Fujimoto. Electronic coupling calculations with transition charges, dipoles, and quadrupoles derived from electrostatic potential fitting. *The Journal of Chemical Physics*, 141(21), 2014.

[535] Bartosz Basiak, Micha Maj, Minhaeng Cho, and Robert W. Gra. Distributed multipolar expansion approach to calculation of excitation energy transfer couplings. *Journal of Chemical Theory and Computation*, 11(7):32593266, 2015.

[536] Carsten Olbrich and Ulrich Kleinekathfer. Time-dependent atomistic view on the electronic relaxation in light-harvesting system ii. *The Journal of Physical Chemistry B*, 114(38):1242712437, 2010.

[537] Joseph E. Subotnik, Sina Yeganeh, Robert J. Cave, and Mark A. Ratner. Constructing diabatic states from adiabatic states: Extending generalized mulliken-hush to multiple charge centers with boys localization. *The Journal of Chemical Physics*, 129(24), 2008.

[538] Chao-Ping Hsu. The electronic couplings in electron transfer and excitation energy transfer. *Accounts of Chemical Research*, 42(4):509518, 2009.

[539] Jos M. F. Ten Berge. J.c. gower and g.b. dijksterhuis.procrustes problems. new york: Oxford university press. *Psychometrika*, 70(4):799801, 2005.

[540] Robert S. Knox and Herbert van Amerongen. Refractive index dependence of the frster resonance excitation transfer rate. *The Journal of Physical Chemistry B*, 106(20):52895293, 2002.

[541] Jacopo Tomasi, Benedetta Mennucci, and Roberto Cammi. Quantum mechanical continuum solvation models. *Chemical Reviews*, 105(8):29993094, 2005.

[542] Maria Francesca Iozzi, Benedetta Mennucci, Jacopo Tomasi, and Roberto Cammi. Excitation energy transfer (eet) between molecules in condensed matter: A novel application of the polarizable continuum model (pcm). *The Journal of Chemical Physics*, 120(15):70297040, 2004.

[543] Carles Curutchet, Aurora Muoz-Losa, Susanna Monti, Jacob Kongsted, Gregory D. Scholes, and Benedetta Mennucci. Electronic energy transfer in condensed phase studied by a polarizable qm/mm model. *Journal of Chemical Theory and Computation*, 5(7):18381848, 2009.

[544] Carles Curutchet, Jacob Kongsted, Aurora Muoz-Losa, Hoda Hossein-Nejad, Gregory D. Scholes, and Benedetta Mennucci. Photosynthetic light-harvesting is tuned by the heterogeneous polarizable environment of the protein. *Journal of the American Chemical Society*, 133(9):30783084, 2011.

[545] Casper Steinmann and Jacob Kongsted. Electronic energy transfer in polarizable heterogeneous environments: A systematic investigation of different quantum chemical approaches. *Journal of Chemical Theory and Computation*, 11(9):42834293, 2015.

[546] Anne B Satterthwaite, Zuomei Li, and Owen N Witte. Btk function in b cell development and response. *Seminars in Immunology*, 10(4):309316, 1998.

[547] Wasif N Khan. Regulation of b lymphocyte development and activation by brutons tyrosine kinase. *Immunologic Research*, 23(23):147156, 2001.

[548] Uwe Schmidt, Nicole Boucheron, Bernd Unger, and Wilfried Ellmeier. The role of tec family kinases in myeloid cells. *International Archives of Allergy and Immunology*, 134(1):6578, 2004.

[549] B. Mller C. Brunner and T. Wirth. Brutons tyrosine kinase is involved in innate and adaptive immunity. *Histology and Histopathology*, page 945955, Jul 2005.

[550] Julie A Di Paolo, Tao Huang, Mercedesz Balazs, James Barbosa, Kai H Barck, Brandon J Bravo, Richard A D Carano, James Darrow, Douglas R Davies, Laura E DeForge, Lauri Diehl, Ronald Ferrando, Steven L Gallion, Anthony M Giannetti, Peter Gribling, Vincent Hurez, Sarah G Hymowitz, Randall Jones, Jeffrey E Kropf, Wyne P Lee, Patricia M Maciejewski, Scott A Mitchell, Hong Rong, Bart L Staker, J Andrew Whitney, Sherry Yeh, Wendy B Young, Christine Yu, Juan Zhang, Karin Reif, and Kevin S Currie. Specific btk inhibition suppresses b cell and myeloid cellmediated arthritis. *Nature Chemical Biology*, 7(1):4150, 2010.

[551] Ranjana H. Advani, Joseph J. Buggy, Jeff P. Sharman, Sonali M. Smith, Thomas E. Boyd, Barbara Grant, Kathryn S. Kolibaba, Richard R. Furman, Sara Rodriguez, Betty Y. Chang, Juthamas Sukbuntherng, Raquel Izumi, Ahmed Hamdy, Eric Hedrick, and Nathan H. Fowler. Bruton tyrosine kinase inhibitor ibrutinib (pci-32765) has significant activity in patients with relapsed/refractory b-cell malignancies. *Journal of Clinical Oncology*, 31(1):8894, 2013.

[552] John C. Byrd, Richard R. Furman, Steven E. Coutre, Ian W. Flinn, Jan A. Burger, Kristie A. Blum, Barbara Grant, Jeff P. Sharman, Morton Coleman, William G. Wierda, Jeffrey A. Jones, Weiqiang Zhao, Nyla A. Heerema, Amy J. Johnson, Juthamas Sukbuntherng, Betty Y. Chang, Fong Clow, Eric Hedrick, Joseph J. Buggy, Danelle F. James, and Susan OBrien. Targeting btk with ibrutinib in relapsed chronic lymphocytic leukemia. *New England Journal of Medicine*, 369(1):3242, 2013.

[553] Michael L. Wang, Simon Rule, Peter Martin, Andre Goy, Rebecca Auer, Brad S. Kahl, Wojciech Jurczak, Ranjana H. Advani, Jorge E. Romaguera, Michael E. Williams, Jacqueline C. Barrientos, Ewa Chmielowska, John Radford, Stephan Stilgenbauer, Martin Dreyling, Wieslaw Wiktor Jedrzejczak, Peter Johnson, Stephen E. Spurgeon, Lei Li, Liang Zhang, Kate Newberry, Zhishuo Ou, Nancy Cheng, Bingliang Fang, Jesse McGreivy, Fong Clow, Joseph J. Buggy, Betty Y. Chang, Darrin M. Beaupre, Lori A. Kunkel, and Kristie A. Blum. Targeting btk with ibrutinib in relapsed or refractory mantle-cell lymphoma. *New England Journal of Medicine*, 369(6):507516, 2013.

[554] Ariela Noy, Sven de Vos, Catherine Thieblemont, Peter Martin, Christopher R. Flowers, Franck Morschhauser, Graham P. Collins, Shuo Ma, Morton Coleman, Shachar Peles, Stephen Smith, Jacqueline C. Barrientos, Alina Smith, Brian Munneke, Isaiah Dimery, Darrin M. Beaupre, and Robert Chen. Targeting bruton tyrosine kinase with ibrutinib in relapsed/refractory marginal zone lymphoma. *Blood*, 129(16):22242232, 2017.

[555] Zhengying Pan, Heleen Scheerens, ShyrJiann Li, Brian E. Schultz, Paul A. Sprengeler, L. Chuck Burrill, Rohan V. Mendonca, Michael D. Sweeney, Keana C. K.

Scott, Paul G. Grothaus, Douglas A. Jeffery, Jill M. Spoerke, Lee A. Honigberg, Peter R. Young, Stacie A. Dalrymple, and James T. Palmer. Discovery of selective irreversible inhibitors for brutons tyrosine kinase. *ChemMedChem*, 2(1):5861, 2006.

[556] Tadeusz Robak and Ewa Robak. Tyrosine kinase inhibitors as potential drugs for b-cell lymphoid malignancies and autoimmune disorders. *Expert Opinion on Investigational Drugs*, 21(7):921947, 2012.

[557] Yan Lou, Timothy D. Owens, Andreas Kuglstatter, Rama K. Kondru, and David M. Goldstein. Brutons tyrosine kinase inhibitors: Approaches to potent and selective inhibition, preclinical and clinical evaluation for inflammatory diseases and b cell malignancies. *Journal of Medicinal Chemistry*, 55(10):45394550, 2012.

[558] Christopher R. Smith, Douglas R. Dougan, Mallareddy Komandla, Toufike Kanouni, Beverly Knight, J. David Lawson, Mark Sabat, Ewan R. Taylor, Phong Vu, and Corey Wyrick. Fragment-based discovery of a small molecule inhibitor of brutons tyrosine kinase. *Journal of Medicinal Chemistry*, 58(14):54375444, 2015.

[559] Wendy B. Young, James Barbosa, Peter Blomgren, Meire C. Bremer, James J. Crawford, Donna Dambach, Steve Gallion, Sarah G. Hymowitz, Jeffrey E. Kropf, Seung H. Lee, Lichuan Liu, Joseph W. Lubach, Jen Macaluso, Pat Maciejewski, Brigitte Maurer, Scott A. Mitchell, Daniel F. Ortwine, Julie Di Paolo, Karin Reif, Heleen Scheerens, Aaron Schmitt, C. Gregory Sowell, Xiaojing Wang, Harvey Wong, Jin-Ming Xiong, Jianjun Xu, Zhongdong Zhao, and Kevin S. Currie. Potent and selective brutons tyrosine kinase inhibitors: Discovery of gdc-0834. *Bioorganic and Medicinal Chemistry Letters*, 25(6):13331337, 2015.

[560] Wendy B. Young, James Barbosa, Peter Blomgren, Meire C. Bremer, James J. Crawford, Donna Dambach, Charles Eigenbrot, Steve Gallion, Adam R. Johnson, Jeffrey E. Kropf, Seung H. Lee, Lichuan Liu, Joseph W. Lubach, Jen Macaluso, Pat Maciejewski, Scott A. Mitchell, Daniel F. Ortwine, Julie Di Paolo, Karin Reif, Heleen Scheerens, Aaron Schmitt, Xiaojing Wang, Harvey Wong, Jin-Ming Xiong, Jianjun Xu, Christine Yu, Zhongdong Zhao, and Kevin S. Currie. Discovery of highly potent and selective brutons tyrosine kinase inhibitors: Pyridazinone analogs with improved metabolic stability. *Bioorganic and Medicinal Chemistry Letters*, 26(2):575579, 2016.

[561] Xiaojing Wang, James Barbosa, Peter Blomgren, Meire C. Bremer, Jacob Chen, James J. Crawford, Wei Deng, Liming Dong, Charles Eigenbrot, Steve Gallion, Jonathon Hau, Huiyong Hu, Adam R. Johnson, Arna Katewa, Jeffrey E. Kropf, Seung H. Lee, Lichuan Liu, Joseph W. Lubach, Jen Macaluso, Pat Maciejewski, Scott A. Mitchell, Daniel F. Ortwine, Julie DiPaolo, Karin Reif, Heleen Scheerens, Aaron Schmitt, Harvey Wong, Jin-Ming Xiong, Jianjun Xu, Zhongdong Zhao,

Fusheng Zhou, Kevin S. Currie, and Wendy B. Young. Discovery of potent and selective tricyclic inhibitors of brutons tyrosine kinase with improved druglike properties. *ACS Medicinal Chemistry Letters*, 8(6):608613, 2017.

[562] Scott H. Watterson, George V. De Lucca, Qing Shi, Charles M. Langevine, Qingjie Liu, Douglas G. Batt, Myra Beaudoin Bertrand, Hua Gong, Jun Dai, Shiuhang Yip, Peng Li, Dawn Sun, Dauh-Rurng Wu, Chunlei Wang, Yingru Zhang, Sarah C. Traeger, Mark A. Pattoli, Stacey Skala, Lihong Cheng, Mary T. Obermeier, Rodney Vickery, Lorell N. Discenza, Celia J. DArienzo, Yifan Zhang, Elizabeth Heimrich, Kathleen M. Gillooly, Tracy L. Taylor, Claudine Pulicicchio, Kim W. McIntyre, Michael A. Galella, Andy J. Tebben, Jodi K. Muckelbauer, ChiehYing Chang, Richard Rampulla, Arvind Mathur, Luisa Salter-Cid, Joel C. Barrish, Percy H. Carter, Aberra Fura, James R. Burke, and Joseph A. Tino. Discovery of 6-fluoro-5-(r)-(3-(s)-(8-fluoro-1-methyl-2,4-dioxo-1,2-dihydroquinazolin-3(4h)-yl)-2-methylphenyl)-2-(s)-(2-hydroxypropan-2-yl)-2,3,4,9-tetrahydro-1h-carbazole-8-carboxamide (bms-986142): A reversible inhibitor of brutons tyrosine kinase (btk) conformationally constrained by two locked atropisomers. *Journal of Medicinal Chemistry*, 59(19):91739200, 2016.

[563] Lee A. Honigberg, Ashley M. Smith, Mint Sirisawad, Erik Verner, David Loury, Betty Chang, Shyr Li, Zhengying Pan, Douglas H. Thamm, Richard A. Miller, and Joseph J. Buggy. The bruton tyrosine kinase inhibitor pci-32765 blocks b-cell activation and is efficacious in models of autoimmune disease and b-cell malignancy. *Proceedings of the National Academy of Sciences*, 107(29):1307513080, 2010.

[564] John C. Byrd, Bonnie Harrington, Susan OBrien, Jeffrey A. Jones, Anna Schuh, Steve Devereux, Jorge Chaves, William G. Wierda, Farrukh T. Awan, Jennifer R. Brown, Peter Hillmen, Deborah M. Stephens, Paolo Ghia, Jacqueline C. Barrientos, John M. Pagel, Jennifer Woyach, Dave Johnson, Jane Huang, Xiaolin Wang, Allard Kaptein, Brian J. Lannutti, Todd Covey, Maria Fardis, Jesse McGreivy, Ahmed Hamdy, Wayne Rothbaum, Raquel Izumi, Thomas G. Diacovo, Amy J. Johnson, and Richard R. Furman. Acalabrutinib (acp-196) in relapsed chronic lymphocytic leukemia. *New England Journal of Medicine*, 374(4):323332, 2016.

[565] Hana Dostlov, Radek Jorda, Eva eznkov, and Vladimr Krytof. Anticancer effect of zanubrutinib in her2-positive breast cancer cell lines. *Investigational New Drugs*, 41(2):210219, 2023.

[566] Niu Huang and Matthew Jacobson. Physics-based methods for studying protein-ligand interactions. *Current opinion in drug discovery and development*, 10:325–31, 06 2007.

[567] Neal K. Broomhead and Mahmoud E. Soliman. Can we rely on computational predictions to correctly identify ligand binding sites on novel protein drug targets? assessment of binding site prediction methods and a protocol for validation of predicted binding sites. *Cell Biochemistry and Biophysics*, 75(1):1523, 2016.

[568] Vittorio Limongelli. Ligand binding free energy and kinetics calculation in 2020. *WIREs Computational Molecular Science*, 10(4), 2020.

[569] Mikael Perkyl and Tapani A. Pakkanen. Quantum mechanical model assembly study on the energetics of binding of arabinose, fucose, and galactose to larabinose-binding protein. *Proteins: Structure, Function, and Bioinformatics*, 20(4):367372, 1994.

[570] Mikael Perkyl and Tapani A. Pakkanen. Model assembly study of the ligand binding by phydroxybenzoate hydroxylase: Correlation between the calculated binding energies and the experimental dissociation constants. *Proteins: Structure, Function, and Bioinformatics*, 21(1):2229, 1995.

[571] Samuel Genheden and Ulf Ryde. How to obtain statistically converged mm/gbsa results. *Journal of Computational Chemistry*, 31(4):837846, 2009.

[572] Michal Kol, Jindich Fanfrlk, and Pavel Hobza. Ligand conformational and solvation/desolvation free energy in proteinligand complex formation. *The Journal of Physical Chemistry B*, 115(16):47184724, 2011.

[573] Ulf Ryde, Lars Olsen, and Kristina Nilsson. Quantum chemical geometry optimizations in proteins using crystallographic raw data. *Journal of Computational Chemistry*, 23(11):10581070, 2002.

[574] Jayashree Srinivasan, Thomas E. Cheatham, Piotr Cieplak, Peter A. Kollman, and David A. Case. Continuum solvent studies of the stability of dna, rna, and phosphoramidatedna helices. *Journal of the American Chemical Society*, 120(37):94019409, 1998.

[575] Peter A. Kollman, Irina Massova, Carolina Reyes, Bernd Kuhn, Shuanghong Huo, Lillian Chong, Matthew Lee, Taisung Lee, Yong Duan, Wei Wang, Oreola Donini, Piotr Cieplak, Jaysharee Srinivasan, David A. Case, and Thomas E. Cheatham. Calculating structures and free energies of complex molecules: combining molecular mechanics and continuum models. *Accounts of Chemical Research*, 33(12):889897, 2000.

[576] Samuel Genheden and Ulf Ryde. The mm/pbsa and mm/gbsa methods to estimate ligand-binding affinities. *Expert Opinion on Drug Discovery*, 10(5):449461, 2015.

[577] M. Rami Reddy and Mark D. Erion. Relative binding affinities of fructose-1,6-bisphosphatase inhibitors calculated using a quantum mechanics-based free energy perturbation method. *Journal of the American Chemical Society*, 129(30):92969297, 2007.

[578] Christopher Cave-Ayland, Chris-Kriton Skylaris, and Jonathan W. Essex. Direct validation of the single step classical to quantum free energy perturbation. *The Journal of Physical Chemistry B*, 119(3):10171025, 2014.

[579] John G. Kirkwood. Statistical mechanics of fluid mixtures. *The Journal of Chemical Physics*, 3(5):300313, 1935.

[580] Michael R. Shirts and Vijay S. Pande. Comparison of efficiency and bias of free energies computed by exponential averaging, the bennett acceptance ratio, and thermodynamic integration. *The Journal of Chemical Physics*, 122(14), 2005.

[581] Johannes Kstner, Hans Martin Senn, Stephan Thiel, Nikolaj Otte, and Walter Thiel. Qm/mm free-energy perturbation compared to thermodynamic integration and umbrella sampling: application to an enzymatic reaction. *Journal of Chemical Theory and Computation*, 2(2):452461, 2006.

[582] Walter Thiel and Gerhard Hummer. Methods for computational chemistry. *Nature*, 504(7478):9697, 2013.

[583] Rajiv K. Kar. Benefits of hybrid qm/mm over traditional classical mechanics in pharmaceutical systems. *Drug Discovery Today*, 28(1):103374, 2023.

[584] Alexander Alex and Paul Finn. Fast and accurate predictions of relative binding energies. *Journal of Molecular Structure: THEOCHEM*, 398399:551554, 1997.

[585] Christian Hensen, Johannes C. Hermann, Kwangho Nam, Shuhua Ma, Jiali Gao, and Hans-Dieter Hltje. A combined qm/mm approach to proteinligand interactions: polarization effects of the hiv-1 protease on selected high affinity inhibitors. *Journal of Medicinal Chemistry*, 47(27):66736680, 2004.

[586] Yuanchao Li, Yadong Yang, Ping He, and Qingwu Yang. Qm/mm study of epitope peptides binding to hlaa*0201: The roles of anchor residues and water. *Chemical Biology and Drug Design*, 74(6):611618, 2009.

[587] Hans Martin Senn and Walter Thiel. Qm/mm methods for biomolecular systems. *Angewandte Chemie International Edition*, 48(7):11981229, 2009.

[588] Romain Berraud-Pache, Cristina Garcia-Iriepa, and Isabelle Navizet. Modeling chemical reactions by qm/mm calculations: The case of the tautomerization in fireflies bioluminescent systems. *Frontiers in Chemistry*, 6, 2018.

[589] Octav Caldararu, Milica Feldt, Daniela Cioloboc, Marie-Cline van Severen, Kerstin Starke, Ricardo A. Mata, Ebbe Nordlander, and Ulf Ryde. Qm/mm study of the reaction mechanism of sulfite oxidase. *Scientific Reports*, 8(1), 2018.

[590] T. J. Zuehlsdorff and C. M. Isborn. Combining the ensemble and franck-condon approaches for calculating spectral shapes of molecules in solution. *The Journal of Chemical Physics*, 148(2), 2018.

[591] Jingcheng Guan, You Lu, Kakali Sen, Jamal Abdul Nasir, Alec W. Desmoutier, Qing Hou, Xingfan Zhang, Andrew J. Logsdail, Gargi Dutta, Andrew M. Beale,

Richard W. Strange, Chin Yong, Paul Sherwood, Hans M. Senn, C. Richard A. Catlow, Thomas W. Keal, and Alexey A. Sokol. Computational infrared and raman spectra by hybrid qm/mm techniques: a study on molecular and catalytic material systems. *Philosophical Transactions of the Royal Society A: Mathematical, Physical and Engineering Sciences*, 381(2250), 2023.

[592] James J. Crawford, Adam R. Johnson, Dinah L. Misner, Lisa D. Belmont, Georgette Castanedo, Regina Choy, Melis Coraggio, Liming Dong, Charles Eigenbrot, Rebecca Erickson, Nico Ghilardi, Jonathan Hau, Arna Katewa, Pawan Bir Kohli, Wendy Lee, Joseph W. Lubach, Brent S. McKenzie, Daniel F. Ortwine, Leah Schutt, Suzanne Tay, BinQing Wei, Karin Reif, Lichuan Liu, Harvey Wong, and Wendy B. Young. Discovery of gdc-0853: A potent, selective, and noncovalent brutons tyrosine kinase inhibitor in early clinical development. *Journal of Medicinal Chemistry*, 61(6):22272245, 2018.

[593] Molecular operating environment (moe), 2022.02.

[594] Thomas A. Halgren. Merck molecular force field. i. basis, form, scope, parameterization, and performance of mmff94. *Journal of Computational Chemistry*, 17(56):490519, 1996.

[595] M. Born. Volumen und hydratationswrme der ionen. *Zeitschrift fr Physik*, 1(1):4548, 1920.

[596] Peter Eastman, Jason Swails, John D. Chodera, Robert T. McGibbon, Yutong Zhao, Kyle A. Beauchamp, Lee-Ping Wang, Andrew C. Simmonett, Matthew P. Harrigan, Chaya D. Stern, Rafal P. Wiewiora, Bernard R. Brooks, and Vijay S. Pande. Openmm 7: Rapid development of high performance algorithms for molecular dynamics. *PLOS Computational Biology*, 13(7):e1005659, 2017.

[597] James A. Maier, Carmenza Martinez, Koushik Kasavajhala, Lauren Wickstrom, Kevin E. Hauser, and Carlos Simmerling. ff14sb: Improving the accuracy of protein side chain and backbone parameters from ff99sb. *Journal of Chemical Theory and Computation*, 11(8):36963713, 2015.

[598] William L. Jorgensen, Jayaraman Chandrasekhar, Jeffry D. Madura, Roger W. Impey, and Michael L. Klein. Comparison of simple potential functions for simulating liquid water. *The Journal of Chemical Physics*, 79(2):926935, 1983.

[599] Tom Darden, Darrin York, and Lee Pedersen. Particle mesh ewald: An nlog(n) method for ewald sums in large systems. *The Journal of Chemical Physics*, 98(12):1008910092, 1993.

[600] Jean-Paul Ryckaert, Giovanni Ciccotti, and Herman JC Berendsen. Numerical integration of the cartesian equations of motion of a system with constraints: molecular dynamics of n-alkanes. *Journal of computational physics*, 23(3):327–341, 1977.

[601] Oded Farago. Langevin thermostat for robust configurational and kinetic sampling. *Physica A: Statistical Mechanics and its Applications*, 534:122210, 2019.

[602] Oleg A. Vydrov, Jochen Heyd, Aliaksandr V. Krukau, and Gustavo E. Scuseria. Importance of short-range versus long-range hartree-fock exchange for the performance of hybrid density functionals. *The Journal of Chemical Physics*, 125(7), 2006.

[603] Oleg A. Vydrov, Gustavo E. Scuseria, and John P. Perdew. Tests of functionals for systems with fractional electron number. *The Journal of Chemical Physics*, 126(15), 2007.

[604] A. Klamt and G. Schrmann. Cosmo: a new approach to dielectric screening in solvents with explicit expressions for the screening energy and its gradient. *J. Chem. Soc., Perkin Trans. 2*, page 799805, 1993.

[605] Andreas Klamt. *COSMO-RS: From Quantum Chemistry to Fluid Phase Thermodynamics*. Elsevier, 2018.